Durham E-Theses

Optical and microwave spectroscopy of Rydberg excitons in Cu$_2$O

GALLAGHER, LIAM,ANDREW,PATRICK

How to cite:

Use policy

Optical and microwave spectroscopy of Rydberg excitons in Cu$_2$O

Liam A. P. Gallagher

A thesis presented for the degree of
Doctor of Philosophy

Quantum Light and Matter
The University of Durham
United Kingdom
24th January 2022

Optical and microwave spectroscopy of Rydberg excitons in Cu_2O

Liam A. P. Gallagher

Abstract

An experiment was developed to create and study excitonic energy levels in cuprous oxide at 4 K. Excitons were excited using both one-photon and two-photon excitation schemes. A variety of methods were used to characterise the resulting emission, including time-resolved single photon counting and high-resolution spectroscopy. Additionally, microwave antennae were developed to apply microwave fields to the sample with the aim of driving electric dipole transitions between excitonic energy levels. The main result presented in this thesis are: (1) A comparative study of synthetic and natural material revealed the presence of copper vacancies in the synthetic material, which was responsible for limiting the Rydberg series. (2) Narrowband second harmonic generation spectroscopy was used to study Rydberg excitons up to $n = 12$ and allowed the lineshape of the high n even-parity exciton states to be studied. (3) The addition of a microwave field significantly modified the exciton absorption lineshape. In the two-photon regime, applying a microwave field demonstrated coherent modulation of the second harmonic, with sidebands observed. The results were modelled based on microwave-driven electric dipole transitions between Rydberg states. With a simple microwave antenna it was possible to reach a regime where the microwave coupling (Rabi frequency) was comparable to the non-radiatively broadened linewidth of the Rydberg excitons. These result demonstrate the first coupling of Rydberg excitons and microwave fields, provide a new way to manipulate excitonic states, and open up the possibility of a cryogenic microwave to optical transducer based on Rydberg excitons.

Supervisors: Matthew P. A. Jones and Charles S. Adams

Acknowledgements

A PhD is not an individual effort and there are many fantastic people I need to thank. First, I would like to thank my supervisor, Matt Jones. Thank you for giving me this opportunity and for your guidance, encouragement and support throughout. Your enthusiasm has been inspirational. A special mention should also go to my secondary supervisor Charles Adams, for his input and ideas at key points of the project. I would also like to thank the rest of Team Cuprite: Josh, Dani and Jon. It has been a pleasure being a member of this group for the last few years. Special thanks go to Josh for putting up with me for almost 4 years, you taught me a huge amount and the times when we were in the lab building the experiment are some of my favourite memories from my PhD. I would also like to thank Rajan Mistry for his work modelling microwave antennae which proved crucial to the understanding of our results.

Thanks also go to the team in Cardiff: Stephen, Wolfgang and Chris. Their help throughout the project was invaluable and it was a privilege to work in their labs. I am also grateful to our theory collaborators, Peter and Valentin. Thank you for helping us understand our results, and thank you for putting up with questions from naive experimentalists. Thank you to Ian Chaplin and Sophie Edwards from the Earth Sciences department at Durham University for their work polishing samples for this project, and thank you to the members of the mechanical and electronic workshops at Durham University.

Outside of the lab I have to thank my fellow members of QLM. Their warm and inclusive atmosphere has made this experience much more enjoyable. I owe a lot to the regular attendees of fAtMol and fitMol, it always gave me something to look forward to. I would also like to thank the Friday Seminar regulars, who were always there to

eat toasties in the Vic.

Beyond Durham, I would like to thank my parents and sisters. I would not be where I am today without them. Finally, special thanks go to my partner Katie who, despite listening to me complain about the lab and writing a thesis, has encouraged and supported me throughout this process. I would not have managed it without you.

Contents

Declaration

The work in this thesis is based on research carried out in Department of Physics, University of Durham, United Kingdom. The work in this thesis was supported by a studentship from EPSRC and a CASE award from DSTL. The data presented in this thesis is available on request form the author. No part of this thesis has been submitted elsewhere for any other degree or qualification, and it is the sole work of the author unless referenced to the contrary in the text.

List of Figures

List of Tables

Nomenclature

AOM acousto-optic modulator

BPD balanced photodiode

CB conduction band

ECDL external cavity diode laser

EOM electro-optic modulator

FPE Fabry-Pérot etalon

FWHM full width half maximum

IR infra-red

LED light emitting diode

NA numerical aperture

PCB printed circuit board

PBS polarising beam splitter

PL photoluminescence

PLE photoluminescence excitation

ppLN periodically-poled lithium niobate

RFA Raman fibre amplifier

SHG second harmonic generation

SPAD single photon avalanche detector

TPE two-photon excitation

VB valence band

Introduction

Rydberg atoms are atoms excited to states of high principal quantum number, n [1]. Due to the highly excited electron, Rydberg atoms are extremely sensitive to changes in their environment, such as the presence of external fields or other Rydberg states [2; 3; 4]. Rydberg atoms show enhanced interactions when compared to ground state atoms. Long-range Van der Waals interactions between Rydberg atoms leads to the "Rydberg blockade" effect, where the presence of one excitation prevents the creation of another excitation within a blockade radius [5; 6; 7]. In the field of nonlinear quantum optics, Rydberg blockade has been exploited to produce single-photon sources [8; 9; 10], single-photon absorbers [11] and single-photon transistors [12; 13; 14; 15].

Rydberg atoms make excellent sensors of electromagnetic fields. Rydberg states of opposite parity are coupled by electric dipole transitions whose strength scales as n^2 [1]. The frequencies of electric dipole transitions between Rydberg states can vary from radio frequencies to THz, allowing sensing and imaging of electromagnetic fields over a broad frequency range [16; 17; 18; 19; 20; 21; 22]. Rydberg atoms have been coupled to microwave cavities [23; 24] and superconducting microwave resonators [25; 26; 27; 28] which led to them being proposed as microwave-to-optical converters for the readout of superconducting quantum bits (qubits) [29; 27; 30; 31]. However, there are challenges in using Rydberg atoms as a readout of superconducting qubits. Rydberg atom sensors essentially operate in a room temperature black-body environment, even when the atoms themselves are ultra-cold. This is necessary due to the optical access and ultra-high vacuum required to cool and trap the atoms. Superconducting qubits however, must operate in a dilution refrigerator to ensure the thermal photon number is well below one at the resonator frequency. This inherently different environment makes building a hybrid quantum system from Rydberg atoms and superconducting qubits

an ongoing challenge.

Solid-state Rydberg systems have recently emerged as a potential alternative platform for Rydberg physics [32]. These Rydberg systems are based on excitons (bound states of an electron and hole in a semiconductor) instead of atoms. Solid-state Rydberg systems require cryogenic cooling and the highest excited states are only observable in dilution refrigerators [33], making them inherently more compatible with superconducting resonators than atomic systems. In this thesis, solid-state Rydberg states are studied using optical and microwave spectroscopy. The coherent modulation of an optical carrier by a microwave field is demonstrated, which is the first step to building a microwave-to-optical converter based on Rydberg excitons.

Excitons were first theoretically proposed by Frenkel [34] and Wannier [35]. Wannier-Mott excitons are analogous to hydrogen atoms and show a similar ladder of Rydberg energy levels which appear below the bandgap of the material [36; 37; 38; 39; 40; 41]. For most semiconductors the low binding energy of the exciton means very few Rydberg states are accessible [42]. However, cuprous oxide shows an extraordinary series of Rydberg lines, with states up to $n = 30$ having been observed in a dilution refrigerator [33]. This observation is by far the highest Rydberg state observed in a solid-state material. The highly excited states are predicted to have an average exciton wavefunction radius of over 1 µm, which is far larger than the lattice constant of $a_l = 4.26$ Å [43]. The first indications of long-range dipole-dipole interactions between excitons have observed with a decrease in oscillator strength of the high n excitons attributed to a Rydberg blockade effect [32; 44; 45]. The observation of interactions in this system has led to proposals for the creation of quantum states of light [46; 47].

Currently, the highest lying Rydberg states exist in naturally occurring material. For any future technological application, it will be essential to be able to grow high quality synthetic material. However, given the sensitivity of high lying states to charged impurities in the material [48], growing synthetic material of sufficient quality is challenging [49; 50; 51; 52]. The current highest n Rydberg states in synthetic material is $n = 10$ [50]. Additionally, excitons have been studied in synthetic thin films [53; 54; 55; 56] along with micro- and nano-structures of cuprous oxide [57; 58].

The aim of the work in this thesis was to investigate whether any of the quantum optical or sensing applications of Rydberg atoms can be demonstrated using Rydberg excitons. For this, an experimental platform for studying Rydberg excitons in cuprous oxide at 4 K was developed. To investigate potential quantum optical applications

of cuprous oxide, the setup was designed to be able to study the photon statistics of the emitted light. A tightly focussed two-photon excitation scheme was used to create an excitation spot smaller than the estimated blockade radius [32]. There are several advantages to using a two-photon excitation for quantum optical applications. Under two-photon excitation the emitted light is at approximately half the wavelength of the excitation laser and so separating the signal light from the excitation laser is easily achieved with optical filters. Additionally, in second harmonic generation spectroscopy, where the detected light is the coherently generated second harmonic of the excitation laser, the emission spectrum is set by the excitation laser and the spectrum does not exhibit the large phonon assisted background which is present in one-photon absorption spectroscopy [59; 60]. In this thesis, the experimental setup and the results of two-photon spectroscopy of Rydberg excitons is discussed. In future, the tightly focussed two-photon excitation scheme should allow the Rydberg blockade to be observed in the photon statistics of the emitted light as anti-bunching.

Just like their atomic counterparts, Rydberg excitons are sensitive to electromagnetic fields. To study this, the experimental setup was designed to couple excitons and microwave fields. This coupling was achieved through electric dipole transitions between excitonic states of opposite parity. Previously, electric dipole transitions between states with low principal quantum number have been widely studied using far infra-red and terahertz spectroscopy [61; 62; 63; 64; 65; 66; 67; 68; 69; 70; 71; 72; 73; 74]. However, transitions between neighbouring Rydberg states have not as yet been studied. The energy separations in a Rydberg series scale with n as n^{-3}. Combined with the reduced Rydberg constant of excitonic states, this scaling means that for the "yellow" series in cuprous oxide, electric dipole transitions accessible to microwave frequencies on the order of a few tens of GHz occur for states as low as $n = 8$. In this thesis, microwave driven electric dipole transitions between Rydberg excitons in cuprous oxide is demonstrated for the first time. Combined with the two-photon excitation scheme, it was possible to observe the coherent modulation of an optical carrier by the microwave field, a crucial step in building a potential microwave-to-optical converter. The electric dipole transitions between Rydberg states provide a new tool for the manipulation and study of excitons. Furthermore, the addition of a microwave field may also have quantum optical applications. Near-resonant microwave radiation could lead to a dramatic extension of the blockade radius, as the interaction switches from a van der Waals to a resonant dipole interaction [75; 76].

Thesis structure

This thesis is organised as follows. In chapter two, the background to cuprous oxide and excitons in cuprous oxide will be given and the relevant optical selection rules will be discussed. In chapter three, the experimental setup is presented. This includes details of the sample preparation and mounting along with details of the optical and microwave spectroscopy setups. In chapter 4, the different samples used in this work are characterised. The samples are characterised using one-photon absorption spectroscopy and photoluminescence spectroscopy. The spatial variation of the samples is also studied. Additionally, this chapter contains details of synthetic cuprous oxide and its comparison to natural material.

In chapter five, two-photon excitation is used to study Rydberg excitons. This is achieved through photoluminescence excitation (PLE) spectroscopy as well as second harmonic generation (SHG) spectroscopy. Using these methods the even-parity Rydberg series is extended up to $n = 12$, which is the highest principal quantum number observed under two-photon excitation. In chapter six, the effect of applying a microwave electric field to the Rydberg series is studied. The microwave field is found to couple opposite parity Rydberg states, leading to a change in one-photon absorption of more than 10%. In two-photon spectroscopy the microwave field is found to introduce coherent sidebands onto the second harmonic, separated by the microwave frequency. A theoretical model is presented based on nonlinear susceptibility and is shown to agree well with the data.

Publications

A list of publications arising from work presented in this thesis are given below:

1. L. A. P. Gallagher, J. P. Rogers, J. D. Pritchett, R. A. Mistry, D. Pizzey, C. S. Adams, M. P. A. Jones, P. Grünwald, V. Walther, C. Hodges, W. Langbein, and S. A. Lynch, "Microwave-optical coupling via Rydberg excitons in cuprous oxide," , Phys. Rev. Research **4**, 013031 (2022). [77].

2. S. A. Lynch, C. Hodges, S. Mandal, W. Langbein, R. P. Singh, L. A. P. Gallagher, J. D. Pritchett, D. Pizzey, J. P. Rogers, C. S. Adams, and M. P. A. Jones, "Rydberg excitons in synthetic cuprous oxide Cu_2O," Phys. Rev. Materials **5**, 084602 (2021) [78].

3. J. P. Rogers, L. A. P. Gallagher, D. Pizzey, J. D. Pritchett, C. S. Adams, M. P. A. Jones, C. Hodges, W. Langbein, and S. A. Lynch, "High resolution nanosecond spectroscopy of even-parity Rydberg excitons in Cu_2O," (2021), arXiv:2111.13062 [cond-mat.mes-hall]. Submitted to Physical Review B [79]

Excitons in Cu$_2$O

2.1 Excitons

In this section a basic hydrogenic picture of excitons will be presented, a more complete description can be found in chapter 6 of [80]. Solving the energy levels of a periodic crystal lattice gives rise to a series of bands, which describe the energy of an electron in the material as a function of its (quasi) momentum. The associated band wavefunctions are delocalised over the whole volume of the crystal. In a semiconductor, these bands are separated by an energy gap, known as the bandgap. The bands below the bandgap are known as the valence bands (VB), and the bands above the bandgap are known as the conduction bands (CB) [80].

In the ground state of a semiconductor, all of the electrons are in the valence band and the conduction band is empty. Through optical excitation, it is possible to excite an electron from the valence band to the conduction band. The missing electron in the valence band is modelled as a positively charged hole. The electron and hole are of opposite charge and so there is a Coulomb attraction between them. The concept of a Mott-Wannier exciton is that the attractive Coulomb interaction between these delocalised quasi-particles can support bound states. These bound states appear as discrete energy levels within the bandgap of the semiconductor, and can be optically excited directly from the valence band. A schematic picture of the concept of excitons is shown in Fig. 2.1.

Under the effective mass approximation, the electron and hole can be treated as free particles, with effective masses, m_e and m_h, given by the curvature of the relevant energy bands. The effective mass approximation amounts to only considering the
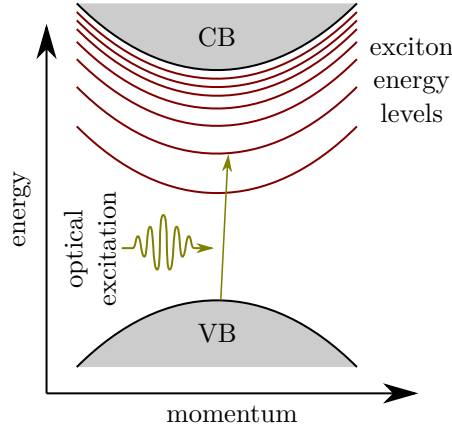
Figure 2.1: Schematic of the concept of excitons. The Coulomb attraction between an electron and hole allows the creation of bound states (known as excitons) which appear as discrete energy levels in the bandgap of the material. In the effective mass approximation the excitons have a parabolic dispersion given by their kinetic energy.

band structure around the Γ point and the band dispersion relations are assumed to be parabolic. In this approximation and assuming spherical symmetry, the resulting Hamiltonian which describes an exciton, H_0, (in the coordinates of the centre of mass of the electron and hole) is given by

$$H_0 = E_{\mathrm{g}} + \frac{\hbar^2}{2M}\nabla_{\vec{R}}^2 + \frac{\hbar^2}{2\mu}\nabla_r^2 + V(r). \tag{2.1}$$

Here, E_{g} is the bandgap energy, $\mu^{-1} = m_{\mathrm{e}}^{-1} + m_{\mathrm{h}}^{-1}$ is the reduced mass, M is the total mass given by $M = m_{\mathrm{e}} + m_{\mathrm{h}}$, and $\vec{R} = (m_{\mathrm{e}}\vec{r}_{\mathrm{e}} + m_{\mathrm{h}}\vec{r}_{\mathrm{h}})/(m_{\mathrm{e}} + m_{\mathrm{h}})$ is the centre of mass coordinate, with $\vec{r}_{\mathrm{e}}$, $\vec{r}_{\mathrm{h}}$ denoting and the position of the electron and hole respectively. The distance between the electron and hole is denoted by r, given by $r = |\vec{r}_{\mathrm{e}} - \vec{r}_{\mathrm{h}}|$. The second term of this Hamiltonian describes the kinetic energy of the centre of mass of the electron and hole. The third term describes the relative motion of the electron and hole. The final term of the Hamiltonian is the Coulomb interaction between the electron and hole, given by

$$V(r) = -\frac{e^2}{4\pi\epsilon_0\epsilon_{\mathrm{r}}r}, \tag{2.2}$$

Note that this Coulomb potential includes the relative permittivity, ϵ_{r}, as the Coulomb attraction is screened by the dielectric material.

The Hamiltonian in equation 2.1 has the same form as the Hamiltonian for a hydrogen atom, only the masses of the (quasi-)particles and dielectric screening are different. The eigen energies of H_0, E_X, are given by

$$E_X = E_g - \frac{R_X}{n^2},\tag{2.3}$$

where n is the principal quantum number of the exciton and R_X is the excitonic Rydberg energy. The second term of equation 2.3 represents the exciton binding energy. As in the hydrogen case, the binding energy scales with principal quantum number as n^{-2}. However, the binding energy of excitonic states are much smaller than states in hydrogen at the same n due to the lower Rydberg energy for excitonic systems. The excitonic Rydberg energy can be related to the hydrogenic Rydberg energy, R_H, by

$$R_X = \frac{\mu}{m_0 \epsilon_r^2} R_H,\tag{2.4}$$

where m_0 is the mass of a free electron. The main contribution to the reduced Rydberg energy comes from the dielectric screening of the Coulomb potential, though the lower reduced mass of the exciton is also a factor.

The wavefunction of the exciton can be obtained by solving the time independent Schrödinger equation. Assuming a spherical symmetry (neglecting the crystal lattice), the wavefunctions have the same form as the hydrogen case, and the relative motion of the exciton and hole are described using the same envelope functions. These envelope functions contain the spherical harmonics, and so the angular momentum quantum numbers l and m can be used to describe the excitons. In truth, the non-spherical symmetry of the crystal means that angular momentum is not a good quantum number, and the envelope functions should be written in terms of the irreducible symmetries of the crystal lattice [81]. However, the angular momentum quantum numbers are often used as an approximation to described excitonic sates, with the states being labelled as having $l =$ S, P, D,... type envelope functions. Details of the fine structure of exciton levels in terms of irreducible symmetries for the yellow series in Cu_2O is given in section 2.2.2.

2.2 Excitons in cuprous oxide

2.2.1 Cuprous oxide

Cuprous oxide (Cu_2O) is a naturally occurring oxide of copper. It was one of the first semiconducting materials ever used in electronics [82; 83], and was the material in which excitons were first experimentally observed [36; 37; 38]. Though its use as a solar cell material has been explored [84], cuprous oxide does not currently have many technological applications. Due to this, there have been only limited attempts to grow high quality synthetic material [49; 50; 51; 78], and the highest quality samples are still natural gemstones. A microscope image of a sliced and polished natural cuprous oxide sample is shown in Fig. 2.2(a) showing its characteristic red colour.

A unit cell of the cuprous oxide lattice is shown in Fig. 2.2(b). Cu_2O has an interleaved cubic lattice. The Cu atoms sit at the lattice points of a face-centred cubic lattice, while the oxygen atoms are located at the lattice points of a body centred cubic lattice. The two interleaved cubic lattices are diagonally offset by one quarter of the lattice constant of $a_l = 4.26$ Å [43]. Cu_2O belongs to the O_h symmetry group [43].

The band structure of Cu_2O has been extensively calculated [85; 86; 87; 88]. Cuprous oxide is a direct bandgap semiconductor with a bandgap energy of approximately 2.172 eV. For the purposes of this thesis, we are interested in electronic structure of the conduction and valence bands around the Γ point. A brief summary of the band structure is presented here. Fig. 2.2(c) shows a schematic of the relevant band structure. Here, the bands are labelled by their irreducible symmetries, $\Gamma_x^\pm$, where the $\pm$ refers to the parity [81]. The valence bands are formed from the 3d copper orbital and are split by spin-orbit coupling. The lowermost conduction band comes from the 4s copper orbital and the upper conduction bands from the 4p copper orbital.

Transitions between the different bands give rise to different exciton series in Cu_2O. The different exciton series are labelled from low to high bandgap energies, as the yellow, green blue and violet exciton series. The corresponding bandgap energies are given in Table 2.1. The yellow exciton series (formed from the uppermost valence band and lowermost conduction band) currently holds the record for the highest principal quantum number exciton state ever observed [33], and the majority of previous work has focussed on this series. However, there have been some studies of other exciton series [89; 90; 91; 92; 93; 94; 95], and transitions between different excitonic series have
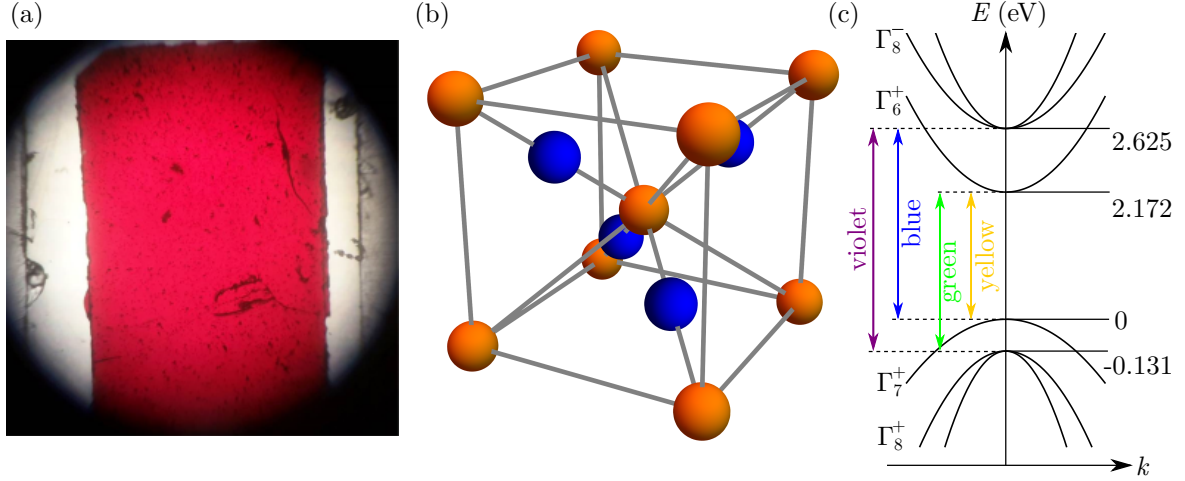
Figure 2.2: (a) Microscope image of a polished thin section (approximately 50 µm thick) of Cu_2O. (b) A unit cell of Cu_2O. Orange balls represent oxygen atoms while blue balls represent copper. The copper atoms sit in a face centred cubic structure while the oxygen atoms sit in a body centred cubic structure. The two lattices are offset diagonally by one quarter of the lattice constant. (c) Zoom of the band structure of Cu_2O around the Γ point. Bands are labelled with their irreducible symmetry representations. There are four possible transitions between the valence bands and the conduction bands, these are labelled (from low to high bandgap energy) as yellow, green, blue and violet.

name	transition	bandgap energy
yellow	$\Gamma_7^+ \rightarrow \Gamma_6^+$	2.17208 [32]
green	$\Gamma_8^+ \rightarrow \Gamma_6^+$	2.3023 [98]
blue	$\Gamma_7^+ \rightarrow \Gamma_8^-$	2.6336 [95]
violet	$\Gamma_8^+ \rightarrow \Gamma_8^-$	2.756 [90]

Table 2.1: Bandgap energies of the different excitonic series in cuprous oxide.

been proposed as electric dipole transitions within the reach of optical frequencies [96; 97]. For this thesis, only the yellow exciton series will be studied.

The excitonic properties of cuprous oxide have been of interest since their first observation in the 1950s [36; 37; 38]. The low energy exciton states of the yellow exciton series were extensively studied in the search for exciton Bose-Einstein condensation (BEC) [99; 100; 101]. The low mass of the exciton meant that a BEC was predicted to form at a much higher temperature than in atomic systems. The long lifetime of the lowest energy exciton state in cuprous oxide made it seem an ideal candidate for observing BEC [102]. However, collisional processes meant that this system was not as ideal for observing BEC as originally thought [101].

More recently, cuprous oxide has emerged as a system for studying Rydberg physics. The yellow exciton series in cuprous oxide has the record for the highest principal quantum number excitons ever observed [32; 33]. One factor which contributes to the observation of high n states is the high excitonic Rydberg energy. The effective masses of the electron and hole are found to be $m_e = 0.99\ m_0$ and $m_h = 0.58\ m_0$ [103; 104]. As the relative permittivity is $\epsilon_\mathrm{r} \approx 7.5$ [103], the Rydberg energy is approximately 90 meV, which is in good agreement with the experimentally measured values [32; 33]. This Rydberg energy is significantly higher than other direct bandgap semiconductors such as 4.2 meV for GaAs [42] and 2.7 meV for Ge [105].

The highly excited Rydberg states which have been observed in the yellow series are extended over large spatial extents (> 1 µm), due to the radius of the exciton wavefunction scaling as n^2. The Bohr radius of an exciton, a_X, can be calculated from the Rydberg energy. The relation between a_X and R_X is given by

$$a_\mathrm{X} = \frac{1}{2}\frac{e^2}{4\pi\epsilon_0\epsilon_\mathrm{r}R_\mathrm{X}}a_\mathrm{H}. \tag{2.5}$$

Taking the experimentally obtained value for the Rydberg energy this gives a value of the Bohr radius of 1.1 nm. Applying the n^2 scaling of the exciton wavefunction, giving a spatial extent of more than 1 µm for the highest n observed so far.

Another property of the exciton which scales with n is the dipole moment, which also scales as n^2. The large dipole moment has led to the observation of long-range van der Waals interactions between Rydberg excitons, with a drop in oscillator strength at high n attributed to a Rydberg blockade effect [32; 45]. The increasing dipole moment should make the high n states very sensitive to external fields. Previous work has looked at the effect of applying DC electric and magnetic fields [106; 107; 108; 109; 110; 111; 112], including studies of quantum chaos in high magnetic fields [113; 114]. In chapter 6 of this thesis, we explore the coupling of Rydberg excitons to microwave fields.

As many of the properties of excitons scale favourably with principal quantum number, it is desirable to reach the highest n state possible. Previous work has studied the limitations to observing higher n in one-photon spectroscopy [115; 116; 117]. It was found that the presence of charges in the material are a limiting factor in observing higher n states. The charges can be either caused by impurities in the material or can be optically or thermally excited [115; 116; 117; 48]. As the observation of the the highest n states was performed at milli-Kelvin temperatures with very low optical intensities, the current limit in observing higher n is set by the concentration of charged impurities in the material, which are estimated to be below 0.01 µm^{-3} [115].

So far in this chapter, excitons have been treated using the hydrogenic picture presented in section 2.1. While this hydrogenic approximation holds up well for the yellow series in Cu_2O, the exciton states show deviations from this simplistic picture. In the remainder of this section, deviations from the hydrogenic picture for the yellow exciton series will be discussed, and the optical selection rules will be presented.

2.2.2 Deviations from the hydrogenenic model

Empirically it is observed, unlike in hydrogen (neglecting the Lamb shift [118]), that different angular momentum states of excitons at the same n are not degenerate. The lifting of the angular momentum degeneracy comes from multiple effects. These effects add additional terms to the Hamiltonian used to describe the excitons (equation 2.1). The total Hamiltonian, H, for the yellow excitons can be written as

$$H = H_0 + H_{CC} + H_{SO} + H_d + H_{exch}. \tag{2.6}$$

In the following, the consequence of each of these terms on the exciton states will be briefly discussed. The forms of each of the terms in the Hamiltonian will not be explicitly given here but are available in the referenced materials. The influence of each of these terms on the fine structure of the $n = 4$ exciton is shown in Fig. 2.3.

The first term which must be added to the Hamiltonian is the central cell corrections [119; 120; 112]. This term describes corrections to the Coulomb potential for small electron-hole separations. The central cell corrections give rise to a non-parabolicity in the valence bands, which primarily influences the lowest lying exciton states. A consequence of the non-parabolicity of the bands is an anomalously high binding energy of the lowest lying exciton states, with the 1S exciton found to have a binding energy of 153 meV [41; 121; 122; 123].

The second term which is added is the spin orbit coupling, H_{SO} [119]. This term occurs from the coupling of the hole spin with the quasi-spin of the valence band and is what leads to the splitting of the valence bands shown in Fig. 2.2(c). The splitting of the valence band gives rise to the yellow and green exciton series.

The third term which is added to the Hamiltonian, H_d mixes the yellow and green exciton series [124; 125]. This term is a correction to the effective mass approximation, and introduces an spatially anisotropic dispersion in the valence band. The term can be split into two separate terms $H_d = H_{d1} + H_{d2}$. The first of these terms, H_{d1} is
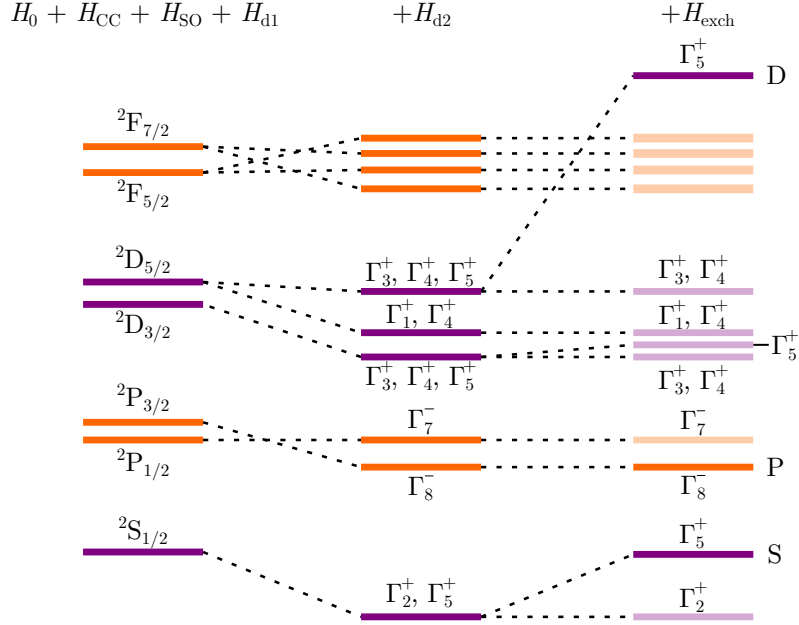
Figure 2.3: Schematic of the fine structure splitting of the $n = 4$ exciton levels. Energy splittings are not to scale. Odd-parity states are shown in orange and even-parity states in purple. First column represents fine structure including the spherically symmetric terms of the Hamiltonian (equation 2.6). The second term shows the splitting caused by the term H_{d2}, which accounts for the cubic symmetry of the crystal. The final column shows the effects of the exchange interaction. In the final column, three states are highlighted in bold. These states are optically active under one and two-photon excitation and will be referred to a S, P and D (from low to high energy) for the remainder of this thesis.

spherically symmetric, while the second term, introduced in [125] accounts for the cubic symmetry of the crystal. The term H_{d1}, leads to a fine structure splitting of the angular momentum states and couples the hole's spin and the angular momentum of the exciton envelope function, analogous to spin orbit coupling in atomic systems. The states can now be characterised in terms of the total angular momentum $J = |s - l|, ..., |s + l|$ where l is the angular momentum quantum number and s is the spin quantum number of the hole ($s = 1/2$ for the yellow exciton series). The resulting states can still be characterised using atomic spectroscopic notation, as $n\,^{\nu}L_J$, where $\nu = 2s + 1$. For example, the lowest and highest energy states at $n = 4$ would be written as $4\,^2S_{1/2}$ and $4\,^2F_{7/2}$ respectively. As only the yellow exciton series is considered here, the spin of the hole is always $1/2$. The first column of Fig. 2.3 schematically shows the energy level splitting of the $n = 4$ states including the terms up to H_{d1}.

The term H_{d2} takes the cubic nature of the crystal into account through a correction to the valence band structure (which influences the kinetic energy of the hole) [125;

123]. At this point J stops being a good quantum number and the states should be represented by their irreducible symmetry representation, $\Gamma_x^\pm$, of the O_h group. The $\pm$ superscript in the symmetry representation is the parity of the state, which remains a good quantum number in cubic crystals [81]. The resulting fine structure splitting including terms up to H_{d2} is shown in the middle column of Fig. 2.3.

The final term that is added to the Hamiltonian is the exchange interaction between the electron and hole, H_{exch} [119]. This term only influences even-parity states because both the electron and hole must have a non-zero probability of being found in the same unit cell for the exchange to occur. The influence of this term is most prominent for the 1S state, where the exchange interaction splits the 1S into a singly degenerate para-exciton and a triply degenerate ortho-exciton with a separation of 12 meV. Direct optical decay from the para-exciton is forbidden to all orders due to requiring a spin flip to occur. The forbidden nature of the decay means that the 1S para-exciton can have long lifetimes, up to 13 µs [102]. The splitting into ortho and para-excitons is not just present for the 1S exciton, there exist a parallel series of Rydberg para-excitons which has been observed up $n = 6$ through the application of magnetic fields [126].

The exchange interaction also has a notable effect on the D states [119]. Again, the exchange interaction lifts the degeneracy of the states, and shifts the states of Γ_5^+ symmetry to higher energy. For the $^2D_{5/2}$ states the Γ_5^+ symmetry state is shifted to a higher energy than the F states, making it the highest energy state at a given principal quantum number [45]. The exchange interaction also mixes the highest energy Γ_5^+ states with the S ortho-excitons (also Γ_5^+ symmetry) making them optically active under two-photon excitation [119]. The influence of the exchange interaction is shown in the final column of Fig. 2.3.

The fine structure splitting of the $n = 4$ states due to different terms in the Hamiltonian in shown in Fig. 2.3. This figure is similar to one which appears in [112]. In the final column, where all terms of the Hamiltonian are included, three states are highlighted in bold. The states in bold are optically active under one and two-photon excitation. In the absence of external fields to modify the selection rules, the states not highlighted in bold are very weak [106; 127; 107; 108; 109; 110; 111; 112]. The majority of the work in this thesis will be studying the optically active states. From now on, unless explicitly stated otherwise, they will be referred to (from low to high energy) as the S, P and D states and their irreducible symmetries will be implied.

To account for the lifted degeneracy of the angular momentum states, a quantum defect

model is used [122]. The quantum defect model is borrowed from atomic physics where it is used to account for the screening of the Coulomb potential observed in alkali atoms [128]. In the quantum defect model, the binding energy of an exciton state, E_{nl}, is given by

$$E_{nl} = -\frac{R_{\mathrm{X}}}{(n - \delta_l)^2},$$

(2.7)

where δ_l is the quantum defect. In alkali atoms the quantum defect is observed to depend weakly on energy. Similarly, n dependent quantum defects have been applied to excitons [122; 129]. However, for the purpose of this thesis, any n dependence of the quantum defect will be neglected.

2.2.3 Selection rules

The selection rules for optical excitation of excitons have similarities to atomic selection rules. In this section, the one-photon and two-photon selection rules will be discussed, and a one-photon absorption spectrum of Rydberg excitons will be presented. The details of the spectroscopy technique are not presented here, but are available in the referenced sections.

2.2.3.1 One-photon excitation

For one-photon absorption, (due to the even-parity of the valence band) the dominant states observed have P type symmetry [130]. Fig. 2.4 shows an example one-photon absorption spectrum of the Rydberg series at 4 K taken with a broadband light source. The experimental setup used to obtain this spectrum is detailed in section 3.4 and the data presented here is discussed in more detail in chapter 4. As well as the P states, higher angular momentum odd-parity states are visible, with the F states appearing as small shoulders on the high energy side of the P states. The F states have an oscillator strength that is approximately 100 times smaller than the P states. In previous studies, higher angular momentum states such as H states have also been observed [131]. High angular momentum states are predicted to have long lifetimes, and using light with orbital angular momentum has been proposed as a way of accessing these states [132].

The green exciton series also overlaps with the energy range of the yellow series. The green 1S exciton is at approximately 2.155 eV [91; 119; 133] between the 2P and the 3P
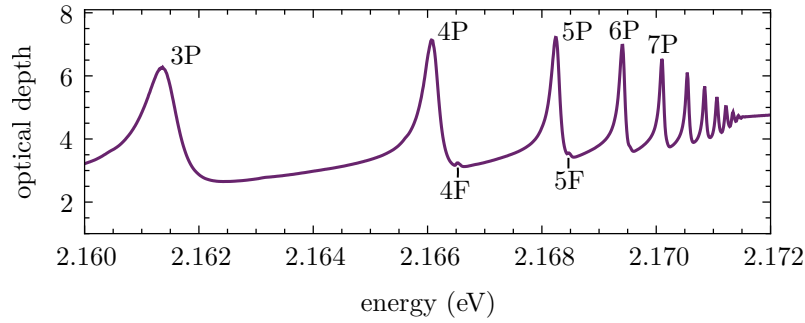
Figure 2.4: One-photon absorption spectrum of excitons in sample AM at 4 K. Details of the experimental setup are in section 3.4. P states dominate the spectrum with F states also visible. The exciton resonances sit on a background due to phonon assisted absorption.

resonances of the yellow series (not shown in Fig. 2.4). The higher lying green excitons are all above the bandgap of the yellow series [133].

The dominant absorption in Fig. 2.4 is not from the Rydberg states. The states appear on top of a large non-resonant background. This background is due to phonon assisted processes [134; 59; 60]. The background occurs through the simultaneous creation of a 1S ortho-exciton and an odd-parity optical phonon. It has been shown that this phonon assisted absorption must occur through an intermediate dipole allowed state, with the dominant contribution to the intermediate states coming from the blue and violet S excitons [60]. The shape of the background is given by the density of states of the phonons, which has a square root dependence on energy [134]. In total there are three optical phonons which contribute to this background process [60]. Additionally, a similar process involving the green 1S exciton and an optical phonon contributes to the background for states above $n = 5$ [60]. As the bandgap is approached, the background gains an exponential component. This exponential component is known as the Urbach tail and smoothly transforms the spectrum from discrete exciton resonances into a continuum [135; 136]. The origin of this exponential was theoretically investigated and shown to be due to charges in the material [48]. These charges can be due to impurity doping of the material as well as being optically or thermally excited.

The width of the exciton resonances in Fig. 2.4 are set by the exciton-phonon scattering rate [137; 138; 120; 139]. The dominant contribution to this width is the scattering from a Rydberg state to the 1S state via optical phonons. The Rydberg exciton can both absorb and emit phonons, though at low temperatures the population of optical phonons is small enough to neglect the absorption of phonons [139].
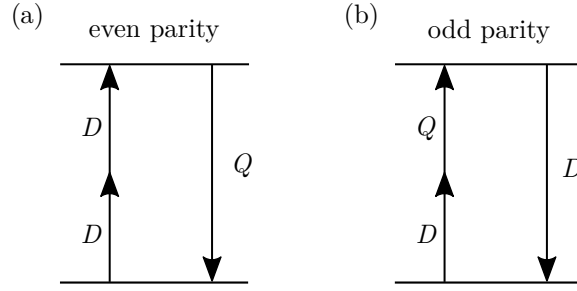
Figure 2.5: Energy level diagram of SHG processes. (a) Energy level diagram for SHG involving even-parity excitons. Excitation is achieved through two dipole processes. Emission occurs through a quadrupole process. (b) Energy level diagram for SHG involving odd-parity excitons. Excitation occurs through one dipole and one quadrupole process. Emission occurs through a dipole process.

The P states show a pronounced asymmetric lineshape. The cause of the lineshape is a matter of debate in the literature. One explanation for the asymmetry is exciton-phonon scattering [137; 138]. However, theoretical work [120] calculated that exciton-phonon scattering alone underestimated the observed asymmetry of the lines and that Fano interference between the Rydberg states and the non-resonant background was a more likely explanation [120; 140]. The Fano interference explanation is disputed in [139], which argues that the exciton-photon scattering is enough to explain the asymmetric lineshape.

2.2.3.2 Two-photon excitation

Under two-photon excitation, the selection rules are more complicated than in the one-photon case. Due to parity being a good quantum number in cuprous oxide, the S and D states dominate the spectrum [141]. However, the selection rules also depend on the orientation of the optical electric field relative to the crystallographic axes. The two-photon polarisation selection rules have been given a comprehensive treatment in previous works [141] and have included the presence of strain in the material [142] as well as external fields [143; 126; 92]. In section 5.3.2 these polarisation selection rules are presented for the S and D excitons, and are then extended to included the effects of a tightly focussed excitation beam and optical birefringence.

Most of the recent work on two-photon spectroscopy has focussed on second harmonic generation (SHG) spectroscopy. SHG is forbidden in centrosymmetric crystals such as Cu_2O under the dipole approximation. However, it is allowed when the finite wavevector of the light is considered, and one of the transitions is described by a

quadrupolar transition [141; 142; 143; 126; 92]. This means that as well as the even-parity S and D states which dominate the SHG spectrum, the odd-parity states can also be observed.

Fig. 2.5 shows energy level diagrams detailing two different SHG processes on the even-parity and odd-parity states. For the even-parity states, the excitation to the Rydberg state is achieved through two dipole steps. From the even-parity state, emission is dipole forbidden, and emission occurs through a quadrupole process. For the odd-parity states, the process is reversed as emission is dipole-allowed but the excitation is dipole-forbidden. This leads to a quadrupole step occurring during the excitation process. Recent work showed that the SHG on the even-parity states is predicted to be stronger than to SHG on the odd-parity states [143].

2.3 Susceptibility description of optical processes in Cu_2O

In this section, a description of linear and nonlinear optical processes in Cu_2O in terms of the susceptibility, χ, is presented. In nonlinear optics the dependence of the polarisation, $\mathcal{P}$, (dipole moment per unit volume) on an optical electric field, $\mathcal{E}$, can be written in terms of a power series

$$\mathcal{P} = \epsilon_0 \left(\chi^{(1)}\mathcal{E} + \chi^{(2)}\mathcal{E}^2 + \chi^{(3)}\mathcal{E}^2 + \cdots \right), \qquad (2.8)$$

where $\chi^{(1)}$ is the linear susceptibility, and $\chi^{(2)}$ and $\chi^{(3)}$ are the second and third order nonlinear susceptibilities respectively [144]. Equation 2.8 is written in terms of scalar fields for simplicity. When vector fields are taken into account, the susceptibilities must be treated as tensors, but for the majority of this thesis the tensor nature of the light-matter coupling will be neglected and an effective scalar coupling will be assumed.

In general, the susceptibility is a complex number, where the imaginary part represents the absorption of the material. Neglecting reflection, the transmission through a material, T, can be modelled with the Bouguer-Beer-Lambert law [145]

$$T = \frac{I}{I_0} = e^{-\alpha L}, \qquad (2.9)$$

where α is the absorption coefficient, L is the length of the material, I is the transmitted intensity and I_0 is the input intensity. The absorption coefficient is related to the imaginary part of the susceptibility, χ, and the wavenumber k by [144]

$$\alpha = k \operatorname{Im}\left(\chi\right). \qquad (2.10)$$

Knowing the functional form of the susceptibility allows the response of the material to optical fields to be predicted. In the case of atomic systems, it is possible to derive the form of the susceptibility using the laws of quantum mechanics. These expressions depend on parameters of the atomic system such as the energy levels and the dipole matrix elements for transitions between energy levels. A comprehensive derivation of the form of the susceptibility from a quantum mechanical perspective is given in chapter 3 of [144]. Previously, atomic like susceptibilities have been used to describe nonlinear optical processes involving excitons [141; 142; 92; 143]. In the following, the functional forms of the susceptibility describing one-photon and two-photon absorption along with second harmonic generation are presented.
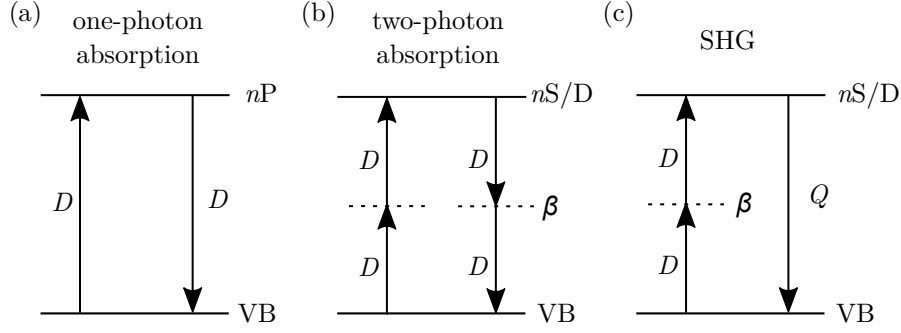
Figure 2.6: Energy level diagrams of three optical processes used in this work. D and Q indicate whether the steps involved are dipole or quadrupole steps respectively. (a) One-photon absorption. (b) Two-photon absorption. (c) Second harmonic generation.

2.3.1 Functional forms of the susceptibility

Energy level diagrams of three optical processes involving exciton in Cu_2O are presented in Fig. 2.6. The three processes considered are one-photon absorption, two-photon absorption, and second harmonic generation. Here, we will restrict ourselves to considering only two-photon processes involving S and D excitons, but it is possible to construct similar forms of the susceptibility for two-photon excitation to odd-parity states [143].

2.3.1.1 One-photon absorption

For the case of one-photon absorption to the Rydberg exciton states in Cu_2O the absorption coefficient can be split into two terms $\alpha = \alpha_{1S} + \alpha_P$ where α_{1S} represents the 1S phonon assisted background and α_P represents the absorption due to the P states. An energy level diagram for the one-photon absorption on P excitons is shown in Fig. 2.6(a).

The absorption due to the P states can be modelled in terms of a $\chi^{(1)}$ linear susceptibility as [144]

$$\alpha_P = k \text{ Im} \left(\sum_n \chi_{nP}^{(1)} \right), \tag{2.11}$$

with

$$\chi_{nP}^{(1)} = \frac{1}{2\epsilon_0 \eta} \frac{\left| D^{\text{VB} \to nP} \right|^2}{\delta_{nP} - i\Gamma_{nP}}. \tag{2.12}$$

Here, $\left|D^{\text{VB}\to n\text{P}}\right|^2$ is the dipole moment per unit volume for the transition between $|n, \text{P}\rangle$ state and the valence band, $\delta_{n\text{P}} = E_{n\text{P}} - E$ is the detuning, $E_{n\text{P}}$ and $\Gamma_{n\text{P}}$ are the energy and width of the $|n, \text{P}\rangle$ state respectively, η is the refractive index of the material and E is the excitation energy. Note that modelling the P states in this way neglects their asymmetric lineshape [138; 134].

If a single isolated resonance is considered, then the form of the absorption coefficient is given by

$$\alpha_{n\text{P}} = \frac{k}{2\epsilon_0 \eta} \frac{\left|D^{\text{VB}\to n\text{P}}\right|^2 \Gamma_{n\text{P}}}{\delta_{n\text{P}}^2 + \Gamma_{n\text{P}}^2}, \tag{2.13}$$

which is a Lorentzian lineshape centred at $\delta_{n\text{P}}$ with a full width half maximum (FWHM) $2\Gamma_{n\text{P}}$.

2.3.1.2 Two-photon absorption

The energy level diagram for two-photon absorption on even-parity exciton states is shown in Fig. 2.6(b). The transition to the even-parity state $|n, l\rangle$ occurs through a dipole transition to an intermediate state β, followed by a dipole transition from β to $|n, l\rangle$. This can be described in terms of a third order nonlinear susceptibility, χ_{nl}^{TPA}, as

$$\chi_{nl}^{\text{TPA}} = \sum_\beta \frac{1}{2\epsilon_0 \eta} \frac{\left|D^{\text{VB}\to\beta}\right|^2 \left|D^{\beta\to nl}\right|^2}{(\delta_{nl} - i\Gamma_{nl})(\delta_\beta - i\Gamma_\beta)^2}. \tag{2.14}$$

Here, $\delta_{nl} = E_{nl} - E$ and $\delta_{nl} = E_\beta - E/2$ where $E = 2hf_{\text{IN}}$ is the two-photon excitation energy. In cuprous oxide, the dominant contribution to the intermediate states β comes from the dipole allowed blue and violet S excitons [60]. As the detuning from the blue and violet excitons, δ_β, is much larger than any other system parameter, it is possible to perform the summation in 2.14 to give

$$\chi_{nl}^{\text{TPA}} = \frac{1}{2\epsilon_0 \eta} \frac{\left|M^{\text{VB}\to nl}\right|^2}{\delta_{nl} - i\Gamma_{nl}}, \tag{2.15}$$

where the effective matrix element describing the two-photon absorption, $M^{\text{VB}\to nl}$, has been introduced. Note the similarities between the equation 2.15 describing the two-photon absorption and equation 2.12 describing the one-photon absorption. However,

as χ_{nl}^{TPA} is a third order susceptibility, the corresponding absorption coefficient is now intensity dependent and is given by

$$\alpha_{\mathrm{TPA}} = k \, \mathrm{Im} \left(\sum_{n,l} \chi_{nl}^{\mathrm{TPA}} \right) \mathcal{E}_{\mathrm{IN}}^2, \tag{2.16}$$

where $\mathcal{E}_{\mathrm{IN}}$ is the input electric field. As in the one-photon cases, when a single exciton resonance is considered, α_{TPA} becomes

$$\alpha_{\mathrm{TPA}} = \frac{k\mathcal{E}_{\mathrm{IN}}^2}{2\epsilon_0 \eta} \frac{\left| M^{\mathrm{VB}\to nl} \right|^2 \Gamma_{nl}}{(\delta_{nl}^2 + \Gamma_{nl}^2)}, \tag{2.17}$$

which is a Lorentzian centred at δ_{nl} with a FWHM of $2\Gamma_{nl}$.

2.3.1.3 Second-harmonic generation

As previously mentioned, the SHG process in Cu_2O occurs through a quadrupole process. An energy level diagram for the SHG process on even-parity excitons is shown in Fig. 2.6(c). The form of the susceptibility describing the SHG process is given by

$$\chi_{nl}^{(2)} = \sum_{\beta} \frac{1}{2\epsilon_0 \eta} \frac{D^{\mathrm{VB}\to\beta} D^{\beta\to nl} Q^{nl\to\mathrm{VB}}}{(\delta_{nl} - i\Gamma_{nl})(\delta_{\beta} - i\Gamma_{\beta})}, \tag{2.18}$$

where $\left| Q^{nl\to\mathrm{VB}} \right|^2$ is the quadrupole moment per unit volume. As in the case of two-photon absorption, the summation over the off resonant intermediate states can be performed to give

$$\chi_{nl}^{(2)} = \frac{1}{2\epsilon_0 \eta} \frac{M^{\mathrm{VB}\to nl} Q^{nl\to\mathrm{VB}}}{\delta_{nl} - i\Gamma_{nl}}. \tag{2.19}$$

The electric field of the SHG, $\mathcal{E}_{\mathrm{SHG}}$, is proportional to the polarisation generated in the material, and so is given by

$$\mathcal{E}_{\mathrm{SHG}} \propto \mathcal{P} = \epsilon_0 \left(\sum_{nl} \chi_{nl}^{(2)} \right) \mathcal{E}_{\mathrm{IN}}^2. \tag{2.20}$$

The intensity of the SHG, I_{SHG} is proportional to the square of the polarisation in the medium and so

$$I_{\mathrm{SHG}} = A \left| \sum_{n,l} \chi_{nl}^{(2)} \right|^2 I_{\mathrm{IN}}^2, \tag{2.21}$$

where I_{IN} is the intensity of the input light and A is a proportionality constant. The proportionality constant can be found by solving the wave equation under the slowly varying envelope approximation [144] and is given by

$$A = \frac{L^2 f_{\mathrm{IN}}^2}{2\eta_{\mathrm{SHG}}\eta_{\mathrm{IN}}\epsilon_0 c^3}\mathrm{sinc}^2\left(\frac{\Delta k L}{2}\right).\tag{2.22}$$

Here f_{IN} is the frequency of the excitation light, $\Delta k = 2k_{\mathrm{IN}} - k_{\mathrm{SHG}}$ is the mismatch in k vectors of the excitation and SHG light, η_{IN}, η_{SHG} are the refractive indices of Cu_2O at the excitation and SHG wavelengths respectively and L is the length of the crystal. The term dependent on Δk represents the phase matching condition. When polaritonic effects are neglected [146; 94], the difference in refractive index at the excitation and emission wavelengths means that SHG is not phase matched in Cu_2O. This lack of phase matching leads to a very low efficiency for the SHG process. For a 40 mW input beam the maximum measured SHG power was approximately 3 fW. Note that the SHG was collected in a back-scattered geometry, which will reduce the efficiency (the geometry of the experimental setup is discussed in chapter 3).

When a single exciton resonance is considered, the form of I_{SHG} becomes

$$I_{\mathrm{SHG}} = AI_{\mathrm{IN}}^2 \frac{\left|M^{\mathrm{VB}\to nl}\right|^2 \left|Q^{nl\to\mathrm{VB}}\right|^2}{\delta_{nl}^2 + \Gamma_{nl}^2}.\tag{2.23}$$

As was seen in the one-photon and two-photon cases, this is a Lorentzian centred at δ_{nl} with a FWHM of $2\Gamma_{nl}$. However, there is a subtle difference in the form of the Lorentzian when compared to equation 2.13 and 2.17. Here, the width does not appear on the numerator.

It should be noted that considering multiple resonances in the SHG case does not lead to a sum of Lorentzians. This is due to the summation in equation 2.21 being performed before the square is taken. The consequences of this for fitting the SHG spectra are discussed in section 5.3.1.1.

2.3.1.4 Dependence of absorption and SHG resonances on principal quantum number

In the final part of this section, the n dependence on the expressions obtained for a single exciton resonance under one-photon absorption (equation 2.13), two-photon absorption (equation 2.17) and SHG (equation 2.23) are studied. In all three cases,

the lineshape of the absorption or SHG resonance is a Lorentzian of FWHM $2\Gamma_{nl}$. The main contribution to the width of the exciton resonances is phonon scattering to the 1S ortho-exciton state [138; 139]. The rate of this phonon scattering decreases with principal quantum number as n^{-3}, leading to a trend in the widths of n^{-3}. The trend in the widths has been observed experimentally, though at high n the measured widths are found to be larger than expected [117] and was attributed to the electric field generated by charges in the material [117; 48]. The energy separation between states of neighbouring n in a Rydberg series scales as approximately n^{-3}. As the widths and the separation have the same scaling, the states should be as resolvable at high n as they are at low n.

The matrix elements in equations 2.13, 2.17 and 2.23 are also dependent on n. For the case of one photon absorption, the matrix element $\left|D^{\mathrm{VB}\to n\mathrm{P}}\right|^2$ is approximately proportional to n^{-3} at high n [32]. For the two-photon absorption case there are two matrix elements $\left|D^{\mathrm{VB}\to\beta}\right|^2$ and $\left|D^{\beta\to nl}\right|^2$. The matrix element for the transition from the valence band to the intermediate state is assumed to be independent of n as the excitation laser is far off resonant from the intermediate states. Since the dominant intermediate states β are compact states belonging to the blue and violet series [60], we predict $|D^{\beta\to nl}|^2 \propto n^{-3}$. For the SHG case, the quadrupole matrix element must also be considered. Assuming a hydrogen like system, again an n^{-3} scaling is obtained for $|Q^{\mathrm{VB}\to nl}|^2$ [127].

With the n dependence of the matrix elements determined, it is now possible to determine the scaling of the peak amplitudes and oscillator strengths with n. Here, the case of a single isolated excitons resonance is considered. The amplitude, A, of the peak is taken as the value on resonance ($\delta_{nl} = 0$). For the one-photon absorption, this gives

$$A_{\mathrm{OPA}} \propto \frac{\left|D^{\mathrm{VB}\to n\mathrm{P}}\right|^2}{\Gamma_{n\mathrm{P}}}. \tag{2.24}$$

For two-photon absorption, the amplitude of the peak is proportional to

$$A_{\mathrm{TPA}} \propto \frac{\left|M^{\mathrm{VB}\to nl}\right|^2}{\Gamma_{nl}}, \tag{2.25}$$

and for the SHG the amplitude is proportional to

$$A_{\mathrm{SHG}} \propto \frac{\left|M^{\mathrm{VB}\to nl}\right|^2 \left|Q^{nl\to\mathrm{VB}}\right|^2}{\Gamma_{nl}^2}. \tag{2.26}$$

In all three of these cases the n dependence of the width cancels with the n dependence of the matrix elements, leading to an amplitude which is independent of n. The

oscillator strength of the resonance (given by its area) is proportional to the product of the amplitude and the width. As the amplitudes are expected to be independent of n, the oscillator strength should scale in the same way as the widths, as n^{-3}.

In practice, the scaling of the amplitudes and oscillator strengths is more complicated. The presence of the green 1S exciton affects the low n matrix elements, while at higher n, the presence of charges in the material, temperature and interactions between excitons can all alter the amplitudes and widths of the exciton resonances [127; 133; 115; 117; 45].

2.4 Summary

Cuprous oxide presents a unique platform for studying Rydberg excitons. The high excitonic Rydberg energy (90 meV) means that highly excited states (up to $n = 30$ [33]) have been observed, which is the highest n exciton observed in any system. As the electronic band structure in cuprous oxide is made up of roughly parabolic bands, it is possible to describe the excitons using the effective mass approximation, where they are analogous to hydrogen atoms.

In general, the atomic picture of the exciton holds up reasonably well in Cu_2O. However, the cubic symmetry of the crystal means the states should be classified in terms of irreducible symmetries rather than angular momentum. For the purposes of this thesis, the atomic physics picture of the exciton will be used, and the states will be labelled in terms of angular momentum quantum number where possible. Empirically, it is found that excitons of the same principal quantum number are not degenerate. To describe this lifting of angular momentum degeneracy, the concept of a quantum defect is borrowed from atomic physics.

The cubic nature of the Cu_2O crystal means that parity is a good quantum number. Due to this, the one- and two-photon selection rules are similar to atomic physics. This similarity allows the construction of atom-like susceptibilities to describe the optical processes in the material. In chapter 6 the susceptibility description will be extended to include the effect of a microwave field.

Experimental setup

In this chapter, the apparatus used for the experiments presented in this thesis is detailed. The experiment was designed to perform optical and microwave spectroscopy of Rydberg excitons in Cu_2O. At the heart of the experimental setup was a closed-loop helium cryostation (Montana Instruments C2 Cryostation) which cooled the Cu_2O samples to 4 K. Rydberg excitons were probed using both one-photon and two-photon optical excitation schemes. Microwave spectroscopy was performed by studying the change in optical properties due to an applied microwave field. The experiment was built to be a modular setup, allowing each section to be removed or replaced as needed. Details of all of these components are provided in this chapter. In addition, details of the experimental apparatus at the University of Cardiff which was used to characterise samples is given.

An overview of the experimental setup is shown in Fig. 3.1. The setup has been split into three parts. The infra-red (IR) laser system provides light between 1140 and 1150 nm and is used for most of the spectroscopy techniques. The experiment section includes the delivery of light to and the collection of light from the sample, along with the geometry for the various spectroscopies. Finally, the detection section details the various detection methods available.

The IR laser system was based around an external-cavity diode laser (ECDL). This laser was tunable from 1140 to 1150 nm, and its wavelength was monitored on a wavemeter. The light from the seed laser was sent to an electro-optic modulator (EOM) which was used to intensity modulate the light into square pulses. The light was amplified using a Raman fibre amplifier (RFA) to give an average power of up to 5 W. An AOM was used to stabilise the laser power.
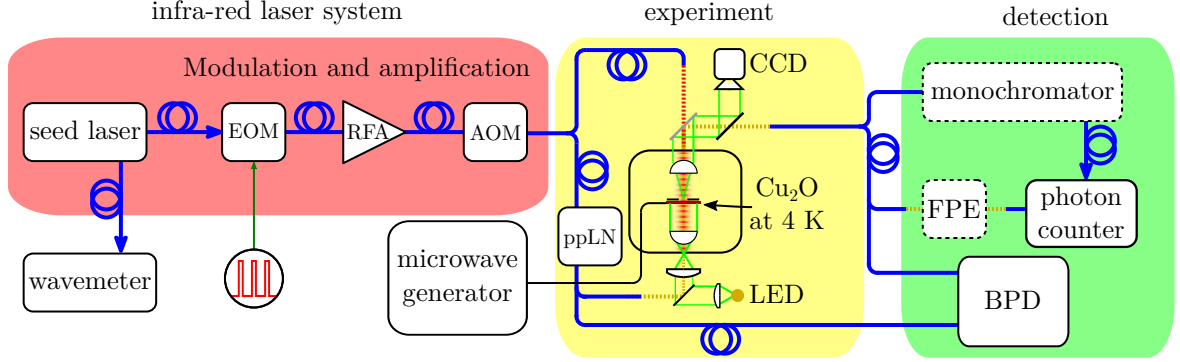
Figure 3.1: Overview of the experimental setup. Blue lines represent optical fibres. Infra-red laser system: Laser system was composed of an ECDL seed laser producing light between 1140 and 1150 nm. The seed laser was intensity modulated into square pulses with an EOM and amplified with a Raman fibre amplifier (RFA). An AOM was used for intensity stabilisation and pulse picking. Experiment: infra-red light from the laser system was focussed onto the Cu_2O sample at for a two-photon excitation of Rydberg excitons. The sample was mounted in the cryostation and cooled to 4 K. The sample emitted light which was collected in a back-scattered geometry. The emitted light was coupled into an optical fibre and sent to the detection optics. Alternatively, the infra-red light could be frequency doubled using a ppLN crystal and transmitted through the sample for absorption measurements. An LED and camera was also set up as a cryogenic microscope for imaging the sample. The sample was placed in the near field of a microwave antenna which is driven by a microwave generator. Changes to the optical signals from the sample due to the microwave field were measured. Detection: The intensity of the light emitted from the sample could be measured on a SPAD. Alternatively, the light could be spectrally resolved using a monochromator or a Fabry-Pérot etalon (FPE). For the laser absorption measurements, a balanced photodiode (BPD) was used.

To perform two-photon spectroscopy of Rydberg excitons the light from the IR laser system was used. The excitation light was focussed onto the Cu_2O sample in the cryostation at 4 K. The light emitted from the sample under two-photon excitation was collected in a back-scattered geometry and coupled into an optical fibre to be sent to the detection optics. The intensity of the emitted light could be measured on a single-photon avalanche detector (SPAD) or spectrally resolved using a monochromator or Fabry-Pérot etalon (FPE).

One-photon absorption spectroscopy could be performed using either a broadband light emitting diode (LED) or a laser. For LED spectroscopy, the light was transmitted through the sample and into the detection fibre. The transmitted light was spectrally resolved using the monochromator to give an absorption spectrum. For one-photon laser spectroscopy, the IR laser system was frequency doubled using a periodically-

poled lithium niobate crystal (ppLN). This light was split into two beams. One beam was sent through the sample and sent to a balanced photodiode (BPD), the other was sent straight to the BPD. The BPD gave the difference in intensity between the two beams, which was proportional to the absorption in the sample.

For microwave experiments, the sample was placed in the near field of a microwave antenna which was placed inside the cryostation. The microwave antenna was driven by an external microwave generator which could provide frequencies of up to 20 GHz. The one- and two-photon spectroscopy techniques were used to observe microwave induced changes to the Rydberg exciton spectrum.

Almost all of the experimental apparatus was computer controlled. All of the experimental control code was written in LabView, and data was also recorded through LabView. Analogue experimental signals (e.g. photodiode voltages) were digitised using National Instruments USB-6008 cards. These cards were also used to provide DC voltages throughout the experiment, for controlling the modulators and temperature controllers. As almost everything was computer controlled, the experiment could be left to run autonomously for long periods of time.

In the following chapter more details will be given on the experimental setup. First, more details will be given on the optical experimental setup. Secondly, the sample preparation and mounting will be discussed along with details of the microwave antennae used. Finally, details of experimental apparatus at the University of Cardiff which was used for characterising the samples used in this work is given.

3.1 Optical setup

The details of the optical experimental apparatus used for experiments in this thesis are given in this section. The section roughly follows the structure given in the experimental overview in Fig. 3.1.

3.1.1 Infrared laser system

3.1.1.1 Seed lasers

Two seed lasers were used for the experiments presented in this thesis. The optical diagrams of both seed lasers are shown in Fig. 3.2. Both were ECDLs operating between 1140 and 1150 nm. One was a commercially available device (TimeBase ECQDL-1146) and the other was a homebuilt device. The homebuilt device was based on a fibre coupled gain chip centred at 1140 nm (Innolume GmbH GM-1140-120-PM-130). Both devices use a diffraction grating in the Littrow configuration [147] as the tuning element.

Fig. 3.2(a) shows the optical layout of the commercial seed laser. The laser had one free space output giving a power of $\approx$ 200 mW at 500 mA of driving current. The driving current and temperature control of the laser was provided by a TimeBase LD1001 laser controller. The output from the seed laser was directed through two optical isolators (OI1; Thorlabs OI-4-1150-VLP) which each provided 38 dB of isolation. The purpose of the isolators was to minimise back reflections into the laser which could disturb operation. As the laser beam was elliptical it was reshaped using two cylindrical lenses (L1 and L2, $f = 25$ mm and $f = 75$ mm) giving an approximately circular beam of waist $\approx$ 2 mm. The polarisation of the beam was cleaned using a polarising beam splitter (PBS) before being coupled into a polarisation maintaining optical fibre. To ensure the polarisation of the light coupling into the fibre was correct, two waveplates were used. The first (WP1; Thorlabs WPH05M-1064) was a $\lambda/2$ plate for 1064 nm light. This waveplate rotated the linear polarisation of the laser light, but as the waveplate was designed for 1064 nm it also introduced some elliptical character to the light. The second waveplate (WP2; Thorlabs WPQ05M-1064) was a $\lambda/4$ waveplate at 1064 nm which was used to compensate for the elliptical nature of the light. The other output of the PBS was used as a pick off to monitor the laser wavelength on the wavemeter.
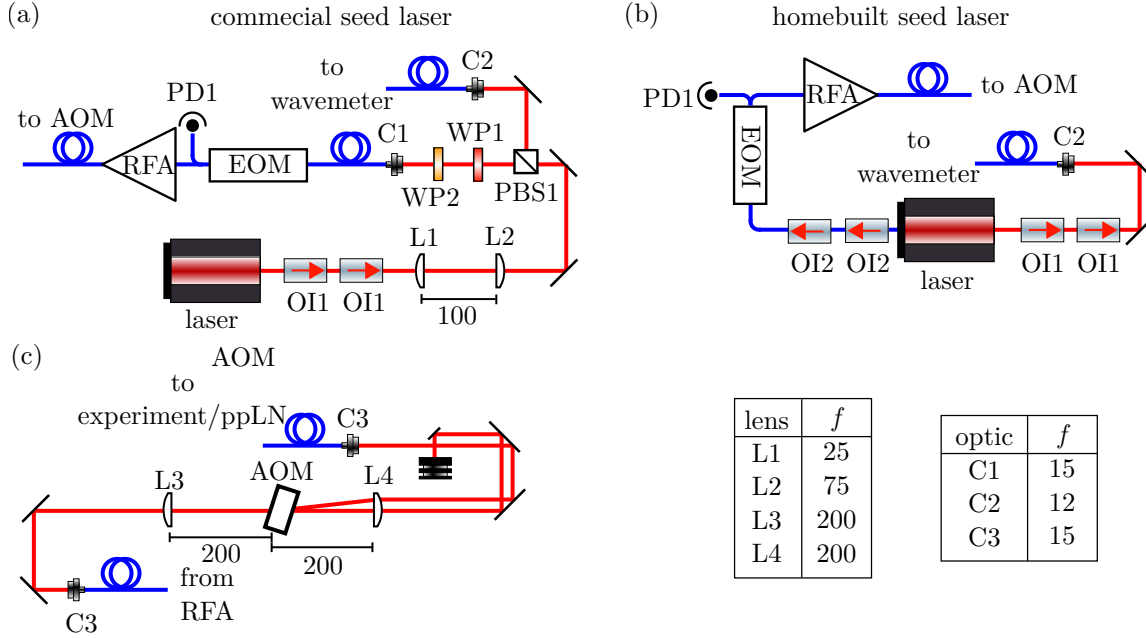
Figure 3.2: Optical diagrams of seed lasers and AOM. Laser light is shown in red, mirrors in black and optical fibres in blue. Key for components labels are in Table 3.1. All lengths and focal lengths are given in mm. (a) Optical diagram of the commercial seed laser. (b) Optical diagram of the home built seed laser. (c) Optical diagram for the AOM setup.

label	meaning	label	meaning
OI	optical isolator	AOM	acousto-optic modulator
L	lens	D	dichroic mirror
PBS	polarising beam splitter	BS	non-polarising beamsplitter
WP	waveplate	AL	aspheric lens
C	fibre coupler/ collimator	F	spectral filter
EOM	electro-optic modulator	GT	Glan-Taylor polariser
PD	photodiode	FPE	Fabry-Pérot etalon
RFA	Rama-fibre amplifier	I	Iris

Table 3.1: Key for labels in optical diagrams in Figs. 3.2, 3.3, 3.4, 3.5, 3.6 and 3.12

The frequency of the commercial seed laser was controlled using a piezo stack to tilt the diffraction grating. A voltage was provided to the piezo stack using a commercial piezo driver (Thorlabs MDT694B). Using a feed-forward method [148], where the piezo-voltage and diode current were varied simultaneously, it was possible to achieve a modehop free tuning range of up to 20 GHz. For frequency scans larger than 20 GHz, manual adjustment of the grating angle was necessary (via a screw behind the grating mount) and multiple 20 GHz scans were stitched together. After each manual tuning of the laser, the optimal current and piezo-voltages for modehop free scanning had to be found.

Fig. 3.2(b) shows the optical layout of the homebuilt laser. The laser has two outputs. One was a fibre coupled and one was free space. The fibre coupled output was passed through two fibre coupled optical isolators (Innolume PMOI-1150-SS-LT) which each provided 20 dB of isolation. After the isolators the light was sent to the rest of the experiment. The free space output was directed through two optical isolators (Thorlabs OI-4-1150-VLP) and coupled into a multimode optical fibre. This output was used for monitoring the laser wavelength.

The homebuilt seed laser was designed to achieve a large modehop free tuning range (> 500 GHz). The large modehop free tuning range was achieved by careful selection of the pivot point of the diffraction grating. There were two automated tuning elements within the device. A piezo stack (driven by the Thorlabs MDT694B driver) allowed fine control of the laser frequency, while a motorised actuator (Thorlabs PIAK10) provided coarse control. The laser current and temperature were controlled through a Koheron CTL200-0 laser controller.

The frequency of both lasers was monitored on a self-calibrating wavemeter (Bristol Instruments 671A). The wavemeter measured the wavelength 4 times per second with an accuracy of ± 60 MHz. A computer controlled servo loop could be used to stabilise the laser frequency to within the accuracy of the wavemeter.

3.1.1.2 Modulation and amplification

To pulse the seed laser, the light was passed through a fibre coupled EOM (EOSpace lithium niobate Mach-Zehnder interferometer). The EOM was sent square electrical pulses from a pulse generator (HP 831A) and could generate square optical pulses as short as 1 ns, with a rise time of 100 ps. Typically, the EOM was used to provide 50 ns

pulses with a repetition rate of 5 MHz. For a 50 ns pulse the laser linewidth was near transform limited to 50 neV.

In order to achieve a high extinction ratio for the pulses generated by the EOM a DC bias voltage was be applied to the EOM. A fibre pickoff and photodiode (PD1) after the EOM monitored the average optical power transmitted by the EOM. For duty cycles less (greater) than 50%, the maximum extinction ratio was achieved by minimising (maximising) the average power transmitted by the EOM. A computer controlled feedback loop was used to adjust the DC bias voltage applied to the EOM in order to minimise (maximise) the average power on PD1. The resulting pulses had an extinction of > 20 dB.

The pulsed light was amplified using a custom made Raman-fibre amplifier (MPB Communications Inc. RFL-P-5-1143-SF-NS). The RFA could achieve output powers of up to 5 W. Note that the RFA was polarisation maintaining. In order to safely seed the RFA, the light entering it had to be quasi-continuous wave. The input into the RFA required an average power > 0.3 mW with a pulse repetition rate of ≥ 5 MHz.

Following the RFA the amplified light was passed through a free space AOM (Isomet 1050-T80L). The drive electronics for the AOM were homebuilt. The AOM driving frequency was set to 50 MHz. An optical diagram of the AOM setup is shown in Fig. 3.2(c). The light was focussed through the AOM and the first order diffracted beam was coupled into an optical fibre.

The AOM served two purposes. It was primarily used to stabilise the power of the IR laser beam. To monitor the excitation power reaching the sample, a pickoff and a photodiode were placed before the IR light entered the cryostation (PD2). A computer controlled feedback loop altered the DC voltage provided to the AOM and stabilised the excitation power to within 1%. For two-photon experiments the average excitation power was typically set to be around 50 mW with a 25% duty cycle.

The other use of the AOM was as a pulse picker. For some time resolved measurements (e.g. measuring the lifetime of long lived exciton states, see section 5.1.1) it was necessary to deliver pulses to the experiment at lower repetition rates than could safely seed the RFA. In this case, the EOM was set to produce pulses at a repetition rate which was high enough to safely seed the RFA. The AOM was pulsed (using a Quantum Composer Pulse Generator 9512) in sync with the EOM but with a lower repetition rate. This allowed the AOM to select specific pulses from the pulse train leaving the RFA. In this way, it was possible to achieve arbitrarily low repetition rates without

damaging the RFA.

3.1.2   The experiment

3.1.2.1   Two-photon laser spectroscopy

In this section, the delivery of the two-photon excitation light to the sample and the collection of the light emitted from the sample is discussed. An overview of the experiment part of the optical table, showing how the geometry of the different spectroscopy techniques is shown in Fig. 3.3. In this diagram the two-photon excitation light is shown in red. A simplified optical diagram showing just the two-photon excitation and collection, along with the relevant focal lengths and distances is shown in Fig. 3.4(a). The two-photon light was delivered by optical fibre to the experiment section of the apparatus. A traditional fibre collimator was not used. Instead, a single lens (L7, $f = 75$ mm) was used to provide a slightly convergent beam. This convergent beam was to compensate for the chromatic aberration of later optics. The polarisation of the excitation light was cleaned up by passing it through a PBS (PBS2). Next, a non-polarising beamsplitter (BS) was used to pick off a small amount of light onto PD2. PD2 was the photodiode used to stablise the laser power, and it fed back to the voltage being sent to the AOM through a computer controlled servo loop. The excitation light was sent through an achromatic $\lambda/2$ waveplate (WP3; Thorlabs AHWP10M-1600) to allow the excitation polarisation to be varied. The excitation light was focussed into the Cu_2O sample in the croystation. For focussing into the sample, an aspheric lens (AL1; Lightpath Technologies 354105) with a numerical aperture (NA) of 0.6 was used. This gave a beam waist of 0.5 µm within the sample. Most of excitation light was transmitted through the sample and collected by a second asphere which collimated the light. The transmitted light was dumped on a beam dump.

Under two-photon excitation, the sample emitted visible light (shown as purple in Fig. 3.3 and Fig. 3.4(a)). The emitted light was collected in a back-scattered geometry using the same aspheric lens that was used for the excitation. As the same lens was used for excitation and collection, and the emitted and excitation light were at different wavelengths, the chromatic aberration of the aspheric lens had to be compensated for. To achieve this, the lens after the input fibre (L7; $f = 75$ mm) for the IR light was positioned 98 mm from the output fibre giving a slightly convergent beam. The beam path from this lens to the apshere was 204 mm, which ensured the excitation light
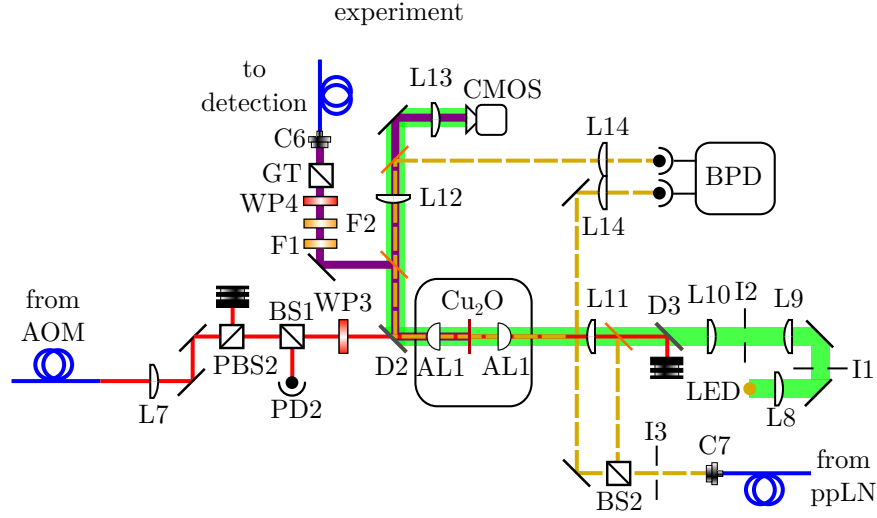
Figure 3.3: Optical diagram of the experiment part of the optical table. There were three excitation methods (two-photon, one-photon, LED). Removable mirrors (shown in orange) were used to switch between different excitation and detection schemes. Two-photon excitation light is shown in red, light emitted from the sample in purple, LED light in green and one-photon laser light as the dashed yellow line. Key for components labels are in Table 3.1. Optical diagrams showing the focal lengths and separations of the lenses involved for the IR illumination and for the microscope imaging are shown in Fig. 3.4.

filled the aspheric lens. Modelling in Zemax showed this produced an almost diffraction limited spot for the IR light (1140 nm) with a waist of 0.5 µm inside the sample and accounted for the chromatic aberration of the aspheric lens.

The light emitted from the sample was separated from the excitation light using a longpass dichroic mirror with the edge at 785 nm (D2; Semrock DI03-R785-T3-25-D). The emitted light was coupled into a multimode optical fibre for detection. Prior to the detection fibre, two shortpass filters (edge at 1000 nm) were used to remove any residual excitation light (F1; 2×Thorlabs FESH1000). A bandpass filter centred at 580 nm with a width of 14 nm (F2; Semrock FF01-580/14) could also be used to separate the coherently generated second harmonic of the laser from other light emitted from the sample. Prior to coupling into the optical fibre, polarisation dependent optics could be inserted. These consisted of a $\lambda/2$ waveplate (WP4; Thorlabs WPH05M-561) and a Glan-Taylor polariser (GT; Thorlabs GT10-A). By rotating the $\lambda/2$ waveplate the polarisation of the emitted light could be measured.

As an alternative to coupling the emitted light into an optical fibre, the emission from the sample could be imaged by forming a cryogenic microscope. Here, a $4f$ imaging

(a)

(b)
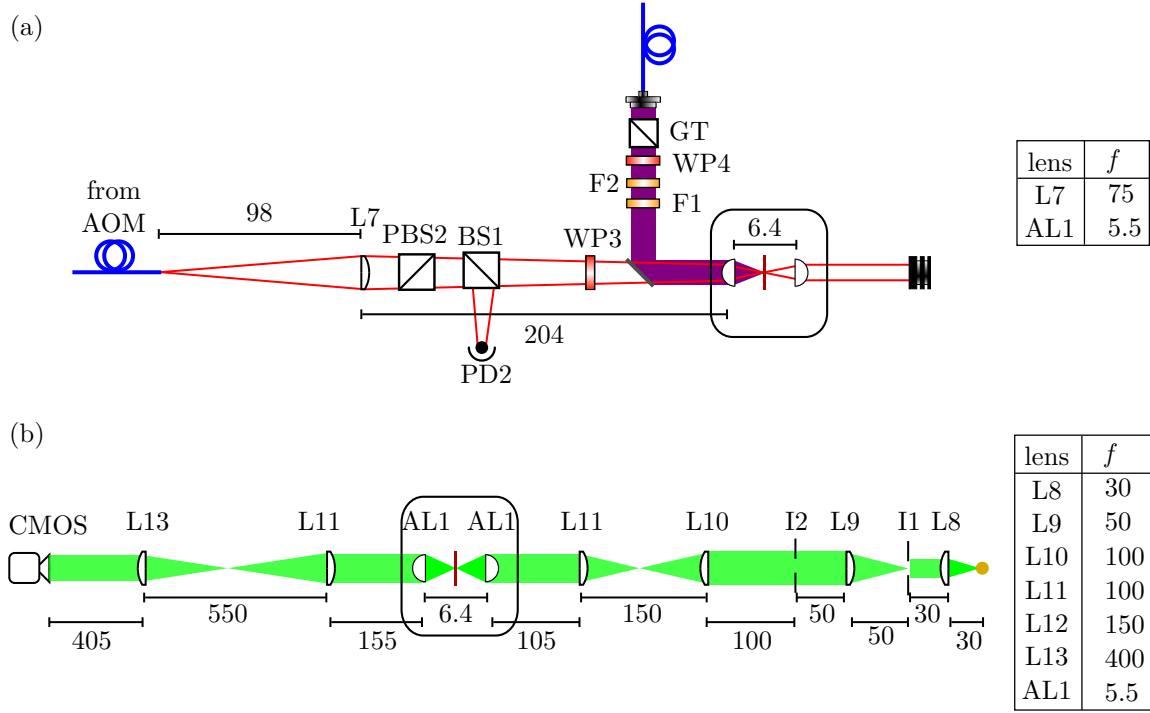
Figure 3.4: Detailed optical diagrams of the IR illumination and the microscope setup. Mirrors have been omitted for clarity. Black lines measure distances between optics, focal lengths and distances are in mm. (a) Detailed diagram of the optical setup for IR illumination. IR light is shown in red and light emitted from the sample is shown in purple. Lens L7 was placed 98 mm from the optical fibre to create a converging beam. This converging beam accounts for the chromatic aberration of aspheric lens AL1. (b) Optical diagram of the microscope setup. Köhler illumination achieves a uniform illumination on the sample. This was achieved by placing iris I1 in the far field of the LED and imaging I1 onto the sample surface. Microscope imaging setup uses four lenses to image the sample surface on the CMOS camera.

setup was used. The aspheric lens AL1 was used as the objective. Details of the imaging setup are shown on the left hand side of Fig. 3.4(b). The asphere was followed by a pair of achromatic lenses separated by the sum of their focal lengths (L12 and L13; $f = 150$ mm and $f = 400$ mm). The light was directed through an eyepiece lens ($f = 5$ mm, Edmund optics 33-305) and onto the CMOS camera (Basler ac2040-120um). The focal lengths of the four lenses involved meant that the magnification of the imaging system was such that one camera pixel corresponded to 2.2 µm on the sample surface. The camera could image at a frame rate of 60 Hz and had an electronic gain for the observation of low light levels.

3.1.2.2 Broadband LED illumination

A green light emitting diode (Lumileds LXML-PX02) was used to provide broadband light to the sample. This LED was used for both imaging the sample and performing broadband absorption spectroscopy. The centre of the LED emission range was 565 nm. A bandpass filter (Semrock FF01-580/14) of width 14 nm centred at 580 nm was used to select a range of LED wavelengths around the yellow exciton series in Cu_2O.

The LED beam path is shown as the thick green line in Fig. 3.3 and Fig. 3.4(b). The LED used a Köhler illumination [149] setup to provide a uniform illumination across the sample. For Köhler illumination an iris (I1) was placed in the far field of the LED. This iris was imaged onto the sample using lenses L9, L10, L11 and AL1. Imaging iris I1 ensured that the light source (here the LED) would never be imaged onto the sample. I1 could also be used to adjust the size of the spot on the sample surface. A second iris, I2, was placed in the imaging plane of the LED. This iris allowed the intensity of the light hitting the sample to be adjusted. It should be noted that a traditional Köhler setup only uses three lenses. However, due to the aspheric lenses already inside the cryostation it was necessary to include two additional lenses in the illumination path (lenses L11 and L12). A more traditional Köhler setup is detailed in section 3.4.

The imaging side of the microscope was the same as used for imaging the light emitted from the sample and is detailed above. The LED light could also be coupled into an optical fibre. This allowed the LED light to be sent to the monochromator to perform broadband LED spectroscopy.

3.1.2.3 One-photon laser spectroscopy

To perform one-photon laser spectroscopy of Rydberg excitons in Cu_2O it was necessary to have a laser capable of scanning from 570–573 nm. To achieve this, the light from the IR laser system described in section 3.1.1 was frequency doubled using a ppLN crystal (Covesion MSHG1120-1.0-20).

A diagram of the doubling setup is shown in Fig. 3.5. IR light from the AOM was focussed into the crystal using a 40 mm focal length lens. The doubled light emerging from the ppLN was collimated using a $f = 100$ mm lens. The IR light was separated from the second harmonic using a dichroic mirror (D1) and dumped. Two shortpass

frequency doubling
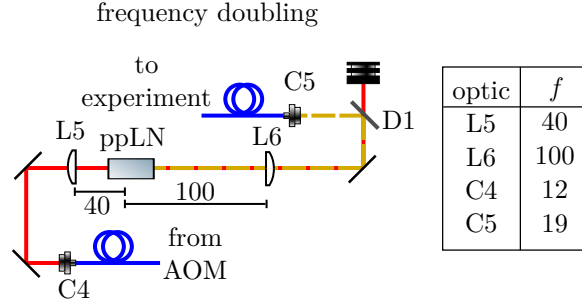
Figure 3.5: Optical setup for frequency doubling. Distances and focal lengths are given in mm. Light from the IR laser system was focussed into a ppLN doubling crystal to generate the second harmonic of the laser. The second harmonic was separated from the IR and coupled into an optical fibre.

filters (Thorlabs FESH1000) removed any residual IR light. The second harmonic was coupled into a polarisation maintaining fibre to be sent to the experiment.

The optimum beam waist in a doubling crystal is related to the ratio of the optical length of the crystal, ηL and the Rayleigh range, z_R, by $\eta L/(2z_\mathrm{R}) = 2.84$ [150] where η is the refractive index of the material and L is the length of the material. The ppLN crystal used was 20 mm long with a refractive index of $\eta = 2.23$ at 1140 nm [151] giving an optimal waist of 35 µm at 1140 nm. The 40 mm focal length lens used was modelled in Zemax and found to give a waist of 34 µm inside the crystal.

In order to achieve efficient second harmonic generation the quasi-phase matching condition of the crystal must be met [144]. To achieve this, the optical length of the ppLN crystal was controlled using a Wavelength Electronics MPT2500 temperature controller. As the wavelength of the IR laser was scanned the optimal temperature of the ppLN varied. A computer controlled feedback loop was written to vary the ppLN temperature depending on the wavelength of the IR laser.

Once coupled into a fibre, the frequency doubled light was sent to the experiment section of the apparatus. The beam path of the frequency doubled light is shown in Fig. 3.3 as the dashed yellow line. The light was collimated using collimator C7 ($f = 35$ mm). The light was split on a non-polarising beam splitter (BS2; Thorlabs BS037) to provide signal and reference beam. The reference beam was sent focussed onto a balanced photodiode (Nirvana 2007) using L14 ($f = 50$ mm). The signal light was coupled into the sample chamber using L11 and the back asphere (AL1). This resulted in a collimated beam going through the sample. A collimated beam was chosen to minimise the excitation intensity at a given laser power. The diameter of the collimated beam could be as large as 0.5 mm. The size of the collimated beam was

controlled by an iris (I3) prior to BS2. Once the light has passed through the sample it was directed onto the other input of the balanced photodiode. The signal from the balanced photodiode was recorded on an oscilloscope (Rohde and Schwarz RTO 1024).

3.1.3 Detection methods

The primary detection method for light emitted from the sample under two-photon excitation was a single photon avalanche detector (MPD PD-050-CTD-FC). The SPAD had a dead time of 77 ns and a dark count of $\approx$ 15 cps. For measurements where only the intensity of the emitted light was relevant, the SPAD was connected to the collection fibre from the experiment directly.

The SPAD was paired with a counting card (TimeHarp 260 Pico) which had a timing resolution of 25 ps. Triggering the counting card required a pulse with an amplitude between -0.2 and -1.2 V and a turn on time of less than 1 ns. This pulse was provided by an arbitrary waveform generator (Tektronix AFG3102C). The arbitrary waveform generator was also used to trigger the pulse generator which was driving the EOM, ensuring that the laser pulses and the detector trigger were in sync. For measurements where the AOM was used as a pulse picker, the arbitrary waveform generator was also used to trigger the pulse generator driving the AOM. The timing resolution of the experiment was limited by the jitter on the output of the arbitrary waveform generator which was 200 ps.

3.1.3.1 Fabry-Pérot etalon

To add spectral resolution to the experiment, the SPAD could be paired with a planar Fabry-Pérot etalon (LightMachinery OP-7423-1686-1). The etalon had a free spectral range (FSR) of 60.1 ± 0.2 GHz and a finesse of 44.5 ± 0.7. A diagram of the optical setup of the FPE setup is shown in Fig. 3.6(a). To achieve the best resolution from the etalon, it was crucial that the light entering the etalon was collimated. To ensure this, a fibre collimator with an adjustable focus was used (C8; Schafter and Kirchoff 60FC-0-M12-33). The light transmitted by the etalon was coupled into a multimode optical fibre and sent to the SPAD.

The transmission peak of the FPE was tuned by varying its temperature. Temperature stabilisation was provided by a Koheron TEC100L temperature controller. To vary the setpoint of the temperature controller a DC voltage was sent to the controller. The

(a)

from
experiment

C9

FPE

C8

to
photon
counter

optic	f
C9	12
C8	12

(b)
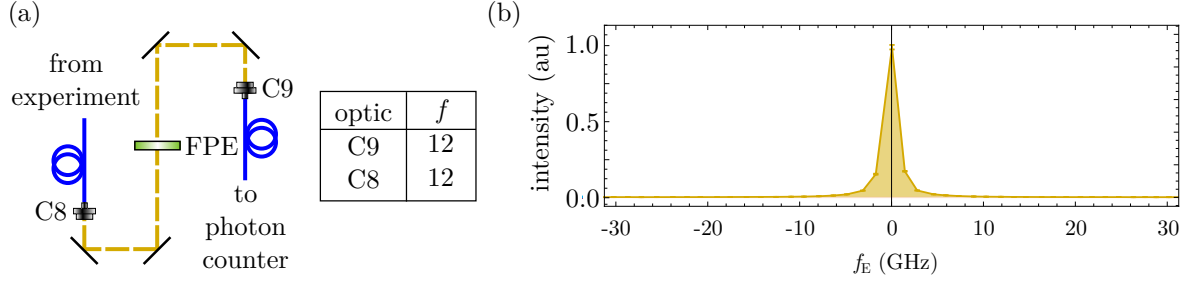
Figure 3.6: Farby-Pérot etalon (FPE) setup. Focal lengths are given in mm. (a) Optical diagram of the FPE setup. Collimated light was passed through the FPE. The transmitted light was coupled into an optical fibre and detected on a SPAD. (b) Transmitted intensity through the etalon as a function of etalon frequency f_E for a laser input at approximately 571 nm. The linewidth of the input light was orders of magnitude smaller than the width of the transmission feature, allowing the finesse of the FPE to be calculated.

temperature could be varied from 18 to 52 °C which corresponded to scanning the transmission peak of FPE approximately 120 GHz. For small changes in the temperature set point (< 1 K) it took approximately 30 seconds for the etalon to reach the new temperature. For larger changes, it could take up to 10 minutes for the temperature to stabilise. To record a transmission spectrum using the FPE the FPE was scanned discretely. A 60 s delay after changing the temperature was employed to allow the FPE temperature to stabilise.

To characterise and calibrate the FPE, frequency doubled light from the ppLN was used. For calibration, the temperature of the etalon was discretely scanned with the laser tuned to different frequencies. By looking at the peak transmission temperature as a function of excitation frequency, it was possible to calibrate the etalon and determine its FSR. The finesse of the etalon was determined by fitting the calibrated transmission spectra with a Lorentzian. The ratio of the width of the Lorentzian to the FSR gives the finesse. The fitting was performed on transmission spectra at multiple laser frequencies and the average of the fits was taken. Using this method the FSR of the etalon was determined to be 60.1 ± 0.2 GHz and the finesse to be 44.5 ± 0.7. A plot of a representative calibrated etalon spectrum is shown in Fig. 3.6(b).

3.1.3.2 Monochromator

To spectrally resolve the emitted light over a broader energy range a monochromator was used. The monochromator (Horiba iHR550) was equipped with 1800 g/mm and
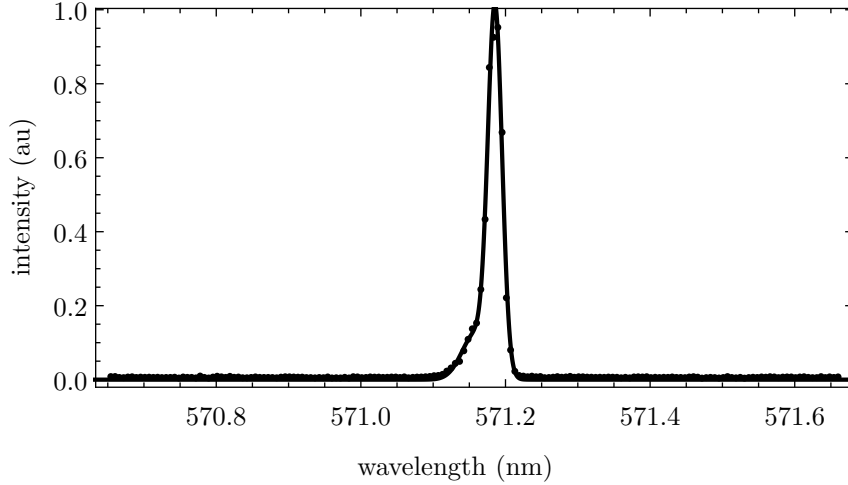
Figure 3.7: Spectral response function of the monochromator. Laser light of approximately 571.2 nm was passed through the monochromator and imaged on the camera to generate a transmission spectrum (black points). The asymmetry of the lineshape indicated misalignment of the monochromator. The transmission spectrum was fitted with a sum of two Gaussians (solid line).

2400 g/mm diffraction gratings which gave resolutions of 110 μeV and 80 μeV respectively. The output of the fibre was placed between the entrance slits of the monochromator and the NA of the fibre was set to match that of the monochromator (NA of monochromator was 0.08). On the output of the monochromator a camera (Basler ac2040-120um, also used for imaging the sample) was used to image the output slit. Due to the narrow widths of the slits (max 2.2 mm), the camera could only image a maximum spectral range of ≈ 1.5 nm without rotating the grating. To build up spectra over a wider range, multiple scans were taken and stitched together.

The monochromator was calibrated using the frequency doubled light from the ppLN. To achieve the best frequency calibration, the monochromator was set to the desired position and the light from the ppLN was sent through the monochromator. This was repeated for multiple laser frequencies. The resulting spectra were fitted to determine the dispersion and frequency offset of the monochromator. This calibration method was only possible when the spectral region of interest was within the frequency range of the doubled laser light (approximately, $570 - 573$ nm). As this was the same spectral range the Rydberg excitons occupy, this was not an issue for most of the experiments performed. However, for regions outside of this range (such as looking at the 1S exciton luminescence) the monochromator was calibrated in the same way, and then the grating in the monochromator was rotated to the desired frequency range. The manufacturers calibration was used to calculate the relative frequency difference between

the calibrated position and the new position.

Using the frequency doubled light from the ppLN it was also possible to measure the spectral response function of the monochromator. A typical spectrum of the frequency doubled light passed through the monochromator is shown in Fig. 3.7. The asymmetry of the transmission peak is an indication of poor alignment into the monochromator. Attempts to improve this alignment were unsuccessful. The method of using an optical fibre as the input slit of the monochromator makes alignment challenging, as there are 5 parameters to optimise (three positional axes, and two angles) which are not independent. In future, exiting the optical fibre and coupling in via free space would make achieving a better alignment easier.

3.2 Sample preparation

Both naturally occurring and synthetic samples of Cu_2O were used in this work. Synthetic samples were grown from copper rods using an optical floating zone technique [51]. Full details of the synthetic crystal growth is available in [78]. The natural material was purchased on the commercial gemstone and mineral markets. Images of the different types of samples are shown in Fig. 3.8. For all types of material, the sample preparation process was the same.

First the sample was orientated to the desired crystal plane using a Laue camera (Multiwire Labs Ltd MWL120). This allowed the sample to be sliced such that the desired crystal plane was parallel with the surface. In this work, the (001) and (111) crystal planes were used. Laue patterns of natural samples orientated to the (001) and (111) planes are shown in Fig. 3.8(d) and (e) respectively.

Once the samples had been sliced along the desired crystal plane, the exposed surface was mechanically polished before being glued to a glass microscope slide. The sample was sliced again to leave a thin section less than 0.5 mm thick glued to the glass slide. The sample was polished down to the desired thickness ($\approx$ 50 µm). The polishing steps were performed by the thin section laboratory in the Earth Sciences Department at Durham University. The polishing was done on lapping machines using Struers consumables. The polish was achieved using the following steps:

1. Rough grind of the surface using a MD-Largo disk together with DiaPro Allegro/Largo 9 µm diamond suspension/lubricant.

2. Rough polish on a Struers DP-DAC satin woven acetate cloth disk together with DiaPro DAC 3 µm diamond suspension/lubricant

3. Fine polish on a DP-NAP cloth together with a 1 µm DiaPro NAP suspension/lubricant

4. Fine polish using a new DP-NAP cloth together with 0.25 µm DiaPro NAP suspension/lubricant.

During the final polishing step the sample was removed and inspected periodically to check the quality of the surface under a microscope. Polishing was halted when the desired surface quality was achieved.
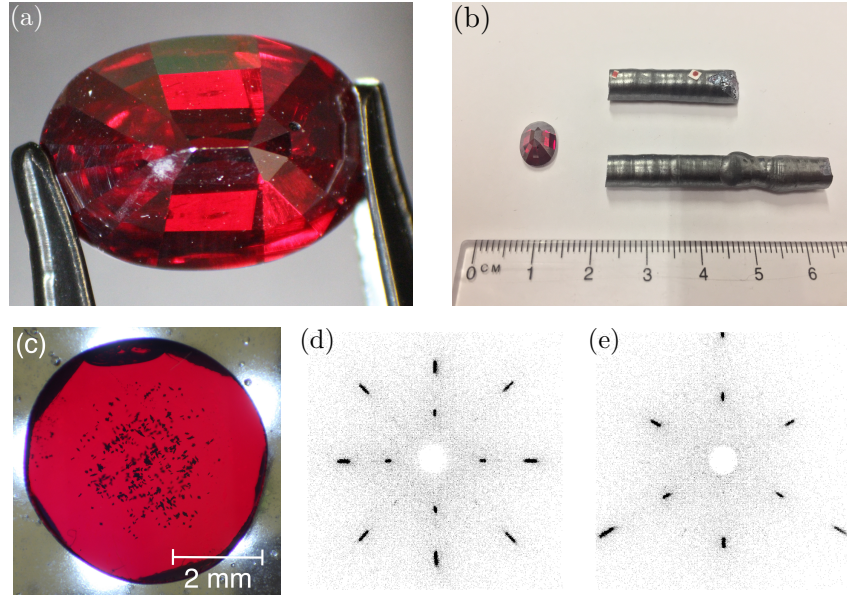
Figure 3.8: Images of different types of samples and example Laue patterns. (a) Natural gemstone purchased on the gemstone market. (b) Natural (left) and synthetic (metallic coloured rods) material. (c) Cross section of one of the synthetic rods showing characteristic red of Cu_2O. (d) Laue pattern from a natural sample orientate to the (001) crystal plane. (e) Laue pattern from a natural sample orientated to the (111) crystal plane.

Once sliced and polished, the sample (still glued to the glass microscope slide) was scored into 2 by 3 mm pieces using a scalpel. The sample was left to soak in acetone for at least 12 hours to remove it from the microscope slide. During this step, the samples often shattered into smaller pieces with irregular shapes. Once removed from the microscope slide, the sample was cleaned using three solvents. First acetone, then isopropyl alcohol and finally methanol. After the sample had been washed it was mounted at quickly as possible.

An image of the sample mount used for most of the experiments is shown in Fig. 3.9(a). The sample was placed between two 5 mm diameter CaF_2 windows. A small amount of glue was applied to one corner of the sample to achieve good thermal contact between the sample and one of the windows. The windows were glued into separate copper mounts. The two copper mounts were bolted together with the sample between them. A spacer with a thickness greater than the sample was used so as the sample was not being strained by the mount. Achieving good thermal contact (so that the sample does not heat under laser excitation) was challenging and in some cases multiple mounting attempts had to be made. The crucial step in achieving good thermal contact was the application of glue to the corner of the sample.
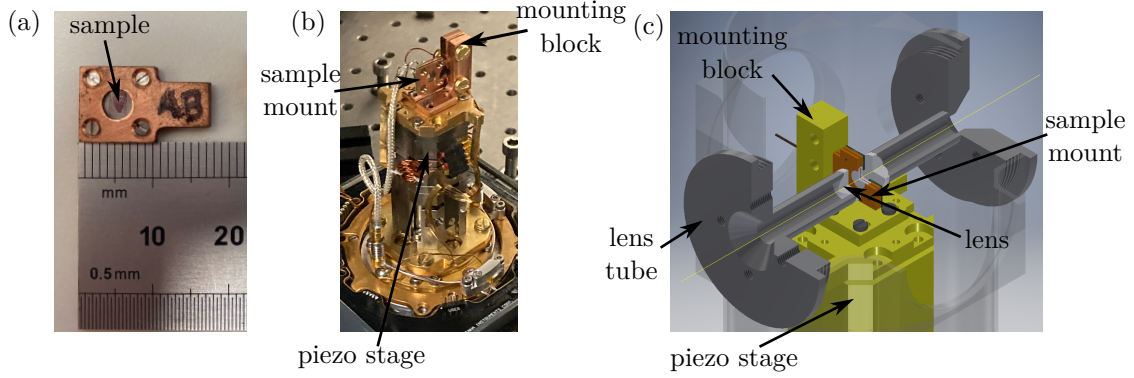
Figure 3.9: Images of the main sample mount used. (a) Photo of the copper sample mount with ruler for scale. The sample was placed between two CaF$_2$ windows which were glued to the copper mount. (b) Photo of the sample mount mounted in the cryostation. The sample mount slots into a mounting block which is bolted to the piezo stage within the cryostation. (c) Rendering of the sample mount in the cryostation with the aspheric lens mounts included. Aspheric lens mounts were attached to the outer heat shield of the cryostation. One quarter of the mounts have been sliced away in this rendering to allow better viewing of the internals. To see the full shape of the lens mounts, see Fig. 3.10(c).

Once mounted, the sample was placed in the cryostation and cooled to 4 K. For all the experiments presented in this work the cryostation base temperature was 4 K. A photo of a sample mounted inside the cryostation is shown in Fig. 3.9(b). The sample mount was attached to a copper block which was atop of a piezo stage (Attocube Systems AG nanopositioners: 2× ANPx101/RES/LT/UHV and 1× ANPz101/RES/LT/UHV). The piezo stage could be moved in three dimensions with a travel of 5 mm and a stability of 0.5 µm. The piezo stage was controlled by an Attocube Systems ANC350 controller. For optical spectroscopy, high NA aspheric lenses were used. The aspheric lenses were mounted in mounts attached to the outer heat shield at 30 K. The aspheric lens mounts are shown in Fig. 3.9(c). The separation between the lens mounts is approximately 5 mm. The aspheric lenses were not mounted on the piezo stage, allowing the sample to be moved relative to the lenses. This meant it was possible to adjust the point in the sample the laser focussed to, ensuring the laser could be focussed into the middle of the sample.

3.3   Microwave delivery

For the microwave experiments presented in chapter 6 the sample was placed in the near field of a microwave antenna. Two different microwave antennae, A1 and A2, were used. Antenna A1 was designed to work with the copper sample mount shown in Fig. 3.9. The antenna consisted of a printed circuit board (PCB) with four pads. Renderings of the front and back of the PCB are shown in the top half of Fig. 3.11(a). The PCB was glued onto one side of the copper sample mount. Electric connections were soldered onto the pads of the PCB. Two of the adjacent pads were connected to a microwave generator and two were grounded.

Antenna A2 was a stripline design with an input and output port. A rendering of the antenna is shown in the lower half of Fig. 3.11(a). A live line and a ground line ran between the input and output ports of the antenna. The sample was placed between these two lines, in a hole to allow optical access. The input port of antenna A2 was connected to a microwave generator and the output port was terminated with a 50 Ω terminator external to the cryostation.

A mounted sample in microwave antenna A2 is shown in Fig. 3.10(a). The sample was glued to a CaF_2 window. This window was glued onto microwave antenna A2 as pictured in Fig. 3.10. The microwave antenna was clamped in a copper mounting block around its base (visible in Fig. 3.10(b)). The CaF_2 window slotted into the back of this copper mount and thermal grease was applied at this interface. However, this mounting method had issues with the sample heating under laser excitation which was attributed to the small contact point between the CaF_2 window and the copper mount. This sample mount was bolted to the piezo stage inside the cryostation (as shown in Fig. 3.10(c)).

The microwave antennae were driven by a Rohde and Schwarz SMB100A microwave generator. The microwave generator was capable of generating frequencies up to 20 GHz at powers of up to 25 mW. The microwave generator had an inbuilt pulse generator, allowing the microwave field to be pulsed. For most experiments, the microwave pulse length was set to 0.5 s with a 1 s period. This pulse regime allowed concurrent measurement of the optical signal with and without the microwave field applied. If desired, the microwave pulse length could be much shorter than this. The shortest pulse length possible was 20 ns.

The signal from the microwave generator was delivered through two electronic feed-
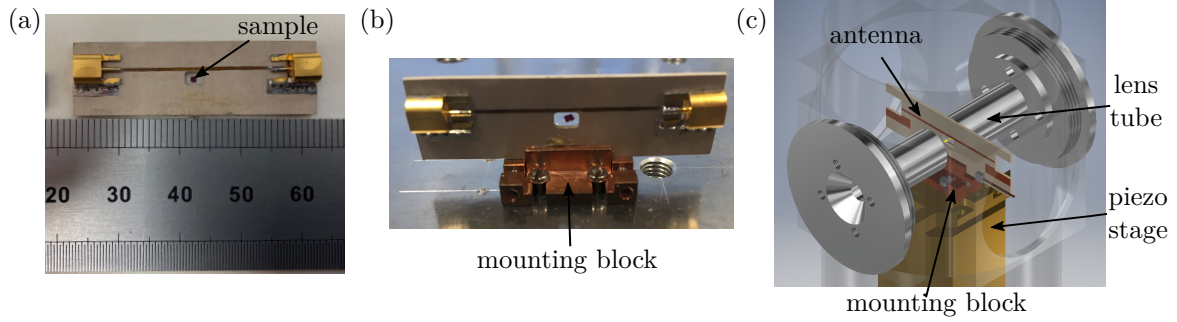
Figure 3.10: Images of the alternative sample mount used for some microwave experiments. (a) Photo of microwave antenna A2. The sample is visible in the hole in the antenna. The sample was glued to a CaF_2 window which was glued to the antenna. (b) Photo of microwave antenna A2 in its mounting block. (c) Rendering of microwave antenna A2 in the cryostation. The mounting block was bolted to the piezo stage and the same aspheric lenses were used as with the sample mount in Fig. 3.9.

throughs into the cryostation. For antenna A1 only one of these was used. For antenna A2, both were used. One was used for the input, and the other was used to terminate the output. These feedthroughs were limited to 28 GHz, but as the microwave generator could only generate up to 20 GHz this was not an issue.

3.3.1 Frequency dependence of microwave antennae

Both antennae were developed to have broadband near-field responses to microwave frequency. However, it became clear from experiments that the antennae were not broadband, and had different microwave frequency responses. Antenna A1 was found to only produce significant microwave fields at small bands of microwave frequencies around 16 and 19 GHz. Antenna A2 had a broadband response superimposed with a forest of narrow resonances.

To investigate the microwave frequency response of the antennae, they were modelled using commercially available finite-element electromagnetic design software (Ansys HFSS and CST Studio Suite). This modelling was performed by Rajan A. Mistry. The frequency response of the antennae was found to be strongly dependent on the presence of other metallic components in the cryostation, especially the aspheric lens mounts. The components included in the simulations are shown in Fig. 3.11(b). Note the inner heat shield of the cryostation was not included in the models.

The results of the simulations are shown in Fig. 3.11(c). Antenna A1 only produces fields at specific microwave frequencies with two sharp low frequency peaks and two
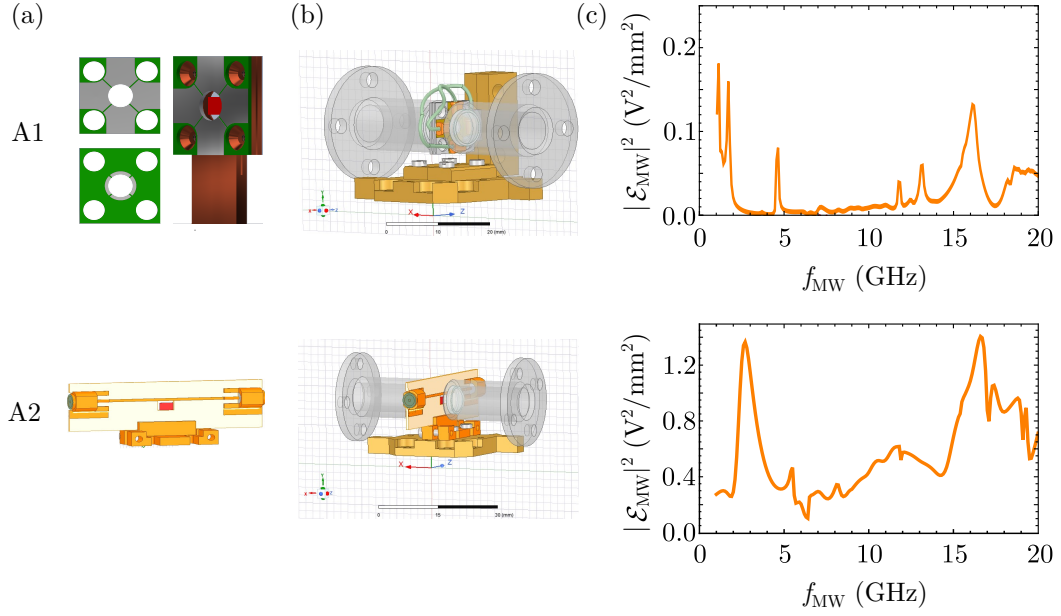
Figure 3.11: Microwave antennae used in this thesis. (a) Renderings of the two antennae, A1 (upper) and A2 (lower), used in this work. (b) Components modelled in the microwave field simulations. Upper panel shows A1 and lower panel A2. The antenna was placed at the centre of the aspheric lens mounts (grey) and mounted to the cold stage of the cryostation (gold). (c) Simulated microwave field strength squared at the sample as a function of microwave frequency for A1 (upper) and A2 (lower). Simulations were performed by Rajan A. Mistry, results reproduced with permission.

broader peaks around 16 and 19 GHz. Antenna A2 produces considerably higher maximal field strengths and has a more broadband response to microwave frequency. The maximal simulated electric field inside the sample with an input microwave power of 25 mW and relative permittivity $\epsilon_r = 7.5$ was found to be 360 V m^{-1} for A1 and 1200 V m^{-1} for A2.

As will be shown in section 6.1.1 these simulations are in reasonable qualitative agreement with the microwave frequency response observed in experiments. Due to the sensitivity of the simulations, and the incomplete nature of the models (e.g. the inner heat shield of the cryostation was not included) the simulations show that the experimentally observed microwave frequency response (measured in chapter 6) was dominated by the response of the antennae.

3.4 Experimental apparatus at the University of Cardiff

Most of the characterisation of the Cu_2O samples used in this work was performed using experimental apparatus at the University of Cardiff. For these experiments, the samples were mounted in the same copper mount described in section 3.2. A Montana instruments C2 cryostation which contained an Attocube piezo stage was also used.

The experiments performed were a mixture of broadband (LED) absorption measurements and photoluminescence (PL). For the absorption measurements, broadband light was transmitted through the sample and spectrally resolved using an imaging spectrometer. The PL measurements consisted of spectrally resolving the light emitted from the sample under above bandgap excitation. The same imaging spectrometer was used for absorption and PL measurements.

The optical layout for the setup at the University of Cardiff is shown in Fig. 3.12. The broadband light source was an LED (Thorlabs M565L3). A bandpass filter (Omega 575BP10) centred at 575 nm with a width of 10 nm width was inserted to limit the excitation spectrum to the yellow exciton series from $n = 3$ upwards and a small range of the continuum. A Köhler illumination setup was used to illuminate the sample with the LED [149], ensuring a uniform illumination across the sample surface. Two irises allowed the intensity and the spot size on the sample to be varied. The LED intensity itself could also be varied. The light transmitted through the sample was directed through a series of lenses into the imaging spectrometer. These lenses imaged the sample onto the entrance slit of the spectrometer. The slit width was set to 20 μm which corresponds to 1.16 μm on the sample surface. The height of the slit allowed a 118 μm vertical strip of the sample to be imaged. By scanning the piezo stage in the dimension perpendicular to the slit, it was possible to collect absorption spectra over wide areas of the sample and extract the spatial dependence of the absorption spectrum.

For most of the PL experiments, a 532 nm diode pumped solid state laser was used. The laser provided 50 mW of power. The laser light was coupled into the beam path using a 4% beamsplitter and focussed onto the sample. The maximum power reaching the sample was 710 μW. The focussing lens was the asphere used from imaging which had an NA of 0.56. Optical density filters were used to vary the laser power reaching the sample, which allowed the power dependence of the PL to be studied. The PL

lens	f
L15	16
L16	200
L17	50
L18	100
AL2	5.5
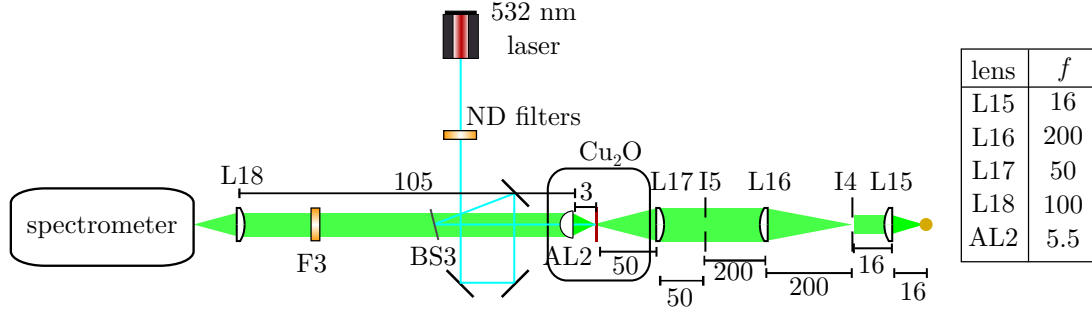
Figure 3.12: Optical setup for experiments performed at the University of Cardiff. Black lines measure distances between optics, focal lengths and distances are in mm. LED light (green) illuminates the sample using a Köhler illumination setup. Light transmitted through the sample was imaged onto the entrance slit of an imaging spectrometer. A 532 nm laser could be used for above bandgap excitation. The light was coupled into the beam path using a 4% reflective beamsplitter (BS3) an focussed onto the sample. The intensity of the excitation light could be adjusted using neutral density (ND) filters. The light emitted from the sample was collected and imaged in the same way as the LED light.

from the sample was collected by the asphere and sent to the spectrometer using the same beam path as the LED. An optical filter (F3; Schott OG530 3mm filter) was used to separate the excitation light from the PL emitted from the sample. For some experiments, an alternative laser (473 nm max power at the sample 50 µW) was used.

The spectrometer used was a custom-built grating spectrometer with a focal length of 1.9 m. The spectrometer had a 1200 g/mm grating of (120×140) mm^2 size, 900 nm blaze wavelength. The grating could be used in either first or second order diffraction, giving a resolution of 70 and 35 µeV (FWHM) respectively. For study of the Rydberg series, the second order diffraction was used. For the PL measurements, the grating was used in first order as it was desirable to cover a larger spectral range. The camera on the spectrometer was a CCD (Roper Pixis) of 1340×100 square pixels of 20 µm size. A neon lamp was used to calibrate the spectrometer.

3.5 Summary

In this chapter, sample preparation and the experimental apparatus used in this thesis was detailed. The experiment was built around a Montana C2 cryostation, which allowed the samples to be cooled to 4 K. Two sample mounts were used, the first was a copper sample mount which placed the sample between two CaF_2 windows. In the second sample mount, the sample was placed on a CaF_2 window which was attached to a microwave antenna. This second sample mount had issues with the sample heating under laser excitation. In both cases, the sample was glued onto the CaF_2 windows to improve thermal contact.

The laser spectroscopy setups were built around an infra-red laser system. The laser system was composed of an ECDL, an EOM, a Raman fibre amplifier and an AOM. The laser system allowed short, intense square pulses of IR light to be generated. The linewidth of the laser for a 50 ns pulse was near transform limited to be 50 neV. The tunablity of the laser system was set by the ECDL, which could be tuned between 1140 and 1150 nm which is the spectral range required to be two-photon resonant with Rydberg excitons in Cu_2O. The laser wavelength was monitored on a wavemeter. Through the EOM, the pulse length could be varied from 1 ns to continuous wave, and through the AOM, the repetition rate could be varied from 5 MHz to single shot. The laser could also be frequency doubled using a ppLN crystal, so that it was one-photon resonant with the Rydberg series.

For the two-photon experiments, the primary detection method was a SPAD. This allowed both intensity and temporal information with a resolution of 200 ps to be recorded. The SPAD could be combined with a Fabry-Pérot etalon or a monochromator to provide spectral information on the studied light. For the one-photon laser experiments, a balanced photodiode was used as the detector.

Broadband illumination was provided by an LED. This allowed the sample to imaged using a microscope setup. In combination with the monochromator, the LED also allowed broadband one-photon absorption spectroscopy to be performed.

To apply microwave fields to the samples two different antennae were used. In both cases, the sample was placed in the near field of the antennae. The antennae were driven by a microwave generator which could provide microwave frequencies of up to 20 GHz. The changes in the optical proprieties of the Rydberg excitons due to the microwave field was studied using the one- and two-photon spectroscopy techniques.

Also detailed in this chapter was the experimental apparatus used for characterising the samples used in this work. This apparatus was located at the University of Cardiff. The apparatus consisted of a high resolution grating spectrometer which was used to perform absorption measurements as well as above bandgap PL measurements.

Sample Characterisation

In this chapter the results from characterising the Cu_2O samples used in this work will be discussed. Both synthetic and natural cuprous oxide samples were studied, with the natural material found to be of higher quality. The natural material was purchased on the commercial gem and mineral markets, while the synthetic material was grown from an oxidised copper rod using a floating zone technique. The details of the growth will not be given here, but are available in [78]. In this chapter, the one-photon absorption and PL spectra from the natural samples will be studied first. This will be followed by a comparison between the highest quality natural sample and the synthetic material.

Table 4.1 lists the samples used in this work. The orientation of the samples, their origin and notes about the quality of their Rydberg series is given. More samples were studied than are presented here. The samples presented here include the ones which are used for further experiments (AM and AB) or are representative of samples of a particular origin. AL is an average sample from a Namibian mine, AH is representative of natural samples studied from outside of Namibia and AG is representative of the synthetic samples grown. All of the samples were prepared and mounted in the same way as described in section 3.2

Sample	Orientation	Origin	Quality
AB	(001)	Natural, Tsumeb mine, Namibia	Good quality
AL	(111)	Natural, Tsumeb mine, Namibia	High quality
AM	(111)	Natural, Tsumeb mine, Namibia	Highest quality
AG	Unorientated	Synthetic, floating zone growth	Poor quality
AH	Unorientated	Natural, Rubtsovskiy mine, Siberia	Very poor quality

Table 4.1: Samples used in this thesis.
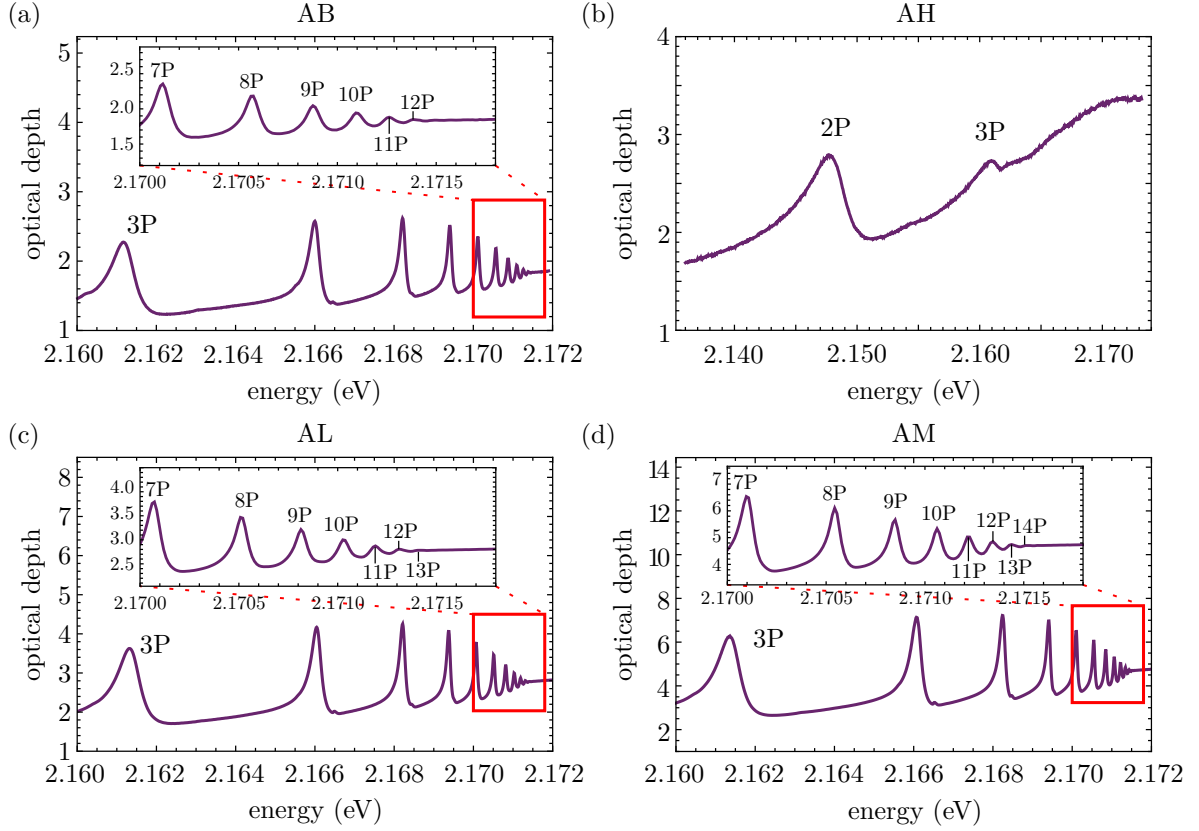
Figure 4.1: LED spectroscopy of the Rydberg exciton series in four natural samples at 4 K. Insets are zooms of regions highlighted by the red boxes. Samples are: (a) AB, (b) AH, (c) AL, (d) AM. Sample AM shows the best Rydberg exciton spectrum, with $n = 14$ visible. The difference in optical depth for the different samples is attributed to varying sample thicknesses.

Defining a figure of merit for a high quality sample is not trivial as there are many potential figures of merit. These include (but are not limited to): the presence of vacancies or bound exciton states, the concentration of inclusions in the sample and the single crystal nature of the material. However, in this thesis, the property of the sample that is most important is the presence of Rydberg excitons. Therefore, the quality of the Rydberg series is used as the main figure of merit when characterising samples.

To measure and characterise the Rydberg series of each of the samples, broadband LED absorption measurements were performed. For this the broadband LED absorption setup at the University of Cardiff described in section 3.4 was used. The input intensity of the LED was approximately 10 mW/cm². The spectrum of the light transmitted through the sample, I, along with a reference spectrum of the LED, I_0, were recorded. The reference spectrum was taken by moving the sample with the piezo stage such that

the transmitted light did not pass through the sample. The ratio of the transmitted intensity to the reference intensity gives the transmittance, $T = I/I_0$. The optical depth is related to the transmittance by optical depth $= -\ln(T)$. The optical depth is proportional to the absorption coefficient and the thickness of the sample as discussed in section 2.3.

The resulting absorption spectra are shown in Fig. 4.1. From these spectra it is clear the three spectra from Namibian samples (AB, AL and AM) are far better than the spectrum from the Siberian sample AH. In sample AH, the Rydberg series is severely limited, with $n = 3$ the highest state observed. The spectra from the three Namibian samples are similar. For samples AB and AL the highest observable state was $n = 12$ and $n = 13$ respectively. Sample AM was the best of the samples with $n = 14$ visible. Sample AM was notably thicker than the other samples, which account for the much higher optical depth. Due to the higher optical depth, the observation of higher n in sample AM is limited by the dynamic range of the spectrometer. For the other samples, the sample quality is believed to be the limiting factor. In the next part of this chapter, the spatial variation in the Rydberg series is studied.

4.1 Spatial inhomogeneity

To further investigate the quality of the samples, the spatial dependence of the Rydberg series was studied. The experimental setup used was the same that used to record the absorption spectra in Fig. 4.1. The imaging spectrometer allowed a 1.16×120 µm strip of the sample to be imaged in a single acquisition. The camera on the spectrometer had 100 pixels in the vertical direction, giving a resolution of 1.2 µm in this dimension. To record spectra at different spatial positions, the piezo stage inside the cryostation was scanned in the horizontal direction. This allowed the sample to be moved and a different area of the sample to be imaged by the spectrometer. The piezo stage was scanned at a speed of approximately $3\,\mathrm{\mu m\,s^{-1}}$. Spectra were taken every second, so each spectra corresponded to averaging over 3 µm of the sample in the scanning direction. The spectra are taken in transmission geometry, and so all of the spectra are averaged over the ≈ 50 µm thickness of the samples. Once a horizontal scan of the scan was complete, the sample was adjusted vertically by 120 µm and the scan was repeated, allowing spectra from the whole sample to be recorded.

To extract spatially dependent data from the scans, the spectra at each location were fitted. Fitting the entire absorption spectrum is challenging, due to the background phonon-assisted absorption. Instead, the peaks were fitted individually. The data was cropped such that only the desired peak was present. This was then fitted with an asymmetric Lorentzian [134; 138; 32] plus a constant background. The asymmetric Lorentzian was defined as

$$\alpha_{n\mathrm{P}} = A_{n\mathrm{P}} \frac{\Gamma_{n\mathrm{P}}/2 + 2q_{n\mathrm{P}}(E - E_{n\mathrm{P}})}{(\Gamma_{n\mathrm{P}}/2)^2 + (E - E_{n\mathrm{P}})^2}, \tag{4.1}$$

where $\alpha_{n\mathrm{P}}$ is the contribution to the absorption coefficient from the nth Rydberg state, $A_{n\mathrm{P}}$, $\Gamma_{n\mathrm{P}}$, $E_{n\mathrm{P}}$, and $q_{n\mathrm{P}}$ are the amplitude, linewidth, energy and asymmetry of the $n\mathrm{P}$ Rydberg state and E is the excitation energy. Once the spectra were fitted, it was possible to plot the fit parameters as a function of position on the sample and construct spatial maps. The spatial maps allowed the sample inhomogeneity to be studied. The main cause of inhomogeneity is strain, which can be caused by external or internal factors. External factors include placing things on the surface [152; 153] or clamping and gluing the sample. Internal strain can be caused by the growth process [52] or the presence of voids and inclusions in the material. Strain in the crystal causes energy shifts and splitting of exciton resonances [154]. Due to the large linewidth of the
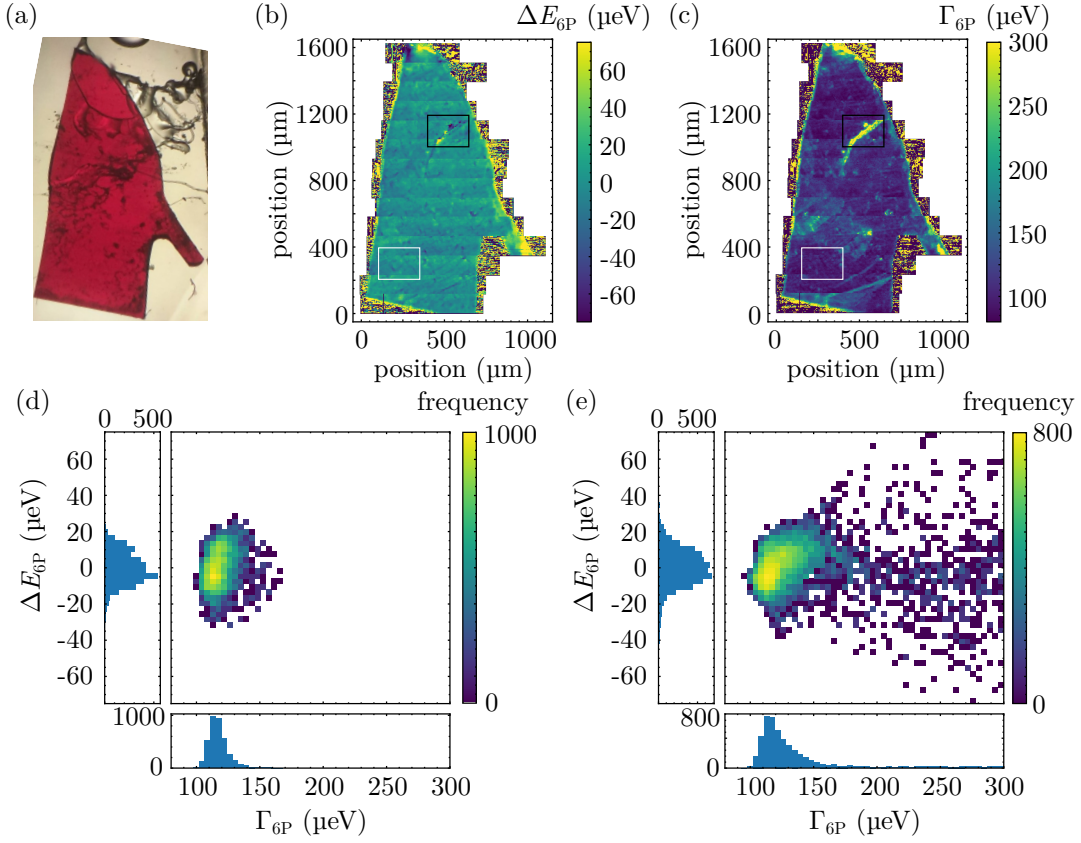
Figure 4.2: Spatial dependence of the energy and linewidth of the 6P exciton resonance on sample AB. (a) Microscope image of sample AB. (b) Spatial map of the energy shift of the 6P resonance (ΔE_{6P}), relative to the mean value across the sample. Two location used in (d) and (e) are highlighted by the white and black rectangles. (c) Spatial map of the linewidth (FWHM) of the 6P resonance, Γ_{6P}. (d) Two-dimensional histogram of the linewidth vs energy shift at the location of the white rectangle in (b) and (c). (e) Two-dimensional histogram of the linewidth vs energy shift at the location of the black rectangle in (b) and (c).

Rydberg states, and the averaging over the sample thickness, splittings of the Rydberg states are generally not observed. Instead a broadening of the Rydberg states was observed. By looking at the energy shifts and linewidths of the fitted exciton peaks, it was possible to visualise the strain in the crystal.

Fig. 4.2(a) shows a microscope image of sample AB. The sample is an irregular shape due to it fragmenting due the sample preparation process. The glue maintaining thermal contact with the CaF_2 window is visible at the top of the image. The surface quality of the sample is poor, with visible imperfections across the sample.

Shown in Fig. 4.2(b) is the spatial dependence of the energy of the 6P resonance. The plotted quantity is given by $\Delta E_{6P} = E_{6P} - \bar{E}_{6P}$, where E_{6P} is the fitted energy and

$\bar{E}_{6P}$ is the mean fitted energy across the whole sample. The noise around the edges of the data are points which are off the edge of the sample. The discontinuities across the sample correspond to the different horizontal scans. The discontinuities at the joins between scans appear due to a slight misalignment of the slit relative to the camera, which leads to a calibration shift across the vertical pixels of the camera. However, this experimental artefact is not the dominant features present in the spatial dependence. At the very top of the sample, there is a highly strained region, which is probably due to the glue holding the sample in place. The edges of the sample also show substantial energy shifts. However, large areas of the sample show very little variation in the exciton energy. Notably, the shifts due to the gluing are localised to the top of the sample, and do not influence the exciton energy away from the glued region. One of the most homogeneous areas on the sample is highlighted by the white box. A less homogeneous region is highlight by the black box. In the inhomogeneous region there is a feature causing large energy shifts. When comparing the energy map to the sample image, it is evident the inhomogeneous region corresponds to an area of the sample with a poor surface quality and that the homogeneous region corresponds to an area of higher surface quality.

A map of spatial dependence of the linewidth (FWHM) of the 6P state is shown in Fig. 4.2(c). Many of the same features observed in Fig. 4.2(b) are also present here. Again, at the top of the sample, there is evidence of strain due to gluing. The feature highlighted by the black box is also more evident here, with the linewidths of the 6P state more than doubling at some locations. Towards the lower right of the sample there are a couple small circular features which do not appear in the energy map. Comparison with Fig. 4.2(a) shows these features are also present in the microscope image. Given that some features are present when looking at the variation in the exciton linewidth but are not present in the spatial map of the exciton energy, it appears the linewidth of the exciton state is a better judge of local sample environment.

To investigate the relationship between linewidth and energy shift, two-dimensional histograms of linewidth vs energy shift are plotted in Fig. 4.2(d) and (e). The two histograms are taken at the homogeneous region highlighted by the white box and the inhomogeneous area highlighted by the black box for (d) and (e) respectively. For the homogeneous region (Fig. 4.2(d)) the resulting histogram is compact. The range of the energy shift is approximately 40 µeV which is comparable to the spectrometer resolution (35 µeV) and smaller than the mean linewidth ($\approx$ 120 µeV). From looking at the one-dimensional histograms on the axes, the energy shift appears symmetrically distributed,
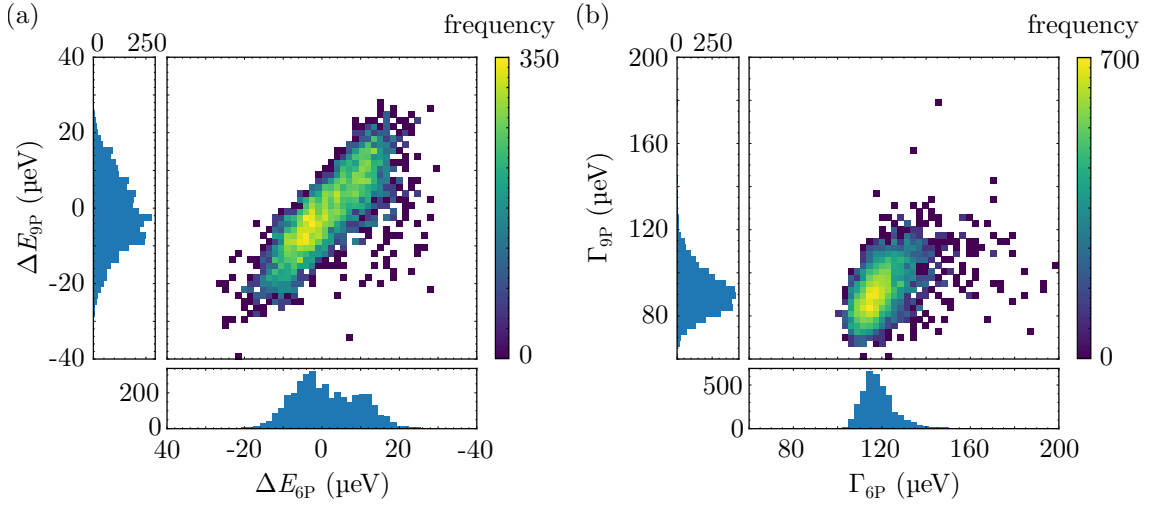
Figure 4.3: Comparison of the spatial variation in energy and linewidth of different Rydberg states on sample AB. The region of the sample studied is shown as the white box in Fig. 4.2(b) and (c). (a) Two-dimensional histogram of the energy shifts across the sample of the 6P and 9P Rydberg states. There is a clear correlation between the energy shifts. (b) Two-dimensional histogram of the linewidths across the sample of the 6P and 9P Rydberg states. The mean linewidth of the 6P state is ≈ 120 μeV and the 9P state is ≈ 90 μeV.

while the histogram of the exciton linewidths is asymmetric. This difference results from the fact that the energy of the state can be either increased or decreased but the linewidth of the state can only increase due to strain. For the inhomogeneous region (Fig. 4.2(e)) the asymmetric behaviour of the linewidth distribution is more apparent. There is also not a direct correlation between the linewidth and the energy shift, with many of the broadened peaks having an unchanged energy. However, if the energy of a state is substantially shifted it is very likely that it is also broadened. Again, this highlights the advantage of using the linewidth as a measure of local sample quality.

To study the n dependence of the sample homogeneity, the fitting process was repeated at $n = 9$. The resulting spatial maps appear very similar to those presented in Fig. 4.2(b) and (c) and so are not presented here. Instead, the shift of the 6P resonance is compared to the shift of the 9P resonance in Fig. 4.3(a). Here, a two dimensional histogram of the energy shift of the 6P and 9P resonances is shown for the homogeneous region of the sample highlighted by the white box in Fig. 4.2(b) and (c). There is a clear correlation between the two energy shifts. Fitting the histogram with a straight line returns a gradient of 0.99 ± 0.02. The correlation between the energy of the 6P and 9P resonances indicates both states are shifted equally, implying strain causes a global shift of the Rydberg series.
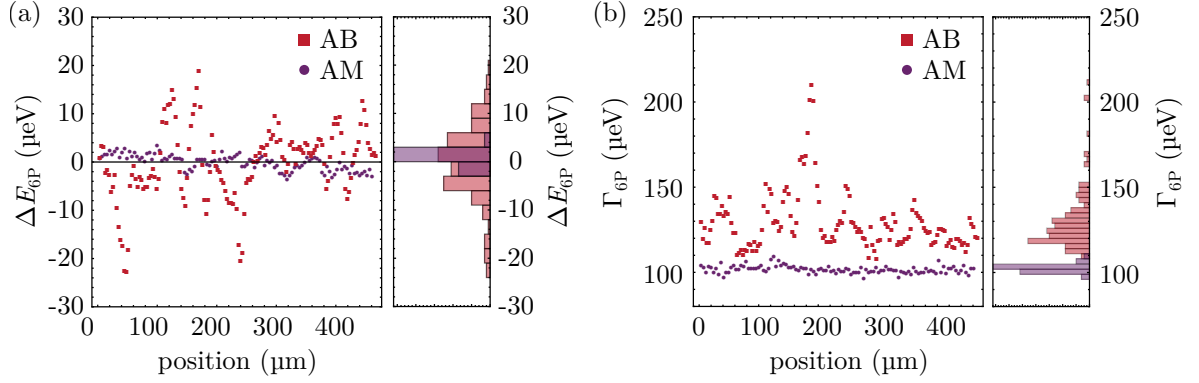
Figure 4.4: Homogeneity comparison of samples AB and AM. The linewidth and energy of the 6P resonance as a function of position was studied. The resolution of the spectrometer is 35 µeV. (a) Variation in energy of the 6P state from the sample mean vs sample position in samples AB and AM. Sample AB shows more variation in energy throughout the range of positions studied. (b) Variation in linewidth vs sample position in samples AB and AM. AB shows a higher linewidth, along with more variation in the linewidth.

Fig. 4.3(b) shows a comparison of the linewidth of the 6P and 9P resonances over the same sample region studied in Fig. 4.3(a). As in the case of the energy shifts, there is a correlation between the linewidth of the different resonances, though it is not as apparent as in Fig. 4.3. On average, the 9P resonance is narrower than the 6P resonance (FWHM of approximately 90 µeV vs 120 µeV). However, the range of linewidths measured at 9P is larger than the range of linewidths measured at 6P. At 9P the linewidths vary from 70 to 120 µeV while at 6P they vary from 105 µeV to 145 µeV. Although in absolute terms the approximate range of values is only 10 µeV larger at 9P, the 9P resonance is on average narrower than the 6P resonance. For the 6P resonance the range of linewidths is approximately 1/3 of the average linewidth, while at 9P it is approximately 2/3 of the average linewidth. This substantial increase shows the higher n excitons are more perturbed by the local sample environment.

For sample AM it was not possible to build a full map of the sample due to an issue with the vertical axis of the piezo stage. Instead, a single strip across AM was recorded. AM was found to be very homogeneous compared to the other samples. Fig. 4.4(a) compares the change in energy of the 6P state (relative to the mean across the sample), ΔE_{6P}, as a function of sample position on samples AB and AM. For sample AB the energy varies by about 40 µeV, while for sample AM the variation is less than 10 µeV which is considerably smaller than the resolution of the spectrometer (35 µeV). The variation in the linewidths of the 6P resonance across the two samples shown in Fig. 4.4(b).

Again, sample AM shows significantly lower variation across the sample. The average linewidth in sample AM is also lower than the average linewidth in sample AB. The lower variation in energy and linewidth (and lower average linewidth) of the 6P state indicates that there is less strain present in sample AM than in sample AB.

Although the Rydberg spectrum is perturbed by the local sample environment, crucially Rydberg excitons are still present at all but the most damaged sample locations. This shows that the while sample quality is important, local strain in a high quality sample is not fatal to the presence of Rydberg excitons. This technique shows that spatial mapping is almost essential, as it provides a way of identifying high quality samples, and allows the highest quality regions of these samples to be identified. As Rydberg excitons can still exist in strained regions there is potential for engineering local strain to trap Rydberg excitons [153]. Deliberately straining the crystal has been previously used to trap ground state excitons [155; 156; 157; 158; 152]. In future, the spatial mapping techniques used here could be applied to characterise structures which have been machined into the sample or placed on the sample surface and find areas of the sample which still exhibit a high quality Rydberg spectrum.

4.2 Photoluminescence spectroscopy

While a high quality sample (AM) was identified by looking at the Rydberg spectrum and its spatial variation under one-photon absorption, it is not clear why this sample is higher quality than the others. To investigate the sample quality further, PL spectroscopy was used. PL spectroscopy consists of an above bandgap excitation to generate free electron-hole pairs. The free electron-hole pairs can form excitons which then radiatively decay, emitting PL. If there are impurities or vacancies in a sample, the excitons can be trapped at these, leading to PL at different energies.

PL in Cu_2O has been extensively studied [159; 160; 161; 162; 163; 164; 165; 52; 95; 33]. In pure samples, the lowest energy exciton state is the 1S para-exciton. However, radiative decay from this state is forbidden to all orders, and so PL is not observed directly from this state. The para-exciton can decay through a weak phonon assisted process, though the main decay pathway is through up conversion to the 1S ortho-exciton state through scattering by acoustic phonons [166; 154]. The 1S ortho-exciton state then radiatively decays directly, or through phonon assisted processes. In high purity samples, such as the one used in [95], the majority of the PL is produced through the phonon assisted decay of the 1S exciton. Atomic scale impurities in samples can lead to the excitons becoming bound at the impurity site [163], leading to sharp spectral features at lower energy than the 1S para-exciton. In addition to impurities, copper and oxygen vacancies form traps for the excitons, leading to broad spectral features at much lower energy than the 1S para-exciton [52; 167; 168].

For most of the PL experiments, the experimental apparatus at the University of Cardiff detailed in section 3.4 was used. For sample AH, AL, AM a 532 nm laser which delivered a maximum power of 710 µW to the sample was used. For sample AB a 473 nm laser was used which delivered a maximum power of 50 µW to the sample. Due to the high resolution of the spectrometer used, it was only possible to record ≈ 0.3 meV of the PL spectrum without rotating the diffraction grating. For features around the 1S exciton, multiple scans from the spectrometer were recorded and stitched together. Due to the large width of the vacancy features (FWHM ≈ 0.2 eV) it was not possible to record the full spectrum over this range. To account for this, spectra at three distinct energies, 1.70, 1.55 and 1.35 eV, were taken. These energies correspond to the peak of the doubly charged oxygen vacancy (V_O^{2+}), singly charged oxygen vacancy (V_O^{1+}) and the copper vacancy (V_{Cu}) respectively [52].
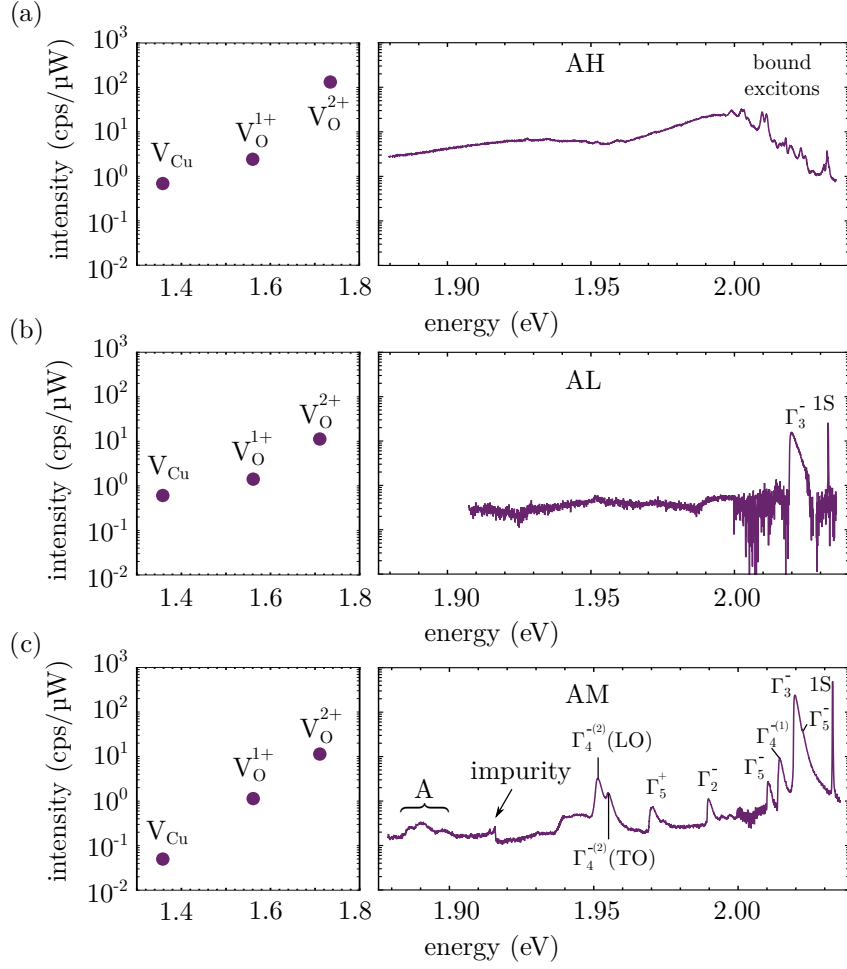
Figure 4.5: One-photon PL from natural samples from above bandgap excitation at 532 nm on three natural gemstones at 4 K. Data from AH and AM were taken at 710 µW and AL at 9 µW of excitation power. (a) PL from sample AH. The label 1S refers to the 1S ortho-exciton. (b) PL from sample AL. (c) PL from sample AM.

Fig. 4.5 shows PL spectra from three of the natural samples measured in counts per second per µW. The spectral region around the 1S state is shown, along with the three points at the vacancy energies. As was seen when looking at the absorption spectra from each sample (Fig. 4.1), sample AH shows a different spectrum to the other samples. In sample AH, the 1S ortho-exciton and its phonon replicas are not visible, indicating the free excitons are being trapped before they radiatively decay. In the spectral region around the 1S state, a series of sharp lines corresponding to bound exciton peaks is present [163]. The bound exciton peaks also sit on a broader feature. This broader feature has been observed in previous work [163; 52] but its origin is not known. Sample AH also shows a high intensity of PL from the doubly charged oxygen vacancies, with the emission at 1.70 eV being more intense than the emission from the

bound excitons. Given the linewidth of the vacancy peaks, this appears to be dominant decay mechanism for excitons in this sample.

The PL from the other two sample shown in Fig. 4.5 are similar. Sample AL shows intense emission from the 1S ortho-exciton and its Γ_3^- phonon replica. The additional noise around the ortho-exciton is a consequence of a shorter exposure time in this spectral region. The laser power is also lower for this sample, as it was found to heat under laser excitation. While there are a few features in the rest of the spectral range shown, it is not possible to assign these features due to the poor signal to noise ratio. From comparison with the PL from sample AM, these features would be expected to be other phonon replicas. Sample AL still shows a reasonable concentration of doubly charged oxygen vacancies, with the peak at 1.70 eV being a comparable intensity to the 1S ortho-exciton peak.

The PL from sample AM shows intense emission from the 1S ortho-exciton, along with emission from multiple phonon replicas. Overall, the PL from this sample looks incredibly similar to the spectra shown in [95]. At energies below 1.95 eV there are two subtle differences though. In the spectrum in [95] a small peak at 1.947 eV, sitting on the red-shifted shoulder of the double-peaked phonon feature above just 1.95 eV is present. This peak does not appear in the data presented here. Additionally, the spectrum in Fig. 4.5(c) shows two sharp peaks at 1.914 eV and 1.916 eV (labelled impurity) which are not present in the spectrum in [95]. These two peaks have been observed in previous PL studies [160; 169] but have not been assigned. The appearance of these peaks implies the presence of trace impurities in the sample. Despite the high quality of the PL spectrum from sample AM there is still a reasonable amount of PL from the vacancy states. As was found in all natural sample studied, the PL from the doubly charged oxygen vacancy is the most intense, with the copper vacancy the weakest. The PL from the oxygen vacancies is more than an order of magnitude weaker than the PL from the 1S ortho-exciton. This is substantially lower than any of the other samples, indicating the vacancy concentration in sample AM is the lowest of the studied samples.

The phonon replicas present in Fig. 4.5(c) can be fitted to extract the corresponding phonon energy and exciton temperature. The lineshape of the phonon replicas can be fitted with the convolution of two terms describing the exciton density of states and thermal occupation statistics respectively [134]. The low-energy side has a rising edge, which scales with the 3D density of states, $g^{3D}(E)$. The high-energy side has an exponential tail from the exciton Bose-Einstein population statistics, which can
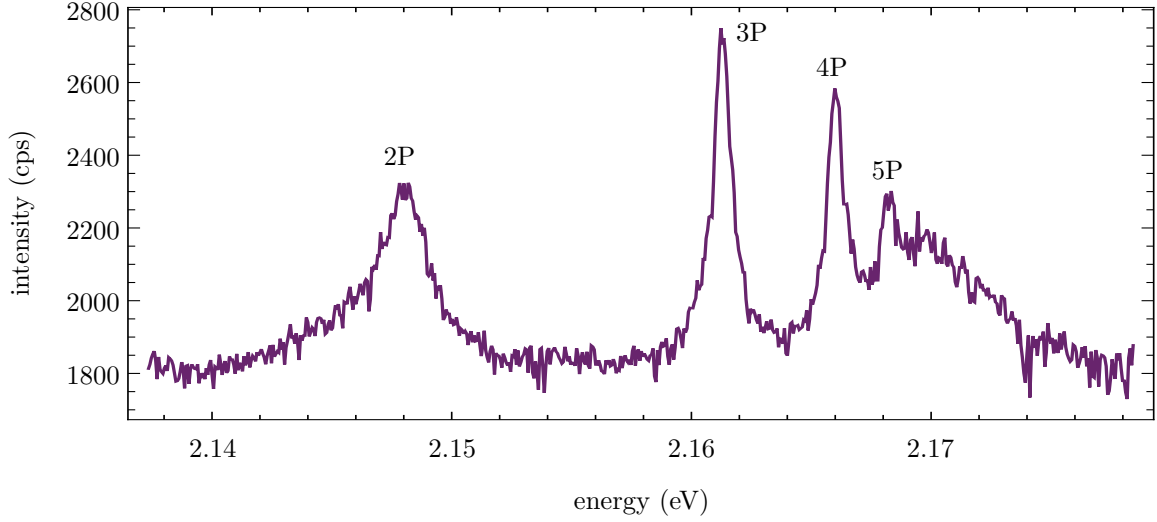
Figure 4.6: One-photon PL from sample AM from above bandgap excitation at 532 nm at 4 K. Rydberg states up to $n = 5$ are visible. States sit on a nonresonant background of unknown origin.

be approximated to the Boltzmann distribution, $f_{\mathrm{B}}(E)$, since the exciton gas is of low-density. The PL intensity $I_{\mathrm{PL}} \propto g^{\mathrm{3D}}(E) f_{\mathrm{B}}(E)$ is then described by,

$$I_{\mathrm{PL}} = A(E - E_0)^{1/2} \exp\left[-\frac{(E - E_0)}{k_{\mathrm{B}} T} \right] \ , \tag{4.2}$$

where A is a proportionality constant and E_0 is the energy of the exciton at zero momentum minus the phonon energy, with the phonon assumed to have no dispersion. A similar lineshape fitting function was used in previous works [160; 95]. The extracted temperature from this fit was more than 12 K, which is considerably higher than the heatsink temperature of the cryostation. This high temperature is investigated further by performing power dependent measurements in section 4.2.1.

The extracted phonon energies from fitting the phonon replicas are given in Table 4.2 and compared to literature values from [95]. The energies of some of the phonons are not reported as they are too weak to reliably extract an energy. There is good agreement between the fitted values and those reported in the literature.

Sample AM also showed weak PL from the Rydberg series. Fig 4.6 shows the PL from the Rydberg states, with exciton states up to 5P resolvable. Previous studies showed that PL from the Rydberg series occurs through a collisional process [95]. The mechanism involves the collision of two excitons which are in either the 1S ortho- or para-exciton states. One of these excitons is excited up to a Rydberg state where it can then decay radiatively. The other exciton radiatively emits at around 1.89 eV.

Phonon	Phonon energy (meV)	[95] (meV)
Γ_3^-	13.6 ± 0.1	13.5
$\Gamma_4^{-(1)}$	18.8 ± 0.1	18.8
Γ_2^-	43.6 ± 0.2	43.4
Γ_5^+	63.5 ± 0.4	63.2
$\Gamma_4^{-(2)}(\text{TO})$	78.5 ± 0.1	78.4
$\Gamma_4^{-(2)}(\text{LO})$	82.1 ± 0.1	82.0

Table 4.2: Energy positions of the phonon assisted lines (in eV). The relative positions with respect to the resonance energy of the yellow 1S ortho-exciton are also tabulated (in meV) and compared with the values reported in [95].

The corresponding emission at 1.89 eV can be seen as weak features in Fig. 4.5(c), labelled as A. The PL from the Rydberg states sits on a non-resonant background. This background emission has not been reported in previous studies of PL from Rydberg states [95; 57].

For sample AB, the PL was studied using different methods. The majority of the PL studies were done under two-photon excitation, though a small amount of one-photon PL was also performed. For the two-photon excitation experiment, the excitation was provided using the infra-red laser system and two-photon spectroscopy setups detailed in section 3.1.1 and 3.1.2.1. For detection, the monochromator described in section 3.1.3.2 was used. The PL spectrum taken at two sample locations with the laser two-photon resonant with the 5D state is shown in Fig. 4.7(a). The average laser power used was 90 mW which is substantially higher than for the one-photon measurements (Fig. 4.5). This is due to the two-photon absorption process being much weaker than the one-photon process. There was no evidence of the PL from the vacancy states, though the signal to noise ratio using this method is poorer than in the one-photon experiments used for the other samples. In both spectra, there is evidence of weak PL from bound excitons. Interestingly, only one of the sample locations shows PL from the 1S state and its ortho-exciton, showing the inhomogeneity of sample AB. This could be an indication that the free excitons are not decaying in the location they are excited, and may be migrating to different sample locations. The migration of excitons due to strain has previously been observed by deliberately straining the crystal [156].

One-photon PL measurements on sample AB allowed the bound exciton states to be studied in more detail. For this, a 473 nm laser which delivered 50 µW to the sample was used. Apart from the excitation laser, the experimental setup was the same as
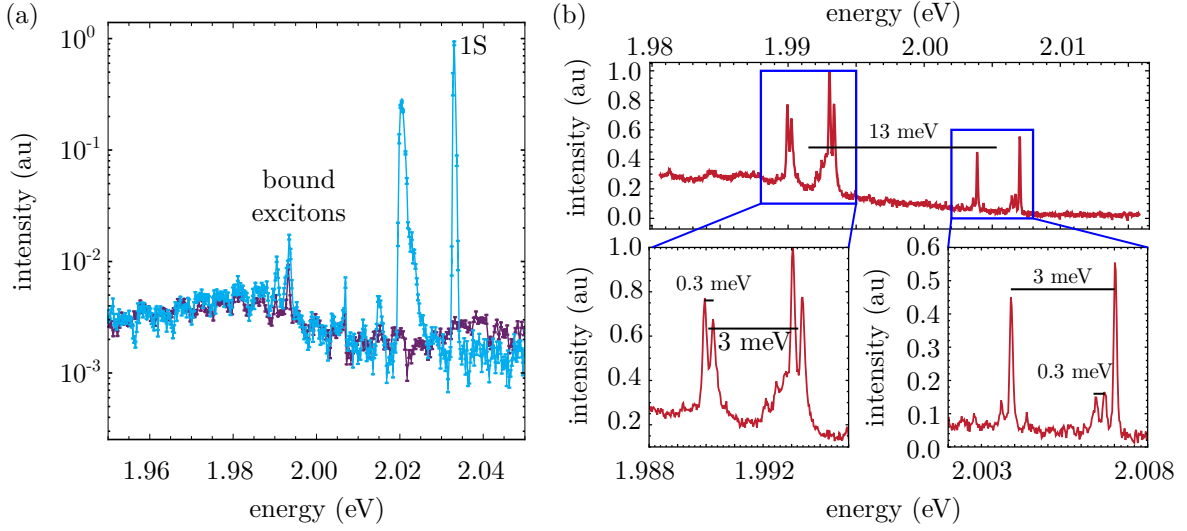
Figure 4.7: PL spectra from sample AB at 4 K. (a) PL spectra under two-photon excitation from sample AB at two different locations. PL from the 1S is only visible at one location. PL from bound excitons is visible from both. (b) High resolution PL from sample AB under one-photon excitation. Zooms show the separation between the bound exciton peaks.

used for the one-photon PL experiments on the other samples. Using this method, there was no visible PL from the 1S ortho-exciton. The energies of the vacancy peaks were not checked for emission. The resulting spectrum is shown in Fig. 4.7(b). The spectrum shows multiple peaks, with two multiplets of peaks at around 1.992 eV and another two around 2.005 eV. Each of the pairs of multiplets is separated by around 3 meV, with the peaks within a multiplet separated by around 0.3 meV. The pairs of multiplets are separated by approximately 13 meV, which is similar to the splitting between the free ortho- and para-exciton (12 meV) [154]. Previous work on bound excitons attributed the bound exciton peaks to trapped ortho- and para-excitons [163]. The peaks in the spectrum from sample AB are at different energies to those observed in [163], implying the bound excitons are caused by different impurities.

4.2.1 Power dependence of PL

To further investigate the PL, power dependent measurements were performed on sample AM. To vary the excitation power of the laser, neutral density filters were inserted into the beam path. The power dependence of the PL from the 1S ortho-exciton at different excitation powers is shown in Fig. 4.8(a). The direct recombination of the ortho-exciton was fitted using a pseudo-Voigt profile plus a constant background (to
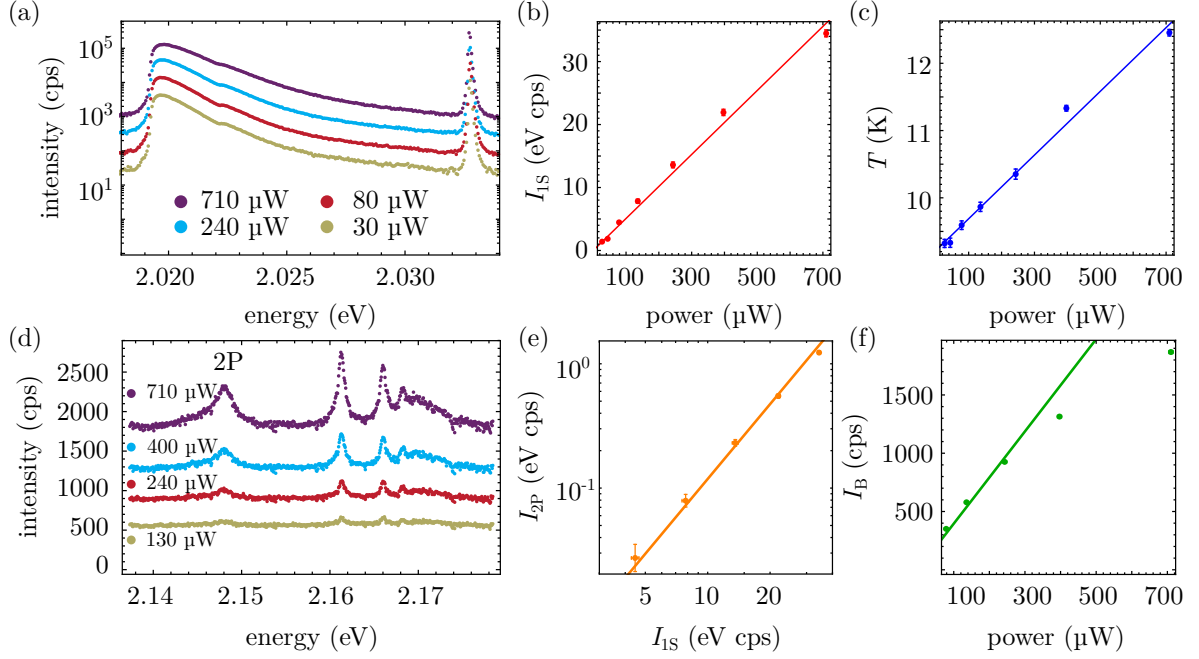
Figure 4.8: Power dependence of photoluminescence from sample AM. (a) Power dependence of the 1S exciton and phonon replicas. (b) Power dependence of the area of the 1S exciton I_{1S}. Red line shows a linear dependence. (c) Extracted temperature from fitting the phonon replicas vs excitation power. Solid line shows a linear fit, with an intercept at $T = 9.2$ K. (d) Power dependence of PL from the Rydberg excitons. The Rydberg excitons sit on a broad background which has not been previously observed. (e) Fitted area of the 2P peak, I_{2P}, vs I_{1S}. Solid line shows a quadratic dependence on I_{1S}. (f) Power dependence of the broad background in (d). Solid line shows a linear dependence. The data has a sub-linear power dependence.

account for the tail of the phonon replica). This fit returned an average linewidth (FWHM) of 80 µeV across all of the scans. The linewidth varied from 70 to 90 µeV in the fits, which is just above the spectrometer resolution of 70 µeV in first order. The integrated intensity of the fitted 1S ortho-exciton, I_{1S}, is plotted against excitation power in Fig. 4.8(b). As would be expected for one-photon processes, the PL intensity from the 1S ortho-exciton is approximately linear with excitation power, with the solid line showing a linear fit to the data.

The phonon replica feature in Fig. 4.8(a) was fitted to extract the exciton temperature. As before, equation 4.2 was used to describe the lineshape of the phonon replicas. The total fit function was a linear sum of two of these lineshape functions to represent the Γ_3^- and Γ_5^- phonons. The temperature parameter was shared between both phonon lineshapes. The extracted temperature vs laser power is shown in Fig. 4.8(c). For all laser powers, the extracted exciton temperature is much higher than the heatsink

temperature of the cryostation (4 K). The lowest extracted temperature is above 9 K, and the highest is above 12 K. The temperatures appear to follow a linear trend with laser power. A fit to this linear trend is shown as the solid line in Fig. 4.8(c). The intercept of this linear fit is 9.2 K, which implies that even at very low excitation powers the exciton temperature will be significantly higher than the heatsink temperature. It should be noted that the fitting the phonon replica provides the exciton temperature. As the excitons may not have thermalised with the lattice, the exciton temperature may be higher than the lattice temperature [170]. However, a 5 K temperature difference between the excitons and the lattice at only 15 µW of excitation power seems large. A more likely explanation for the high temperature is that the sample is not at the heatsink temperature. This could be caused by poor thermal contact between the sample and the CaF_2 window it is mounted on.

The power dependence of the PL from Rydberg states was also studied and is shown in Fig. 4.8(d). While both the intensity of the background and the Rydberg states grow as the excitation power is increased, they clearly have different power dependencies. To investigate this further, the 2P Rydberg state was fitted with a Lorentzian lineshape plus a constant background. As previously discussed, the PL from Rydberg states is due to a collisional process involving two free excitons, which leads to a quadratic dependence on the free exciton density [95]. Here, the luminescence from the direct recombination of the 1S ortho-exciton is assumed to be proportional to the free exciton density. Fig. 4.8(e) shows the integrated intensity of the 2P peak, I_{2P}, plotted against the integrated intensity of the 1S peak, I_{1S}. The solid line represents a quadratic fit. The data agrees well with the solid line, indicating the PL from Rydberg states is indeed caused by a collisional process of free excitons. The background extracted from fitting the 2P resonances is plotted as a function of excitation power in Fig. 4.8(f). The solid line shows a linear trend. The background clearly has a sub-linear dependence on laser power. This indicates the background is not caused by the collisional process that causes PL from the Rydberg excitons, and must be due to a different mechanism.

In this section, PL from natural samples was studied. Out of the samples studied, AM was found to have the lowest concentration of vacancies and did not show the characteristic PL peaks caused by bound excitons. The high purity of sample AM is consistent with the absorption spectra, which showed AM had the best Rydberg series and was the most spatially homogeneous of the studied samples. Sample AH showed the highest intensity of vacancy and impurity luminescence out of all of the samples, indicating it was the poorest quality. Again, this was consistent with the absorption

spectra, where only excitons up to $n = 3$ were visible in sample AH. Sample AL possessed the second best Rydberg series of the samples presented. In this sample, the PL did not indicate the presence of bound excitons, though there was a higher concentration of oxygen vacancies than in sample AM. From looking at these three samples, there appears to be a correlation between the concentration of doubly charged oxygen vacancies and the quality of the Rydberg spectrum. Recent theoretical work supports this correlation, where it was shown that charges in the crystal can limit the observation of high n Rydberg states [48]. Unfortunately the vacancy luminescence from sample AB was not thoroughly studied. However, the PL from sample AB did show PL from bound excitons, indicating the crystal was not pure. This is interesting, as it indicates a reasonably good Rydberg series can exist in a sample which contains impurities.

The power dependencies of the PL was studied. As expected, the 1S ortho-exciton was found to have a linear dependence on excitation power. From fitting the phonon replica of the 1S ortho-exciton it was possible to extract an exciton temperature. Even at low excitation powers, this temperature was found to be much higher than the cryostation temperature, potentially indicating that the sample is in poor thermal contact with the cryostation. The power dependence of the PL from the Rydberg states was also studied. Here, it was found that the intensity of PL from the Rydberg states was proportional to the exciton density squared. This was in agreement with the literature, which shows PL from Rydberg states occurs through collisional processes [95].

4.3   Synthetic material

For any future application of Rydberg excitons in Cu_2O, it will be necessary to be able to produce high quality synthetic material. In this section, synthetic material grown by the floating zone method [78] is compared to high quality natural material (sample AM). The synthetic material was found to be of lower quality than the natural sample, and was found to have a high concentration of copper vacancies.

The Rydberg series from synthetic sample AG is shown in Fig. 4.9(a). The setup used was the same as in Fig. 4.1. For comparison, the spectrum from the highest quality natural sample (AM) is also shown (Fig. 4.9(b)). In the synthetic sample, Rydberg states up to 9P (possibly 10P) are visible, indicating the synthetic sample is as high quality as previously studied synthetic samples [50]. However, the peaks $n > 10$ are missing, and so the material is lower quality than the natural sample.

There are also additional peaks present in the synthetic sample. At higher n, peaks appear between the P resonances. This is most apparent between the 8P and 9P states. By comparing the energies of these additional peaks with the energies obtained from two-photon spectroscopy [141] (further details in chapter 5) these peaks have been assigned to the D states. The appearance of D states is forbidden due to parity selection rules. However, if the crystal symmetry is broken, (e.g. with external fields) forbidden angular momentum states can be observed [171; 107; 108; 109; 110; 111; 112]. The appearance of these additional peaks leads to a crowding of the spectrum at high n, and makes observing higher lying states impossible.

As no external fields are applied in this measurement, the appearance of forbidden states must be due to a property of the sample itself. One possible explanation is strain within the crystal. Strain has been previously shown to split lines and allow the observation of forbidden transitions, such as the 1S para-exciton [156]. As previously discussed, strain can also lead to a broadening of the resonances, which could lead to the disappearance of high n excitons into a continuum.

The homogeneity of the sample was studied in the same way as the natural samples in section 4.1, by taking absorption spectra at different sample locations. The high n cutoff in the Rydberg series was found to be independent of the location on the sample, and the additional peaks were visible at all sample locations studied. However, there was variation in the Rydberg spectrum across the sample. Fig. 4.10(a) shows the variation in the energy of the $n = 6$ peak (ΔE_{6P}) across the sample. For comparison,
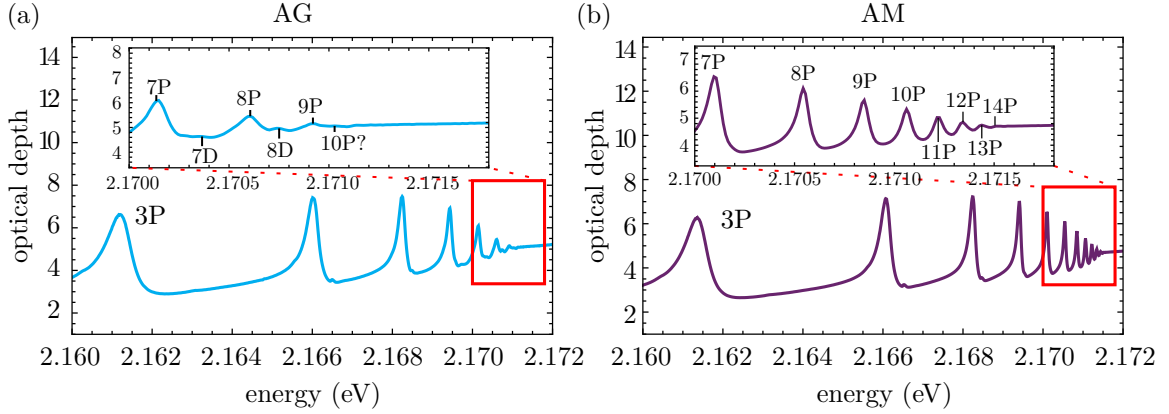
Figure 4.9: Absorption spectra from a synthetic sample (AG) and a natural sample (AM). Plotted quantity $-\ln(T)$ is proportional to the absorption coefficient. (a) Synthetic sample AG (b) Natural sample AM. The Rydberg spectrum does not extend to as high n in the synthetic sample. Additional peaks (D states) also appear between the P resonances at higher n.

the variation from sample AM is also shown. The synthetic sample appears reasonably homogeneous, though there are a couple of points where the energy of the 6P peak shifts substantially. The linewidth of the 6P state across sample AG is compared to the linewidth of the 6P state on sample AM in Fig. 4.10(b). As with the energies, the linewidth of the 6P resonance on sample AG shows a couple of locations where it changes substantially, indicating strain. The linewidth is also significantly higher than the linewidth in sample AM. Overall, the synthetic sample shows poorer homogeneity when compared with the best natural sample and a significantly broader peak, both of which indicate the sample is strained. However, given that the high n cutoff does not vary with sample position, and that the forbidden states are present across the sample, it seems unlikely that the strain is the limiting factor in observing higher lying Rydberg states.

Another possibility for the disappearance of the high lying states is the presence of impurities or defects in the material. Recent theoretical work has predicted that charged impurities can cause the disappearance of high n exciton resonances, as well as the appearance of forbidden peaks [48]. In the highest quality natural samples it was shown that the charges in the material were the limiting factor in reaching higher n [45]. To identify impurities in the sample, PL spectroscopy was used.

PL spectroscopy was performed using the setup described in section 3.4. This is the same setup that was used in section 4.2 for samples AH, AL and AM. Fig. 4.11 shows the resulting PL spectrum around the 1S exciton and at the energy of the vacancy
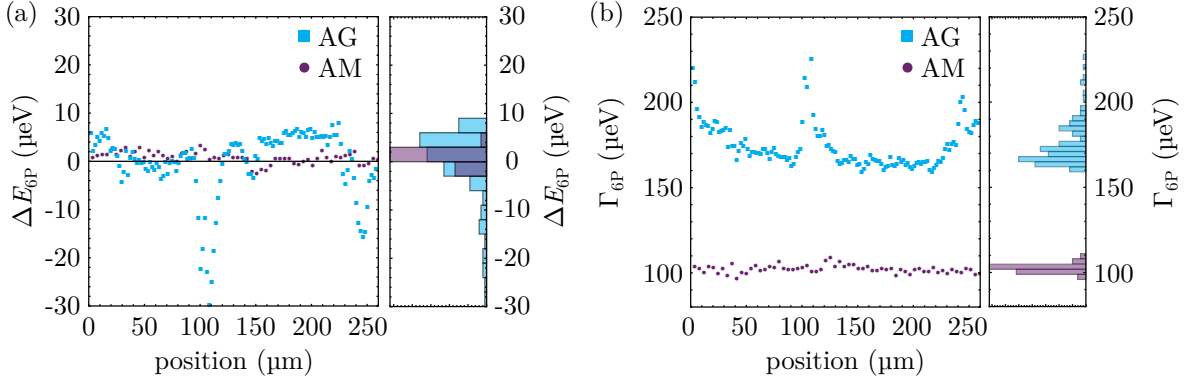
Figure 4.10: Variation in the energy and linewidth of the 6P resonance as a function of position on the sample for synthetic sample AG and natural sample AM. The resolution of the spectrometer is 35 µeV. (a) Variation in energy from the mean vs sample position in samples AG and AM. The synthetic sample (AG) shows more variation in energy, with a couple of dips where the energy changes dramatically. (b) Variation in linewidth (FWHM) of the 6P exciton resonance vs sample position in samples AG and AM. AG shows a higher linewidth, along with more variation in the linewidth.

states for synthetic sample AG and for natural sample AM. There was no PL observed from the Rydberg series in the synthetic sample. Around the energy of the 1S exciton the PL from sample AM and AG look very similar. Both show the sharp feature at 2.033 eV corresponding to the direct recombination of the 1S ortho-exciton. Multiple phonon replicas are also present in both samples. Crucially, there are no signs of any bound excitons in the synthetic sample. The main difference between the two PL spectra around the energy of the 1S exciton is the intensity of the PL. The PL from sample AM is more than 10 times brighter than from AG. However, there are major differences between the two spectra at the energies of the vacancy peaks. The synthetic sample shows a high PL intensity at the energy of the copper vacancies. PL from the copper vacancies was not observed in any natural sample studied.

The high concentration of copper vacancies indicate there are charges in the material. These charges are believed to be the limiting factor in observing higher n states. As well as imposing a limit on the highest n observable, charged impurities also broaden exciton resonances. This may account for the exciton resonances being broader in the synthetic sample in Fig. 4.10. Previous work on the effect of impurities in Cu_2O studied impurity densities up to 10^{11} cm^{-3}, which led to the predicted Rydberg series being limited to $n = 13$ [48]. Here, the density must be larger than this to cause the Rydberg spectrum to be limited to lower n. To be able to reach $n > 20$ it is predicted the impurity density would have to be reduced by more than an order of magnitude.
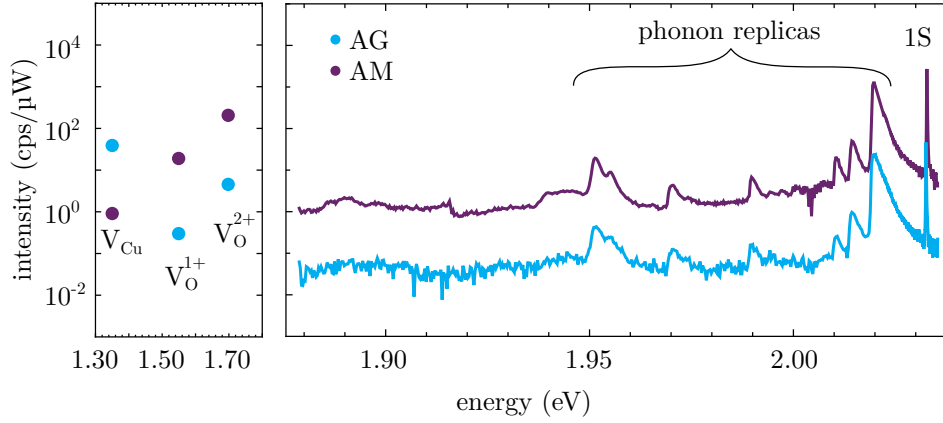
Figure 4.11: PL spectra from synthetic sample AG and natural sample AM. In the region around the 1S exciton the spectra look very similar, though the emission from AG is weaker. When looking at the energy of the vacancy peaks, AG shows a high concentration of copper vacancies, whereas the copper vacancy concentration in AM is very small.

The copper vacancies in the synthetic samples made it impossible to perform any two-photon measurements. The low energy tail of the copper vacancy peak extends below 1140 nm which led to significant one-photon absorption from the synthetic samples under the IR laser excitation at 1140 nm. The one-photon absorption caused large amounts heating under laser excitation, as well as sample damage at the highest excitation powers.

In summary, the synthetic material was of inferior quality to the high quality natural samples. The synthetic material showed indications of strain, but the main issue was the presence of copper vacancies. The copper vacancies limited the observation of higher n and caused the sample to heat significantly under two-photon excitation. Due to the heating under two-photon excitation, the synthetic material will not be used for the other experiments performed in this thesis. The appearance of the copper vacancies is a consequence of the oxidation process (oxidation of a high purity copper rod) [51]. In future, post growth treatments, such as annealing, could be employed to reduce the presence of copper vacancies. Annealing has been previously shown to reduce the concentration of copper vacancies [49; 172; 50; 51]. Alternatively, as the copper vacancies are believed to occur during the initial oxidation phase of the growth, changes to this step could be considered. For example, rather than oxidising a high purity copper rod, copper powder could be oxidised before being used in the floating zone technique. This may allow more controlled oxidation of the copper, and a reduction in the vacancy concentration.

4.4 Summary

In this chapter the results from characterising the Cu_2O samples used in this work were presented. The primary property of interest was the quality of the Rydberg exciton spectrum. To characterise this, one-photon absorption was used. Sample AM was the highest quality sample studied, which showed Rydberg states up to $n = 14$ in absorption. It was found that other samples from Namibia were also high quality, while samples from other sources were of lower quality.

The spatial homogeneity of the Rydberg series was studied. Again, sample AM proved to be the highest quality, and possessed the least spatial variation of the Rydberg spectrum out of the measured samples. The spatial mapping showed that although local sample quality perturbs the Rydberg series it does not destroy the Rydberg states. This is a promising conclusion, as it means future work on trapping Rydberg excitons may be possible. In future, the spatial mapping techniques described here could be used to characterise structures placed on the sample surface or engineered into the sample.

To further characterise the samples, PL spectroscopy was used. It was found that as well as possessing the best Rydberg spectrum, sample AM appeared to be purest sample studied. Sample AM had a low PL intensity from vacancy states and showed very few peaks associated with impurities. It also had the closest spectrum to literature results from high quality samples [95]. Interestingly, sample AB showed a high quality Rydberg spectrum, but in PL bound exciton states dominated the emission. This indicated that impurities do not necessarily destroy the Rydberg series. However, a correlation between presence of copper and oxygen vacancy states and the quality of the Rydberg spectrum was found.

Finally, synthetic material was compared to the best natural sample. The synthetic material was found to have a poor Rydberg spectrum, limited to around $n = 10$, which is comparable to previous studies on synthetic Cu_2O. PL spectroscopy of the synthetic material showed a high concentration of copper vacancies, which are believed to be limiting factor in observing higher n. In future, post growth treatments may be able to reduce the concentration of copper vacancies and extend the Rydberg series to higher n. Future work looking at engineering structures into the sample or placing structures on the surface will need disposable material of reasonable quality to work with. Although the highest n excitons are not present in the synthetic material, it may prove perfect

for this task, as it is possible to produce large quantities of material.

In the remainder of this thesis, results from samples AB and AM are presented. As sample AM is the highest quality sample identified, the majority of the results are from this sample. However, some experiments were performed on sample AB prior to AM being purchased.

Two-photon Excitation

In this chapter, two-photon excitation is used to study Rydberg excitons in Cu_2O. Both photoluminescence excitation spectroscopy (PLE) and second harmonic generation spectroscopy (SHG) are used. Exciton resonances up to $n = 12$ are observed, which is the highest n observed so far using two-photon excitation. The limiting factors in observing higher n are discussed, with heating due to one-photon absorption of the excitation laser a possible limiting factor. Finally, the polarisation dependencies of the second harmonic are studied, showing there is significant birefringence in the optical setup.

Two-photon spectroscopy of Cu_2O was first performed using two-photon absorption spectroscopy, where excitons up to $n = 5$ were observed [119]. More recently, SHG spectroscopy has been performed using a broadband femtosecond laser pulse [141]. The broadband excitation laser excites many Rydberg states simultaneously, and the emitted SHG is resolved using a spectrometer to reveal the exciton resonances. Using this method, states up to $n = 9$ have been observed and the effects of crystal orientation and external fields on SHG have been extensively studied [142; 126; 143; 92; 94].

In the femtosecond pulse SHG experiments [141; 142; 126; 143; 92; 94] the observation of high n states is limited by two things. Firstly, the resolution of the spectrometer sets an experimental limit on the highest state which can be resolved. Secondly, the use of a broad excitation pulse means that when exciting high n states some of the excitation light is above the bandgap. The above bandgap excitation can create free charges, which limit the observation of higher n. In this chapter we use a narrowband laser to overcome both of these challenges. The exciton states are resolved by scanning the laser frequency and measuring the intensity of light emitted from the sample. Using this

method means the spectral resolution is set by the laser linewidth ($\sim$ 50 neV for 50 ns pulse) which is significantly smaller than the linewidths of the exciton resonances. The narrow linewidth of the excitation laser also means there is no above bandgap illumination and allows the lineshape of the exciton resonances to be studied.

In this chapter, the infrared laser system discussed in section 3.1.1 is used as the excitation laser. Unless otherwise stated, the laser was used in 50 ns pulses with a 200 ns pulse period. The primary detector used was the SPAD. For spectrally resolved measured measurements the monochromator (section 3.1.3.2) and temperature tuned Fabry-Pérot etalon (section 3.1.3.1) were used.
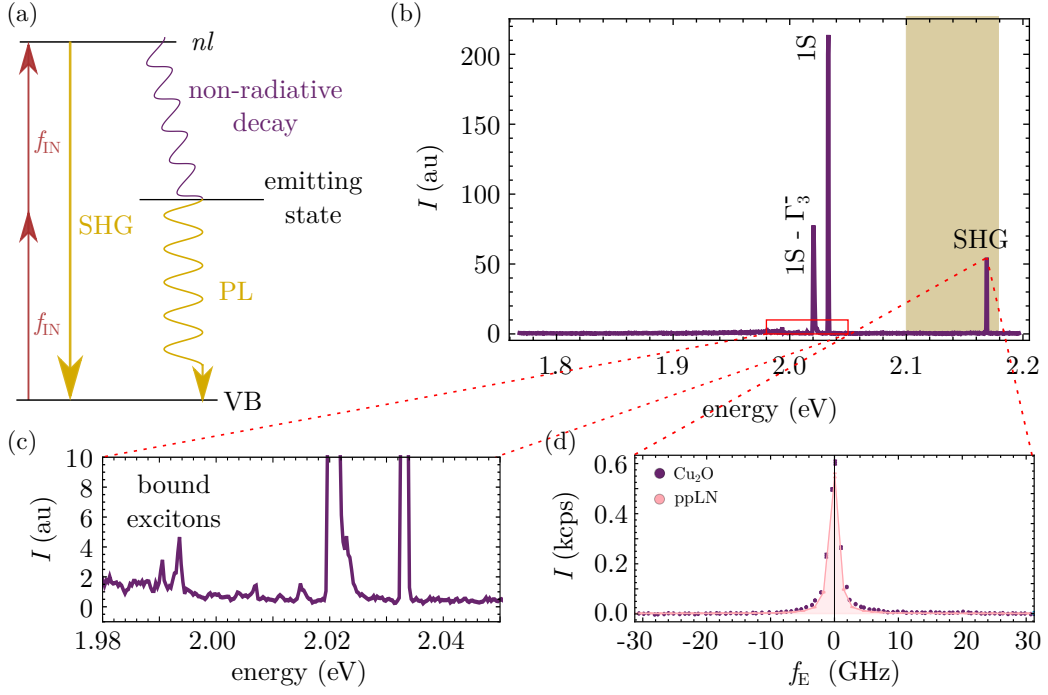
Figure 5.1: Emission spectrum under two-photon excitation. (a) Energy level diagram of emission processes under two-photon excitation. A Rydberg state, $|n, l\rangle$, is excited by two photons of frequency f_{IN}. The Rydberg state can either coherently emit at twice the input frequency through an SHG process, or non-radiatively decay to an emitting state before incoherently emitting. (b) Emission spectrum from sample AB with two-photon excitation energy resonant with the 5D state. Shaded region indicates bandpass filter used to separate SHG light from PL. Red box shows zoomed region plotted in (c). (c) Zoom of bound exciton emission from sample AB. (d) SHG emission from Cu_2O compared with SHG from a ppLN crystal.

5.1 Emission paths under two-photon excitation

Here we study the possible emission pathways for excitons under two-photon excitation. An energy level diagram of the possible emission pathways is shown in Fig. 5.1(a). Two-photon excitation from the valence band creates a Rydberg exciton in the state $|n, l\rangle$. From the Rydberg state three processes can occur:

1. Non-radiative decay followed by incoherent emission (PL)

2. Coherent emission at twice the input frequency (SHG)

3. Incoherent emission directly from the Rydberg state

Process 1 is very similar to the one-photon PL spectroscopy studied in section 4.2. The difference here is the excitation is directly to a Rydberg exciton, rather than an above bandgap excitation creating free electron-hole pairs. However, once the Rydberg exciton decays through phonon scattering, the resulting PL spectrum is similar. Shown in Fig. 5.1(b) is a typical emission spectrum from sample AB under two-photon excitation. Direct emission from the 1S state along with the Γ_3^- phonon replica are clearly visible, as well as PL from the bound excitons (zoom in Fig. 5.1(c)).

Second harmonic generation is visible as the single high energy peak in Fig. 5.1(b). The SHG process has several advantages over the PL process. One advantage is the non-radiative decay to the 1S state is no longer involved and does not have to be considered when constructing a model to describe the process. The main advantage however, is that the emission is coherent and the emission spectrum is set by the input laser. Shown in Fig. 5.1(d) is an emission spectrum from sample AM taken with the temperature tuned Fabry-Pérot etalon (section 3.1.3.1). The emission spectrum from the sample is compared to the second harmonic generated by the ppLN crystal described in section 3.1.2.3. As can be seen, the widths are in excellent agreement with each other, verifying this is indeed the coherently generated second harmonic of the laser. To separate the SHG from the PL, a bandpass filter is used (Semrock FF01-580/14). The transmission window of this filter is shown as the shaded region in Fig. 5.1(b).

Process 3 is PL directly from the Rydberg states. As was shown in section 4.2, PL from the Rydberg states was found to be a very weak process. However, it is still visible under two-photon excitation. As PL from the Rydberg states occurs at a similar energy to the SHG process, it is not removed from the signal by the bandpass filter. It is therefore important to study the relative intensities of the SHG and the incoherent emission from the Rydberg states. The relative intensity was found to be dependent on the two-photon excitation energy, E, and the sample used.

The SHG process and the incoherent emission from the Rydberg states can be separated using the Fabry-Pérot etalon. SHG gives rise to narrow peaks with a width set by the FPE finesse, while the incoherent emission will appear as much broader features. Note that the etalon can only resolve the energy separation modulo the 60 GHz FSR, and so different PL features may overlap. The emission spectra (relative to the second harmonic of the laser, taken using the Fabry-Pérot etalon) from two different samples are shown in Fig. 5.2. Three different excitation energies were used. Sample AB (Fig. 5.2(a)) shows a narrow peak at 0 GHz corresponding to the second harmonic, but
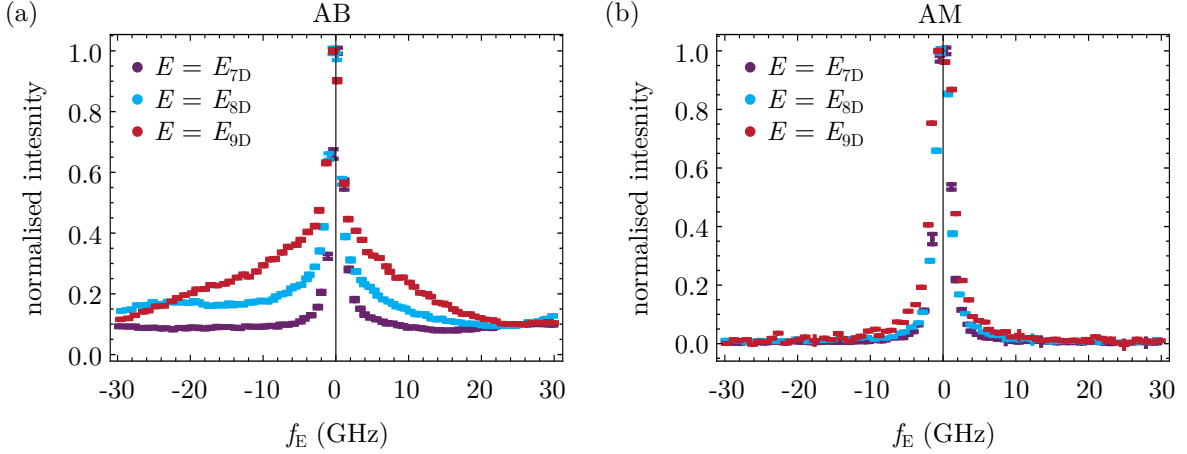
Figure 5.2: Emission spectra from Rydberg states under two-photon excitation. Spectra were taken using the Fabry-Pérot etalon described in section 3.1.3.1. The etalon frequency f_E is taken relative to the second harmonic frequency. Two-photon excitation energies resonant with exciton states 7D, 8D and 9D are shown. (a) Emission spectra from sample AB. (b) Emission spectra from sample AM.

also shows a broader feature. This broad feature corresponds to incoherent emission from the Rydberg states. The intensity of the incoherent emission increases in relative intensity as excitation energy is increased. Note that normalised intensity is plotted here, the absolute intensity drops as the two-photon excitation energy is increased, as will be shown in section 5.3.1. In sample AM (Fig. 5.2(b)) the incoherent emission is not obviously present, though there is a slight broadening of the peak in the $E = E_{9D}$ scan. It should also be noted that the absolute intensity of the light was roughly 10 times higher for the same laser power in sample AM, so it is possible the incoherent emission is the same strength in both samples but the SHG is much stronger in AM.

The difference between the emission spectra from the two samples (Fig. 5.2) may be due to the orientation of the samples. Sample AB and AM were oriented such that the (001) and (111) crystal planes were parallel with the sample surface respectively. The SHG selection rules depend on the crystal orientation [141; 142; 143; 92] and when the excitation light propagating normal to the (001) plane SHG is forbidden [142]. This difference in orientation explains why the intensity of SHG is much stronger from sample AM, and may also account for the difference in relative intensities of the incoherent emission and the SHG.

For the remainder of this thesis, all light emitted from the Rydberg states under two-photon excitation will be referred to as SHG. This is mostly done for practicalities, as separating the true SHG from the incoherent emission is experimentally challenging.
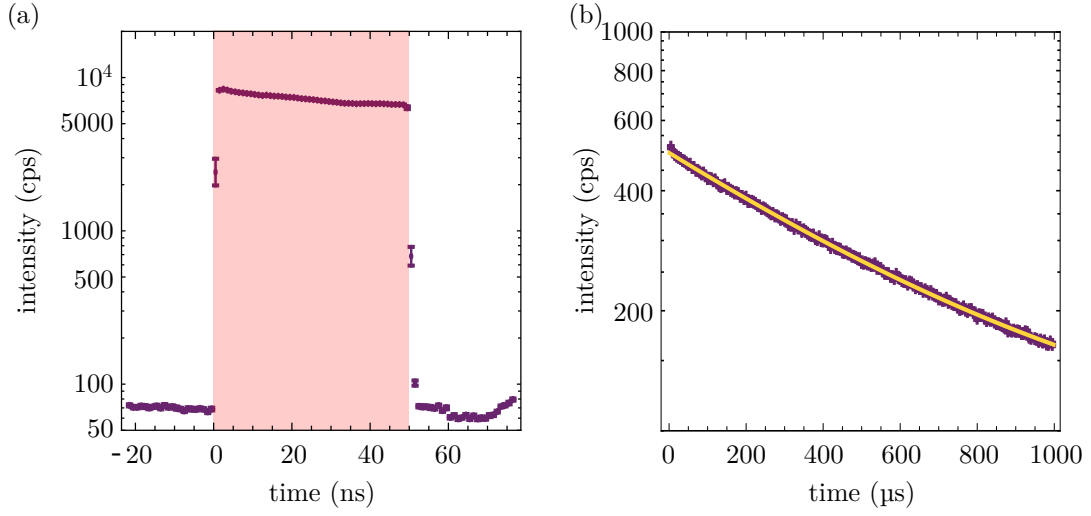
Figure 5.3: Temporal dependence of different emission pathways under two-photon excitation. (a) Temporal profile of the SHG process. Here, square laser pulses with a width of 50 ns and period of 200 ns were used. The shaded region shows the laser pulse. As expected, the temporal profile of the SHG was set by the excitation laser. (b) Temporal dependence of the emission from bound excitons. The excitation laser pulse length was 1 ns with a 1 ms period. By fitting the decay with an exponential (yellow line) the lifetime of the bound exciton states was found to be 640 ± 10 µs.

In the case of sample AM, this is a good approximation. However, for sample AB a large proportion of the light will be incoherent. To account for this, the majority of the SHG experiments are performed on sample AM.

5.1.1   Time resolved measurements of emission

In this section the temporal dependence of the different emission pathways is studied. This method can be used to determine the lifetime of the emitting states. First, the temporal dependence of the SHG light will be studied. For this, the laser pulse length was set to 50 ns and the period to 200 ns. The bandpass filter was inserted so that only light from the Rydberg series was detected. Shown in Fig. 5.3(a) is a histogram of the temporal response of the SHG. The shaded region shows the length of the excitation pulse. As expected, the SHG pulse shape is set by the excitation laser. There is a slight drop in SHG intensity during the pulse, this is attributed to pile up on the detector due to the detector deadtime of 77 ns.

The temporal response of the photoluminescence from sample AB was also studied. For this, the laser pulse length was 1 ns with a 1 ms period. The laser was tuned

to be two-photon resonant with the 9D peak. The resulting histogram is shown in Fig. 5.3(b). Here, the counts have been binned into 1 µs bins. The PL shows a long lifetime, on the order of a millisecond. As the pulse period is also 1 ms, the count rate never goes to zero as the emission from excitons generated during the previous laser pulse is still significant. A shorter decay (on the order of a few nanoseconds) was also observed at $t = 0$, but is not plotted here. This shorter decay is attributed to the 1S ortho-exciton [173]. To extract a lifetime from the long-lived decay, the decay is fitted with an exponential plus a constant offset:

$$I = Ae^{-t/\tau} + B. \tag{5.1}$$

Here, τ is the lifetime of the decaying state, A is an amplitude and B is a constant to account for count rate not going to zero. The resulting fit is shown as the yellow line in Fig. 5.3(a). The fit returns a value of 640 ± 10 µs for the lifetime of the emitting state. This lifetime is very large compared to other exciton lifetimes in Cu_2O. The 1S ortho-exciton lifetime is around 2 ns (depending on the crystal temperature) and is limited by conversion to the 1S para-exciton state [102; 101]. Direct emission from the para-exciton is forbidden to all orders and the radiative lifetime of the para-exciton is estimated to be 7 ms [162]. However, the para-exciton can also recombine through phonon assisted processes or up conversion to the ortho-exciton [166]. In high quality samples the longest measured para-exciton lifetime is 13 µs [102].

Here, the measured lifetime is almost 50 times longer than the previously measured para-exciton lifetime. Of the samples studied under two-photon excitation (samples AB and AM), this long lived decay was only present in sample AB. The two samples studied had different emission spectra (see section 4.2) with sample AB the only one to possess bound exciton states [163]. We tentatively attribute this long lifetime to the sharp spectral features of the bound excitons. As discussed in [163] some of the bound exciton peaks are attributed to trapped para-excitons. We hypothesise that the long lifetime observed is due to trapped para-excitons which are decoupled from the crystal lattice and so cannot recombine through phonon assisted processes. Furthermore, the trapped nature of the bound excitons means that collisional processes, such as Auger recombination [162], are not relevant. Both of these factors lead to a long radiative lifetime for the bound exciton states, which is significantly longer than previously observed para-exciton lifetimes. Further studies are required to definitively assign this long lived decay. For example, the temporal measurements could be combined with the spectral resolution of either the monochromator or the Fabry-Pérot etalon.

5.2 Two-photon photoluminescence excitation spectroscopy

Two-photon photoluminescence excitation spectroscopy was used to study the Rydberg excitons in Cu_2O. The excitation energy was scanned and the total PL intensity as a function of excitation energy was recorded. For the experiments presented here, sample AB was used. The excitation pulse was 1 ns with a 100 ns period. In these experiments, there was no filter inserted to block the coherently generated second harmonic meaning the resulting signal will include both PL and SHG. However, in sample AB the SHG was only about 2% of the total intensity and so this component is assumed to be negligible. In sample AM, the proportion of the intensity which was SHG was found to be significantly higher, on the order of 70%. PLE spectroscopy in this sample is not presented here and would require filtering of the emitted light to study the PL.

The two-photon PLE spectrum is presented in Fig. 5.4 at an average laser power of $P_{IN} = 2$ mW. Here, the excitation laser is scanned from the 5D exciton resonance to the band edge. Exciton resonances from $n = 5$ to $n = 11$ are present, though it is not possible to discern individual angular momentum states at $n = 11$. As expected, the S and D states are the dominant features, though the P states are also visible [141; 143]. As n is increased, the P states seem to grow relative to the S and D states.

The exciton resonances in Fig. 5.4 appear to sit on a background and the PL intensity becomes constant at the highest excitation energies. The origin of this background is unknown, and we note it has previously been observed in two-photon absorption studies [119]. In one-photon spectroscopy the exciton resonances also sit on a background. In this case, the background is due to the simultaneous excitation of the 1S ortho-exciton and an optical phonon [59; 60]. It is possible a similar process is occurring under two-photon excitation. Due to parity conservation, any phonon assisted process in the two-photon case will involve opposite parity phonons to the one-photon case. The background observed in the two-photon PLE spectrum is of a similar size to the exciton resonances, whereas in the one-photon case the non-resonant background is larger than the exciton resonances.

To investigate the background further, the PLE spectrum should be extended to lower excitation energy. By looking at the excitation energy at which the background first appears it should be possible to gain some clues to its origin. If the background is due to a phonon assisted absorption process, then the background should start at the
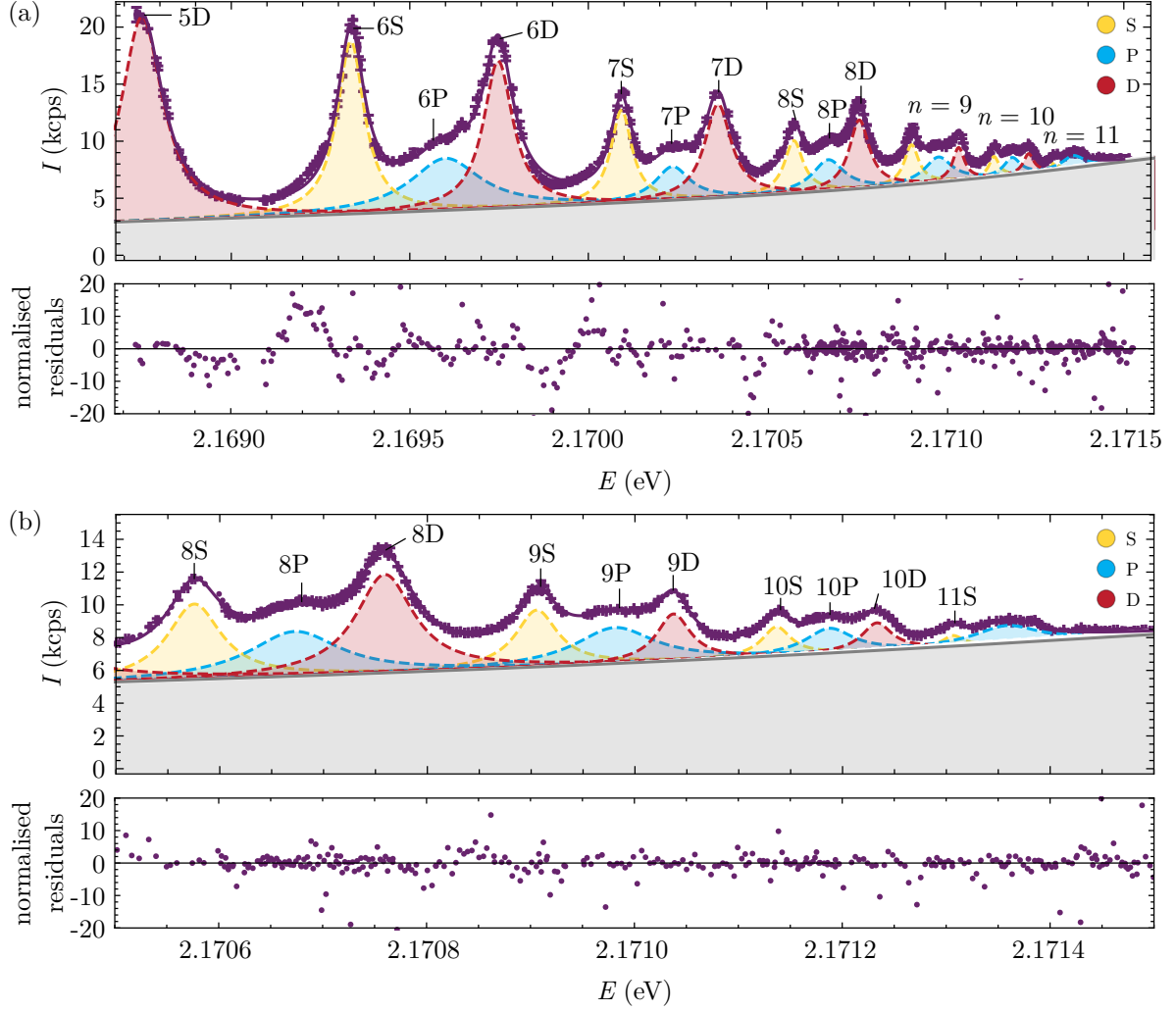
Figure 5.4: Two-photon photoluminescence excitation spectrum at $P_{IN} = 2$ mW. Exciton states from 5D to the band edge are shown. The highest resolvable states is 11S. The spectrum was fitted with sum of Lorentzian peaks plus a background (see equation 5.2). Each individual fitted peak is shown as shaded peaks below the spectrum, and coloured by angular momentum quantum number. The background is shown as the shaded grey region. (a) Spectrum from 5D to the band edge. (b) Zoom of spectrum showing the high n region, from 8S to the band edge.

energy of the 1S state plus the energy of the relevant phonon. The background should also have a square root dependence on excitation energy due to the density of states of the phonons [134; 59; 60].

To fit the PLE excitation spectrum a sum of Lorentzian profiles was used for the exciton resonances. To account for the unknown background a linear offset was used so the total fit function was given by

$$I = \sum_{n,l} \left(\frac{A_{nl}\Gamma_{nl}^2}{(E - E_{nl})^2 + \Gamma_{nl}^2} \right) + BE + C, \qquad (5.2)$$

where E is the excitation energy, B and C are constants associated with the background, A_{nl}, Γ_{nl} and E_{nl} are the amplitude, width and energy of the $|n, l\rangle$ exciton state respectively. The linear offset used to represent the background does not fully capture the background lineshape. During the fitting, it was found that one of the Lorentzians would fit the background rather than the exciton resonances. To account for this, an additional Lorentzian was added to the fit function. The resulting fit is shown in figure 5.4. Each of the individual Lorentzian peaks is shown as the shaded peaks below the spectrum and the background is shown as the grey shaded region. Due to the approximate nature of the background fitting, the fit parameters for the exciton peaks may not be an accurate representation of the underlying exciton properties. This is especially true for the amplitudes and widths of the higher n states, where the exciton peaks are less well resolved.

The energy of the exciton states can be described by the quantum defect model introduced in section 2.2.2. The angular momenta series from S to D were each fitted with equation 2.7 with the Rydberg energy and bandgap energy shared between all series. The quantum defects for each series were constrained to be between 0 and 1. In Fig. 5.5(a) the binding energy ($E_g - E_{nl}$) of the exciton states for the three series is plotted against n along with the quantum defect fits. For these fits the bandgap energy and the Rydberg energy were found to be $E_g = 2.172054(2)$ eV and $R_X = 82.7 \pm 0.3$ meV respectively. The quantum defects were found to be $\delta_S = 0.49 \pm 0.01$, $\delta_P = 0.22 \pm 0.01$, and $\delta_D = 0$ for the S, P and D series. The errors quoted on these parameters are the errors returned from the fitting algorithm. However, the parameters in this fit are highly correlated, which is not reflected in the quoted errors. The value for the D quantum defect returns zero, which is a constraint of the fitting. Removing this constraint on the fitting, and keeping all other parameters constant, returns a negative quantum defect of $\delta_D = -0.02 \pm 0.01$
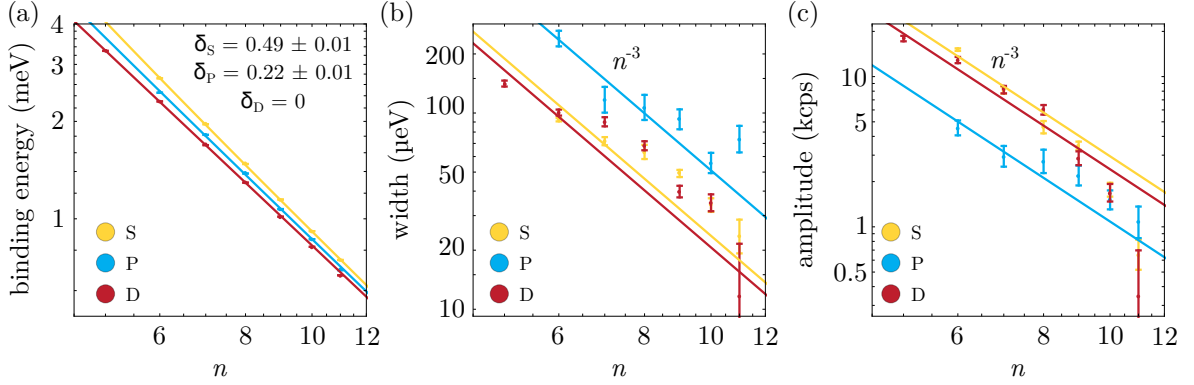
Figure 5.5: Trends in fitted parameters vs n for the two-photon PLE spectrum. (a) Exciton binding energy vs n. Solid lines show a quantum defect (equation 2.7) fit to each of the angular momentum series. The Rydberg energy and bandgap energy from this fit are $R_X = 82.7 \pm 0.3$ meV and $E_g = 2.172054(2)$ eV respectively. The quantum defects for each of the fits are shown in the figure. (b) Linewidths of exciton resonances (FWHM) vs n. Solid lines are fits using the expected n^{-3} trend. (c) Amplitudes of exciton resonances vs n. Solid lines are fits using an n^{-3} trend.

The bandgap and Rydberg energy are in good agreement with previous studies which quote 2.172053 eV and 86 meV respectively [33]. The quantum defects for the S and P series are also in good agreement with literature values of 0.5 and 0.23 respectively [129; 32]. However, the quantum defect for the D series does not agree with the literature value of 0.2 [129]. The value of $\delta_D = 0.2$ was determined from the centre of gravity of a multiplet of D states observed in absorption spectra under an external electric field [129; 122]. The multiplet of D states is not active under two-photon excitation (see Fig. 2.3 for the exciton fine structure splitting). The D states studied in this thesis are the highest energy D states (Γ_5^+ symmetry), which explains the much lower value obtained for the quantum defect.

The trends in the widths (FWHM) of the states with principal quantum number are shown in Fig. 5.5(b) with the diagonal lines representing fits to the data with the expected n^{-3} scaling [32]. The width of the P states is noisy but appears to generally follow the expected trend, whereas the S and D states are broader than expected in the high n region. Previous work observed a broadening for states $n > 8$ which was attributed to charges in the material [48].

The amplitudes of the peaks vs n are shown in Fig. 5.5(c) with the solid lines showing a fitted n^{-3} trend. All three series show a decreasing amplitude as n is increased. At the lower values of n, the amplitudes seem to follow this trend well, however as higher n is approached the amplitudes of the S and D states seem to fall faster than n^{-3}, whereas

the P states fall slower than n^{-3}. This is apparent when looking at the spectrum in Fig 5.4. The 6P peak appears small relative to 6S and 6D, whereas the 10P peak is of comparable size to 10S and 10D.

This trend in the amplitudes of the states is not what is expected. Assuming the PLE signal is proportional to the two-photon absorption, the amplitude of the peaks should be independent of n (see section 2.3.1.4). Here, the states clearly show a decreasing amplitude with n. There are a few possible explanations for this, one is that the signal is not proportional to the two-photon absorption. However, previous studies found the trends in the oscillator strength of the exciton states were the same under one-photon absorption and one-photon PLE [32; 33]. A more likely explanation is that the amplitudes of the exciton states are reduced by some other mechanism, such as free charges.

In this section the Rydberg exciton series has been studied using two-photon PLE spectroscopy. Even-parity exciton states up to $n = 11$ were studied. In section 5.3.1 the limiting factors in observing higher n using two-photon spectroscopy will be discussed. The lineshape of the exciton states was well described by a Lorentzian profile. However, the exciton resonances were found to sit on a non-resonant background of unknown origin. As observed in one-photon absorption spectroscopy, the background becomes more significant as the band edge is approached. Due to this, the background is postulated to have a similar phonon-assisted origin to the one-photon case. Further studies will be required to determine the origin of the background. For the remainder of this chapter SHG spectroscopy will be used to study the Rydberg excitons.

5.3 Second harmonic generation spectroscopy

In this section second harmonic generation spectroscopy is used to study Rydberg excitons in Cu_2O. SHG spectroscopy has several advantages over the PLE spectroscopy presented in section 5.2. The emission spectrum of the SHG is set by the excitation laser, and it will be shown that the non-resonant background observed under PLE is not present in the SHG excitation spectrum.

The SHG was collected in a back-scattered geometry, using the same lens as the excitation. A bandpass filter (centred at 580 nm with width 14 nm) was used to separate the SHG from the PL studied in section 5.2. As SHG is generated in the forward direction due to phase matching [144], the SHG detected here must have been reflected from the back surface of the sample. For future experiments, collecting in the forward direction would improve collection efficiency and changes to the experimental apparatus to allow this are planned.

5.3.1 Excitation spectrum

An excitation spectrum is taken by scanning the laser frequency and recording the SHG intensity using the SPAD. Fig. 5.6 shows an SHG excitation spectrum from sample AB and excitation spectra from two locations separated by 100 µm on sample AM. The significantly higher count rate from sample AB is due to the much higher laser power used ($P_{IN} = 500$ mW for AB and $P_{IN} = 40$ mW for AM). When input power is adjusted for, the SHG from sample AM is roughly 10 times more intense.

In Fig. 5.6 the excitation energy is varied from $n = 6$ to the band edge. Exciton resonances from $n = 6$ to $n = 12$ are visible. As seen in the two-photon PLE spectrum (Fig. 5.4) the S and D states are dominant, though odd-parity states are also present. A discussion of the SHG process on even and odd-parity exciton states is given in section 2.2.3.2.

The states between the P and D states in the spectrum have been assigned as F states (Γ_8^- symmetry) due to the energy they appear at in the spectrum. However, it is also possible that they are lower energy D states [112] (see Fig. 2.3 for the fine structure of exciton states). Both the F states and the lower energy D states should be weak under two-photon excitation [127] and appear at very similar energies [131; 112]. Future work, for example using external fields, is required to definitively assign these peaks.
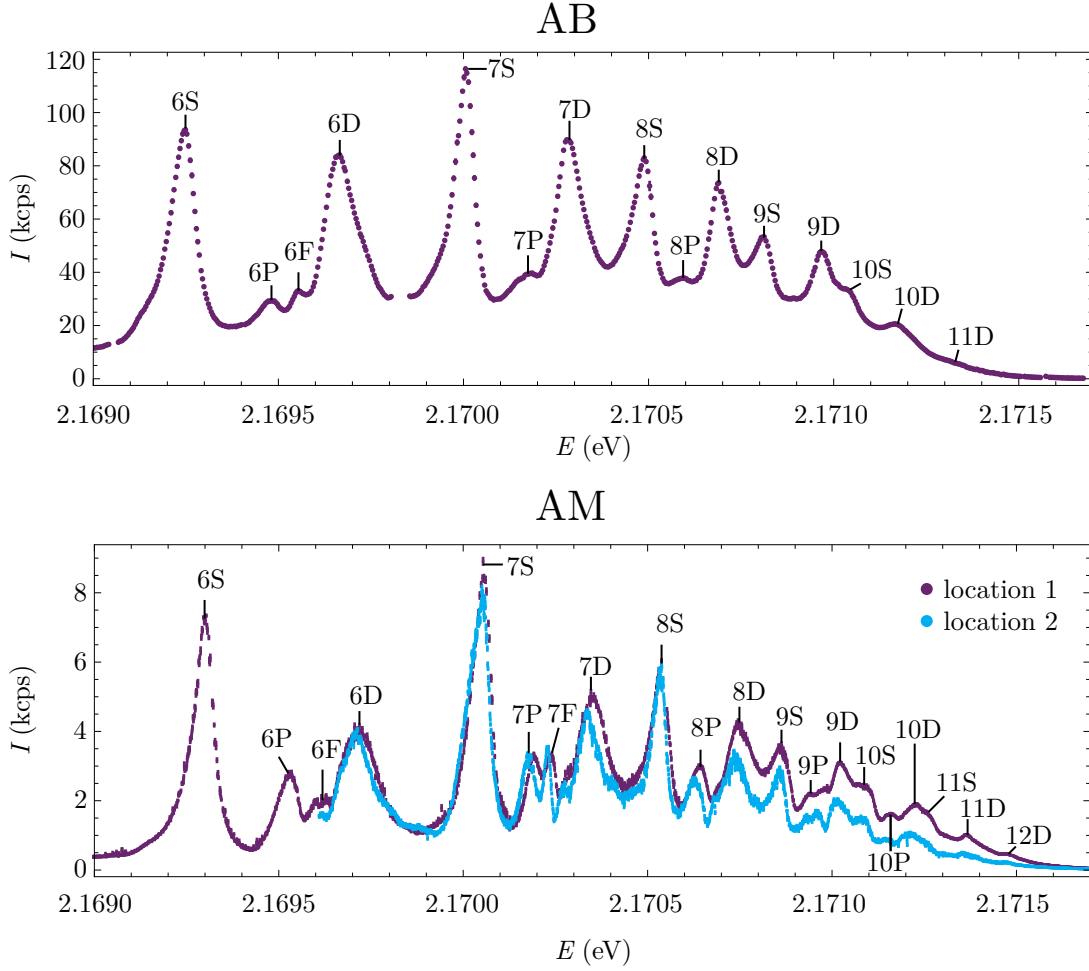
Figure 5.6: SHG excitation spectra on two different samples. States from 6S to the band edge are visible. (a) SHG excitation spectrum from sample AB taken at laser power $P_{\text{IN}} = 500$ mW (b) SHG excitation spectrum from sample AM at two different locations separated by 100 µm taken at laser power $P_{\text{IN}} = 40$ mW.

Interestingly, the odd-parity states are more prominent in the spectra obtained from sample AM. A potential explanation is the orientation of the samples. Sample AM was orientated along the (111) crystal plane, and sample AB along the (001) plane. The selection rules for SHG depend on the crystal orientation and the polarisation of the light, with the different angular momentum states having different polarisation selection rules [141; 143]. The different orientation of the samples could lead to different relative intensities of the even and odd-parity states. The polarisation selection rules for SHG are discussed in section 5.3.2. Another potential explanation for the difference in relative intensities could be due to strain in the crystal making the odd-parity states more prominent. However, it seems unlikely there is more strain in sample AM as in section 4.1 AM was shown to be of higher quality and possess less spatial variation

than AB.

The spectrum from sample AB (Fig. 5.6(a)) shows a shift of about 30 μeV to lower energy when compared to the spectra from sample AM (Fig. 5.6(b)). This shift is due to heating due to the higher laser power used to obtain the spectrum from sample AB (500 mW vs 40 mW). The power dependence of the excitation spectrum is discussed in section 5.3.1.3.

There are clear differences between the two spectra taken on sample AM. Most notably, in the high n region location 2 is significantly less intense than location 1. As well as changes in peak amplitudes there are small energy shifts and lineshape changes throughout the spectrum. The spectrum at location 2 also shows some features which are not present at location 1. For example, there appear to be additional peaks on the low energy side of the D states. These peaks could be attributed to D states of other symmetry [112]. The appearance of forbidden peaks could indicate location 2 is more strained than location 1. The spatial inhomogeneity is in contrast to the one-photon spatial measurements performed on AM in section 4.1. In the one-photon spatial measurements, sample AM was found to be the most homogeneous of all the samples, with the energy of the 6P state varying by < 10 μeV over 400 μm of the sample. However, previous SHG studies observed similar fluctuations in the intensity of the SHG signal from the 1S exciton [142], here the authors showed that strain modifies the local SHG selection rules as well as giving rise to an energy shift. From the difference between the two spectra shown in Fig. 5.6(b) and the one-photon spatial homogeneity observed in section 4.1 we conclude that SHG is more sensitive to the local sample environment than one-photon absorption spectroscopy.

When comparing the SHG excitation spectra (Fig. 5.6) to the two-photon PLE spectrum (Fig. 5.4) there are clear differences. Most notably there is no non-resonant background on the excitation spectrum for SHG, and the intensity drops to zero as the band edge is approached. This shows the mechanism for the non-resonant background in two-photon PLE spectroscopy is not probed by SHG. The odd-parity angular momentum states are also more noticeable in the SHG spectrum, and peaks are observed which are not present in the two-photon PLE spectrum.

5.3.1.1 Fitting the excitation spectrum

The narrowband excitation laser used to obtain the SHG excitation spectra in Fig. 5.6 allows the lineshape of the SHG resonances to be studied. To study the lineshape in

more detail the SHG excitation spectrum was fitted. Two fitting functions were used. The first fitting function using the form of the nonlinear susceptibility, whereas the second approximates each resonance to have a Lorentzian profile. Unlike in the fitting of the two-photon PLE spectrum, none of the fitting methods used for fitting the SHG excitation spectrum require the addition of non-resonant background terms.

The nonlinear susceptibility describing SHG on an exciton resonance is given in section 2.3.1.3. Each resonance in the excitation spectrum contributes a complex pole to the nonlinear susceptibility. The total intensity of the SHG is therefore the square of a sum of complex poles,

$$I_{\mathrm{SHG}} = \left| \sum_{n,l} \frac{\tilde{A}_{nl} e^{\phi_{nl}}}{(\delta_{nl} - i\Gamma_{nl})} \right|^2 , \tag{5.3}$$

with the detuning given by $\delta_{nl} = E - E_{nl}$. Here, $E = 2hf_{\mathrm{IN}}$ is the excitation energy and E_{nl}, Γ_{nl} and $\tilde{A}_{nl}$ are the energy, width and magnitude of the amplitude of the $|n, l\rangle$ exciton resonance. In general the amplitude of a complex pole is a complex number, here this complex dependence is represented by the phase ϕ_{nl}.

Fitting with a sum of complex poles is an example of an inverse problem. There is not enough information in the intensity distribution to uniquely determine the fit parameters. It has been shown there are 2^N sets of equivalent parameters, where N is the number of complex poles in the fit function [174]. Given there are 22 resonances in the spectrum, this produces a large ($\approx 10^6$) number of equivalent fit parameters. This large number of equivalent fit parameters makes extracting useful information from the fit parameters an unfeasible task.

To demonstrate the issues of fitting with a sum of complex poles, Fig. 5.7 shows three fits to the same dataset from sample AM at location 1. In each of the fits, the fitting algorithm was given different starting values for the fit parameters. All three of the fits shown in Fig. 5.7 provide similar quality fits to the data (reduced χ^2 [175] from top to bottom: 10.4, 9.4, 9.4) and show similar residuals. However, the fitted parameters from each of the fits are different. The right hand side of Fig. 5.7 shows phasor plots of the amplitude and phase parameters from each of the fits. Here the amplitude is represented by the length of the line, and the phase by its angle. The lines have been coloured by the angular momentum of the state they correspond to. All three of the phasor plots are different, showing that the fit parameters are not uniquely determined
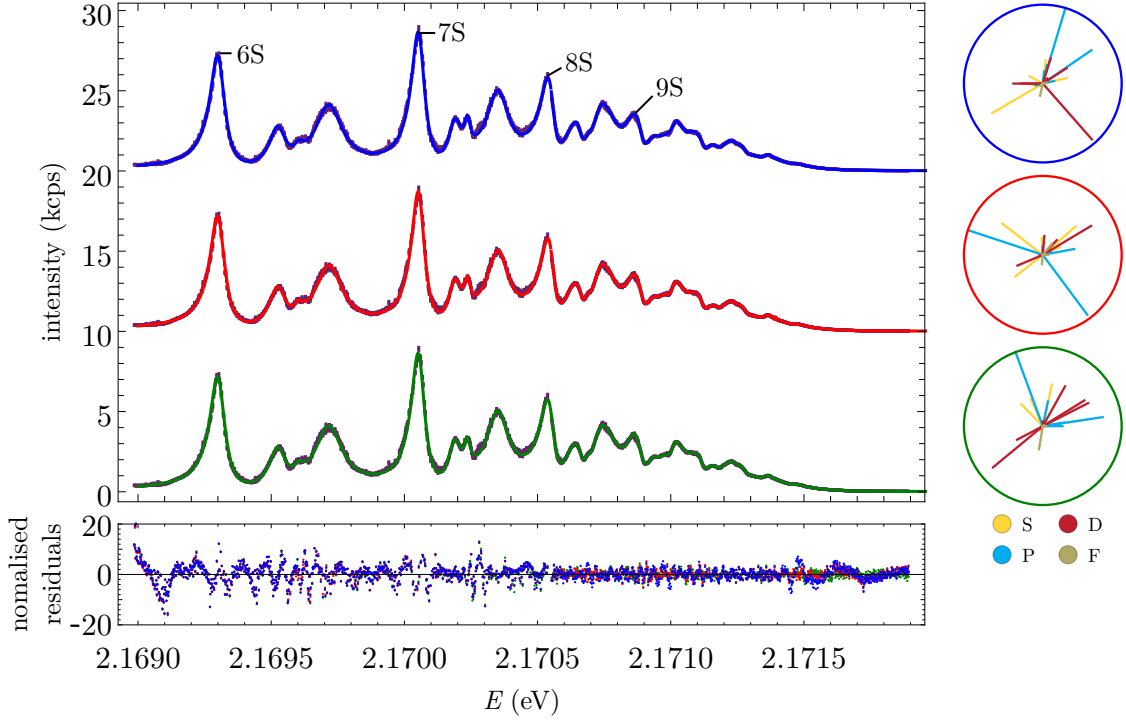
Figure 5.7: SHG excitation spectrum fitted with sum of complex poles (equation 5.3). Three fits to the same dataset using different starting parameters are shown. All three fits provide a good fit to the data (reduced χ^2 values of 10.4, 9.4 and 9.4 from top to bottom) and show similar structure in the residuals. Phasor plots on the right hand side show the corresponding amplitudes and phase parameters from each fit showing that while the total fit functions are similar, the fit parameters are different.

by this fit function. In each of these fits the widths and energies also show variation, but this is not shown here.

In view of the challenges of fitting with a sum of complex poles, a well determined set of fit parameters is obtained by approximating the fit function as a sum of Lorentzian peaks. The sum of Lorentzian peaks is equivalent to taking the summation in equation 5.3 before squaring, which neglects any of the interference terms between the complex poles. The resulting fit function is given by

$$I_{\mathrm{SHG}} = \sum_{n,l} \frac{\tilde{A}_{nl}}{\left(\delta_{nl}^2 + \Gamma_{nl}^2\right)}. \tag{5.4}$$

The resulting fit using equation 5.4 is shown in Fig. 5.8. To achieve this fit, the normalised residuals were weighted to favour a good fit in the high n region of the spectrum. This weighting was necessary as the fit does not fully capture the exciton
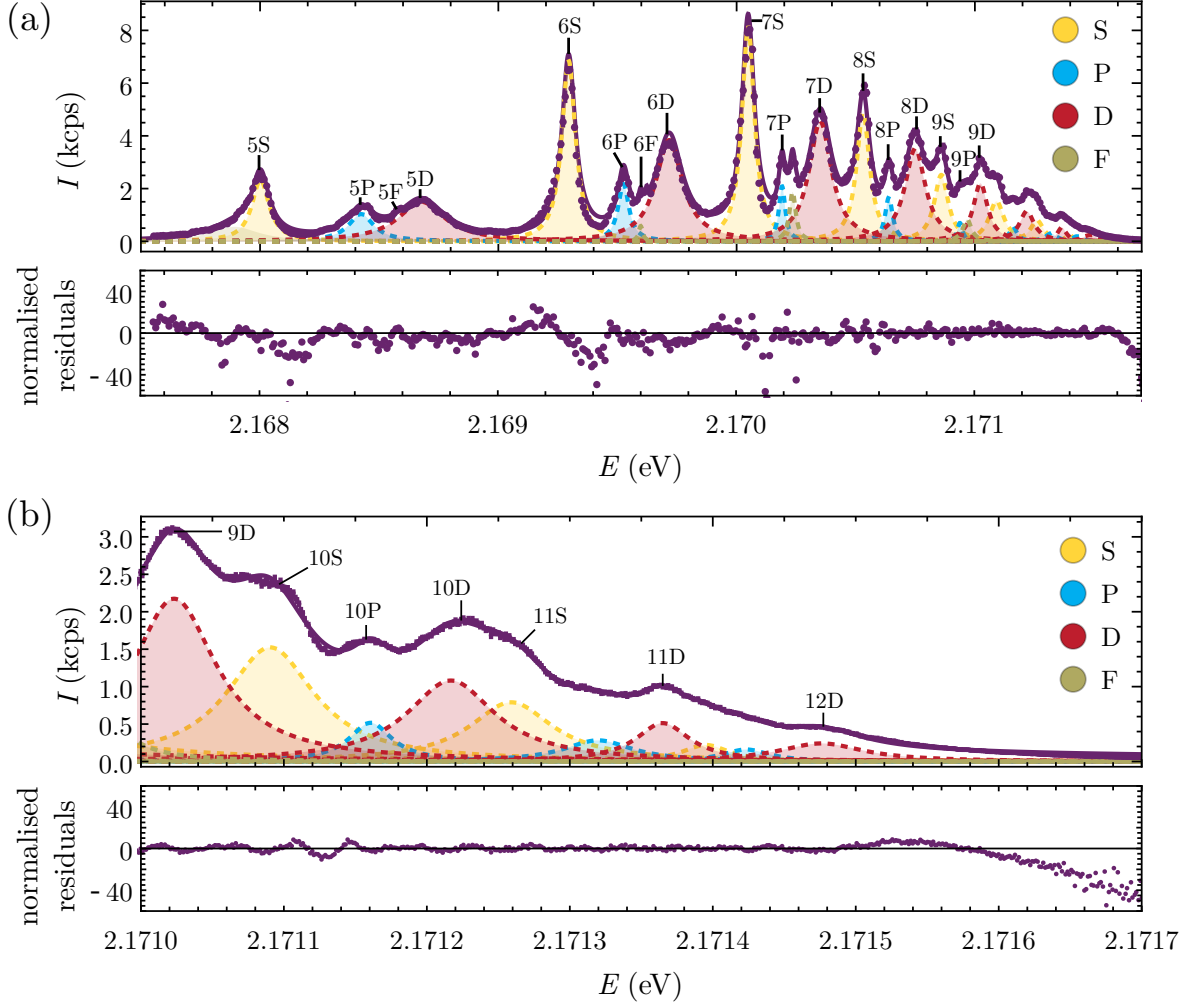
Figure 5.8: SHG excitation spectrum from sample AM fitted with a sum of Lorentzians (equation 5.4). Shaded peaks show the individual Lorentzian components of the fit and are coloured by angular momentum quantum number. (a) Spectrum from 5S to the band edge. (b) Spectrum from 9D to the band edge.

lineshape at low n, which was dominating the residuals. The weighting was achieved by providing artificially low uncertainties to the fitting algorithm for the high n region.

The fit in Fig. 5.8 is reasonably good throughout the full range of n though at low n it provides a worse fit than using complex poles (Fig. 5.7). The quality of the fit using the sum of Lorentzians in the high n region indicates that the interference terms between the complex poles (which are neglected by using the Lorentzian fit) are not significant. In the high n region, the resonances overlap much more than in the lower n region. The increased overlap between the resonances means there are more complex poles contributing to the intensity at a given energy. Assuming there is no structure to the phases in equation 5.3, the interference terms will result in complex phasors with quasi-

random orientation and magnitude. The random orientation of the complex phasors will lead to a cancellation of the interference terms. At lower n, there are far fewer resonances which contribute at a given energy (as the separation relative to the state widths is larger), meaning the cancellation of the interference terms will not occur to the same degree. This potentially explains the poorer fit achieved in the lower n region, where the asymmetry of the peaks is not captured by the model.

The advantage of the Lorentzian fit over fitting with complex poles is that the fit parameters are uniquely determined. This allows the energies, widths and amplitudes of the exciton states to be extracted from the model. The parameters obtained from the Lorentizian fit to the SHG excitation spectra on sample AM are presented in Fig. 5.9. To determine errors on the fit parameters multiple datasets were fitted. Fourteen excitation spectra were taken under identical conditions on sample AM at location 1. The data presented in Fig. 5.6 is an average of all these spectra. Each excitation spectrum was individually fitted with the sum of Lorentzians. From these individual fits, the mean and standard error on each parameter was determined. The fit shown in Fig. 5.8 uses the mean parameters. The errors on the fit parameters were found to be small. For energies, the median fractional error was extremely small, at $2 \times 10^{-5}\%$. The widths and amplitudes showed more variation between the fits with median fractional errors of 4% and 2% respectively.

Determining the errors on the fit parameters in this way means they are a measure of the reproducibility of the fit and the data. However, these errors do not take into account any systematic errors, for example due to the approximated Lorentzian fit function. These errors also do not account for the variation due to the spatial inhomogeneity of the samples. To try to address the issue of spatial inhomogeneity, the spectrum taken at location 2 was also fitted with the sum of Lorentzians. The variation in fit parameters between the two locations was found to be much larger than the variation between the spectra taken at location 1, especially for the width and amplitude parameters. The energy of the exciton resonances was not found to vary much between the two locations though there was a slight red shift of the peaks at location 2 of $< 10\,\mu\text{eV}$. The widths of the states varied more, with a median change of 10%. The amplitudes varied the most, with a median change of almost 20%. The large variation in amplitude and width is not unexpected given the differences observed between the spectra in Fig. 5.6(b).

As was done in the case of the two-photon PLE spectrum, the trends in fitting parameters vs n can be studied. The energies of the exciton states are expected to follow the quantum defect model (equation 2.7). The bandgap energy and Rydberg energy
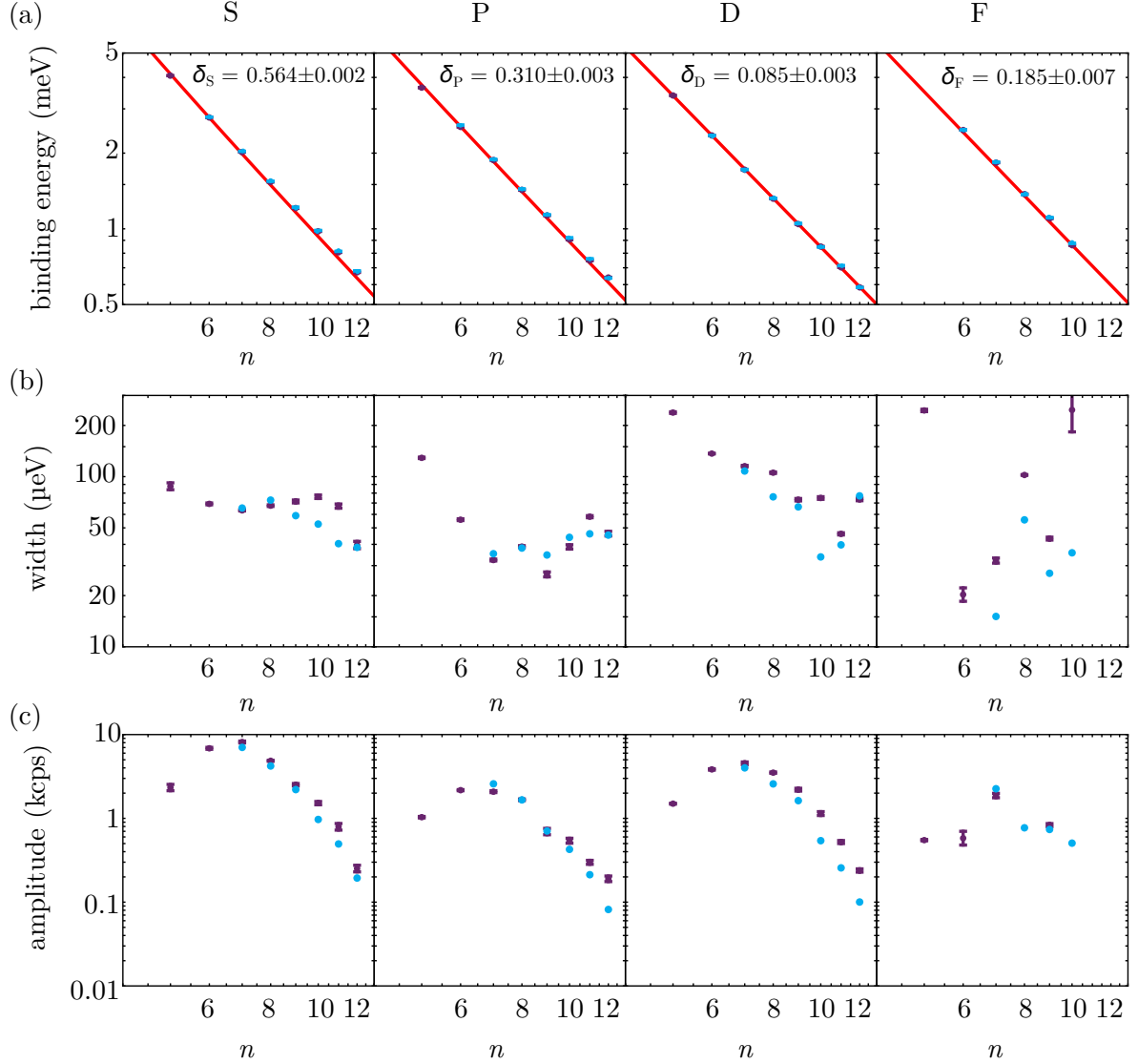
Figure 5.9: Trends in fit parameters for the SHG excitation spectrum vs principal quantum number, n. Multiple datasets were fitted at location 1 (purple points) on sample AM to obtain errors on the fit parameters. Also shown is a fit to the spectrum at location 2 (blue points). The variation in the amplitude and widths between the two locations is much larger than the errors obtained from the multiple fits at location 1. Panels represent different angular momentum quantum numbers (from left to right S, P, D, F). (a) Binding energy vs n. Solid line represents a quantum defect fit (equation 2.7). The bandgap and Rydberg energy obtained from this fit are 2.1720780(4) eV and 82.40 ± 0.05 meV respectively. (b) Width (FWHM) of the exciton resonances vs n (c) Amplitude of the exciton resonances vs n.

	SHG	two-photon PLE
R_X	82.40 ± 0.05 meV	82.7 ± 0.3 meV
E_g	$2.1720780(4)$ eV	$2.172054(2)$ eV
δ_S	0.564 ± 0.002	0.49 ± 0.01
δ_P	0.310 ± 0.003	0.22 ± 0.01
δ_D	0.085 ± 0.003	0
δ_F	0.185 ± 0.007	

Table 5.1: Comparison of quantum defect fit parameters between SHG and two-photon PLE spectroscopy. The parameters are in reasonable agreement with each other. Note that the spectra were taken from different samples and at different excitation powers.

are taken to be global fit parameters across all of the angular momentum series. Unlike in the two-photon PLE case it was not necessary to restrict the values of the quantum defect. The results of this fit are shown as the solid line in Fig. 5.9(a). The binding energies follow the expected trends very well. From this fit, the bandgap and Rydberg energies are found to be $E_g = 2.1720780(4)$ eV and $R_X = 82.40 \pm 0.05$ meV respectively. The quantum defects were found to be $\delta_S = 0.564 \pm 0.002$, $\delta_P = 0.310 \pm 0.003$, $\delta_D = 0.085 \pm 0.003$, $\delta_F = 0.185 \pm 0.007$ for the S, P, D and F states respectively. The errors on these values are probably an under estimate of the true uncertainty. These errors do not account for any systematic errors (such as the exciton lineshape not being captured by the fit), the correlation between the parameters or the spatial variation of the Rydberg energies.

The parameters for the quantum defect fits to the SHG data are compared to the values obtained from fitting the two-photon PLE spectrum (section 5.2) in Table 5.1. There is a good agreement for the value of the Rydberg energy between the two methods. However, the quantum defect and the bandgap energy vary by much more than their associated errors. The quantum defect values and the bandgap are highly correlated parameters. Repeating the quantum defect fits on the PLE spectrum with the bandgap fixed to $E_g = 2.1720780$ eV returns values of $\delta_S = 0.53 \pm 0.01$, $\delta_P = 0.32 \pm 0.01$ and $\delta_D = 0.01 \pm 0.01$, which are in excellent agreement with the values obtained from the SHG spectrum, indicating the peaks appear at the same energy in both the PLE and SHG spectra. The different values obtained from the two methods also highlights the problem that the correlation between parameters causes in the quantum defect fits.

As the comparison to literature values was discussed in section 5.2 for the two-photon PLE fit it will not be repeated here. However, the quantum defect for the F states was not obtained in section 5.2. Previous work estimated the F state quantum defect

to be ≈ 0.1 [122]. In this work, the F quantum defect is found to be larger. The lower energy D states (which should not be observed under two-photon excitation, see section 2.3) were found to have a quantum defect of ≈ 0.2 [122] which may indicate the states which have been assigned as F states in the SHG excitation spectra may be one of the lower energy D states. As previously discussed, further work is required to definitively assigned these states.

The widths of the exciton states as a function of principal quantum number are plotted in Fig. 5.9(b). The widths are expected to follow an n^{-3} scaling. However, the widths plotted here do not follow an obvious trend. For $n > 8$, all the series show significant extra broadening, with the width almost saturating rather than decreasing with n. The widths extracted from fitting the two-photon PLE spectrum show a similar but less pronounced trend (Fig. 5.5(b)).

Similar excess broadening for $n > 8$ was also observed in one-photon absorption spectroscopy of the nP states, even in high quality samples at < 1 K temperature [117]. This broadening was attributed to charges in the material [48]. Here the effect is more pronounced, suggesting a higher concentration of charges. The widths not decreasing as expected with n explains why the spectrum becomes crowded at high n.

The amplitudes do not have an obvious n dependence. The state with the largest amplitude is 7S. For $n > 7$, the amplitudes show a decreasing trend. This trend in amplitudes at low n is in contrast to the two-photon PLE spectrum (section 5.2), where the amplitudes fell as the principal quantum number was increased. The lower than expected amplitude at low n could be due to the green 1S exciton which has been previously shown to perturb low n states during SHG [126].

In the higher n region, the amplitudes of the peaks in the two-photon PLE spectrum and the SHG spectrum show similar trends, with the amplitudes decreasing as the band edge is approached. In both cases, the P states seem to show a more gradual decrease in amplitude. In the following section, the sharp drop in the amplitude of the SHG at high n is discussed.

5.3.1.2 Limitations in observing higher n

The observation of 12D in Fig. 5.6(b) is the highest excitonic state observed in two-photon spectroscopy. However, it is not clear why higher lying states are not observed. Interestingly the SHG intensity tends to zero as the bandgap is approached. This

implies that inhomogeneous broadening cannot be responsible for the disappearance of the exciton resonances, as inhomogeneous broadening (for example due to strain in crystal) would lead to a constant SHG intensity. There are two mechanisms which have been previously shown to limit the observation of higher n exciton states. These are, van der Waals interactions between excitons and charges in the material.

Van der Waals interactions between Rydberg excitons have been previously shown to lower the oscillator strength of the exciton resonances [32; 45]. However, these effects were observed at a much higher n than studied here. Given the inefficiency of the two-photon excitation process, and the lower n involved, it seems unlikely that sufficient exciton density has been achieved for exciton-exciton interactions to be playing a significant role.

A more likely explanation for the limit in n is the presence of charges in the material. Charges in the material cause an effective shift of the bandgap to lower energy [115; 116]. When the effective bandgap becomes lower than the exciton energy, the exciton state can no longer exist. Furthermore, exciton states close to the effective bandgap have their linewidths increased and oscillator strengths reduced [116; 139; 117; 48]. There are several mechanisms which can cause charges to be present in the material. Some of these are:

1. Charges due to impurities in the material

2. Optical production of electron-hole plasma

3. Collisional processes between excitons which generate electron-hole plasma

4. Optical ionisation of excitons

5. Thermally excited electron-hole plasma

In the highest quality natural samples, it was found that charges due to impurities in the material were the limiting factor in observing very high n states [117; 45; 33]. However, in this case, higher n states have been observed using a different spectroscopy technique. In Fig. 5.10 the SHG excitation spectra is compared to one-photon laser absorption spectroscopy. The one-photon laser absorption measurement was performed by Jon D. Pritchett using the setup described in section 3.1.2.3 at an excitation power of 10 µW. Exciton resonances up to 17P are visible in the one-photon data, while the highest resolved state in the SHG spectrum is 12D. It is also striking how crowded the
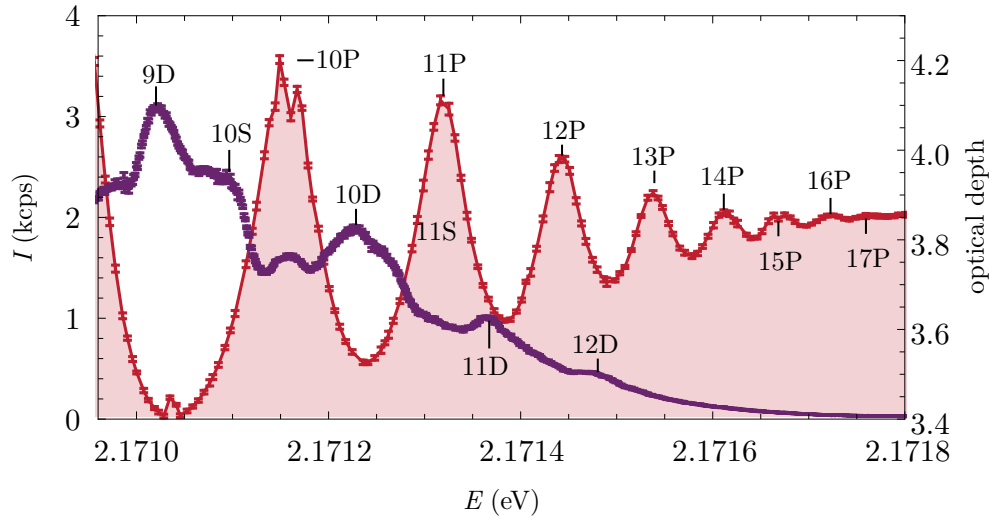
Figure 5.10: Comparison of SHG excitation spectrum and one-photon laser absorption spectrum in sample AM. SHG data is shown in purple and corresponds to left axis. Red shading (right axis) shows one-photon laser absorption in the same sample. Noise around 10P in one-photon data is due to laser being multimode. One-photon absorption data courtesy of Jon D. Pritchett, reproduced with permission.

SHG spectrum is at high n. In the SHG spectrum the resonances are split by less than their widths, leading to overlapping features. As only the P resonances are visible in the one-photon data, this problem is not as evident. As higher n states can be resolved in one-photon spectroscopy the presence of charges due to impurities in the material cannot be the liming factor in only observing $n = 12$.

In previous work, electron-hole plasma was deliberately generated by above bandgap optical excitation [115]. Optical generation of free carries is also thought to be the limiting factor in observing higher n in previous two-photon experiments [141]. In this previous work, femtosecond pulses were used. Due to the spectrally broad nature of the excitation light, some of the light caused above bandgap two-photon excitation. Here, a narrow-band laser used is used, meaning there is no two-photon above bandgap excitation, and the optical creation of electron-hole plasma would be a three-photon process. Another mechanism for generating electron-hole plasma are collisional processes, such as Auger recombination. These collisional processes are dependent on exciton density [163; 176; 95]. As the two-photon excitation process is inefficient, the exciton density is assumed to be low and these processes are probably not a limiting factor. Similarly, optical ionisation of the exciton states is assumed to be a weak process, as this would be a three-photon process. However, these process cannot be completely ruled out.

The final way of producing free charges in the material is thermal excitation. Previous work has studied the effects temperature on the Rydberg spectrum [116]. It was found that to limit the one-photon Rydberg spectrum to $n = 12$ the temperature had to greatly exceed 25 K. While this is far higher than the 4 K base temperature of the cryostation, it is believed the samples in this work are not at the cryostation base temperature, even under very low intensity excitation (see section 4.2.1). Given the high excitation powers used for SHG spectroscopy, it is conceivable that the samples are reaching high temperatures.

Temperature can also limit the observation of higher lying Rydberg states through thermal ionisation. Once the thermal energy in the crystal exceeds the binding energy of the exciton, thermal ionisation can occur. However, previous work showed that the rate of thermal ionisation is negligible compared to the lifetime of the Rydberg states at temperatures below 50 K, and so is not an important factor in observing high n states [139]

5.3.1.3 Power dependence

All of the methods for generating electron-hole plasma discussed in the previous section are dependent on excitation power. To investigate the limit in observing higher n states, power dependent measurements were performed. For this experiment the average power, P_{IN}, was varied and the pulsed excitation was fixed to 50 ns pulses with a 200 ns period. First, the power dependence of the emission spectrum using the Fabry-Pérot etalon (section 3.1.3.1) was studied. An SHG emission spectrum was taken at two-photon excitation energy $E = E_{8\mathrm{S}}$ on sample AM using the FPE detailed in section 3.1.3.1. The peak in the emission spectrum was fitted with a Lorentzian. The amplitude obtained from this fit is plotted vs laser power in Fig. 5.11(a). The diagonal line shows a quadratic fit to the data. The data is in good a agreement with the quadratic dependence, showing some saturation at the highest powers. The saturation is probably due to heating of the sample.

The excitation spectrum from sample AB at 5 different laser powers, P_{IN}, is shown in Fig. 5.11(b). At the lowest excitation powers, more features in the spectrum are visible, and higher lying exciton states (up to $n = 12$) are visible. The spectra at the two lowest powers are similar to the spectra from sample AM in Fig. 5.6(b) indicating that many of the differences between the two samples may have been due to the different excitation powers used. There is also a clear shift in the position of the peaks with excitation
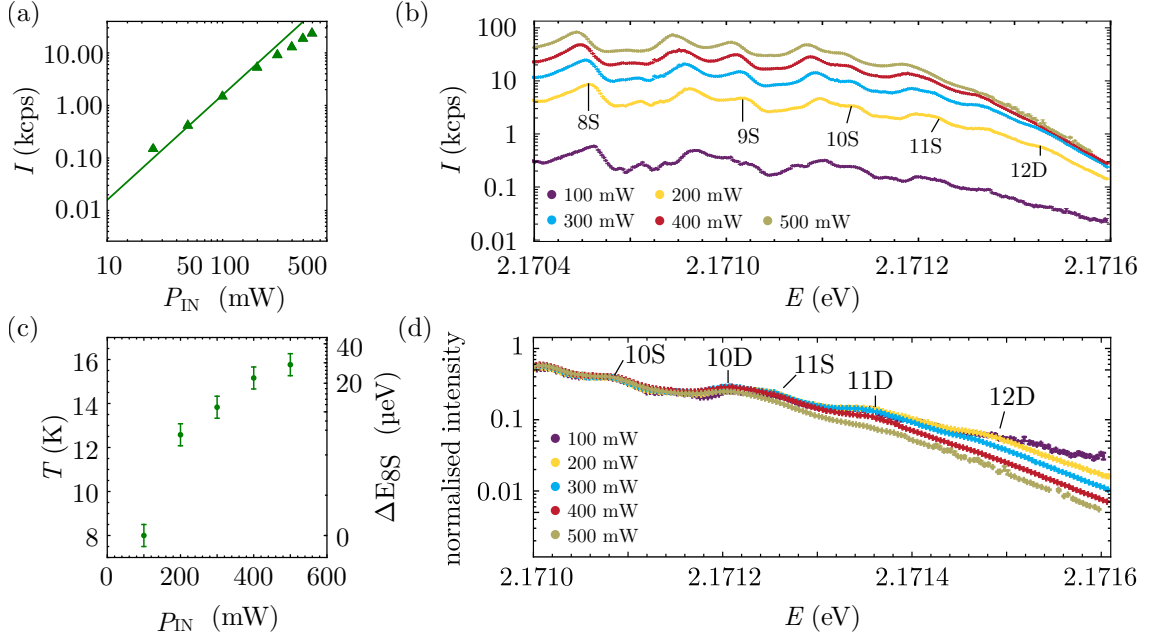
Figure 5.11: SHG power dependence. (a) Intensity of spectrally resolved SHG emission (using FPE in section 3.1.3.1) vs excitation power P_{IN} from sample AM using. Solid line shows a quadratic fit to the data. (b) Excitation spectra from sample AB at excitation powers from 100 to 500 mW. (c) Estimated sample temperature from the shift in the 8S resonance. The magnitude of the shift is plotted on the right axis. (d) Normalised excitation spectra from sample AB at excitation powers from 100 to 500 mW. The spectra have been normalised to the amplitude of the 8S resonance. The energy axes have been adjusted such that the 8S resonance is at the same energy for every excitation power.

energy. At the lowest excitation power, the energy of the 8S peak is within 5 µeV of the energy of the 8S peak in the spectra from sample AM in Fig. 5.6(b).

The exciton resonances in Fig. 5.11 are red shifted as the excitation power is increased which is a clear indication of sample heating and can be attributed to a shift of the absolute bandgap with temperature. Note that this shift is not related to the change in effective bandgap mentioned previously. The temperature dependence of the bandgap energy, E_g, in semiconductors can be phenomenologically described by

$$E_g(T) = E_g(0) - a\left(1 + \frac{2}{e^{b/T} - 1}\right), \tag{5.5}$$

where a and b are parameters which depend on the material [177]. Previous work has determined $a = 14.6 \pm 0.6$ meV and $b = 110 \pm 3$ K in Cu_2O [161; 178]. The exciton temperature in the $P_{IN} = 100$ mW scan is assumed to be 8 ± 1 K (this temperature was obtained from fitting the phonon-replica in the PL spectrum in Fig. 5.1(b) which was

taken at $P_{IN} = 90$ mW). Assuming that the shift in energy of the 8S state is entirely due to the bandgap shift, it is possible to extract an approximate temperatures for each of the scans.

The extracted exciton temperature vs laser power is shown in Fig. 5.11(c). The magnitude of the shift of the 8S resonance is plotted on the right hand axis. As expected, the exciton temperature increases with excitation power. At the highest excitation powers, the exciton temperature exceeds 15 K, which is considerably higher than the 4 K base temperature of the cryostation. Previous work on the temperature dependence of the exciton series managed to observe up to $n = 17$ in one-photon absorption at 15 K [116]. However, the highest n visible in Fig. 5.11(b) is only $n = 11$ at the highest excitation powers. These previous studies were performed on very high quality samples where the impurity concentration is estimated to be less than 0.01 µm^{-3} [115]. Here, the impurity concentration is probably higher, meaning there is a higher concentration of charges in the material at a given temperature. This higher concentration of charges would cause the effective bandgap to be at a lower energy for a given temperature, potentially limiting the Rydberg series to lower n.

To investigate the tail off in SHG intensity at high n, the normalised intensity at each of the 5 powers is plotted in Fig. 5.11(d). Here, the data has been normalised by the intensity of the 8S peak, and the energy axes have been adjusted so the 8S peak is at the same energy at every excitation power. In the high n region, all of the spectra show a fast decrease in SHG intensity as the excitation energy is increased. The slope of the signal appears the same for all of the scans apart from the 100 mW scan which is affected by dark counts. The onset of the slope occurs at lower energy for the higher power scans and the highest n resonances are not present in the high power scans.

The power dependent measurements of the high n region are all consistent with the limitations to the Rydberg series being due to the presence of charges in the material. The sample temperature was found to be considerably higher than the heatsink temperature and dependent on excitation power. Therefore, thermally excited free charges are the most likely explanation for the limitations to the Rydberg series. However, other power dependent mechanisms for generating free charges, such as Auger recombination and optical ionisation of excitons, have not been ruled out. These other effects should have nonlinear dependencies on excitation power, while heating should have a linear dependence. By performing experiments where the peak power of the laser is kept constant but the average power is varied, it should be possible to distinguish between the mechanisms.

One question which remains is what causes the increase in temperature. The most likely candidate is be one-photon absorption at vacancies in the crystal. The copper vacancy peak is centred around 920 nm and is broad (FWHM $\approx$ 150 nm) [52], so if there are any copper vacancies in the crystal a small amount of one-photon absorption will occur. In synthetic samples, which were shown to have high concentrations of copper vacancies (section 4.3), the heating was so substantial that sample damage occurred and two-photon spectroscopy could not be performed. If the heating is entirely due to residual copper vacancies then higher quality samples will show less heating and higher n excitons should be observable. However, another possibility is off resonant one-photon absorption to the exciton states themselves. If this is the case then it is intrinsic to the material and it will always be a limiting factor in reaching higher n.

In future, several improvements to the experimental setup could be made to try and observe higher n excitons. Improving the thermal contact between the sample and the cryostation would help achieve a lower sample temperature. Switching to a forward collection geometry would greatly improve the collection efficiency and allow lower excitation powers to be used. Repeating the power dependent experiments on sample AM would also allow lower excitation powers to be used, as the SHG is more efficient in this sample due to its orientation. Furthermore, the use of a larger laser spot would allow a reduced excitation intensity while still retaining a reasonable count rate on the detector. The quadratic power dependence of the SHG process could also be exploited. As the heating should be dependent on the average excitation power a pulsed regime with a high peak power and low average power would minimise heating while still generating a measurable amount of SHG. A combination of these features should allow the average intensity of the excitation light to be significantly reduced and the sample temperature to be closer to the cryostation base temperature.

In this section, it was shown that the excitation power could be limiting the observation of higher n states. A shift in the energy of the exciton resonances as the excitation power was increased showed the sample was heating under higher excitation powers. From this shift, it was estimated the sample was reaching more than 15 K under the highest excitation powers. The higher excitation powers also caused the highest n exciton states to vanish. All of these observations are consistent with thermally excited free charges in the material limiting the observation of higher n. While thermally excited free charges are most likely limiting factor, other effects which generate free charges in the material have not been ruled out, and further experiments are required. In the final part of the this chapter, the polarisation dependence of the SHG is dis-
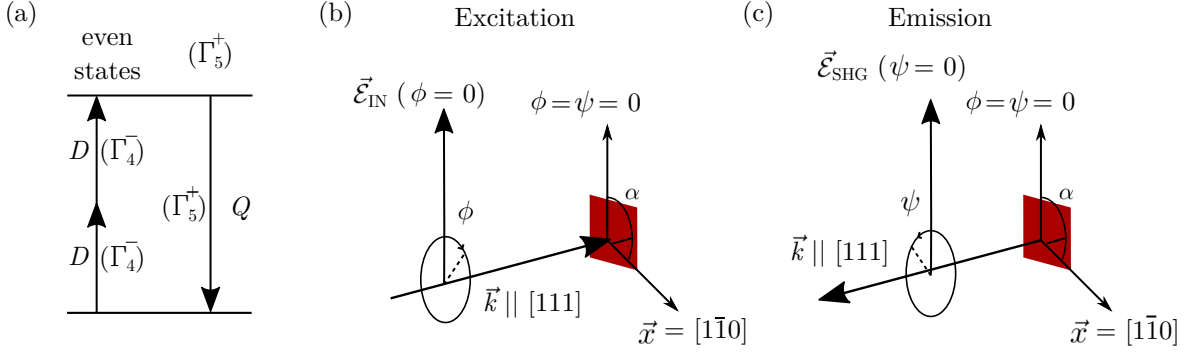
Figure 5.12: (a) Schematic of the SHG process. Two electric dipole transitions of Γ_4^- symmetry excite an even-parity state of Γ_5^+ symmetry. Emission from this state occurs through a quadrupole transition of Γ_5^+ symmetry. (b) and (c) Diagrams of the geometry of the geometry of the polarisation experiments. Sample is shown in red. (b) Geometry of the excitation beam. The excitation beam is directed onto the sample such that the k vector of the beam is parallel to the [111] vector. Polarisation angle of the beam is ϕ. In the crystal coordinates, the vector $[1\bar{1}0]$ is taken as 0°. The offset angle, α, defines the angle between $\phi = 0°$ and the vector $[1\bar{1}0]$. (c) Geometry of the SHG beam. The light is emitted in the opposite direction from the excitation beam with a polarisation angle ψ.

cussed.

5.3.2 Polarisation Selection Rules

In general, light-matter coupling is a tensor depending on the crystallographic orientation and the polarisation of the light fields. So far in this chapter, the polarisation dependence of the coupling has been neglected. In the following, polarisation selection rules for SHG in Cu_2O are presented. This model has been previously derived [141; 142; 143; 92] and is based on a group theoretical approach [81]. The model from the literature is presented here, before being extended to include the effects of tightly focussed laser beams and window birefringence. Here we only consider the derivation of the selection rules for SHG resonant with even-parity (S and D) states of Γ_5^+ symmetry, though similar expressions for SHG resonant with states of other symmetry can also be derived [141; 142; 143; 92].

For SHG to be possible both the absorption and the emission processes must be allowed. The energy level diagram in Fig 5.12(a) shows the steps involved during SHG involving an even-parity exciton of Γ_5^+ symmetry. Absorption occurs through two electric dipole processes. As one-photon emission from an even-parity state is forbidden in dipole

approximation, emission occurs through an electric quadrupole transition. The SHG intensity is proportional to a product of both of these processes. To derive expressions for these processes, we start by considering the electric field vectors of the excitation and the SHG light. For linearly polarised light we can describe the electric fields of the excitation light, $\vec{\mathcal{E}}_{\text{IN}}$, and the second harmonic light, $\vec{\mathcal{E}}_{\text{SHG}}$ in the laboratory frame by

$$\vec{\mathcal{E}}_{\text{IN}}(\phi) = \mathcal{E}_{\text{IN}} \begin{pmatrix} \cos\phi \\ \sin\phi \\ 0 \end{pmatrix}, \tag{5.6}$$

and

$$\vec{\mathcal{E}}_{\text{SHG}}(\psi) = \mathcal{E}_{\text{SHG}} \begin{pmatrix} \cos\psi \\ -\sin\psi \\ 0 \end{pmatrix}, \tag{5.7}$$

respectively. Here ϕ and ψ are the polarisation angles of the excitation and SHG light and $\mathcal{E}$ is the magnitude of the electric fields. Due to the back-scattered geometry of the experiment, a negative sign is required for the angle in equation 5.7. For this analysis, it is necessary to convert to the coordinate frame of the crystal. We assume that the light propagates perpendicular to the crystal surface and so $\vec{k} \parallel [a_1a_2a_3]$, where $[a_1a_2a_3]$ is the vector normal to the crystal surface. In this reference frame $\vec{k}$ and electric field of the incoming light are given by:

$$\vec{k} = \begin{pmatrix} k_1 \\ k_2 \\ k_3 \end{pmatrix}, \quad \vec{\mathcal{E}}_{\text{IN}}(\phi) = \mathcal{E}_{\text{IN}} \begin{pmatrix} u(\phi) \\ v(\phi) \\ w(\phi) \end{pmatrix}. \tag{5.8}$$

Throughout this analysis light is treated as a plane wave, and so $\vec{k} \cdot \vec{\mathcal{E}} = 0$. The limitations of the plane wave assumption are discussed when the model is applied to a high numerical aperture lens in section 5.3.2.1. Similarly, the electric field for the emission, $\vec{\mathcal{E}}_{\text{SHG}}$, in the crystal coordinates is given by:

$$\vec{\mathcal{E}}_{\text{SHG}}(\psi) = \mathcal{E}_{\text{SHG}} \begin{pmatrix} m(\psi) \\ n(\psi) \\ o(\psi) \end{pmatrix}. \tag{5.9}$$

See Fig. 5.12(b) and (c) for diagrams of the geometry of the system. Transformation between the laboratory and the crystal coordinate frames is achieved through a

transformation matrix,

$$\mathbf{T}(\vec{k}, \vec{x}, \vec{y}) = \begin{pmatrix} x_1 & y_1 & k_1 \\ x_2 & y_2 & k_2 \\ x_3 & y_3 & k_3 \end{pmatrix}, \tag{5.10}$$

where the vectors $\vec{x}$ and $\vec{y}$ correspond to polarisations $\phi = \psi = 0$ and $\phi = \psi = \pi/2$ in the crystal frame. However, in the experiment, the orientation of the vector $\vec{x}$ was not known in the lab frame. Therefore, an offset angle, α, was introduced as the angle between $\vec{\mathcal{E}}(\phi = 0)$ and $\vec{x}$. Later, the offset angle α will be determined by fitting the data.

The dipole operator, O_D, is a unit vector proportional to the electric field vector [143], and so for the excitation we have

$$O_D(\phi) = \begin{pmatrix} u(\phi) \\ v(\phi) \\ w(\phi). \end{pmatrix} \tag{5.11}$$

To describe the excitation to the Γ_5^+ state the dipole operator is applied twice. This is achieved through taking a symmetrical cross product of the dipole operator with itself [143; 92]. The symmetrical cross product is between two vectors is defined as

$$\begin{pmatrix} a_1 \\ a_2 \\ a_3 \end{pmatrix} \otimes \begin{pmatrix} b_1 \\ b_2 \\ b_3 \end{pmatrix} = \frac{1}{\sqrt{2}} \begin{pmatrix} a_3 b_2 + a_2 b_3 \\ a_1 b_3 + a_3 b_1 \\ a_2 b_1 + a_1 b_2 \end{pmatrix}, \tag{5.12}$$

where $\otimes$ denotes the symmetrical cross product. The operator describing the two-photon absorption, O_{TPA}, is then

$$O_{TPA}(\phi) = O_D(\phi) \otimes O_D(\phi) = \sqrt{2} \begin{pmatrix} v(\phi)w(\phi) \\ u(\phi)w(\phi) \\ u(\phi)v(\phi) \end{pmatrix}. \tag{5.13}$$

The emission process occurs through a quadrupole transition of Γ_5^+ symmetry which is proportional to the symmetric cross product of $\vec{k}$ and the emitted electric field

$$O_{EMS}(\psi, \vec{k}) \propto \vec{\mathcal{E}}_{SHG}(\psi) \otimes \vec{k}$$

$$O_{EMS}(\psi, \vec{k}) = \frac{1}{\sqrt{2}} \begin{pmatrix} k_2 o(\psi) + k_3 n(\psi) \\ k_3 m(\psi) + k_1 o(\psi) \\ k_1 n(\psi) + k_2 m(\psi) \end{pmatrix}. \tag{5.14}$$
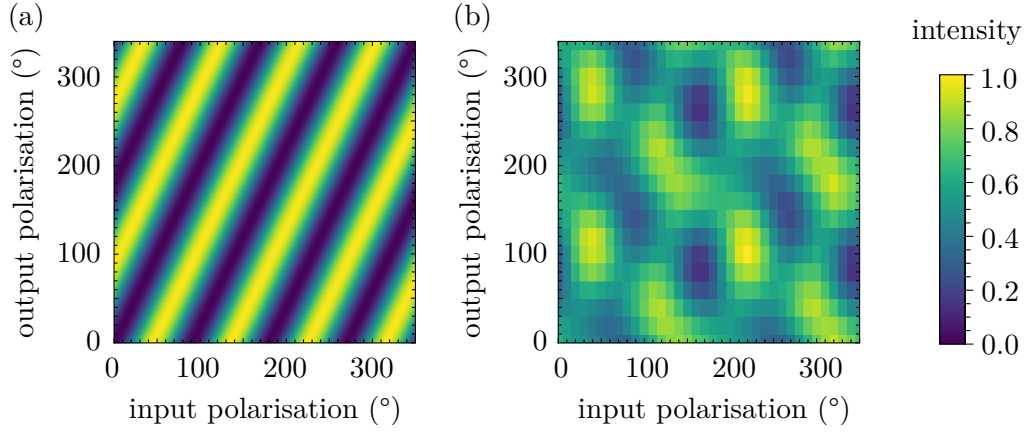
Figure 5.13: Polarisation dependence of SHG intensity. (a) Predicted SHG intensity as a function of input and output polarisation angles for excitation light with $\vec{k} \parallel [111]$ and $\vec{x} \parallel [1\bar{1}0]$. (b) Measured SHG intensity as a function of input and output polarisation angles for excitation light with $\vec{k} \parallel [111]$. Here, the excitation energy was resonant with the 8S state. Note that 0° for both the input and output polarisation is not the same in (a) and (b).

Finally, the intensity of the SHG emission is proportional to the square of the product of the absorption and emission operators

$$I_{\mathrm{SHG}}(\phi, \psi, \vec{k}) \propto |O_{\mathrm{TPA}}(\phi)O_{\mathrm{EMS}}(\psi, \vec{k})|^2. \tag{5.15}$$

The predicted intensity as a function of input (ϕ) and output (ψ) polarisation angles is plotted in Fig. 5.13(a). Here, we have taken $\vec{k} \parallel [111]$, $\vec{x} \parallel [1\bar{1}0]$ and set $\alpha = 0°$. For a fixed input polarisation, the output polarisation has a sinusoidal dependence, with a period of π. When the output polarisation is fixed, the dependence on the input polarisation is also sinusoidal, though this time with a period of $\pi/2$. A very similar plot to Fig. 5.13(a) appears in [143]. However, the plot here is mirrored, due to the back-scattered geometry of the experiment.

The polarisation dependencies of the SHG were measured experimentally. Here, sample AM which was orientated with the (111) crystal plane parallel to the surface was used. The measurements were performed by rotating the half-waveplate in the excitation beam path and inserting a half wave-plate and Glan-Taylor polariser in the collection beam path. Full details of the experimental setup for the polarisation experiments are in section 3.1.2.1.

The measured polarisation dependencies of the SHG intensity is shown in Fig. 5.13(b). When compared with the predicted polarisation dependence (Fig. 5.13(a)) there are
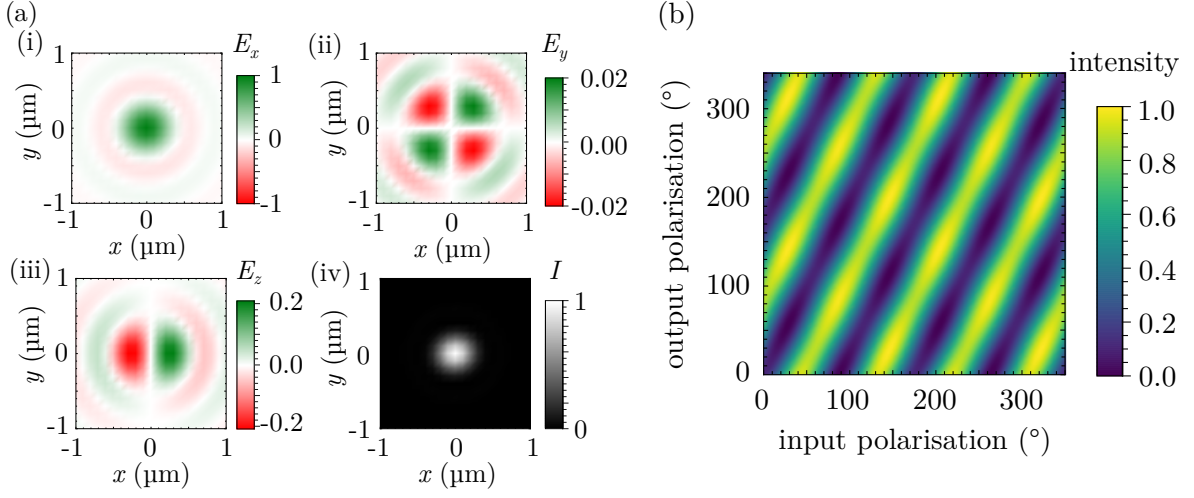
Figure 5.14: SHG polarisation dependence including a tightly focussed excitation beam. (a) Plots of the spatial patterns in the focal plane of the (i) x, (ii) y, and (iii) z components of the electric field for an input Gaussian beam linearly polarised along x. (iv) Shows the resulting intensity pattern. (b) SHG intensity dependence on input and output polarisation angles, taking into account the change in polarisation due to the tightly focussed excitation beam.

clear disagreements. Note that 0° for the theory and experimental plots are not the same as the offset angle α is unknown.

In the remainder of this section two possible explanations for the disagreement between experiment and theory will be explored. First, the model will be extended to include the effects of the tightly focussed excitation beam. Second, window birefringence will be added to the model.

5.3.2.1 Tightly focussed excitation beam

In the model presented above, the input light was treated as a plane wave. However, tightly focussed light can no longer be treated as a plane wave and the vector nature of light must be accounted for. Tightly focussing a linearly polarised Gaussian beam leads to a longitudinal polarisation component around the focus [179]. As our experiments use a tightly focussed laser beam for the excitation, the longitudinal component becomes a significant proportion of the electric field. The high refractive index of cuprite leads to a tighter focus and a larger proportion of the electric field in the longitudinal direction [180].

For a given input polarisation, ϕ, the electric field in the focal plane was computed

using the integrals for the different Cartesian components of the electric field found in [179]. The input laser was taken have a Gaussian intensity profile. To account for focussing into a dielectric, the integrals were calculated with the wavelength of the light inside Cu_2O [181]. In truth, focussing into a dielectric is more complicated than scaling the wavelength. A more complete approach for the focussing of Gaussian beams through dielectric interfaces can be found in [180].

The Cartesian components of the electric field in the focal plane for $\phi = 0$ are shown in Fig. 5.14(a) along with the resulting intensity pattern. As the input beam was polarised along x, the largest component of the electric field is still along x (Fig. 5.14(a)(i)). There is a small component in the y direction (Fig. 5.14(a)(ii)), and a significant component in the z direction (Fig. 5.14(a)(iii)). The resulting intensity pattern retains the expected Gaussian profile (Fig. 5.14(a)(iv)).

To account for the change in polarisation due to focussing, $\vec{\mathcal{E}}_{IN}(\phi)$ was sampled in a 50 x 50 grid covering the range ± 1 µm in the x y plane. $I_{SHG}(\phi, \psi, \vec{k})$ was calculated for each $\vec{\mathcal{E}}_{IN}(\phi)$ and summed with a weight given by $\left|\vec{\mathcal{E}}_{IN}(\phi)\right|^2$ to give the total SHG intensity at a given input polarisation ϕ. The input polarisation, ϕ, was then varied and the process was repeated to build up a polarisation dependence. Note that only the polarisation in the focal plane was sampled. As SHG is not only generated in the focal plane, a more complete model would sample a range of z too. However, the longitudinal component of the electric field is largest in the focal plane, and so the resulting polarisation dependence will show an upper limit on the potential variation due to the tight focussing.

Including the tightly focussed excitation beam leads to slight changes in the predicted polarisation dependence. Fig. 5.14(b) shows the SHG polarisation dependence when the tightly focussed beam is taken into account. The resulting polarisation dependence looks similar to Fig. 5.13(a) though there are subtle changes. The clean diagonal lines observed in Fig. 5.13(a) are slightly perturbed. As the effect of the tightly focussed excitation light is only a small perturbation of the polarisation dependence it does not account for the disagreement observed between the theory and experiment in Fig. 5.13. In the remainder of this section and alternative explanation for the discrepancy, optical birefringence, will be studied.

5.3.2.2 Birefringence

In this section the effect of optical birefringence is added to the polarisation model. Given the tightly focussed excitation beam had little effect on the predicted polarisation dependence, in this section it will be neglected and the light will be treated as plane waves. Nothing in the excitation or emission beam path is intrinsically birefringent (other than the waveplates). However, the CaF_2 windows in the sample mount may be exhibiting stress induced birefringence [182]. The windows are glued into the copper mount (section 3.2) and the differing thermal expansions will result in stress on the window as it is cooled to 4 K. The resulting birefringence is modelled using a Jones matrix approach [183]. For this, the form of the model in section 5.3.2 is used, where the excitation light is treated as a plane wave.

The Jones matrix for a birefringent material with a phase difference between the fast and slow axes of ζ orientated at an angle θ is given by:

$$\mathbf{M}(\zeta, \theta) = e^{-\frac{i\zeta}{2}} \begin{pmatrix} \cos^2 \theta - e^{i\zeta} \sin^2 \theta & (1 - e^{i\zeta}) \cos \theta \sin \theta & 0 \\ (1 - e^{i\zeta}) \cos \theta \sin \theta & \sin^2 \theta + e^{i\zeta} \cos^2 \theta & 0 \\ 0 & 0 & 1 \end{pmatrix}. \qquad (5.16)$$

Note that normally Jones matrices are written as 2×2 matrices. Here though, a third dimension (corresponding to the direction of propagation) has been added to be consistent with the notation in section 5.3.2. The Jones matrices do not alter any polarisation component in the direction of propagation. The Jones matrix is applied to the electric fields of the excitation and SHG light to give new forms of equations 5.6 and 5.7:

$$\vec{\mathcal{E}}_{\text{IR}}(\phi, \zeta, \theta, \alpha) = \mathcal{E}_{\text{IR}} \mathbf{M}(\zeta, \theta) \cdot \begin{pmatrix} \cos(\phi + \alpha) \\ \sin(\phi + \alpha) \\ 0 \end{pmatrix}, \qquad (5.17)$$

$$\vec{\mathcal{E}}_{\text{SHG}}(\psi, \zeta, \theta, \alpha) = \mathcal{E}_{\text{SHG}} \mathbf{M}(\zeta, -\theta) \cdot \begin{pmatrix} \cos(\psi + \alpha) \\ -\sin(\psi + \alpha) \\ 0 \end{pmatrix}. \qquad (5.18)$$

As the excitation and SHG light pass through the same CaF_2 window (due to the back-scattered geometry used in the experiment) they are assumed to see the same phase shift. This is not strictly true, as the wavelength of the two beams are different. However, it is a reasonable assumption as the refractive index of CaF_2 is varies by less than 1% over this range [184]. Note that the angle of the fast axis is negative in the
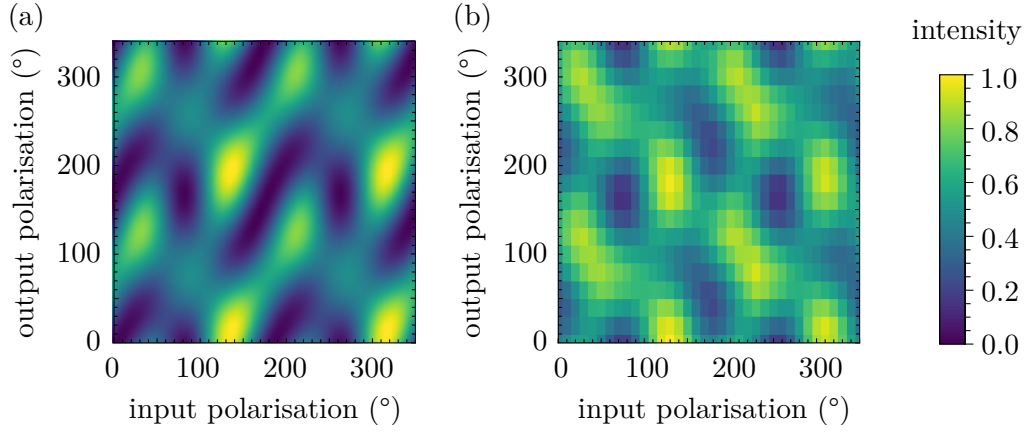
Figure 5.15: SHG polarisation dependence including birefringence. (a) Predicted SHG intensity as a function of input and output polarisation angles including birefringence. Here, $\vec{k} \parallel [111]$ and $\vec{x} \parallel [1\bar{1}0]$. Model was fitted to data in (b) giving a phase shift of $\zeta = 60 \pm 10°$ at angle of $\theta = 65 \pm 5°$ from $\vec{x}$ (b) Measured SHG intensity as a function of input and output polarisation angles for excitation light with $\vec{k} \parallel [111]$. Here, the polarisations have been adjusted by α (relative to Fig 5.13) so that $0°$ is the same in (a) and (b).

Jones matrix applied to the SHG light due to the fact the SHG light passes through the window in the opposite direction from the excitation light. Here the offset angle, α, is explicitly included.

Once the birefringence of the window has been included, the method to calculate the SHG intensity, $I_{SHG}(\phi, \psi, \zeta, \theta, \alpha)$, is the same as section 5.3.2. ζ, θ and α are unknown, so are taken as free parameters. The result of fitting $I_{SHG}(\phi, \psi, \zeta, \theta, \alpha)$ to the experimental data is shown in Fig. 5.15. The best fit parameters were found to be $\zeta = 60 \pm 10°$, $\theta = 65 \pm 5°$ and $\alpha = 80 \pm 5°$.

In Fig. 5.15 there is reasonable agreement between the experimental data and the model, with the major features of the data being recreated by the model. The reasonable agreement shows that window birefringence is an issue in the experimental setup and is responsible for the polarisation dependence not being what was expected.

Experiments were attempted to try and remove the birefringence from the setup. To achieve this, the front window of the sample mount was removed. However, it was found that without the front window the sample was heating significantly more under two-photon excitation. The increased heating made it impossible to repeat the experiment without the front window.

In future, more care could be taken to mount the sample so there is no birefringence

induced in the windows. This could be done by using thermal grease rather than glue to hold the window in place. Alternatively, a new sample mount could be designed which either uses a thicker window which is less likely to be stressed, or designed in such a way that the sample is in good thermal contact without the need for the front window.

5.4 Summary and outlook

In this chapter, the Rydberg exciton series has been studied using two-photon excitation. Under two-photon excitation, the sample can either coherently (SHG) or incoherently emit light (PL). Through the use of spectral filters, it was possible to switch between these two regimes.

In the case of sample AB, the majority of the incoherently emitted light comes from the radiative decay of bound excitons. The temporal capabilities of the detection allowed the lifetime of these states to be measured. The lifetime was found to $640 \pm 10 \, \mu s$ which is significantly longer than the lifetimes of other exciton states measured in Cu_2O. The previous longest lifetime measured is the 1S para-exciton, the lowest energy exciton state in a pure sample, at 13 µs [102].

By scanning the excitation laser energy and looking at the intensity of the emitted light an excitation spectrum was recorded in both the PL and SHG regimes. Both these methods allowed the observation of Rydberg states, with the SHG method revealing states up to $n = 12$. There were clear differences between the PLE and SHG methods. In the case of two-photon PLE the exciton resonances sit on top of a non-resonant background, and the spectrum tends to a constant value once the exciton states are no longer resolvable. For the SHG excitation spectrum there is no background, and the SHG intensity tends to 0 at high energy. This indicates the PLE method is probing a non-resonant effect which is not present under SHG. The origin of this effect is unknown and requires further study.

The observation of $n = 12$ using two-photon excitation is the highest energy even-parity state observed so far in Cu_2O. The narrowband excitation laser allowed the lineshape of the high n Rydberg states to be measured for the first time, and the trends in the energies, widths and amplitudes of the states studied. Comparisons between the one-photon and two-photon spectra revealed that considerably higher n was observed under one-photon excitation. In the one-photon absorption spectrum, it was possible to observe $n = 17$ in the same sample indicating the Rydberg series was not limited by the sample quality. The power dependence of the signal (section 5.3.1.3) indicated that excitation power was limiting the observation of higher n. A shift in the exciton resonances to lower energy as the laser power was increased indicated the sample was heating under laser excitation. Thermally excited free charges are probably the limiting factor in observing higher exciton states. However, other effects which create free

charges (such as Auger recombination or optical ionisation of excitons) would also be dependent on excitation power and so cannot be completely ruled out. Further power dependent measurements should indicate what is limiting the observation of higher n. By lowering the repetition rate of the excitation pulses, it should be possible to minimise the sample heating and extend the Rydberg series to higher n.

In future, the SHG experiments should switch to a forward collection geometry. As SHG is generated in the forward direction this should significantly improve detection efficiency and allow lower excitation powers to be used.

At high n Rydberg states it should be possible to observe long-range interactions between excitons. Previous work has focussed on the decrease in absorption due to effects such as Rydberg blockade [32; 45]. One advantage of the two-photon excitation scheme is that the emitted light can be easily separated from the excitation light. The tight focussing means that the excitation light should be focussed below the blockade radius at high n [32]. By looking at the photon statistics of the emitted light, it might be possible to observe van der Waals interactions between the excitons [44]. If the Rydberg blockade radius is larger than the excitation spot size, then the light should display anti-bunching, which would be the first step to producing a single photon source based on Rydberg excitons [47]. Adjusting the current experimental setup to perform this measurement will not be challenging, the addition of a beam splitter on the collection and a second SPAD will allow photon correlations to be measured.

Overall, two-photon excitation is a complementary tool to one-photon studies of Rydberg excitons. While it has not been possible to reach as high n in the Rydberg series, two-photon excitation has several advantages over one-photon processes. There is no large phonon-assisted background and it is easy to separate the emitted light from the excitation light.

Exciton-microwave coupling

In this chapter the first coupling of Rydberg excitons to a microwave field in Cu_2O is demonstrated. Both one and two-photon excitation schemes are used to probe Rydberg excitons. The microwave field will be shown to have a substantial effect on the Rydberg exciton spectrum. The results are consistent with a model based on the microwave electric field driving electric dipole transitions between excitonic states of opposite parity. The model is based entirely on an "atomic physics" view of the exciton.

The first electric dipole coupling between excitonic states in Cu_2O was observed in studies of the 2P→1S transition [61]. Here, a model was constructed using a nonlinear susceptibility [185; 62; 64; 63]. The models presented in this thesis are also based on a nonlinear susceptibility, and in the limit of isolated resonances and low microwave field strengths the results of earlier studies are recovered [61].

In general, light-matter coupling is a tensor depending on the crystallographic orientation and the polarisations of the relevant fields. However, for the majority of this chapter an effective scalar coupling will be used. This is due to optical birefringence (section 5.3.2.2) and the complex polarisation dependence of the microwave field. The exception is in section 6.2.3 where the polarisation selection rules presented in section 5.3.2 are extended to include the effect of a microwave field.

6.1 LED transmission spectroscopy with a microwave field

In this section we study the effect of a microwave field on the one-photon absorption spectrum in Cu_2O. The data in this section was taken using sample AM which is orientated with the (111) crystal plane parallel to the crystal surface. For microwave delivery antennae A1 and A2 were used (see section 3.3).

An energy level diagram of the LED experiment is shown in Fig. 6.1(a). The broadband LED light excites odd-parity P states. The microwave field introduces a coupling between the odd-parity P states and the even-parity S and D states through electric dipole transitions. This coupling leads to a change in the transmitted LED intensity. The transmission spectrum was measured using the monochromator detailed in section 3.1.3.2.

6.1.1 Experimental results

The resulting transmission spectrum with and without a microwave field at microwave frequency $f_{MW} = 15$ GHz and microwave power $P_{MW} = 25$ mW using antenna A2 is shown in Fig. 6.1(b). The exciton spectrum from $n = 5$ to the band edge is shown, with resonances up to 11P visible. The observation of higher states is limited by the resolution of the monochromator. For $n > 7$ the spectrum is substantially modified by the presence of the microwave field. To highlight the changes due to the microwave field the fractional change in the transmission, $\Delta T/T_{off} = (T_{on} - T_{off})/T_{off}$, is plotted in Fig. 6.1(c). Here, it is clear the transmitted intensity is changed by more than 10% at some energies. The transmission is enhanced (corresponding to reduced absorption) at the P states and is reduced (increased absorption) either side, at energies close to the S and D states.

The changes to the transmission spectrum seen in Fig. 6.1(b) and (c) can be understood in terms of state mixing. The S and D states acquire some P character which leads to an increase in absorption at the energy of the S and D states. Similarly, the P states acquire some S and D character, resulting in a decrease in absorption at the P states.

The microwave frequency response of the exciton-microwave coupling is expected to be broadband. This is due the separation between the exciton states (8P to 8S is 23 GHz) being comparable to the widths of the states (FWHM of 8P is 14 GHz). The
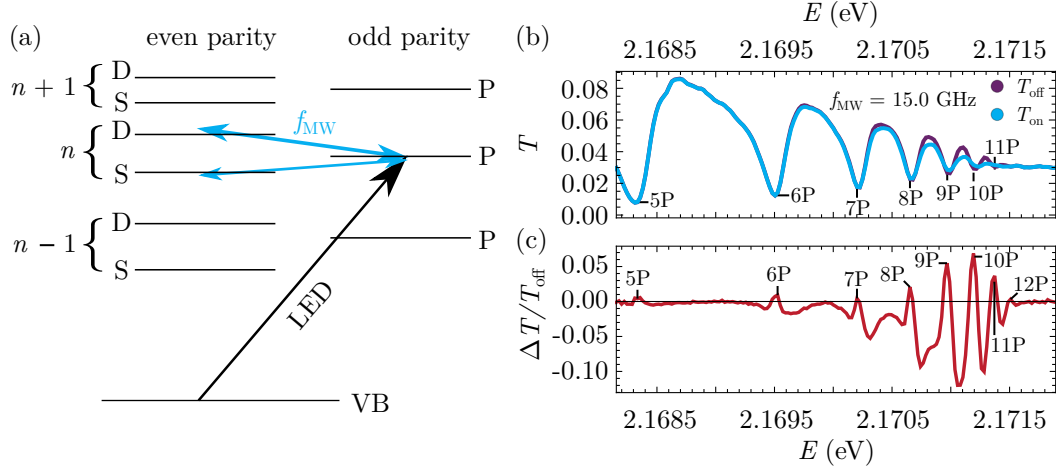
Figure 6.1: LED transmission spectra with a microwave field. (a) Energy level diagram of the LED experiment. A broadband LED excites odd-parity (P) excitons. A microwave field couples the even- and odd-parity exciton states through electric dipole transitions. (b) LED transmission spectrum with (blue) and without (purple) a microwave field at $f_{MW} = 15.0$ GHz and $P_{MW} = 25$ mW. (c) Fractional change in transmission due to the microwave field.

broadband response is the reason multiple exciton states are affected by applying a single microwave frequency ($f_{MW} = 15$ GHz in Fig. 6.1). The broadband frequency response is a notable difference between Rydberg excitons and atomic Rydberg systems. In atomic Rydberg systems the linewidth of the states is considerably smaller than the state separation, leading to resonances at particular microwave frequencies.

The experimentally measured microwave frequency dependence is shown in Fig. 6.2 for antenna A1 (a) and A2 (b). There are clear differences between the two heatmaps. Antenna A1 only shows a discernible signal at two narrow bands around 16 and 19 GHz. Antenna A2 however, shows a response over a broad range of microwave frequencies which appears independent of the excitation energy, E. To view the microwave frequency dependence more explicitly, cross sections of the heatmaps in Fig. 6.2(a) and (b) at $E = E_{9D}$ are shown in Fig. 6.2(b) and (c). Note, that $-\Delta T/T_{off}$ is plotted here as the transmission is reduced at the D states. Also shown in Fig. 6.2(c) and (d) is the simulated microwave frequency dependence of the antennae (see section 3.3.1 for details of the simulations). For antenna A1 (Fig. 6.2(c)) there is reasonable agreement between the simulated field strength and the microwave frequency response of the experiment. The simulation predicts a few narrow features with peaks centred at 16 and 19 GHz. We note there are a few peaks predicted by the simulation which are not observed in the experiment. For antenna A2 (Fig. 6.2(d)) the simulation predicts a
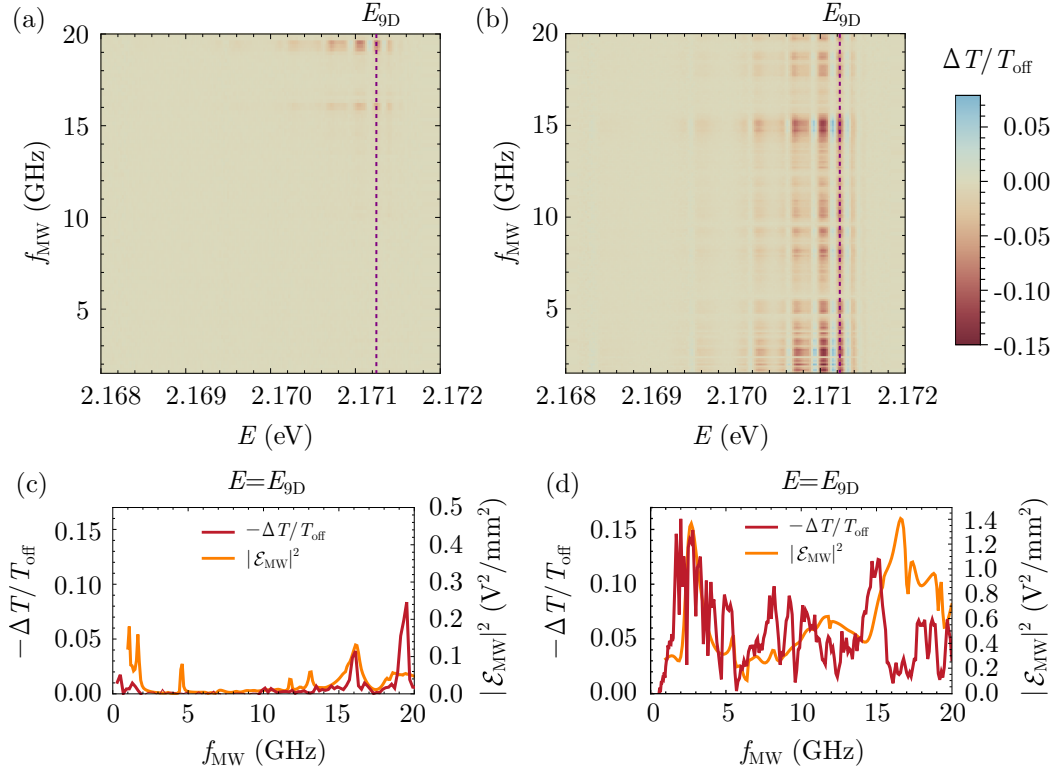
Figure 6.2: Fractional change in LED transmission, $\Delta T / T_{\text{off}}$, as a function of microwave frequency, f_{MW}, and excitation energy, E, for antenna A1 (a) and A2 (b) taken at $P_{\text{MW}} = 25$ mW. (c) Cross section of (a) at $E = E_{\text{9D}}$ (indicated by dashed red line in (a)). (d) Cross section of (b) at $E = E_{\text{9D}}$ (indicated by dashed red line in (b)). (c) and (d) also show simulated microwave frequency dependence (orange line). Simulations were performed by Rajan A. Mistry. Results reproduced with permission.

more broadband response and successfully predicts the large low frequency feature seen in the experimental data. However, the simulation does not predict the fine structure observed in the experimental data. The simulations show that the underlying broadband microwave response of the material is modulated by the response of the antenna, giving the experimentally observed microwave frequency dependence.

6.1.2 Theory

To model the change in the absorption due to the microwave field we use a nonlinear susceptibility to describe the light-matter interaction. As shown in section 2.3.1.1 one-photon absorption on the P states can be modelled using a linear susceptibility. The

contribution to the absorption coefficient from the P states, α_{P}, is given by

$$\alpha_{\mathrm{P}} = k \, \mathrm{Im} \left(\sum_n \chi_{n\mathrm{P}}^{(1)} \right), \tag{6.1}$$

with

$$\chi_{n\mathrm{P}}^{(1)} = \frac{1}{2\epsilon_0 \eta} \frac{\left| D^{\mathrm{VB} \to n\mathrm{P}} \right|^2}{\delta_{n\mathrm{P}} - i\Gamma_{n\mathrm{P}}}. \tag{6.2}$$

The total absorption coefficient is given by $\alpha = \alpha_{1\mathrm{S}} + \alpha_{\mathrm{P}}$ where $\alpha_{1\mathrm{S}}$ is the contribution to the absorption coefficient from the phonon-assisted background.

The addition of the microwave field adds an additional term, $\Delta\alpha$, to the absorption coefficient, giving $\alpha = \alpha_{1\mathrm{S}} + \alpha_{\mathrm{P}} + \Delta\alpha$. In a similar way to previous works [61; 62] this can be described in terms of a $\chi^{(3)}$ nonlinear susceptibility

$$\Delta\alpha = k \, \mathrm{Im} \left(\sum_{n,n',l',\pm} \chi_{n\mathrm{P}n'l'}^{(3)} \right) \mathcal{E}_{\mathrm{MW}}^2, \tag{6.3}$$

where $\mathcal{E}_{\mathrm{MW}}$ is the effective microwave electric field inside the sample and

$$\begin{aligned} \chi_{n\mathrm{P}n'l'}^{(3)} &= \frac{1}{2\epsilon_0 \eta} \frac{\left| D^{\mathrm{VB} \to n\mathrm{P}} \right|^2 \left| d^{n\mathrm{P} \to n'l'} \right|^2}{(\delta_{n\mathrm{P}} - i\Gamma_{n\mathrm{P}})^2 (\delta_{n'l'}^{\pm} - i\Gamma_{n'l'})} \\ &= \chi_{n\mathrm{P}}^{(1)} \frac{\left| d^{n\mathrm{P} \to n'l'} \right|^2}{(\delta_{n\mathrm{P}} - i\Gamma_{n\mathrm{P}})(\delta_{n'l'}^{\pm} - i\Gamma_{n'l'})}. \end{aligned} \tag{6.4}$$

Here, $\delta_{n'l'}^{\pm} = E_{n'l'} - (E \pm h f_{\mathrm{MW}})$ is the detuning from the $|n', l'\rangle$ state and $d^{n\mathrm{P} \to n'l'}$ is the dipole matrix element given by $d^{n\mathrm{P} \to n'l'} = \langle n', l' | e \cdot \mathbf{r} | n, \mathrm{P} \rangle$ is the dipole matrix element. Note that the plus or minus in the detuning accounts for either absorption or emission of a microwave photon respectively. Both processes must be included as the linewidths of the states involved are comparable to the microwave frequency, hence the rotating-wave approximation cannot be made.

To relate the absorption coefficient to the transmission measured in the experiments, the normalised spectral response of the monochromator, S, must be taken into account. The measured transmission is a convolution of the spectral response function (see section 3.1.3.2) and the underlying spectrum. Taking this into account equation 2.9 becomes

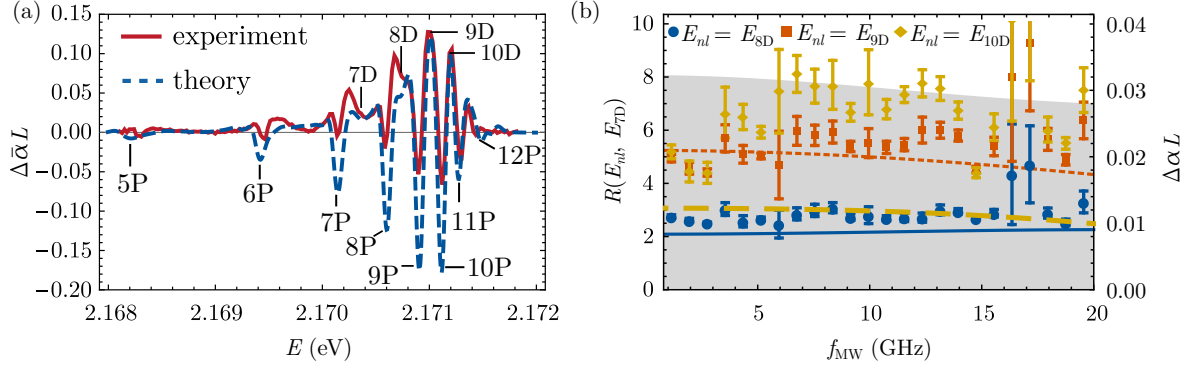$$T = S \star e^{-\alpha L}, \tag{6.5}$$

Figure 6.3: Comparison of the predicted and measured change in absorption due to the microwave field. (a) Change in absorption due to the microwave field, $\Delta\bar{\alpha}L$, as a function of energy, E, at microwave frequency $f_{\mathrm{MW}} = 15.0$ GHz. The range of E spans from the $n = 5$ state up to the band edge. Experimental data is shown as solid red line, and theoretical predictions as dashed blue line for $\mathcal{E}_{\mathrm{MW}} = 400$ V m^{-1}. (b) Predicted change in absorption as a function of f_{MW} (shaded background, right axis) at $E = E_{7\mathrm{D}}$. Also shown are the measured (points) and predicted (lines) ratios $R(E_{nl}, E_{7\mathrm{D}})$ for the 8D (blue circles, solid line) 9D (orange squares, dotted line) and 10D (gold diamonds, dashed line) states.

where $\star$ represents the convolution operator. As can be seen from the experimental results in Fig. 6.1(b), $\alpha_{1\mathrm{S}} \gg \alpha_{\mathrm{P}}, \Delta\alpha$. Taking a Taylor expansion around $\alpha = \alpha_{1\mathrm{S}}$ and assuming that $\alpha_{1\mathrm{S}}$ is constant over the range of E considered gives

$$-\frac{\Delta T}{T_{\mathrm{off}}} \approx (S \star \Delta\alpha)L \equiv \Delta\bar{\alpha}L. \tag{6.6}$$

where the convolved quantity, $\Delta\bar{\alpha}$, has been introduced.

The parameters in equations 6.3, 6.4 and 6.6 can be experimentally measured or theoretically calculated. $\chi_{n\mathrm{P}}^{(1)}$ can be obtained from fitting the transmission spectrum in the absence of the microwave field. Similarly, the energies and widths of the states can be obtained from fitting the one and two-photon spectra in Fig. 4.1 and Fig. 5.6 respectively. S was measured by passing laser light through the monochromator (Fig. 3.7). The matrix elements, $d^{n\mathrm{P}\to n'l'}$, were taken from previous calculations using theoretical exciton wavefunctions [121; 44].

Fig. 6.3(a) shows the predicted $\Delta\bar{\alpha}L$ as a function of E at $f_{\mathrm{MW}} = 15.0$ GHz. Here the effective (unpolarized) electric field strength $\mathcal{E}_{\mathrm{MW}}$ is used as a fitting parameter and found to be 400 ± 100 V m^{-1}. This value is in reasonable agreement with the predicted field inside the sample for antenna A2 of 1200 V m^{-1} (which assumes zero insertion loss and does not take into account polarisation). There is good qualitative agreement

between the model and the experimental data. The major features in the experimental data are reproduced by the model. However, the model overestimates the reduction in absorption seen at the P states.

We note that equation 6.4 is the first term in a series expansion of the nonlinear susceptibility. By neglecting higher order terms in the susceptibility, we are taking a perturbative approach which assumes that the Rabi frequency, $\Omega_{n\mathrm{P}n'l'} = d^{n\mathrm{P}\rightarrow n'l'}\mathcal{E}_{\mathrm{MW}}/\hbar$, is smaller than the linewidth of the state. However, for the 8S→8P transition with an effective field strength of $400\ \mathrm{V\,m^{-1}}$ the effective Rabi frequency is $\Omega_{8\mathrm{P}8\mathrm{S}} = 2\pi \times 9\ \mathrm{GHz}$ and the ratio of the Rabi frequency to the linewidth is $\Omega_{8\mathrm{P}8\mathrm{S}}/\Gamma_{8\mathrm{P}} \approx 0.4$. This ratio increases with n; for the 10P→10D transition we obtain $\Omega_{10\mathrm{P}10\mathrm{D}}/\Gamma_{10\mathrm{D}} \approx 0.9$. These values show that it is possible to achieve a coupling strong enough to match the large non-radiative contribution to Γ even with the simple antenna designs used in this work.

As we are in a regime where $\Omega_{n\mathrm{P}n'l'}$ is comparable to $\Gamma_{n'l'}$, we are reaching the limits of the perturbative approach which may account for some of the discrepancies between experiment and theory in Fig. 6.3(a). Previous work has considered extending the nonlinear susceptibility to higher order terms. For two isolated resonances it was possible to derive a susceptibility which described the light-matter interaction to all orders of the coupling field [185; 62; 63; 64]. However, the summation over many resonances in equation 6.3 means that the extending the model in this way is not possible. Instead, alternative approaches such as Floquet theory could be applied [186; 187].

The microwave frequency dependence predicted by the model at $E = E_{7\mathrm{D}}$ is shown as the shaded background in Fig. 6.3(b). As expected, the response is broadband due to the large number of states that contribute. To compare to experiment, we remove the microwave frequency response of the antenna by taking the ratio of the microwave response at different excitation energies, $R(E_1, E_2) = \Delta\bar{\alpha}(E_1)/\Delta\bar{\alpha}(E_2)$. In Fig. 6.3(b) we show $R(E_{8\mathrm{D}}, E_{7\mathrm{D}})$, $R(E_{9\mathrm{D}}, E_{7\mathrm{D}})$, and $R(E_{10\mathrm{D}}, E_{7\mathrm{D}})$, which is similar for all three states. Furthermore, $R(E_{8\mathrm{D}}, E_{7\mathrm{D}})$ and $R(E_{9\mathrm{D}}, E_{7\mathrm{D}})$ show quantitative agreement between theory and experiment with no free parameters, while $R(E_{10\mathrm{D}}, E_{7\mathrm{D}})$ is underestimated by the theory which we attribute to the likely breakdown of the perturbative approach discussed above.

Here, it was shown that the microwave field can alter one-photon absorption by introducing a coupling between the even- and odd-parity exciton states. A value for the ratio of the Rabi frequency to exciton linewidth was extracted which showed that even

with the simple microwave antenna used it was possible to reach a regime where the Rabi frequency is comparable to the exciton linewidth. However, there are disadvantages to the LED experiment detailed here. The broadband nature of the LED means the spectral resolution of the monochromator becomes a limiting factor in the experiment. Furthermore, the large phonon assisted background observed in one-photon experiments is not coupled to the microwave field meaning that most of the absorption cannot be influenced by the microwave field. In the rest of this chapter we will attempt to address these challenges by adding a microwave field to the two-photon spectroscopy experiments presented in chapter 5.

6.2 Microwave modulation of coherent SHG in Cu$_2$O

In this section the effect of a microwave field on the coherently generated second harmonic is studied. SHG spectroscopy offers several advantages. The second harmonic is coherently generated with an emission spectrum determined by the excitation laser, and is easily separated from the excitation light. In addition, the second harmonic generation spectrum does not exhibit the large phonon-assisted background observed in one-photon absorption spectroscopy [59; 32; 60]. Together these advantages enable us to observe the modulation of an optical carrier by the microwave field. The experiments presented in this section were performed on sample AM using antenna A1.

An energy level diagram of the SHG experiment with a microwave field is shown in Fig. 6.4(a). Two-photon excitation to an even-parity state is achieved through two electric dipole transitions. In the absence of the microwave field, coherent emission can occur from this state through an electric quadrupole process as discussed in section 2.2.3.2. The addition of the microwave field couples the even- and odd-parity states through an electric dipole transition. This leads to the possibility of a four-wave mixing type process occurring and the appearance of two new frequency components in the emission spectrum, at $\pm f_{\mathrm{MW}}$ from the SHG carrier.

6.2.1 Experimental results

Fig. 6.4(b) shows the effect of the microwave field on the SHG excitation spectrum. Here, the microwave field is tuned to $f_{\mathrm{MW}} = 19.5$ GHz and the power set to $P_{\mathrm{MW}} = 25$ mW. Exciton resonances from $n = 7$ to $n = 12$ are shown. The microwave field alters the SHG spectrum throughout the range of excitation energies shown. Some exciton resonances are enhanced while others are suppressed. To highlight this, the fractional change in intensity $\Delta I / I_{\mathrm{off}} = (I_{\mathrm{on}} - I_{\mathrm{off}}) / I_{\mathrm{off}}$ is shown in Fig. 6.4(d). In some regions the fractional change in intensity is greater than 40%.

The microwave frequency dependence of the signal is shown in Fig. 6.4(c). Due to the linewidths of the exciton states involved, the microwave frequency response of the four-wave mixing process is expected to be broadband. However, as shown previously, the frequency dependence is dominated by the response of the antenna. As this data
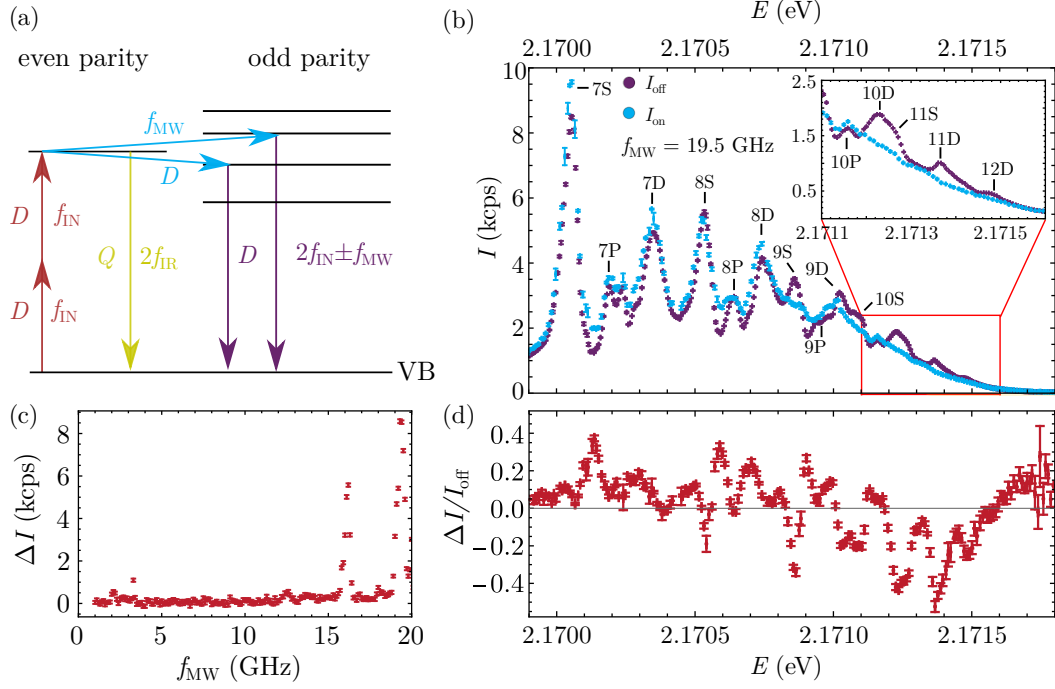
Figure 6.4: Second harmonic generation spectroscopy with a microwave field. (a) Energy level diagram of the SHG experiment with a microwave field. Labels D and Q indicate whether a step is an electric dipole or quadrupole process respectively. (b) SHG excitation spectrum with (blue) and without (purple) a microwave field applied at microwave frequency $f_{MW} = 19.5$ GHz and microwave power $P_{MW} = 25$ mW. (c) Microwave frequency dependence of signal with $E = E_{7S}$ (d) Fractional change in intensity $\Delta I / I_{off} = (I_{on} - I_{off})/I_{off}$ of the excitation spectrum.

was taken using antenna A1, a response is only seen at narrow bands of microwave frequency around 16 and 19 GHz.

6.2.1.1 Spectrally resolved emission

To investigate the effects of the microwave field further, the Fabry-Pérot etalon discussed in section 3.1.3.1 was used to perform high resolution spectroscopy of the SHG. The resulting emission spectra with an without the microwave field at two different excitation energies are shown in Fig. 6.5. When no microwave field is applied, the emission spectrum shows a single frequency component, as would be expected for SHG. The addition of the microwave field sees the appearance of sidebands on the SHG, separated from the SHG carrier by the microwave frequency. We have not observed higher order sidebands. These sidebands are due to the four-wave mixing process depicted in the energy level diagram of Fig. 6.4(a). The width of the sidebands is set by the resolu-

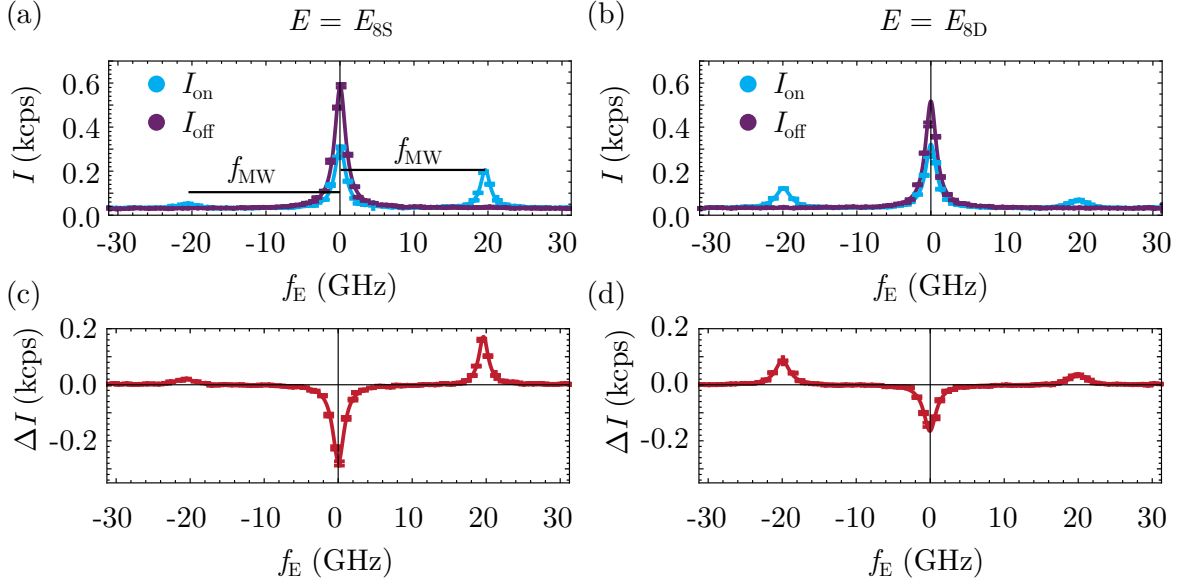Figure 6.5: Spectrally resolved SHG emission with a microwave field. Spectra were taken using the FPE discussed in section 3.1.3.1. Microwave frequency is $f_{\mathrm{MW}} = 19.5$ GHz and microwave power is $P_{\mathrm{MW}} = 25$ mW. (a) Two-photon excitation energy, E, resonant with 8S exciton. (b) Two-photon excitation energy resonant with 8D exciton. (c) Change in intensity due to the microwave field at $E = E_{8\mathrm{S}}$. (d) Change in intensity due to the microwave field at $E = E_{8\mathrm{D}}$.

tion of the FPE, indicating the effect is coherent within our experimental resolution. From looking at the subtracted data (Fig. 6.5(c) and (d)) it is clear the microwave field also reduces the intensity of the SHG carrier peak. Note that the reduction in carrier intensity is not the same as the gain in sideband intensity.

There is a clear dependence of the sideband strength on excitation energy. When the excitation is resonant with an S state (Fig. 6.5(a)), the higher energy (blue) sideband is larger, and when resonant with a D state (Fig. 6.5(b)) the lower energy (red) sideband is larger. The observed asymmetry between the S and D states is a direct consequence of the fact that the nearest odd-parity state to the nS state is the nP state at higher energy, whereas for the nD state it is at lower energy.

The microwave frequency dependence of the blue sideband using antenna A1 is shown in Fig. 6.6. Here, the change in intensity due to the microwave field is plotted as a function of microwave frequency f_{MW} and etalon frequency f_{E}. The excitation laser was two-photon resonant with the 8S exciton. As shown in Fig. 6.5(a), when two-photon resonant with 8S, the blue sideband is significantly larger than the red. In the dataset presented in Fig. 6.6, the red sideband is not visible above the noise and so is not shown. The blue sideband is only visible at microwave frequencies around 16 and
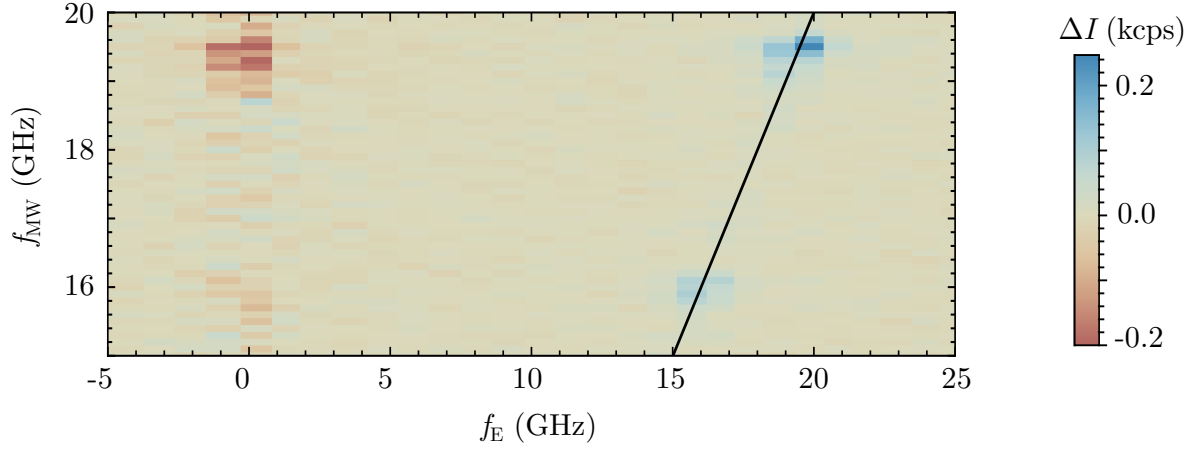
Figure 6.6: Heatmap of the change in intensity due to the microwave field as a function of microwave frequency, f_{MW}, and etalon frequency, f_E. Solid black line shows the $f_E = f_{MW}$ line. The increase in intensity is shown in blue and corresponds to the blue sideband. The blue sideband traces the $f_E = f_{MW}$ line.

19 GHz due to the microwave frequency response of the antenna. As would be expected from the four-wave mixing process, the sideband appears on the $f_E = f_{MW}$ line (shown as a black line in Fig. 6.6). The blue sideband was fitted with a Lorentzian at each microwave frequency. The value of f_E extracted from this fit was plotted against the microwave frequency and fitted with a straight line. The straight line fit gave a gradient of 1.02 ± 0.01, showing the sideband frequency closely follows the microwave frequency.

6.2.1.2 Temporal dependence of microwave response

The response time of the microwave signal is shown in Fig. 6.7. For this experiment, the laser was continuous wave and the microwave pulses were shortened to 100 ns. In Fig. 6.7(b) the normalised intensity of the SHG is plotted against time relative to the microwave pulse trigger. The excitation laser tuned to $E = E_{8S}$, the microwave frequency and power were $f_{MW} = 19.5$ GHz and $P_{MW} = 25$ mW respectively. Also plotted in Fig. 6.7 is the microwave pulse shape. The microwave pulse shape was measured on an oscilloscope using the pulse video output of the microwave generator. As can be seen in Fig. 6.7 the SHG intensity traces out the microwave pulse shape, indicating the response time of the system is at least as fast as the switching time of the microwave source. This fast response time is a direct consequence of the large linewidth of the exciton states. The large exciton linewidth leads to a short exiton lifetime, and the response time of the system will be set by the exciton lifetime.
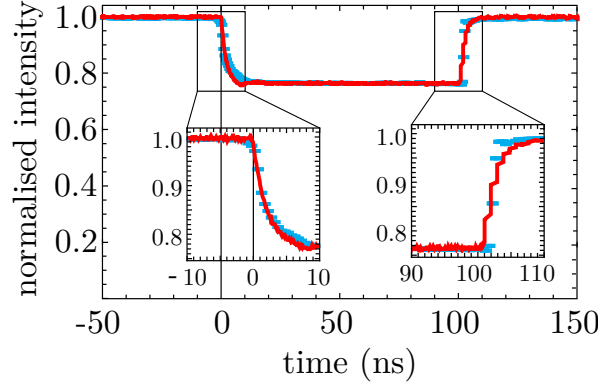
Figure 6.7: Time dependence of microwave response compared with turn on and off times of microwave pulse. Normalised SHG intensity as a function of time relative to the microwave pulse trigger. Data taken with two-photon excitation energy, $E = E_{8S}$, $f_{MW} = 19.5$ GHz and $P_{MW} = 25$ mW. The microwave field causes a decrease in the intensity of the light detected (blue data). The red curve shows the microwave pulse shape as measured on an oscilloscope. Insets show zoom of the turn on and turn off times.

6.2.2 Theory

In this section we present a theoretical model to describe the microwave modulation of the coherent second harmonic presented in section 6.2.1. The model is based on the exciton-polariton description of light-matter coupling and is an extension of the nonlinear susceptibility models used in the previous section. The derivation of the model will not be presented here, details are available in [77]. Here, we will only consider two-photon excitation to S and D states.

The form of the nonlinear susceptibility describing the SHG process on even-parity exciton states is discussed in section 2.3.1.3. The intensity of the SHG without the microwave field is given by

$$
\begin{aligned}
I_{\text{off}} &= A I_{\text{IN}}^2 \left| \sum_{n,l=\text{S},\text{D}} \frac{1}{\epsilon_0 \hbar} \frac{Q^{nl \to \text{VB}} M^{\text{VB} \to nl}}{\delta_{nl} - i\Gamma_{nl}} \right|^2, \\
&= A I_{\text{IN}}^2 \left| \sum_{n,l=\text{S},\text{D}} \chi_{nl}^{(2)} \right|^2.
\end{aligned}
\tag{6.7}
$$

The first two steps of the four-wave mixing process involving the microwave field are the same as the SHG process and can be described by the same effective matrix element,

M. The microwave field introduces an electric dipole coupling to odd-parity Rydberg states $|n', l'\rangle$ which results in an additional electric dipole-allowed emission process. This leads to the generation of sidebands on the SHG signal. Again, we note that the large linewidth of the exciton resonances compared to their separation means that the conventional near-resonant rotating-wave approximation cannot be made and all dipole-allowed transitions must be considered.

The intensity of the sidebands, I_{SB}, can be described by

$$I_{\text{SB}}^{\pm} = A I_{\text{IN}}^2 \left| \sum_{n,l=\text{S,D}} \sum_{n'l'} \frac{1}{\epsilon_0} \frac{D^{n'l'\to\text{VB}} \hbar \Omega_{nln'l'} M^{\text{VB}\to nl}}{(\delta_{nl} - i\Gamma_{nl})(\delta_{n'l'}^{\pm} - i\Gamma_{n'l'}) - i\hbar^2 \Omega_{nln'l'}^2 \left(1 + \frac{\delta_{n'l'}^{\pm} - i\Gamma_{n'l'}}{\delta_{n'l'}^{\mp} - i\Gamma_{n'l'}}\right)} \right|^2,$$
(6.8)

where the $\pm$ corresponds to the blue and red sidebands respectively. Note that in the low field microwave field limit, where $\Omega_{nln'l'} < \Gamma_{nl}$ the second term on the denominator of equation 6.8 is negligible. In this limit the intensity of the sidebands can be written as

$$I_{\text{SB}}^{\pm} = A I_{\text{IN}}^2 \left| \sum_{n,l=\text{S,D}} \sum_{n'l'} \frac{1}{\epsilon_0} \frac{D^{n'l'\to\text{VB}} \hbar \Omega_{nln'l'} M^{\text{VB}\to nl}}{(\delta_{nl} - i\Gamma_{nl})(\delta_{n'l'}^{\pm} - i\Gamma_{n'l'})} \right|^2,$$
(6.9)

which is of a similar form to the susceptibilities used to describe the change in one-photon absorption in section 6.1.2.

As can be seen in Fig. 6.5(c) and (d) the intensity of the carrier peak is also altered by the presence of the microwave field. The intensity of the carrier peak when the microwave field is on, I_{CAR}, is given by

$$I_{\text{CAR}} = A I_{\text{IN}}^2 \left| \sum_{n,l=\text{S,D}} \sum_{n'l'} \frac{1}{\epsilon_0} \frac{Q^{nl\to\text{VB}} M^{\text{VB}\to nl}}{h(\delta_{nl} - i\Gamma_{nl}) + \hbar^2 \Omega_{nln'l'}^2 \left(\frac{1}{\delta_{n'l'}^{-} - i\Gamma_{n'l'}} + \frac{1}{\delta_{n'l'}^{+} - i\Gamma_{n'l'}}\right)} \right|^2.$$
(6.10)

The change in carrier intensity, ΔI_{CAR} due to the microwave field is given by

$$\Delta I_{\text{CAR}} = I_{\text{CAR}} - I_{\text{off}}.$$
(6.11)

For comparison to experiment, the spectrally resolved SHG emission with a microwave field (examples shown in Fig. 6.5) were fitted using Lorentzian lineshapes with a width
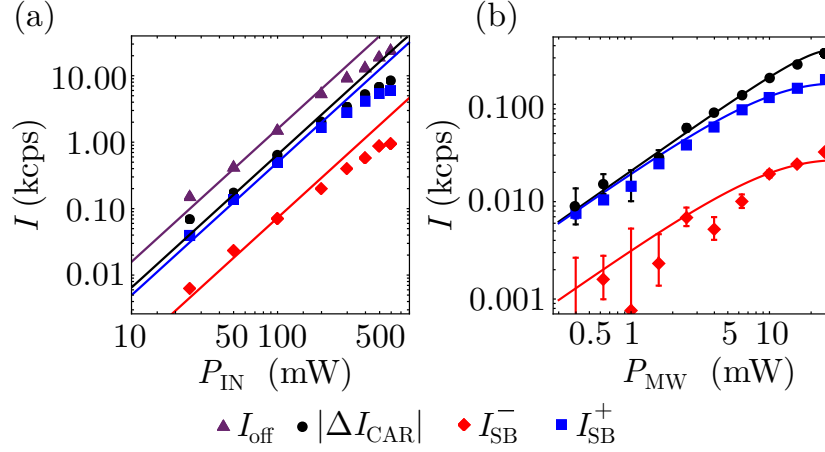
Figure 6.8: Power dependencies of sideband and carrier amplitudes. (a) Laser power, P_{IN} dependency of SHG (triangles), magnitude of carrier depletion (circles), blue sideband (squares) and red sideband (diamonds) at microwave power $P_{MW} = 25$mW and $E = E_{8S}$. Diagonal lines show quadratic dependencies on P_{IN}. (b) Microwave power dependencies of the magnitude of carrier depletion (circles), blue sideband (squares) and red sideband (diamonds) at $P_{IN} = 50$ mW and $E = E_{8S}$. Solid lines show predicted power dependencies from equations 6.8 and 6.10.

fixed to the width of the etalon response function. The matrix elements M were determined from the Lorentzian fit to the SHG excitation spectra in section 5.3.1.1. All of the other parameters are measured or calculated in the same way as in previous sections. The only remaining parameter is an overall amplitude which is equivalent to the parameter A in equations 6.8 and 6.10.

6.2.2.1 Testing the model

The dependencies of the carrier and sideband amplitudes on the microwave, P_{MW}, and laser, P_{IN}, power are predicted by equations 6.7, 6.8 and 6.11 as $P_{IN} \propto I_{IN}$ and $P_{MW} \propto \sqrt{\Omega_{nln'l'}}$. As is expected for SHG, I_{off} has a quadratic dependence on P_{IN} and this is maintained for I_{SB} and ΔI_{CAR}. At low microwave powers, the dependence of I_{SB} and ΔI_{CAR} on P_{MW} is linear. However, as the microwave power increases and $|\Omega_{nln'l'}|^2$ becomes comparable to $\Gamma_{nl}\Gamma_{n'l'}$ this is no longer true, and saturation will occur.

The experimentally measured excitation power dependence of the sidebands and carrier are shown in Fig. 6.8(a). Here $E = E_{8S}$ and $f_{MW} = 19.5$ GHz. All four features show a quadratic dependence on P_{IN} at low powers before deviating from this at about 200 mW. The deviation from the quadratic dependence appears to occur at the same value of P_{IN} for all of the features. We attribute this deviation to effects such as localised heating
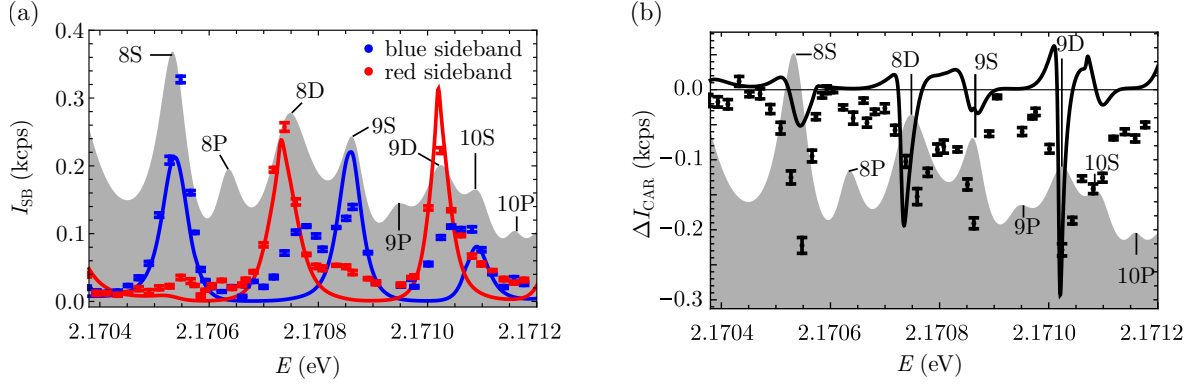
Figure 6.9: Dependence of sideband and carrier amplitudes on two-photon excitation energy, E. (a) Theory curve (solid) from equation 6.8 and experimental data (points) showing the intensity of the blue and red sidebands at microwave frequency $f_{MW} = 19$ GHz and microwave power $P_{MW} = 3$ mW as a function of E. (b) Theory curve (solid) from equation 6.11 and experimental data (points) showing change in carrier intensity at $f_{MW} = 19$ GHz and $P_{MW} = 3$ mW as a function of E. The shaded backgrounds is the fit to the SHG excitation spectrum to show the range of exciton states explored.

which are not included in the model. The heating of the sample under two-photon excitation is discussed in section 5.3.1.3.

Fig. 6.8(b) shows the dependence on P_{MW}. The dependence on P_{MW} is linear at low microwave powers and shows some saturation at the highest microwave powers as predicted by equations 6.8 and 6.10. The power dependencies in Fig. 6.8(b) can be fitted using equations 6.8 and 6.10. For this fit, a free parameter B is introduced which relates the power produced by the microwave generator to the effective field in the sample by $P_{IN} = B|\mathcal{E}_{MW}|^2$. The parameter B accounts for the efficiency of the antenna, the dielectric screening, and any losses in the feedthroughs to the cryostation. B is a shared parameter between the fits for all three features. The fitted curves are shown in Fig. 6.8(b). For a single value of B, a good fit is achieved for all three features. At the maximum input power ($P_{MW} = 25$ mW) the effective field in the sample was found to be 200 ± 50 V m^{-1} which gives $\Omega_{8S8P}/\Gamma_{8S} \approx 0.3$.

As was shown in section 6.2.1.1, the sideband intensity has a clear dependence on the two-photon excitation energy. An asymmetry was observed: when two-photon resonant with an S state the blue sideband is larger, whereas the opposite is true when resonant with a D state. As discussed, this is due to whether the nearest odd-parity state is at higher or lower energy to the initial state. This dependence can be seen explicitly in equation 6.8 where it arises from the relative sizes of the positive and negative detunings, $\delta_{n'l'}^{\pm}$ in the $(\delta_{n'l'}^{\pm} - i\Gamma_{n'l'})$ term.
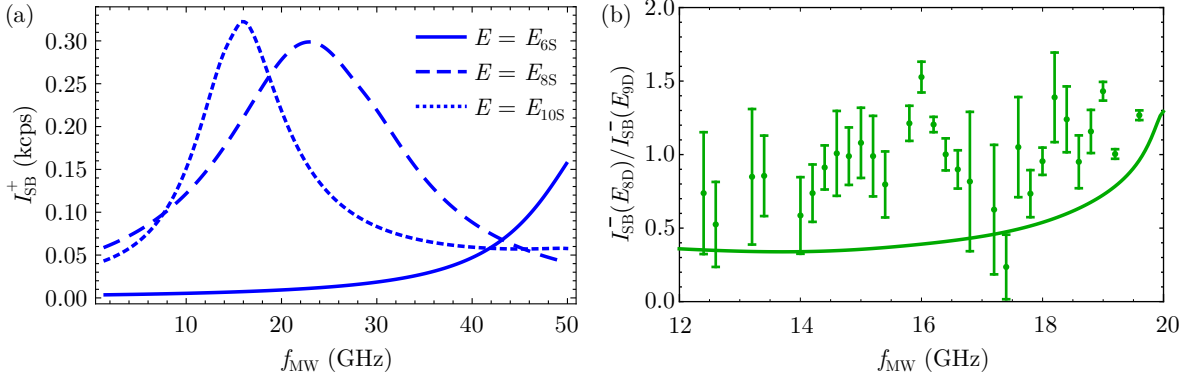
Figure 6.10: Microwave frequency dependence of sideband intensities. (a) Predicted microwave frequency dependence of blue sideband intensity. Excitation energies resonant with three different states are plotted, $E = E_{6S}$ (solid), $E = E_{8S}$ (dashed), $E = E_{10S}$ (dotted). (b) Ratio of red sideband intensity at two excitation energies ($E = E_{8D}$ and $E = E_{9D}$) as function of microwave frequency. Solid line shows predictions from equation 6.8 with $\mathcal{E}_{MW} = 200$ V m^{-1}. Points are experimentally measured.

The predicted sideband intensity as a function of E along with experimentally measured values is shown in Fig. 6.9(a). Here, the microwave power is set to $P_{MW} = 3$ mW and the microwave frequency is 19.0 GHz. The only fit parameter is the an overall amplitude scaling, which is constrained to be the same for both the red and blue sidebands. Similarly, the carrier depletion as a function of E is shown in Fig. 6.9(b). Note that a different scaling factor is used for the carrier depletion curve. The shaded backgrounds in Fig. 6.9 show the range of Rydberg states covered in this range of E. Overall, the model provides good agreement over the full range of E considered here. Given the complexity of the experiment this agreement demonstrates that the model, which is based on an atomic picture of the exciton, provides a solid basis for understanding the observed microwave-exciton coupling. However, there are regions of E where the agreement is less good. There are additional features in the sideband intensity (Fig. 6.9(a)) which are not reproduced by the model, the most obvious of these appear around the 8D state for the blue sideband and around the 9S state for the red sideband. This would imply the model is lacking some of the relevant states. The model includes S, P, D and F states. As discussed in section 2.2.2 there are multiple other states (e.g D states of Γ_1^+ and Γ_3^+ symmetry or P states of Γ_7^- symmetry) which are not currently included in the model. We also note that the model predicts regions of E where the carrier is enhanced, whereas the model only predicts a suppression in carrier intensity.

As stated previously, the microwave frequency dependence of the signal at a fixed ex-

citation energy is broadband, due to the linewidths of the exciton states involved. In Fig. 6.10(a) the predicted blue sideband intensity as a function of f_{MW} with E resonant with three different exciton states is shown, highlighting the broadband response. The peak sideband intensity shifts to lower frequency when the two-photon excitation energy is resonant with higher lying states. This is a consequence of the spacing between the Rydberg states decreasing with principal quantum number. The experimentally measured microwave frequency dependence was dominated by the antenna response. To account for this the ratio of the response at two different states is taken. The ratio of the red sideband intensity at $E = E_{8D}$ to $E = E_{9D}$ as a function of microwave frequency is shown in Fig. 6.10(b). The model underestimates the ratio. However, it predicts the observed trend that the ratio increases as we approach higher f_{MW}. Note that the ratio of the red sideband at 8D to 9D is also underestimated by the model in Fig. 6.9(a).

Overall, the model presented in the section is in good agreement with the experimental data. The microwave power dependence of the sidebands and carrier was successfully predicted, along with the excitation energy dependence of the sidebands. In future, experiments increasing the microwave field strength would be interesting. Higher microwave field strengths would allow the strong coupling regime (where $\Omega > \Gamma$) to be reached. Currently, $\Omega/\Gamma \approx 0.3$ and increasing the field strength by more than factor of 10 should be easily achievable with a microwave resonator. In this regime, multiphoton effects, such as higher order sidebands may be observed, and the model will have to be extended to include these processes.

6.2.3   Polarisation dependence

In this section, we extend the model presented in section 5.3.2 to include the effect of the microwave field. Here we will consider the four-wave mixing process which leads to the appearance of sidebands on the second harmonic observed in section 6.2.1. The case where an even-parity (S or D state) of Γ_5^+ symmetry is coupled through an electric-dipole transition to a P state of Γ_8^- symmetry is studied. A schematic of the energy level diagram with the symmetries of the transitions and states is shown in Fig. 6.11(a).

To describe the process we recall from section 5.3.2 the operator describing two photon
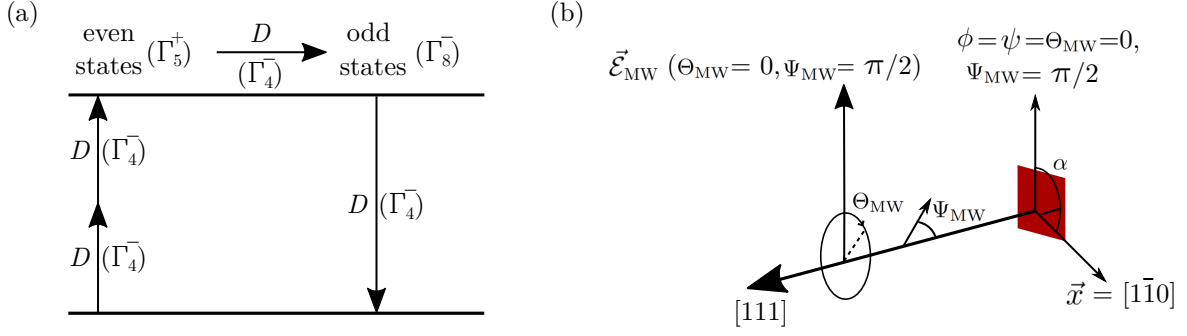
(a)

(b)

Figure 6.11: (a) Schematic energy level diagram of the sideband generation process due to a microwave field. Two electric dipole transitions of Γ_4^- symmetry excite an even-parity state of Γ_5^+ symmetry. The microwave field drives an electric dipole transition (Γ_4^- symmetry) to an odd-parity state (Γ_8^-). Emission from the odd-parity state occurs through an electric dipole transition (Γ_4^-). (b) Diagram showing the angle of the microwave electric field relative to the other angles in the system. sample is shown as red square. The microwave electric field direction is defined by an azimuthal angle, Θ_{MW}, and an inclination angle Ψ_{MW}. The azimuthal angle rotates the microwave electric field in the (111) crystal plane (when $\Psi_{\mathrm{MW}} = \pi/2$). The inclination angle is the angle of the microwave electric field relative to the [111] vector. Note that $\Theta_{\mathrm{MW}} = 0$ is defined to be the same as $\phi = \psi = 0$ and so the offset angle α muct again be taken into account.

absorption to a state of Γ_5^+ symmetry is given by

$$O_{\mathrm{TPA}}(\phi) = \sqrt{2} \begin{pmatrix} v(\phi)w(\phi) \\ u(\phi)w(\phi) \\ u(\phi)v(\phi) \end{pmatrix}. \tag{6.12}$$

To describe the electric dipole coupling between the even- and odd-parity states we introduce the microwave electric field vector in the laboratory frame as

$$\vec{\mathcal{E}}_{\mathrm{MW}} = \mathcal{E}_{\mathrm{MW}} \begin{pmatrix} \cos\Theta_{\mathrm{MW}} \sin\Psi_{\mathrm{MW}} \\ \sin\Theta_{\mathrm{MW}} \sin\Psi_{\mathrm{MW}} \\ \cos\Psi_{\mathrm{MW}} \end{pmatrix}, \tag{6.13}$$

where Θ_{MW} is the azimuthal angle of the microwave field and Ψ_{MW} is the inclination angle. It is defined such that when $\Psi_{\mathrm{MW}} = \pi/2$ it is in the same plane as $\vec{\mathcal{E}}_{\mathrm{SHG}}$ and $\vec{\mathcal{E}}_{\mathrm{IN}}$. Transformation into the crystal coordinates is done using the same transformation matrix, $\mathbf{T}(\vec{k}, \vec{x}, \vec{y})$, from equation 5.10. Note that $\vec{k}$ here corresponds to the k vector of the excitation light which is used to a define a direction in the new coordinate system. It is not the k vector of the microwave field, as we are in the near field of the microwave antenna. Once transformed into the crystal coordinates the microwave field is given

by

$$\vec{\mathcal{E}}_{\text{MW}} = \mathcal{E}_{\text{MW}} \begin{pmatrix} a(\Theta_{\text{MW}}, \Psi_{\text{MW}}) \\ b(\Theta_{\text{MW}}, \Psi_{\text{MW}}) \\ c(\Theta_{\text{MW}}, \Psi_{\text{MW}}) \end{pmatrix}. \tag{6.14}$$

The operator describing an electric dipole transition is proportional to the electric field vector [143], and so is

$$O_{\text{MW}} = \begin{pmatrix} a(\Theta_{\text{MW}}, \Psi_{\text{MW}}) \\ b(\Theta_{\text{MW}}, \Psi_{\text{MW}}) \\ c(\Theta_{\text{MW}}W, \Psi_{\text{MW}}) \end{pmatrix}. \tag{6.15}$$

Combining the operators for the two-photon absorption (O_{TPA}) and the microwave transition (O_{MW}) through symmetrical cross product (see section 5.3.2) gives:

$$O_{\text{TPA+MW}} = \begin{pmatrix} b(\Theta_{\text{MW}}, \Psi_{\text{MW}})u(\phi)v(\phi) + c(\Theta_{\text{MW}}, \Psi_{\text{MW}})u(\phi)w(\phi) \\ a(\Theta_{\text{MW}}, \Psi_{\text{MW}})u(\phi)v(\phi) + c(\Theta_{\text{MW}}, \Psi_{\text{MW}})v(\phi)w(\phi) \\ a(\Theta_{\text{MW}}, \Psi_{\text{MW}})\,u(\phi)w(\phi) + b(\Theta_{\text{MW}}, \Psi_{\text{MW}})v(\phi)w(\phi) \end{pmatrix}. \tag{6.16}$$

Emission from the P state occurs through an electric dipole process, so in this case the emission operator is given by:

$$O_{\text{EMS}} = \begin{pmatrix} m(\psi) \\ n(\psi) \\ o(\psi) \end{pmatrix}. \tag{6.17}$$

Again, the product of the excitation and emission operators squared gives us the intensity,

$$I_{\text{SB}}(\Theta_{\text{MW}}, \Psi_{\text{MW}}, \phi, \psi) \propto |O_{\text{TPA+MW}}(\Theta_{\text{MW}}, \Psi_{\text{MW}}, \phi)O_{\text{EMS}}(\psi)|^2. \tag{6.18}$$

The above equations are valid for any general orientation of the microwave field. Simulations performed of the electric field produced by microwave antenna A1 (details in section 3.3.1) showed that the microwave electric field was predominately in the plane of the microwave antenna (x-y plane, the same as the plane of the sample). Depending on the simulation method and microwave frequency the microwave electric field component squared in the direction normal to this plane (z direction) was between 3 and 15% of the total field strength squared for antenna A1.

As was seen in section 5.3.2.2 there is significant birefringence on both the excitation and emission beam paths. We account for this in the same way as previously, using
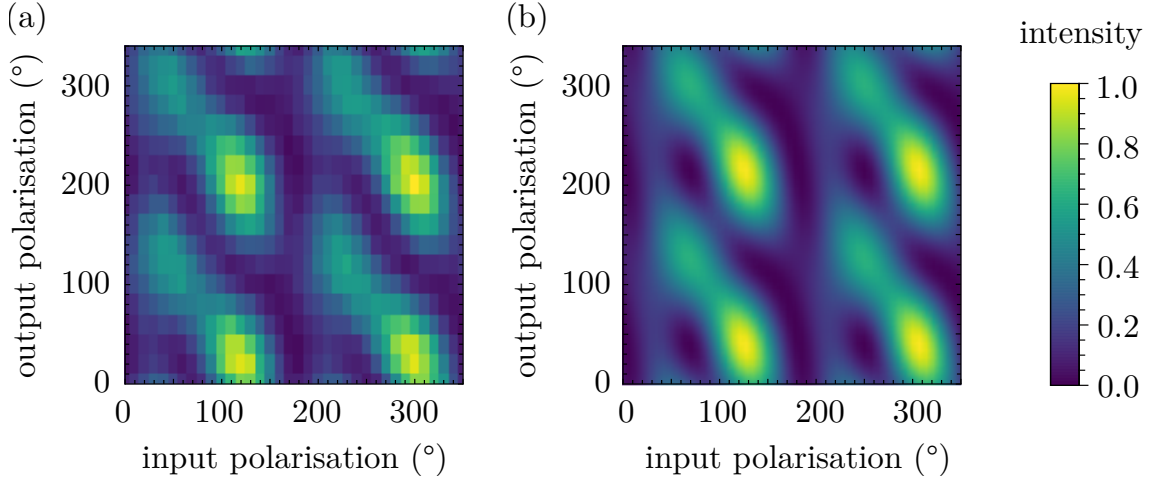
Figure 6.12: Dependence of blue sideband intensity on input and output optical polarisation. (a) Experimentally measured optical polarisation dependence of blue sideband intensity. Here, $E = E_{8S}$, $f_{MW} = 19$ GHz and $P_{MW} = 25$ mW (b) Predicted polarisation dependence of sideband intensity. The microwave electric field direction is taken as a free parameter and is fitted to give $\Theta_{MW} = 185 \pm 5°$ and $\Psi_{MW} = 80 \pm 5°$ for the azimuthal and inclination angles.

a Jones matrix approach to modify $\vec{\mathcal{E}}_{IN}$ and $\vec{\mathcal{E}}_{SHG}$. The fitted values of $\zeta = 60 \pm 10°$, $\theta = 65 \pm 5°$ and $\alpha = 80 \pm 5°$ from section 5.3.2.2 are used. This leaves two undetermined parameters, the azimuthal (Θ_{MW}) and inclination (Ψ_{MW}) angles of the microwave electric field, which are used as fitting parameters when compared to the experimental data.

The experimental polarisation dependence of the sidebands was measured using the same setup as in section 5.3.2. Shown in Fig. 6.12(a) is the experimentally measured polarisation dependence of the blue sideband at $E = E_{8S}$, $f_{MW} = 19$ GHz and $P_{MW} = 25$ mW. Both the red and blue sidebands were found to have the same polarisation dependence. Fig. 6.12(b) shows the modelled polarisation dependence of the sideband intensity. Θ_{MW} and Ψ_{MW} were found to be $185 \pm 5°$ and $80 \pm 5°$. There is excellent agreement between the theory and model, showing the potential of this method to determine the direction of the microwave electric field. The fitted values for the angles of the microwave electric field mean that 5% of the total field strength squared is in the z direction which is in good agreement with the simulations of the microwave field strength.

In this section, microwave modulation of the coherently generated second harmonic was studied. The microwave field was found to produce sidebands on the second harmonic, which appear coherent within the resolution limit of the experiment (set by the

FPE). A model was presented which successfully predicted the microwave power and excitation energy dependence of the sidebands. The optical polarisation dependence of the sidebands was also studied, and found to be in excellent a agreement with a model based on polarisation selection rules. this model allowed the direction of the microwave field vector to be extracted. In the final section of the chapter, the microwave effect on the PL emitted under two-photon excitation will be studied.

6.3 Two-photon photoluminescence spectroscopy with a microwave field.

As discussed in chapter 5, second harmonic generation is not the only emission pathway under two-photon excitation; PL is also emitted. In this section, preliminary results on the microwave field induced changes to the PL excitation spectrum is studied. The PL regime provides a complementary signal to the SHG regime, and may be of interest for future experiments. The results are modelled using a nonlinear susceptibility with a similar form to the one used in section 6.1.2. The microwave field was applied using antenna A1. Results presented here were taken on sample AB which was orientated such that the surface was parallel with the (001) plane.

An energy level diagram for the experiment is shown in Fig. 6.13(a). A two-photon excitation excites excitons in the even-parity state, $|n, l\rangle$. A microwave field couples the state $|n, l\rangle$ with the odd-parity states, $|n', l'\rangle$ through electric dipole transitions. All of the Rydberg states can decay nonradiatively to the emitting state, which for sample AB was found to be predominantly bound exciton states, though in a higher quality sample would be the 1S exciton (see section 4.2). The resulting photoluminescence from the emitting state is collected on the SPAD.

6.3.1 Experimental results

The excitation spectrum from the $n = 9$ to $n = 11$ states with and without a microwave field at $f_{\mathrm{MW}} = 19.0$ GHz is shown in Fig. 6.13(b). The microwave field causes a reduction in intensity when the two-photon excitation is resonant with the S and D states and an enhancement on the high energy side of the D states. In Fig. 6.13(c) the fractional change in intensity $(\Delta I / I_{\mathrm{off}} = (I_{\mathrm{on}} - I_{\mathrm{off}})/I_{\mathrm{off}})$ is plotted, showing the enhancements in intensity can be as high as 8%. In the I_{off} data, the $n = 11$ states are hard to resolve, however when looking a the fractional change, they are clearly altered by the microwave field.

The spectrum in Fig. 6.13(c) is notably different from the equivalent spectrum in the SHG regime (Fig. 6.4(d)). In the SHG spectrum, only a reduction in SHG intensity is observed around the $n = 9$ to $n = 11$ resonances. Whereas in the PL regime enhancements are observed between the nD and $(n + 1)$S resonances. This different
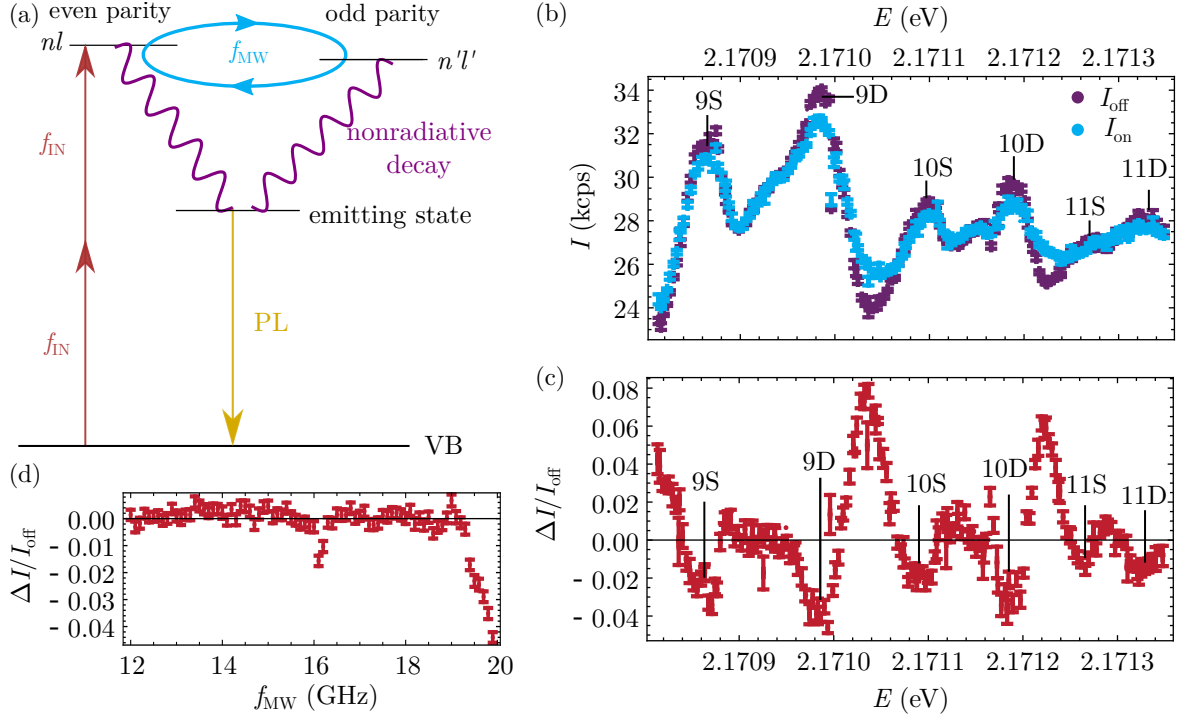
Figure 6.13: Two-photon PLE spectroscopy with a microwave field. (a) Energy level diagram of the experiment. A two-photon excitation creates even-parity Rydberg excitons. A microwave field introduces a coupling between the even- and odd-parity exciton states. Rydberg excitons decay nonradiatively to the emitting state, which for sample AB was bound excitons states (see section 4.2). The PL from the emitting state is filtered from the excitation light and collected on the SPAD. (b) Excitation spectrum with (blue) and without (purple) a microwave field at 19.0 GHz covering the $n = 9$ to $n = 11$ resonances. Intensity of PL is reduced when on resonant with an S or D exciton and enhanced between the nD and $(n+1)$S resonances. (c) Fractional change in the excitation spectrum due to the microwave field. (d) Microwave frequency dependence of the fractional change in intensity at $E = E_{9D}$.

microwave response highlights the importance of studying the effect of a microwave field in both the coherent SHG and the incoherent PL regimes.

The microwave frequency dependence of the signal is shown in Fig. 6.13(d). As previously discussed the microwave frequency dependence is expected to be broadband due to the linewidth of the exciton states. However, the response is dominated by the antenna, giving resonances around 16 and 20 GHz.

6.3.2 Theory

To describe the observed exciton-microwave coupling in section 6.3 a similar approach to section 6.1.2 using a nonlinear susceptibility is used. Here, we assume the microwave-exciton coupling occurs through electric dipole transitions between Rydberg states, the possibility of microwave coupling to the bound exciton states in discussed in Appendix A. There are two ways the microwave field can have an impact on the intensity of the two-photon PL. The first is that the microwave field alters the two-photon absorption, the second is that the microwave field alters the rate the Rydberg excitons decay to the 1S exciton. The model presented in this section assumes only the former process occurs. This assumption is reasonable as the linewidths of neighbouring exciton states are similar.

The nonlinear susceptibility describing two-photon absorption involving even parity exciton resonances is given in section 2.3.1.2. Two-photon absorption is described by a third order susceptibility, χ_{nl}^{TPA}. From section 2.3.1.2, the two-photon absorption coefficient on the S and D resonances is given by

$$\alpha_{\mathrm{TPA}} = k \, \mathrm{Im} \left(\sum_{n,l=\mathrm{S,D}} \chi_{nl}^{\mathrm{TPA}} \right) \mathcal{E}_{\mathrm{IN}}^2 = \mathrm{Im} \left(\sum_{n,l=\mathrm{S,D}} \frac{1}{2\epsilon_0 \eta} \frac{\left| M^{\mathrm{VB} \to nl} \right|^2}{\delta_{nl} - i\Gamma_{nl}} \right) \mathcal{E}_{\mathrm{IN}}^2. \tag{6.19}$$

Following a similar approach to section 6.1.2 the influence on the electric field can be modelled as a higher order nonlinear susceptibility, in this case a $\chi^{(5)}$

$$
\begin{aligned}
\chi_{nln'l'}^{(5)} &= \frac{1}{2\epsilon_0 \eta} \frac{\left| M^{\mathrm{VB} \to nl} \right|^2 \left| d^{nl \to n'l'} \right|^2}{(\delta_{nl} - i\Gamma_{nl})^2 (\delta_{n'l'}^{\pm} - i\Gamma_{n'l'})} \\
&= \chi_{nl}^{\mathrm{TPA}} \frac{\left| d^{nl \to n'l'} \right|^2}{(\delta_{nl} - i\Gamma_{nl})(\delta_{n'l'}^{\pm} - i\Gamma_{n'l'})}.
\end{aligned}
\tag{6.20}
$$

Assuming that the change in absorption is proportional to the experimentally observed change in intensity, ΔI, we obtain

$$\Delta I \propto \mathrm{Im} \left(\sum_{n,l,n',l',\pm} \chi_{nln'l'}^{(5)} \right) \mathcal{E}_{\mathrm{IN}}^4 \mathcal{E}_{\mathrm{MW}}^2. \tag{6.21}$$

As in previous cases, the rotating-wave approximation cannot be made and all dipole-allowed transitions must be taken into account. The parameters in equations 6.19 to 6.20 are measured or calculated using the same methods as in previous sections.
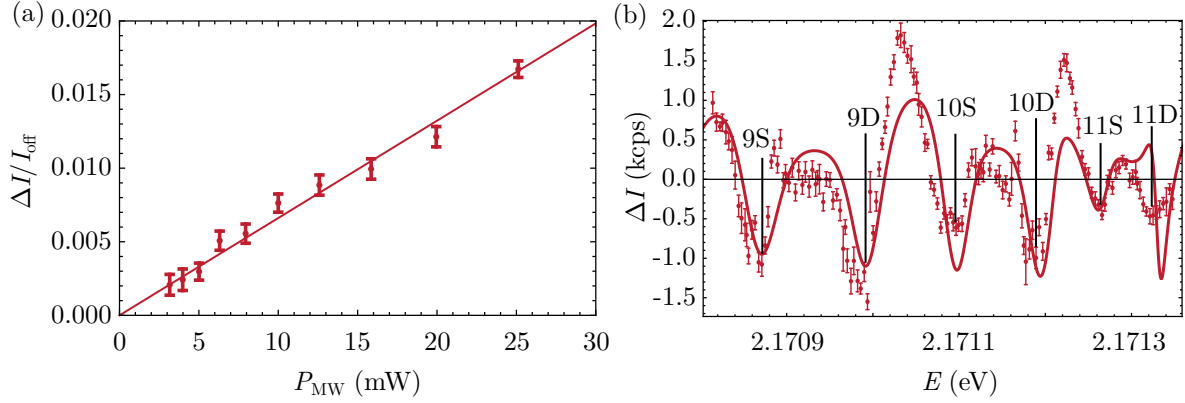
Figure 6.14: Comparison of the predicted and measured change in two-photon photoluminescence due to the microwave field. (a) Microwave power dependence change in two-photon excitation PL intensity due to a microwave field. Here, $f_{\mathrm{MW}} = 16.1$ GHz and $E = 2.17105$ eV. Solid line shows linear fit to the data. (b) Comparison of predicted and experimentally measured change in intensity due to the microwave field against excitation energy at $f_{\mathrm{MW}} = 19.0$ GHz. Solid line shows the predicted ΔI according to equations 6.20 and 6.21, there is one free parameter in the model which is an amplitude scaling factor.

From equation 6.21 the change in PLE intensity due to the microwave field, ΔI is predicted to have a linear dependence on microwave power, as $P_{\mathrm{MW}} \propto \mathcal{E}_{\mathrm{MW}}^2$. To experimentally investigate the microwave power dependence of the change in intensity due to the microwave field, the microwave power was varied from 3 to 25 mW. The excitation energy was fixed to $E = 2.17105$ eV and the microwave frequency was set to $f_{\mathrm{MW}} = 16.1$ GHz. The resulting data is shown in Fig. 6.14(a). The change in intensity shows the predicted linear dependence on microwave power. The solid line shows a linear fit to the data which is constrained to go through the origin.

As shown in Fig. 6.13 the sign and magnitude of ΔI depends on the excitation energy. The experimentally measured and predicted dependence of ΔI on E is shown in Fig. 6.14(b) at $f_{\mathrm{MW}} = 19.0$ GHz. Here, there is one free parameter which is the amplitude scaling of the theory curve. There is good agreement between the experiment and theory curves, especially for the decrease in intensity.

As in the one-photon case in section 6.1.2, the discrepancies between the model and experiment could be due to the neglecting of higher order terms in the susceptibility. Another possibility is that some exciton states which should have been included in the model were neglected. For example, the P states are visible in the PLE spectrum in Fig. 5.4 but optical excitation to these states is not included in the model.

In this section we have shown preliminary results that the addition of a microwave field can alter the intensity of PL under two-photon excitation. We constructed a model to explain the change in PL intensity based on electric-dipole transitions between the Rydberg exciton states. The model showed good qualitative agreement between the theory and experiment, indicating it is a good description of the underlying process. In future, studying the effect of a microwave field on the PLE spectrum will provide a complementary tool to the SHG spectroscopy which was studied in detail in section 6.2. The PL regime may also be useful for future experiments involving photon statistics, potentially allowing microwave induced resonant dipole-dipole interactions to be observed.

6.4   Summary and outlook

In this chapter the coupling of Rydberg excitons and a microwave electric field was observed for the first time. The coupling was studied using both one and two-photon excitation schemes. In both cases an "atomic physics" view of the process, based on electric dipole transitions between excitonic states of opposite parity, provided a convincing explanation of the observed results. The dominant contribution of the crystalline environment was found to be the broadening of the excitonic states due to phononic decay channels which led to a broadband microwave frequency response. Another effect of the solid-state environment was the dielectric screening of the material. The dielectric screening reduces the binding energy of the excitons which leads to a higher dipole moment. However, this effect is cancelled by the dielectric screening of the microwave electric field, leading to similar Rabi frequencies to atomic systems at the same principal quantum number, n.

The one-photon transmission measurements show that the microwave field has a sizeable effect on the optical properties. Even with our inefficient microwave antennae, we achieved a coupling parameter Ω/Γ of 0.9. Reaching the strong-driving limit ($\Omega/\Gamma > 1$) should be straightforward with experimental improvements such as, using a microwave amplifier or a copper coplanar resonator [25]. In this limit, we anticipate that the physics will change significantly. New effects could include microwave-induced dipole-dipole interactions [188; 189; 76], which could potentially be stronger and longer range ($\propto R^{-3}$) [190] than the van der Waals interactions so far observed in Cu_2O ($\propto R^{-6}$) [44; 45]. Multi-photon processes, such as the appearance of higher order sidebands on the second harmonic, will also play a significant role, and a new model will be required. Furthermore, the higher microwave field strengths may lead to ionisation of the exciton states. As the exciton linewidths are comparable to the separation between the exciton states, reaching the strong driving limit also implies a new regime where the Rabi frequency is comparable to the transition frequency between adjacent dipole-coupled states. In this regime approaches such as Floquet theory could be useful in describing the observed effects [186; 187].

While higher microwave fields strengths are an obvious way to reach the strong coupling regime, another method would be to go to higher n states, where the nonradiative broadening of the exciton linewidth is smaller. For the two-photon experiments presented here this may be experimentally challenging. However, it is possible to reach up to $n = 17$ in one-photon laser spectroscopy (Fig. 5.10). Combining one-photon laser

spectroscopy and microwave fields provides another interesting direction for future experiments.

The SHG measurements clearly demonstrate the modulation of an optical carrier by a microwave field, a crucial feature for microwave-to-optical frequency conversion. This effect appears coherent, though the current experiments are limited by the resolution of the FPE. An obvious future direction is to perform more detailed measurements of the coherence using e.g. homodyne detection of the optical beat signal. Furthermore, Hanbury Brown Twiss-type measurements, would provide information on the quantum statistics of the generated light, which may be modified by effects such as microwave induced dipole-dipole interactions between excitons [46]. For the measurements of photon statistics, the SHG regime may not be the best choice, as the SHG is coherently generated. Here, the PL regime (preliminary results in section 6.3) may be more suited for quantum optical measurements.

The polarisation dependent measurements showed it is possible to determine the direction of the microwave field in the material. Combining this with the linear dependence on microwave power (at low microwave powers) and the fact that the sidebands are separated from the carrier by the microwave frequency could allow Cu_2O to be used for detecting and characterising the magnitude, polarisation and frequency of microwave fields.

Furthermore, Cu_2O could be used to image microwave fields. As shown in the section 6.1.1 at some excitation energies the change in one-photon absorption can be more than 10%. By illuminating the sample with a single frequency laser tuned to the correct excitation energy it should be possible to image the spatial dependence of the microwave field induced change in absorption. Due to the large (more than 10%) change in absorption and fast response times (on the order of nanoseconds) this could be performed at high frame rates. It should be noted however, that the wavelength of the microwave field at 20 GHz is ≈ 1.5 cm in vacuum and so unless larger samples were used, cuprous oxide would be most useful for imaging in the near field. This method could be combined with the polarisation measurements to characterise the near field of cryogenic microwave devices, such as superconducting resonators.

In summary, the coupling between Rydberg excitons and microwave electric fields has been studied using one-photon and two-photon spectroscopy techniques. Despite the inefficient microwave coupling, a significant effect is observed and the coherent modulation of an optical carrier was achieved. In the short term, this work provides a new

tool for manipulating Rydberg exciton states. Longer term this tool could be useful for microwave sensing or near field imaging of cryogenic microwave devices. With the introduction of a microwave resonator we expect to reach the strong driving regime, where this control will extend to many-body physics and quantum states of light.

Conclusions

In this thesis, Rydberg excitons in cuprous oxide were studied using both optical and microwave spectroscopy techniques. An experimental platform to perform one and two-photon spectroscopy of Rydberg excitons was developed. Details of the experimental apparatus were given in chapter 3.

In chapter 4 the samples were characterised using both one-photon absorption and PL spectroscopy. One sample was found to be of higher quality than the others, exhibiting an absorption spectrum with states up to $n = 14$ along with the highest quality PL spectrum. Here, the observation of higher n states was limited by the experimental setup rather than the sample itself. The spatial dependence of the absorption spectrum was also studied. It was found that the sample with highest quality Rydberg spectrum also showed the least spatial variation. In future, the spatial imaging technique presented in this chapter could be used to characterise the effects of structures which have been engineered into the sample.

Synthetic Cu_2O samples were also studied in chapter 4. Currently, synthetic material is found to be a lower quality than the best natural samples. However, any future technological application of Cu_2O will require the ability to grow high quality synthetic material. The synthetic material studied here was grown using a floating zone method [78]. The synthetic samples were found to have a comparable Rydberg spectrum to previous attempts to grow synthetic material [50]. However, the Rydberg spectrum was limited to $n = 10$ and showed the appearance of forbidden exciton resonances at high n. When compared to natural samples, the Rydberg lines were found to be broader in the synthetic material and less spatially homogeneous, indicating the synthetic material was strained. Using PL spectroscopy it was found that the synthetic

material exhibited a large excess of copper vacancies. Charges in the material due to the copper vacancies are the most likely cause for limiting the observation of higher n Rydberg states [48].

In future, post growth treatments could be employed to reduce the concentration of copper vacancies in the synthetic material. Previous work has shown annealing the samples can substantially reduce defect concentrations [49; 50; 172; 51]. However, growing very high quality synthetic samples will always be challenging due to the low impurity concentration that must be achieved to observe the highest n states. For the highest quality natural samples the impurity concentration is estimated to be below $0.01\,\mu\text{m}^{-3}$ [115] while the impurity concentration in the synthetic material is estimated to be more than an order of magnitude greater than this [48].

In chapter 5 two-photon excitation was used to study excitons in Cu_2O. The temporal resolution of the detector allowed the observation of a long exciton lifetime in the material. The lifetime was found to be $640 \pm 10\,\mu\text{m}$ which is almost 50 times longer than the previous longest observed lifetime, the 1S para-exciton [102]. This long lifetime was only observed in sample AB and is tentatively attributed to the bound excitons which were present in sample AB. However, future work is required to definitively characterise and identify the source of this long lifetime.

Rydberg excitons were studied using two-photon PLE spectroscopy. Using this method it was possible to observe excitons up to $n = 11$. The exciton resonances were found to sit on a non-resonant background of unknown origin. It was postulated that this background was due to a similar process as the background in one-photon spectroscopy, though further measurements are required to confirm this.

SHG spectroscopy was also used to study Rydberg excitons. This method is similar to the PLE experiment, but a filter is inserted to collect only the coherently generated second harmonic of the excitation laser. Here, states up to $n = 12$ were observed, which is the highest observed state under two-photon excitation. The narrowband spectroscopy technique allowed the lineshapes of the exciton states to be investigated. From studying the power dependence of the SHG excitation spectrum, it was clear that sample heating was an issue. The increase in sample temperature is potentially the limiting factor in observing higher n states. However, other power dependent mechanisms for generating free charges have not been ruled out. Future power dependent experiments where the peak excitation power is kept constant but the average power is varied should allow the different mechanisms to be studied. Furthermore, experiments

at a much lower average power may allow the observation of higher n states.

In the final part of chapter 5, the polarisation dependence of the SHG signal was studied. It was found that the experimental polarisation dependence did not agree with the basic polarisation model. Including a birefringent material in the optical path was enough to explain the discrepancy. The most likely candidate for the birefringence was the CaF_2 windows in the sample mount. These windows were glued into the sample mount and are believed to be exhibiting stress induced birefringence. By redesigning the sample mount, perhaps with thicker windows which are not glued in place, it should be possible to eliminate this birefringence.

Future iterations of the experiment should look at collecting SHG in the forward direction. Currently, the experimental setup is configured to collect back-scattered SHG. As SHG is a process which conserves momentum, it is preferentially generated in the forward direction. Switching to this collection geometry should drastically improve the collection efficiency, and may allow lower excitation powers to be used.

In future, the quantum statistics of the light emitted under two-photon excitation could be studied. This would provide a new tool for studying exciton-exciton interactions. As the tightly focussed two-photon excitation light is focussed to a spot smaller than the predicted blockade radius [32] the Rydberg blockade effect should lead to anti-bunching of the light emitted from the sample. The observation of anti-bunching would be the first step in creating a single-photon source based on Rydberg excitons [47]. However, the short lifetime of the Rydberg excitons may make observing anti-bunching due to Rydberg blockade challenging.

In the final chapter of this thesis, the effects of a microwave field on the Rydberg exciton spectrum were studied. The microwave-exciton coupling was studied using three excitation schemes, broadband one-photon absorption, SHG and two-photon PL. In all three cases a significant change to the Rydberg spectrum was observed and the results were modelled based on microwave-driven electric dipole transitions between Rydberg exciton states. In all of the excitation regimes it was found that the microwave frequency response was dominated by the response of the antenna. The underlying microwave frequency response was broadband, due to the nonradiative broadening of the exciton linewidths.

In the one-photon absorption experiments it was possible to estimate the microwave electric field strength. This estimation showed that even with the simple microwave antennae used in this work, it was possible to reach a regime where the Rabi frequency

of the microwave driven transition was comparable to the linewidth of the exciton states. The obvious next experimental step is to try and increase the microwave field strength and reach the strong driving limit (where the Rabi frequency exceeds the exciton linewidth). This could be achieved either through the use of a microwave amplifier, or a new antenna design, such as a copper resonator. Longer term, much higher field strengths could be achieved through the use of superconducting resonators. Once the Rabi frequency exceeds the linewidth new effects should become apparent. Multi-photon processes will become significant and effects such as microwave-induced dipole-dipole interactions may be present. It should also be noted that once the Rabi frequency exceeds the linewidth, it will also be comparable to the frequency of the transition it is driving [187], allowing a new regime to be explored. Here, Floquet theory may prove a useful tool for describing this new regime [186].

In the SHG regime it was found that the microwave field created sidebands on the second harmonic. These sidebands clearly show the modulation of an optical carrier by a microwave field. Within the resolution of the experiment, the sidebands appear coherent. In future, techniques such as homodyne detection could be used to confirm the coherence of this process. Coherent microwave-to-optical conversion has been demonstrated to varying degrees with mechanical oscillators [191; 192], nonlinear crystals [193] and Rydberg atoms [18; 28; 31; 30; 22]. Here, Rydberg excitons have the advantage of a broadband frequency response, which not only allows broadband microwave to optical conversion, but would also enable high a bandwidth.

The polarisation dependence of the microwave response was also studied. Despite the optical birefringence, this allowed the polarisation of the microwave field to be determined. In future, cuprous oxide could be used as a microwave field sensor, allowing the magnitude, frequency and polarisation of the field to be characterised. Furthermore, by optically exciting and imaging large areas of the sample, it may be possible to image microwave fields using this technique.

Looking further ahead, there is the potential to engineer an optical-to-microwave interface at the quantum level, with potential applications in quantum computing. The mapping of a single microwave photon in a cavity to a single optical photon could improve the readout of superconducting quantum circuits. Reaching the strong coupling regime for a single microwave photon in a cavity is a challenge due to the large non-radiative decay rate of the Rydberg excitons. However, the collective strong coupling regime, where a collective enhancement of the coupling strength is achieved, may be reachable [194; 195]. Coupling to a single optical photon would also be a challenge.

In one-photon spectroscopy the Rydberg states sit on the non-resonant phonon background which dominates the absorption. There are recent proposals to overcome this background using electromagnetically induced transparency [196] which could potentially be combined with the microwave spectroscopy. For read-out via SHG, the main issue is the low efficiency of the SHG process due to the centro-symmetric nature of the crystal and the absence of phase-matching. Here, the use of external fields or strain fields could be used to break the symmetry of the system and improve the efficiency of the SHG process. This could be combined with optical waveguides or resonators to increase the local pump intensity. Furthermore, phase matching can potentially be improved through exploiting polaritonic effects [146; 94].

Rydberg excitons in cuprous oxide provide an interesting platform for the exploration of Rydberg physics. The coupling of Rydberg excitons to microwave fields opens up opportunities for further study of this system, with the potential to see microwave induced interactions between exciton states. On the application side, using cuprous oxide for microwave field sensing or microwave-to-optical conversion could be considered.

The effect of the microwave field on bound exciton emission

In section 4.2 it was shown that the bound exciton states are made up of several multiplets with splittings on the order of tens of GHz. It is therefore conceivable that the microwave field could couple to the bound exciton states. If this was the case, it would change the interpretation of the results in section 6.3, where it was assumed the microwave field was coupling to the Rydberg state.

To investigate the possibility of the microwave field coupling to the bound exciton states time dependent measurements were performed. For this, the microwave field was pulsed. If the microwave-exciton coupling was occurring when the excitons were bound to a defect, then the long 640 µs lifetime of the bound states means that timing of the microwave pulse relative to the laser pulse would not influence the signal. However, if the microwave-exciton coupling occurs when the exciton is in the Rydberg state, then a response to the microwave field would only be seen when the microwave pulse coincides with the laser pulse and Rydberg excitons are present in the material.

For these time resolved measurements, the excitation laser was tuned to $E = 2.1704$ eV between the 9D and 10S resonances. The laser is pulsed into 1 ns pulses with a 10 µs period. The microwave pulse was synchronised with the laser pulse and used in two timing regimes depicted in Fig. A.1(a). Regime 1 (Fig. A.1(a)(i)) involved a 2 µs microwave pulse centred on the laser pulse. Regime 2 (Fig. A.1(a)(ii)) used an 8 µs microwave pulse which was offset such that there is no microwave field present during the laser pulse. Due to the short lifetime of the Rydberg excitons (hundreds of picoseconds) there were no Rydberg excitons present during the microwave pulse in
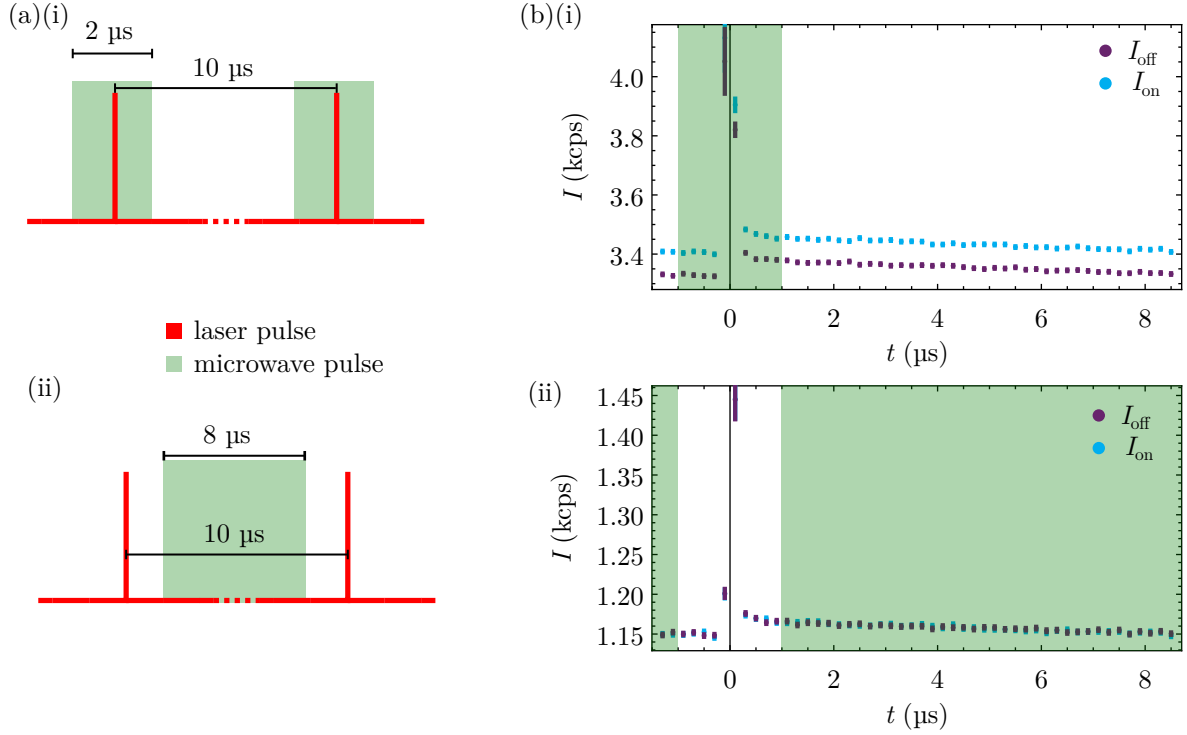
Figure A.1: Effect of microwave field on bound exciton emission. (a) Timing diagrams of the two regimes. Laser is pulsed into 1 ns pulses with a 10 µs period. Period of microwave pulses is also 10 µs. Microwave pulses are square pulses with (i) a length of 2 µs centred on the laser pulse or (ii) a length of 8 µs with no overlap with the laser pulse. (b) Histograms of photon counts vs time relative to the laser pulse with (blue) and without (purple) a microwave field at 19 GHz. Here the excitation energy is tuned to $E = 2.17104$ (between the 9D and 10S resonances) and microwave power is set to 25 mW. Shaded background shows the time when the microwave pulse is on. In (i) the microwave pulse overlaps with the laser pulse, in (ii) it does not.

regime 2.

The resulting histograms for the two timing regimes are shown in Fig. A.1(b). For reference, the histograms with no microwave field present are shown in purple. As the lifetime of the bound states (640 ± 10 µs) is considerably longer than the pulse period used in this experiment, the PL from the bound states appears constant with time. The peak at $t = 0$ is PL from the 1S ortho-exciton, which has a lifetime of a few nanoseconds [173]. The large difference in count rate between the I_{off} curves in Fig. A.1(b)(i) and (ii) is attributed to alignment differences in the experiment.

In timing regime 1 (shown in Fig. A.1(b)(i)) there is an enhancement in PL at all times, not just when the microwave pulse is applied. This is in contrast to timing regime 2 (Fig. A.1(b)(ii)) where no change is observed due to the microwave field.

This indicates the microwave field does not couple to the bound exciton states, and the exciton-microwave coupling is occurring when the excitons are in the Rydberg state, validating the approach used to construct a model in section 6.3.2.

Bibliography

[1] T. Gallagher, A. Dalgarno, C. U. Press, F. Read, and R. Zare, *Rydberg Atoms*, Cambridge Monographs on Atomic, Molecular and Chemical Physics (Cambridge University Press, 1994).

[2] J. D. Pritchard, K. J. Weatherill, and C. S. Adams, "Nonlinear optics using cold Rydberg atoms," Annual Review of Cold Atoms and Molecules: Volume 1 , 301 (2013).

[3] N. Šibalić and C. S. Adams, *Rydberg Physics*, 2399-2891 (IOP Publishing, 2018).

[4] C. S. Adams, J. D. Pritchard, and J. P. Shaffer, "Rydberg atom quantum technologies," Journal of Physics B: Atomic, Molecular and Optical Physics **53**, 012002 (2019).

[5] E. Urban, T. A. Johnson, T. Henage, L. Isenhower, D. D. Yavuz, T. G. Walker, and M. Saffman, "Observation of Rydberg blockade between two atoms," Nature Physics **5**, 110 (2009).

[6] A. Gaëtan, Y. Miroshnychenko, T. Wilk, A. Chotia, M. Viteau, D. Comparat, P. Pillet, A. Browaeys, and P. Grangier, "Observation of collective excitation of two individual atoms in the Rydberg blockade regime," Nature Physics **5**, 115 (2009).

[7] T. Wilk, A. Gaëtan, C. Evellin, J. Wolters, Y. Miroshnychenko, P. Grangier, and A. Browaeys, "Entanglement of two individual neutral atoms using Rydberg blockade," Phys. Rev. Lett. **104**, 010502 (2010).

[8] M. M. Müller, A. Kölle, R. Löw, T. Pfau, T. Calarco, and S. Montangero, "Room-temperature Rydberg single-photon source," Phys. Rev. A **87**, 053412 (2013).

[9] F. Ripka, H. Kübler, R. Löw, and T. Pfau, "A room-temperature single-photon source based on strongly interacting Rydberg atoms," Science **362**, 446 (2018).

[10] D. P. Ornelas-Huerta, A. N. Craddock, E. A. Goldschmidt, A. J. Hachtel, Y. Wang, P. Bienias, A. V. Gorshkov, S. L. Rolston, and J. V. Porto, "On-demand indistinguishable single photons from an efficient and pure source based on a Rydberg ensemble," Optica **7**, 813 (2020).

[11] C. Tresp, C. Zimmer, I. Mirgorodskiy, H. Gorniaczyk, A. Paris-Mandoki, and S. Hofferberth, "Single-photon absorber based on strongly interacting Rydberg atoms," Phys. Rev. Lett. **117**, 223001 (2016).

[12] H. Gorniaczyk, C. Tresp, J. Schmidt, H. Fedder, and S. Hofferberth, "Single-photon transistor mediated by interstate Rydberg interactions," Phys. Rev. Lett. **113**, 053601 (2014).

[13] D. Tiarks, S. Baur, K. Schneider, S. Dürr, and G. Rempe, "Single-photon transistor using a Förster resonance," Phys. Rev. Lett. **113**, 053602 (2014).

[14] H. Gorniaczyk, C. Tresp, P. Bienias, A. Paris-Mandoki, W. Li, I. Mirgorodskiy, H. P. Büchler, I. Lesanovsky, and S. Hofferberth, "Enhancement of Rydberg-mediated single-photon nonlinearities by electrically tuned Förster resonances," Nature Communications **7**, 12480 (2016).

[15] Y. M. Hao, G. W. Lin, X. M. Lin, Y. P. Niu, and S. Q. Gong, "Single-photon transistor based on cavity electromagnetically induced transparency with Rydberg atomic ensemble," Scientific Reports **9**, 4723 (2019).

[16] J. A. Sedlacek, A. Schwettmann, H. Kübler, R. Löw, T. Pfau, and J. P. Shaffer, "Microwave electrometry with Rydberg atoms in a vapour cell using bright atomic resonances," Nature Physics **8**, 819 (2012).

[17] J. A. Gordon, C. L. Holloway, A. Schwarzkopf, D. A. Anderson, S. Miller, N. Thaicharoen, and G. Raithel, "Millimeter wave detection via Autler-Townes splitting in rubidium Rydberg atoms," Applied Physics Letters **105**, 024104 (2014).

[18] H. Fan, S. Kumar, J. Sedlacek, H. Kübler, S. Karimkashi, and J. P. Shaffer, "Atom based RF electric field sensing," Journal of Physics B: Atomic, Molecular and Optical Physics **48**, 202001 (2015).

[19] C. G. Wade, N. Šibalić, N. R. de Melo, J. M. Kondo, C. S. Adams, and K. J. Weatherill, "Real-time near-field terahertz imaging with atomic optical fluorescence," Nature Photonics **11**, 40 (2017).

[20] L. A. Downes, A. R. MacKellar, D. J. Whiting, C. Bourgenot, C. S. Adams, and K. J. Weatherill, "Full-field terahertz imaging at kilohertz frame rates using atomic vapor," Phys. Rev. X **10**, 011027 (2020).

[21] D. H. Meyer, Z. A. Castillo, K. C. Cox, and P. D. Kunz, "Assessment of Rydberg atoms for wideband electric field sensing," Journal of Physics B: Atomic, Molecular and Optical Physics **53**, 034001 (2020).

[22] A. Chopinaud and J. Pritchard, "Optimal state choice for Rydberg-atom microwave sensors," Phys. Rev. Applied **16**, 024008 (2021).

[23] M. Brune, S. Haroche, V. Lefevre, J. M. Raimond, and N. Zagury, "Quantum nondemolition measurement of small photon numbers by Rydberg-atom phase-sensitive detection," Phys. Rev. Lett. **65**, 976 (1990).

[24] J. M. Raimond, M. Brune, and S. Haroche, "Manipulating quantum entanglement with atoms and photons in a cavity," Rev. Mod. Phys. **73**, 565 (2001).

[25] S. D. Hogan, J. A. Agner, F. Merkt, T. Thiele, S. Filipp, and A. Wallraff, "Driving Rydberg-Rydberg transitions from a coplanar microwave waveguide," Phys. Rev. Lett. **108**, 063004 (2012).

[26] A. A. Morgan and S. D. Hogan, "Coupling Rydberg atoms to microwave fields in a superconducting coplanar waveguide resonator," Phys. Rev. Lett. **124**, 193604 (2020).

[27] H. Hattermann, D. Bothner, L. Y. Ley, B. Ferdinand, D. Wiedmaier, L. Sárkány, R. Kleiner, D. Koelle, and J. Fortágh, "Coupling ultracold atoms to a superconducting coplanar waveguide resonator," Nature Communications **8**, 2254 (2017).

[28] B. T. Gard, K. Jacobs, R. McDermott, and M. Saffman, "Microwave-to-optical frequency conversion using a cesium atom coupled to a superconducting resonator," Phys. Rev. A **96**, 013833 (2017).

[29] N. Daniilidis and H. Häffner, "Quantum interfaces between atomic and solid-state systems," Annual Review of Condensed Matter Physics **4**, 83 (2013).

[30] D. Petrosyan, K. Mølmer, J. Fortágh, and M. Saffman, "Microwave to optical conversion with atoms on a superconducting chip," New Journal of Physics **21**, 073033 (2019).

[31] J. Han, T. Vogt, C. Gross, D. Jaksch, M. Kiffner, and W. Li, "Coherent microwave-to-optical conversion via six-wave mixing in Rydberg atoms," Phys. Rev. Lett. **120**, 093201 (2018).

[32] T. Kazimierczuk, D. Fröhlich, S. Scheel, H. Stolz, and M. Bayer, "Giant Rydberg excitons in the copper oxide Cu_2O," Nature **514**, 343 (2014).

[33] M. A. M. Versteegh, S. Steinhauer, J. Bajo, T. Lettner, A. Soro, A. Romanova, S. Gyger, L. Schweickert, A. Mysyrowicz, and V. Zwiller, "Giant Rydberg excitons in Cu_2O probed by photoluminescence excitation spectroscopy," (2021), arXiv:2105.07942 [cond-mat.mes-hall] .

[34] J. Frenkel, "On the transformation of light into heat in solids. I," Phys. Rev. **37**, 17 (1931).

[35] G. H. Wannier, "The structure of electronic excitation levels in insulating crystals," Phys. Rev. **52**, 191 (1937).

[36] M. Hayashi and K. Katsuki, "Absorption spectrum of cuprous oxide," Journal of the Physical Society of Japan **5**, 380B (1950).

[37] M. Hayashi and K. Katsuki, "Hydrogen-like absorption spectrum of cuprous oxide," Journal of the Physical Society of Japan **7**, 599 (1952).

[38] E. F. Gross, "Optical spectrum of excitons in the crystal lattice," Il Nuovo Cimento **3**, 672 (1956).

[39] V. T. Agekyan, "Spectroscopic properties of semiconductor crystals with direct forbidden energy gap," physica status solidi (a) **43**, 11 (1977).

[40] M. A. Washington, A. Z. Genack, H. Z. Cummins, R. H. Bruce, A. Compaan, and R. A. Forman, "Spectroscopy of excited yellow exciton states in Cu_2O by forbidden resonant Raman scattering," Phys. Rev. B **15**, 2145 (1977).

[41] G. M. Kavoulakis, Y.-C. Chang, and G. Baym, "Fine structure of excitons in Cu$_2$O," Phys. Rev. B **55**, 7593 (1997).

[42] S. B. Nam, D. C. Reynolds, C. W. Litton, R. J. Almassy, T. C. Collins, and C. M. Wolfe, "Free-exciton energy spectrum in GaAs," Phys. Rev. B **13**, 761 (1976).

[43] B. K. Meyer, A. Polity, D. Reppin, M. Becker, P. Hering, B. Kramm, P. J. Klar, T. Sander, C. Reindl, C. Heiliger, M. Heinemann, C. Müller, and C. Ronning, "Chapter six - the physics of copper oxide (Cu$_2$O)," in *Oxide Semiconductors*, Semiconductors and Semimetals, Vol. 88, edited by B. G. Svensson, S. J. Pearton, and C. Jagadish (Elsevier, 2013) pp. 201 – 226.

[44] V. Walther, S. O. Krüger, S. Scheel, and T. Pohl, "Interactions between Rydberg excitons in Cu$_2$O," Phys. Rev. B **98**, 165201 (2018).

[45] J. Heckötter, V. Walther, S. Scheel, M. Bayer, T. Pohl, and M. Aßmann, "Asymmetric Rydberg blockade of giant excitons in cuprous oxide," Nature Communications **12**, 3556 (2021).

[46] V. Walther, R. Johne, and T. Pohl, "Giant optical nonlinearities from Rydberg excitons in semiconductor microcavities," Nature Communications **9**, 1309 (2018).

[47] M. Khazali, K. Heshami, and C. Simon, "Single-photon source based on Rydberg exciton blockade," Journal of Physics B: Atomic, Molecular and Optical Physics **50**, 215301 (2017).

[48] S. O. Krüger, H. Stolz, and S. Scheel, "Interaction of charged impurities and Rydberg excitons in cuprous oxide," Phys. Rev. B **101**, 235204 (2020).

[49] R. D. Schmidt-Whitley, M. Martinez-Clemente, and A. Revcolevschi, "Growth and microstructural control of single crystal cuprous oxide Cu$_2$O," Journal of Crystal Growth **23**, 113 (1974).

[50] T. Ito, H. Yamaguchi, K. Okabe, and T. Masumi, "Single-crystal growth and characterization of Cu$_2$O and CuO," Journal of Materials Science **33**, 3555 (1998).

[51] K. B. Chang, L. Frazer, J. J. Schwartz, J. B. Ketterson, and K. R. Poeppelmeier, "Removal of copper vacancies in cuprous oxide single crystals grown by the floating zone method," Crystal Growth & Design **13**, 4914 (2013).

[52] L. Frazer, E. J. Lenferink, K. B. Chang, K. R. Poeppelmeier, N. P. Stern, and J. B. Ketterson, "Evaluation of defects in cuprous oxide through exciton luminescence imaging," Journal of Luminescence **159**, 294 (2015).

[53] N. Naka, S. Hashimoto, and T. Ishihara, "Thin films of single-crystal cuprous oxide grown from the melt," Japanese Journal of Applied Physics **44**, 5096 (2005).

[54] C. Malerba, F. Biccari, C. Leonor Azanza Ricardo, M. D'Incau, P. Scardi, and A. Mittiga, "Absorption coefficient of bulk and thin film Cu_2O," Solar Energy Materials and Solar Cells **95**, 2848 (2011).

[55] K. Iwamitsu, S. Aihara, A. Ota, F. Ichikawa, T. Shimamoto, and I. Akai, "Stress effects on nP yellow excitons in Cu_2O thin films recrystallized epitaxially in a sample gap between paired MgO substrates," Journal of the Physical Society of Japan **83**, 124714 (2014).

[56] K. Iwamitsu, S. Aihara, M. Okada, and I. Akai, "Bayesian analysis of an excitonic absorption spectrum in a Cu_2O thin film sandwiched by paired MgO plates," Journal of the Physical Society of Japan **85**, 094716 (2016).

[57] S. Steinhauer, M. A. M. Versteegh, S. Gyger, A. W. Elshaari, B. Kunert, A. Mysyrowicz, and V. Zwiller, "Rydberg excitons in Cu_2O microcrystals grown on a silicon platform," Communications Materials **1**, 11 (2020).

[58] K. Orfanakis, S. K. Rajendran, H. Ohadi, S. Zielińska-Raczyńska, G. Czajkowski, K. Karpiński, and D. Ziemkiewicz, "Quantum confined Rydberg excitons in Cu_2O nanoparticles," Phys. Rev. B **103**, 245426 (2021).

[59] P. W. Baumeister, "Optical absorption of cuprous oxide," Phys. Rev. **121**, 359 (1961).

[60] F. Schöne, H. Stolz, and N. Naka, "Phonon-assisted absorption of excitons in Cu_2O," Phys. Rev. B **96**, 115207 (2017).

[61] D. Fröhlich, A. Nöthe, and K. Reimann, "Observation of the resonant optical Stark effect in a semiconductor," Phys. Rev. Lett. **55**, 1335 (1985).

[62] D. Fröhlich, K. Reimann, and R. Wille, "Optical Stark effect of excitons in semiconductors," Journal of Luminescence **38**, 235 (1987).

[63] D. H. Fröhlich, C. Neumann, B. Uebbing, and R. H. Wille, "Three-level optical Stark effect in semiconductors," in *Nonlinear Optical Materials and Devices for Photonic Switching*, Vol. 1216, edited by N. Peyghambarian, International Society for Optics and Photonics (SPIE, 1990) pp. 198 – 205.

[64] D. Fröhlich, C. Neumann, B. Uebbing, and R. Wille, "Experimental investigation of three-level optical Stark effect in semiconductors," physica status solidi (b) **159**, 297 (1990).

[65] M. Jörger, E. Tsitsishvili, T. Fleck, and C. Klingshirn, "Infrared absorption by excitons in Cu_2O," physica status solidi (b) **238**, 470 (2003).

[66] F. Bassani, G. La Rocca, and M. Artoni, "Electromagnetically induced transparency in bulk and microcavity semiconductors," Journal of Luminescence **110**, 174 (2004).

[67] M. Kuwata-Gonokami, M. Kubouchi, R. Shimano, and A. Mysyrowicz, "Time-resolved excitonic Lyman spectroscopy of Cu_2O," Journal of the Physical Society of Japan **73**, 1065 (2004).

[68] M. Kubouchi, K. Yoshioka, R. Shimano, A. Mysyrowicz, and M. Kuwata-Gonokami, "Study of orthoexciton-to-paraexciton conversion in Cu_2O by excitonic Lyman spectroscopy," Phys. Rev. Lett. **94**, 016403 (2005).

[69] T. Tayagaki, A. Mysyrowicz, and M. Kuwata-Gonokami, "The yellow excitonic series of Cu_2O revisited by Lyman spectroscopy," Journal of the Physical Society of Japan **74**, 1423 (2005).

[70] R. Huber, B. A. Schmid, Y. R. Shen, D. S. Chemla, and R. A. Kaindl, "Stimulated terahertz emission from intraexcitonic transitions in Cu_2O," Phys. Rev. Lett. **96**, 017402 (2006).

[71] K. Yoshioka, T. Ideguchi, and M. Kuwata-Gonokami, "Laser-based continuous-wave excitonic Lyman spectroscopy in Cu_2O," Phys. Rev. B **76**, 033204 (2007).

[72] R. Huber, B. A. Schmid, R. A. Kaindl, and D. S. Chemla, "Femtosecond THz studies of intra-excitonic transitions," physica status solidi (b) **245**, 1041 (2008).

[73] K. Yoshioka, T. Ideguchi, A. Mysyrowicz, and M. Kuwata-Gonokami, "Quantum inelastic collisions between paraexcitons in Cu_2O," Phys. Rev. B **82**, 041201 (2010).

[74] K. Yoshioka and M. Kuwata-Gonokami, "Relaxation explosion of a quantum degenerate exciton gas in Cu_2O," New Journal of Physics **14** (2012).

[75] E. Brekke, J. O. Day, and T. G. Walker, "Excitation suppression due to interactions between microwave-dressed Rydberg atoms," Phys. Rev. A **86**, 033406 (2012).

[76] S. Sevinçli and T. Pohl, "Microwave control of Rydberg atom interactions," New Journal of Physics **16**, 123036 (2014).

[77] L. A. P. Gallagher, J. P. Rogers, J. D. Pritchett, R. A. Mistry, D. Pizzey, C. S. Adams, M. P. A. Jones, P. Grünwald, V. Walther, C. Hodges, W. Langbein, and S. A. Lynch, "Microwave-optical coupling via Rydberg excitons in cuprous oxide," Phys. Rev. Research **4**, 013031 (2022).

[78] S. A. Lynch, C. Hodges, S. Mandal, W. Langbein, R. P. Singh, L. A. P. Gallagher, J. D. Pritchett, D. Pizzey, J. P. Rogers, C. S. Adams, and M. P. A. Jones, "Rydberg excitons in synthetic cuprous oxide Cu_2O," Phys. Rev. Materials **5**, 084602 (2021).

[79] J. P. Rogers, L. A. P. Gallagher, D. Pizzey, J. D. Pritchett, C. S. Adams, M. P. A. Jones, C. Hodges, W. Langbein, and S. A. Lynch, "High resolution nanosecond spectroscopy of even-parity Rydberg excitons in Cu_2O," (2021), arXiv:2111.13062 [cond-mat.mes-hall] .

[80] M. Cardona and Y. Y. Peter, *Fundamentals of semiconductors*, 4th ed. (Springer, 2005).

[81] G. F. Koster, *Properties of the thirty-two point groups* (M.I.T. Press, Cambridge, Mass., 1963).

[82] L. O. Grondahl and P. H. Geiger, "A new electronic rectifier," Journal of the A.I.E.E. **46**, 215 (1927).

[83] L. O. Grondahl, "The copper-cuprous-oxide rectifier and photoelectric cell," Rev. Mod. Phys. **5**, 141 (1933).

[84] L.-C. Chen, "Review of preparation and optoelectronic characteristics of Cu_2O-based solar cells with nanostructure," Materials Science in Semiconductor Processing **16**, 1172 (2013), Advanced Oxides for Electronics.

[85] J. Dahl and A. Switendick, "Energy bands in cuprous oxide," Journal of Physics and Chemistry of Solids **27**, 931 (1966).

[86] L. Kleinman and K. Mednick, "Self-consistent energy bands of Cu_2O," Phys. Rev. B **21**, 1549 (1980).

[87] J. Robertson, "Electronic structure and x-ray near-edge core spectra of Cu_2O," Physical Review B **28**, 3378 (1983).

[88] M. French, R. Schwartz, H. Stolz, and R. Redmer, "Electronic band structure of Cu_2O by spin density functional theory," Journal of Physics: Condensed Matter **21**, 015502 (2008).

[89] S. Brahms and S. Nikitine, "Intrinsic absorption and reflection of cuprous oxide in the 2.5 to 6.5 ev region," Solid State Communications **3**, 209 (1965).

[90] A. Daunois, J. Deiss, and B. Meyer, "Étude spectrophotométrique de l'absorption bleue et violette de Cu_2O," Journal de Physique **27**, 142 (1966).

[91] R. Forman, W. Brower, and H. Parker, "Phonons and the green exciton series in cuprous oxide, Cu_2O," Physics Letters A **36**, 395 (1971).

[92] P. Rommel, J. Main, A. Farenbruch, J. Mund, D. Fröhlich, D. R. Yakovlev, M. Bayer, and C. Uihlein, "Second harmonic generation of cuprous oxide in magnetic fields," Phys. Rev. B **101**, 115202 (2020).

[93] J. Schmutzler, D. Fröhlich, and M. Bayer, "Signatures of coherent propagation of blue polaritons in Cu_2O," Phys. Rev. B **87**, 245202 (2013).

[94] A. Farenbruch, D. Fröhlich, H. Stolz, D. R. Yakovlev, and M. Bayer, "Second-harmonic generation of blue series excitons and magnetoexcitons in Cu_2O," Phys. Rev. B **104**, 075203 (2021).

[95] M. Takahata and N. Naka, "Photoluminescence properties of the entire excitonic series in Cu_2O," Phys. Rev. B **98**, 195205 (2018).

[96] S. O. Krüger and S. Scheel, "Interseries transitions between Rydberg excitons in Cu_2O," Phys. Rev. B **100**, 085201 (2019).

[97] P. Rommel, J. Main, S. O. Krüger, and S. Scheel, "Interseries dipole transitions from yellow to green excitons in cuprous oxide," Phys. Rev. B **104**, 085204 (2021).

[98] T. Itoh and S.-i. Narita, "Analysis of wavelength derivative spectra of exciton in Cu$_2$O," Journal of the Physical Society of Japan **39**, 140 (1975).

[99] J. L. Lin and J. P. Wolfe, "Bose-Einstein condensation of paraexcitons in stressed Cu$_2$O," Phys. Rev. Lett. **71**, 1222 (1993).

[100] D. Snoke, "Spontaneous Bose coherence of excitons and polaritons," Science **298**, 1368 (2002).

[101] D. Snoke and G. M. Kavoulakis, "Bose–Einstein condensation of excitons in Cu$_2$O: progress over 30 years," Reports on Progress in Physics **77**, 116501 (2014).

[102] A. Mysyrowicz, D. Hulin, and A. Antonetti, "Long exciton lifetime in Cu$_2$O," Phys. Rev. Lett. **43**, 1123 (1979).

[103] J. W. Hodby, T. E. Jenkins, C. Schwab, H. Tamura, and D. Trivich, "Cyclotron resonance of electrons and of holes in cuprous oxide, Cu$_2$O," Journal of Physics C: Solid State Physics **9**, 1429 (1976).

[104] N. Naka, I. Akimoto, M. Shirai, and K.-i. Kan'no, "Time-resolved cyclotron resonance in cuprous oxide," Phys. Rev. B **85**, 035209 (2012).

[105] G. Macfarlane, T. McLean, J. Quarrington, and V. Roberts, "Exciton and phonon effects in the absorption spectra of germanium and silicon," Journal of Physics and Chemistry of Solids **8**, 388 (1959).

[106] J. Heckötter, M. Freitag, D. Fröhlich, M. Aßmann, M. Bayer, M. A. Semina, and M. M. Glazov, "High-resolution study of the yellow excitons in Cu$_2$O subject to an electric field," Phys. Rev. B **95**, 035210 (2017).

[107] J. Heckötter, M. Freitag, D. Fröhlich, M. Aßmann, M. Bayer, M. A. Semina, and M. M. Glazov, "Dissociation of excitons in Cu$_2$O by an electric field," Phys. Rev. B **98**, 035150 (2018).

[108] J. Heckötter, M. Freitag, D. Fröhlich, M. Aßmann, M. Bayer, M. A. Semina, and M. M. Glazov, "Influence of the wavefunction distribution on exciton dissociation in electric field," Physics of the Solid State **60**, 1506 (2018).

[109] J. Heckötter, D. Fröhlich, M. Aßmann, and M. Bayer, "Influence of magnetic confinement on the yellow excitons in cuprous oxide subject to an electric field," Physics of the Solid State **60**, 1595 (2018).

[110] J. Heckötter, J. Thewes, D. Fröhlich, M. Aßmann, and M. Bayer, "Landau-level quantization of the yellow excitons in cuprous oxide," Physics of the Solid State **60**, 1625 (2018).

[111] P. Rommel, F. Schweiner, J. Main, J. Heckötter, M. Freitag, D. Fröhlich, K. Lehninger, M. Aßmann, and M. Bayer, "Magneto-Stark effect of yellow excitons in cuprous oxide," Phys. Rev. B **98**, 085206 (2018).

[112] J. Heckötter, P. Rommel, J. Main, M. Aßmann, and M. Bayer, "Analysis of the fine structure of the *D*-exciton shell in cuprous oxide," physica status solidi (RRL) – Rapid Research Letters **15**, 2100335 (2021).

[113] M. Aßmann, J. Thewes, D. Fröhlich, and M. Bayer, "Quantum chaos and breaking of all anti-unitary symmetries in Rydberg excitons," Nature Materials **15**, 741 (2016).

[114] M. Freitag, J. Heckötter, M. Bayer, and M. Aßmann, "Role of phonons in the quantum chaos of Rydberg excitons," Phys. Rev. B **95**, 155204 (2017).

[115] J. Heckötter, M. Freitag, D. Fröhlich, M. Aßmann, M. Bayer, P. Grünwald, F. Schöne, D. Semkat, H. Stolz, and S. Scheel, "Rydberg excitons in the presence of an ultralow-density electron-hole plasma," Phys. Rev. Lett. **121**, 097401 (2018).

[116] J. Heckötter, M. Freitag, M. Aßmann, D. Fröhlich, M. Bayer, P. Grünwald, and S. Scheel, "Critical dependence of the excitonic absorption in cuprous oxide on experimental parameters," Physics of the Solid State **60**, 1618 (2018).

[117] J. Heckötter, D. Janas, R. Schwartz, M. Aßmann, and M. Bayer, "Experimental limitation in extending the exciton series in Cu_2O towards higher principal quantum numbers," Phys. Rev. B **101**, 235207 (2020).

[118] W. E. Lamb and R. C. Retherford, "Fine structure of the hydrogen atom by a microwave method," Phys. Rev. **72**, 241 (1947).

[119] C. Uihlein, D. Fröhlich, and R. Kenklies, "Investigation of exciton fine structure in Cu_2O," Phys. Rev. B **23**, 2731 (1981).

[120] F. Schweiner, J. Main, and G. Wunner, "Linewidths in excitonic absorption spectra of cuprous oxide," Phys. Rev. B **93**, 085203 (2016).

[121] F. Schöne, S.-O. Krüger, P. Grünwald, H. Stolz, S. Scheel, M. Aßmann, J. Heck-ötter, J. Thewes, D. Fröhlich, and M. Bayer, "Deviations of the exciton level spectrum in Cu_2O from the hydrogen series," Phys. Rev. B **93**, 075203 (2016).

[122] F. Schöne, S.-O. Krüger, P. Grünwald, M. Aßmann, J. Heckötter, J. Thewes, H. Stolz, D. Fröhlich, M. Bayer, and S. Scheel, "Coupled valence band dispersions and the quantum defect of excitons in Cu_2O," Journal of Physics B: Atomic, Molecular and Optical Physics **49**, 134003 (2016).

[123] F. Schweiner, J. Main, G. Wunner, and C. Uihlein, "Even exciton series in Cu_2O," Phys. Rev. B **95**, 195201 (2017).

[124] A. Baldereschi and N. O. Lipari, "Spherical model of shallow acceptor states in semiconductors," Phys. Rev. B **8**, 2697 (1973).

[125] A. Baldereschi and N. O. Lipari, "Cubic contributions to the spherical model of shallow acceptor states," Phys. Rev. B **9**, 1525 (1974).

[126] A. Farenbruch, D. Fröhlich, D. R. Yakovlev, and M. Bayer, "Rydberg series of dark excitons in Cu_2O," Phys. Rev. Lett. **125**, 207402 (2020).

[127] F. Schweiner, J. Ertl, J. Main, G. Wunner, and C. Uihlein, "Exciton-polaritons in cuprous oxide: Theory and comparison with experiment," Phys. Rev. B **96**, 245202 (2017).

[128] C. Foot, *Atomic Physics*, Oxford Master Series in Physics (OUP Oxford, 2004).

[129] S. O. Krüger, *Rydberg excitons in external fields*, Ph.D. thesis, Universität Rostock (2020).

[130] R. J. Elliott, "Symmetry of excitons in Cu_2O," Phys. Rev. **124**, 340 (1961).

[131] J. Thewes, J. Heckötter, T. Kazimierczuk, M. Aßmann, D. Fröhlich, M. Bayer, M. A. Semina, and M. M. Glazov, "Observation of high angular momentum excitons in cuprous oxide," Phys. Rev. Lett. **115**, 027402 (2015).

[132] A. M. Konzelmann, S. O. Krüger, and H. Giessen, "Interaction of orbital angular momentum light with Rydberg excitons: Modifying dipole selection rules," Physical Review B **100**, 115308 (2019).

[133] P. Rommel, P. Zielinski, and J. Main, "Green exciton series in cuprous oxide," Phys. Rev. B **101**, 075208 (2020).

[134] R. J. Elliott, "Intensity of optical absorption by excitons," Phys. Rev. **108**, 1384 (1957).

[135] J. D. Dow and D. Redfield, "Toward a unified theory of Urbach's rule and exponential absorption edges," Phys. Rev. B **5**, 594 (1972).

[136] S. John, C. Soukoulis, M. H. Cohen, and E. N. Economou, "Theory of electron band tails and the Urbach optical-absorption edge," Phys. Rev. Lett. **57**, 1777 (1986).

[137] Y. Toyozawa, "Theory of line-shapes of the exciton absorption bands," Progress of Theoretical Physics **20**, 53 (1958).

[138] Y. Toyozawa, "Interband effect of lattice vibrations in the exciton absorption spectra," Journal of Physics and Chemistry of Solids **25**, 59 (1964).

[139] H. Stolz, F. Schöne, and D. Semkat, "Interaction of Rydberg excitons in cuprous oxide with phonons and photons: optical linewidth and polariton effect," New Journal of Physics **20**, 023019 (2018).

[140] U. Fano, "Effects of configuration interaction on intensities and phase shifts," Phys. Rev. **124**, 1866 (1961).

[141] J. Mund, D. Fröhlich, D. R. Yakovlev, and M. Bayer, "High-resolution second harmonic generation spectroscopy with femtosecond laser pulses on excitons in Cu_2O," Phys. Rev. B **98**, 085203 (2018).

[142] J. Mund, C. Uihlein, D. Fröhlich, D. R. Yakovlev, and M. Bayer, "Second harmonic generation on the yellow $1S$ exciton in Cu_2O in symmetry-forbidden geometries," Phys. Rev. B **99**, 195204 (2019).

[143] A. Farenbruch, J. Mund, D. Fröhlich, D. R. Yakovlev, M. Bayer, M. A. Semina, and M. M. Glazov, "Magneto-Stark and Zeeman effect as origin of second harmonic generation of excitons in Cu_2O," Phys. Rev. B **101**, 115201 (2020).

[144] R. W. Boyd, *Nonlinear Optics, Third Edition*, 3rd ed. (Academic Press, Inc., USA, 2008).

[145] C. S. Adams and I. G. Hughes, "Optics f2f: From Fourier to Fresnel," (Oxford University Press, Oxford, 2018) Chap. 13.

[146] D. Fröhlich, G. Dasbach, G. Baldassarri Höger von Högersthal, M. Bayer, R. Klieber, D. Suter, and H. Stolz, "High resolution spectroscopy of yellow 1S excitons in Cu_2O," Solid State Communications **134**, 139 (2005), spontaneous Coherence in Excitonic Systems.

[147] C. J. Hawthorn, K. P. Weber, and R. E. Scholten, "Littrow configuration tunable external cavity diode laser with fixed direction output beam," Review of Scientific Instruments **72**, 4477 (2001).

[148] C. Petridis, I. D. Lindsay, D. J. M. Stothard, and M. Ebrahimzadeh, "Mode-hop-free tuning over 80 GHz of an extended cavity diode laser without antireflection coating," Review of Scientific Instruments **72**, 3811 (2001).

[149] A. Köhler, "New method of illumination for photomicrographical purposes," Journal of the Royal Microscopical Society **14**, 261 (1894).

[150] G. D. Boyd and D. A. Kleinman, "Parametric interaction of focused Gaussian light beams," Journal of Applied Physics **39**, 3597 (1968).

[151] D. E. Zelmon, D. L. Small, and D. Jundt, "Infrared corrected Sellmeier coefficients for congruently grown lithium niobate and 5 mol.% magnesium oxide–doped lithium niobate," J. Opt. Soc. Am. B **14**, 3319 (1997).

[152] C. Sandfort, J. Brandt, C. Finke, D. Fröhlich, M. Bayer, H. Stolz, and N. Naka, "Paraexcitons of Cu_2O confined by a strain trap and high magnetic fields," Phys. Rev. B **84**, 165215 (2011).

[153] S. O. Krüger and S. Scheel, "Waveguides for Rydberg excitons in Cu_2O from strain traps," Phys. Rev. B **97**, 205208 (2018).

[154] J. Jang and J. Wolfe, "Exciton decay in Cu_2O at high density and low temperature: Auger recombination, spin–flip scattering, and molecule formation," Solid State Communications **137**, 91 (2006).

[155] D. P. Trauernicht, A. Mysyrowicz, and J. P. Wolfe, "Strain confinement and thermodynamics of free excitons in a direct-gap semiconductor," Phys. Rev. B **28**, 3590 (1983).

[156] D. P. Trauernicht, J. P. Wolfe, and A. Mysyrowicz, "Thermodynamics of strain-confined paraexcitons in Cu_2O," Phys. Rev. B **34**, 2561 (1986).

[157] N. Naka and N. Nagasawa, "Nonlinear paraexciton kinetics in a potential trap in Cu_2O under two-photon resonance excitation," Phys. Rev. B **65**, 245203 (2002).

[158] N. Naka and N. Nagasawa, "Two-photon tomography of strain-induced potential wells of excitons in Cu_2O," Phys. Rev. B **70**, 155205 (2004).

[159] A. Compaan and H. Z. Cummins, "Raman scattering, luminescence, and exciton-phonon coupling in Cu_2O," Phys. Rev. B **6**, 4753 (1972).

[160] Y. Petroff, P. Y. Yu, and Y. R. Shen, "Study of photoluminescence in Cu_2O," Phys. Rev. B **12**, 2488 (1975).

[161] T. Ito and T. Masumi, "Detailed examination of relaxation processes of excitons in photoluminescence spectra of Cu_2O," Journal of the Physical Society of Japan **66**, 2185 (1997).

[162] K. E. O'Hara, J. R. Gullingsrud, and J. P. Wolfe, "Auger decay of excitons in Cu_2O," Physical Review B **60**, 10872 (1999).

[163] J. I. Jang, Y. Sun, B. Watkins, and J. B. Ketterson, "Bound excitons in Cu_2O: Efficient internal free exciton detector," Phys. Rev. B **74**, 235204 (2006).

[164] H. Solache-Carranco, G. Juárez-Díaz, A. Esparza-García, M. Briseño-García, M. Galván-Arellano, J. Martínez-Juárez, G. Romero-Paredes, and R. Peña-Sierra, "Photoluminescence and x-ray diffraction studies on Cu_2O," Journal of Luminescence **129**, 1483 (2009).

[165] J. Li, Z. Mei, D. Ye, H. Liang, L. Liu, Y. Liu, A. Galeckas, A. Y. Kuznetsov, and X. Du, "Engineering of optically defect free Cu_2O enabling exciton luminescence at room temperature," Opt. Mater. Express **3**, 2072 (2013).

[166] J. I. Jang, K. E. O'Hara, and J. P. Wolfe, "Spin-exchange kinetics of excitons in Cu_2O: Transverse acoustic phonon mechanism," Phys. Rev. B **70**, 195205 (2004).

[167] S. Koirala, N. Naka, and K. Tanaka, "Correlated lifetimes of free paraexcitons and excitons trapped at oxygen vacancies in cuprous oxide," Journal of Luminescence **134**, 524 (2013).

[168] S. Koirala, M. Takahata, Y. Hazama, N. Naka, and K. Tanaka, "Relaxation of localized excitons by phonon emission at oxygen vacancies in $Cu_2 2O$," Journal of Luminescence **155**, 65 (2014).

[169] K. E. O'Hara, *Relaxation kinetics of excitons in cuprous oxide*, Ph.D. thesis, University of Illinois (1999).

[170] H. Stolz, R. Schwartz, F. Kieseling, S. Som, M. Kaupsch, S. Sobkowiak, D. Semkat, N. Naka, T. Koch, and H. Fehske, "Condensation of excitons in Cu_2O at ultracold temperatures: experiment and theory," New Journal of Physics **14**, 105007 (2012).

[171] J. Heckötter, M. Freitag, D. Fröhlich, M. Aßmann, M. Bayer, M. A. Semina, and M. M. Glazov, "Scaling laws of Rydberg excitons," Phys. Rev. B **96**, 125142 (2017).

[172] R. G. Kaufman and R. T. Hawkins, "Annealing of copper and oxygen vacancies in cuprous oxide films monitored by low temperature luminescence," Journal of The Electrochemical Society **133**, 2652 (1986).

[173] J. Weiner, N. Caswell, P. Yu, and A. Mysyrowicz, "Ortho- to para-exciton conversion in Cu_2O: A subnanosecond time-resolved photoluminescence study," Solid State Communications **46**, 105 (1983).

[174] B. Busson and A. Tadjeddine, "Non-uniqueness of parameters extracted from resonant second-order nonlinear optical spectroscopies," The Journal of Physical Chemistry C **113**, 21895 (2009).

[175] I. G. Hughes and T. P. A. Hase, "Measurements and their uncertainties," (Oxford University Press, Oxford, 2010) Chap. 6.

[176] J. P. Wolfe and J. I. Jang, "The search for Bose–Einstein condensation of excitons in Cu_2O: exciton-Auger recombination versus biexciton formation," New Journal of Physics **16**, 123048 (2014).

[177] K. P. O'Donnell and X. Chen, "Temperature dependence of semiconductor band gaps," Applied Physics Letters **58**, 2924 (1991).

[178] D. D. Kang, A. Gross, H. Yang, Y. Morita, K. S. Choi, K. Yoshioka, and N. Y. Kim, "Temperature study of Rydberg exciton optical properties in Cu_2O," Phys. Rev. B **103**, 205203 (2021).

[179] C. S. Adams and I. G. Hughes, "Optics f2f: From Fourier to Fresnel," (Oxford University Press, Oxford, 2018) Chap. 12.

[180] L. Novotny and B. Hecht, "Propagation and focusing of optical fields," in *Principles of Nano-Optics* (Cambridge University Press, 2006) Chap. 3, p. 45–88.

[181] H. Ling and S.-W. Lee, "Focusing of electromagnetic waves through a dielectric interface," J. Opt. Soc. Am. A **1**, 965 (1984).

[182] Y. Kitamura and N. Miyazaki, "Birefringence simulations of single crystals," Mechanical Engineering Reviews **4**, 16 (2016).

[183] R. C. Jones, "A new calculus for the treatment of optical systems. description and discussion of the calculus," J. Opt. Soc. Am. **31**, 488 (1941).

[184] D. B. Leviton, B. J. Frey, and T. J. Madison, "Temperature-dependent refractive index of CaF_2 and Infrasil 301," in *Cryogenic Optical Systems and Instruments XII*, Vol. 6692, edited by J. B. Heaney and L. G. Burriesci, International Society for Optics and Photonics (SPIE, 2007) pp. 20 – 30.

[185] S. Saikan, N. Hashimoto, T. Kushida, and K. Namba, "Variation of inverse Raman spectrum near resonance," The Journal of Chemical Physics **82**, 5409 (1985).

[186] M. G. Bason, M. Tanasittikosol, A. Sargsyan, A. K. Mohapatra, D. Sarkisyan, R. M. Potvliege, and C. S. Adams, "Enhanced electric field sensitivity of rf-dressed Rydberg dark states," New Journal of Physics **12**, 065015 (2010).

[187] J. D. R. Tommey and S. D. Hogan, "Resonant Rydberg-atom–microwave-field interactions in the ultrastrong-driving regime: Beyond the rotating-wave approximation," Phys. Rev. A **100**, 053417 (2019).

[188] H. Park, P. J. Tanner, B. J. Claessens, E. S. Shuman, and T. F. Gallagher, "Dipole-dipole broadening of Rb $ns - np$ microwave transitions," Phys. Rev. A **84**, 022704 (2011).

[189] M. Tanasittikosol, J. D. Pritchard, D. Maxwell, A. Gauguet, K. J. Weatherill, R. M. Potvliege, and C. S. Adams, "Microwave dressing of Rydberg dark states," Journal of Physics B: Atomic, Molecular and Optical Physics **44**, 184020 (2011).

[190] D. Barredo, H. Labuhn, S. Ravets, T. Lahaye, A. Browaeys, and C. S. Adams, "Coherent excitation transfer in a spin chain of three Rydberg atoms," Phys. Rev. Lett. **114**, 113002 (2015).

[191] K. Stannigel, P. Rabl, A. S. Sørensen, P. Zoller, and M. D. Lukin, "Optomechanical transducers for long-distance quantum communication," Phys. Rev. Lett. **105**, 220501 (2010).

[192] M. Forsch, R. Stockill, A. Wallucks, I. Marinkovic, C. Gärtner, R. A. Norte, F. van Otten, A. Fiore, K. Srinivasan, and S. Gröblacher, "Microwave-to-optics conversion using a mechanical oscillator in its quantum ground state," Nature Physics **16**, 69 (2020).

[193] L. Fan, C.-L. Zou, R. Cheng, X. Guo, X. Han, Z. Gong, S. Wang, and H. X. Tang, "Superconducting cavity electro-optics: A platform for coherent photon conversion between superconducting and photonic circuits," Science Advances **4** (2018).

[194] C. Weisbuch, M. Nishioka, A. Ishikawa, and Y. Arakawa, "Observation of the coupled exciton-photon mode splitting in a semiconductor quantum microcavity," Phys. Rev. Lett. **69**, 3314 (1992).

[195] F. Bernardot, P. Nussenzveig, M. Brune, J. M. Raimond, and S. Haroche, "Vacuum Rabi splitting observed on a microscopic atomic sample in a microwave cavity," Europhysics Letters (EPL) **17**, 33 (1992).

[196] V. Walther, P. Grünwald, and T. Pohl, "Controlling exciton-phonon interactions via electromagnetically induced transparency," Phys. Rev. Lett. **125**, 173601 (2020).

Colophon

This thesis is based on a template developed by Matthew Townson and Andrew Reeves. It was typeset with LaTeX 2_ε. It was created using the *memoir* package, maintained by Lars Madsen, with the *madsen* chapter style. The font used is Latin Modern, derived from fonts designed by Donald E. Kunith.